Diamond Light Source Ltd Review 2019/20

Contents

Foreword

The past year has seen Diamond rise to a series of very testing challenges, from major upgrades to ensure that it continues to offer researchers in UK universities and industry the very best opportunities for world-leading research, to the arrival of COVID-19, and to meet them all successfully.

Planning the Diamond-II programme, an integrated upgrade of the synchrotron, beamlines and computational facilities has been underway for several years, and 2019/20 saw the achievement of some significant milestones. The Conceptual Design Report for Diamond-II passed an external expert review with flying colours, a new organisational structure was established to complete all further planning stages, and a major report on deliverability and costing was completed for UKRI/STFC.

Diamond engaged with the challenges presented by COVID-19 at a very early stage, making some of the earliest high-resolution measurements on key elements of the SARS-CoV-2 virus responsible for the illness. As the impact of COVID-19 became increasingly severe in March 2020, Diamond sent almost all staff home, but managed to continue to support work on the virus as well as many other core activities, the continued planning of technical projects and the completion and roll-out of a new system for staff appraisals. Considerable challenges lie ahead for the months and perhaps years to come as plans are refined to get more staff safely back to work and to broaden support for our users. However, the ability to adapt to changing circumstances that Diamond has shown in recent months bodes very well for the future.

Professor Sir Adrian Smith
Chairman of the Board of Directors

> “The Conceptual Design Report for Diamond-II passed an external expert review with flying colours”

CEO Welcome

March 2020 saw the outbreak of Coronavirus sweeping through Europe leading to a transformation of our workplaces, economies and societies. Diamond was tested to its limits and it responded extremely well to these very different challenges, and in a manner that exemplified the organisation's strength in depth and resilience.

After delivering the Science Case for Diamond-II back in November 2018, a conceptual design report (CDR) was produced in April 2019, to provide the first design of what the new synchrotron machine would look like. In the same month, the CDR was peer-reviewed by a team of machine experts from across the Globe, receiving highly positive feedback, particularly commenting on the efficient design with regard to the number of insertion devices – photon sources points - for a ring of its size. This set us in good stead for review by the Science Advisory Committee (SAC) and the Diamond Board in the first quarter of the financial year.

After these achievements, it was clear that the Science and Technology Facilities Council (STFC) - with UK Research & Innovation (UKRI) reshuffle well underway - required adjustment of their processes. They designed a new Critical Design Review gateway process, the first of which was CD-1 where they would review our planning and proposed management of the programmes underpinning Diamond-II. This was set up to assess the readiness of programmes to progress for further consideration by UKRI and ultimately BEIS and the Treasury. Diamond are also engaging fruitfully with the Wellcome Trust to develop a case for complementary funding for Diamond-II.

Dr Laurent Chapon was appointed Director of the Diamond-II Programme and established a set of interlinking committees to guide the development of the machine and beamline elements of the Programme, underpinned by a Science Strategy Committee and overseen by a Programme Board. A model of management that will be taken forward into the next phase – the Technical Design Report.

The Diamond-II upgrade programme is centred on the transformation of the storage ring through a new technology that offers up to 100 times increase in brightness and coherence at the highest energies. Diamond has developed its own unique design for the storage ring that offers transformational improvements in capacity and, potentially serving many more users through additional, flagship beamlines, while also offering step-changes in Diamond's ability to support *operando* experiments, probing processes and operating devices directly, accelerating the speed of materials and drug discovery, and opening up spectroscopy to detect much heavier elements, many of which are involved in nuclear waste storage and remediation processes. The CD-1 report was delivered in early April 2020.

At the end of the financial year, Diamond had to prepare transformational changes in anticipation of the impact of COVID-19 on its operations. A dedicated response team rapidly identified the key issues in ensuring the safety and wellbeing of staff, planning for almost all of them to switch to home working while still operating the facility in a much reduced capacity specifically for COVID-19 related research.

Having designed a unique offer to the structural biology community, it became clear that our facilities were to play a key role in helping advance knowledge on the virus. From high resolution structural information on the key components of the virus, like the proteases from both synchrotron and CryoEM techniques, to the work of the XChem fragment screening facility which started identifying small molecules that could provide some of the building blocks for drugs to inhibit the virus' infection cycle. Such work has attracted strong interest from the press and a dedicated website set up by Diamond to inform the public about the structural biology involved and Diamond's contribution had received well over 1 million visits by April 2020.

With a large, and growing userbase we have seen a rapidly swelling number of peer-reviewed journal articles, reaching a total of 9,000 in March 2020. It is a time to pause and reflect on the achievements made by our funding agencies STFC and the Wellcome Trust, whose respective commitment have been rewarded with brilliant science as the output of Diamond surpasses the previous UK synchrotron, the Synchrotron Radiation Source at Daresbury, which achieved 5,000 peer-review publications throughout its lifetime 1981-2008 with a total of 30 beamlines. To date, Diamond has 32 operational beamlines, and in less than 15 years, has achieved 9,000 publications. However, Diamond's output is not just characterised by volume: the facility h-index[1] currently stands at 150, and a recent analysis showed that 25% of publications are found in journals with an impact factor of nine and above. The recent completion of the Phase III instrument programme has added 10 beamlines, which ensures that the investment in Diamond fully maximises return on the initial capital investment.

Diamond's 9,000th paper was reached with work led by researchers from Aalto University in Finland through measurements on the high throughput Small Angle X-ray Scattering (SAXS) beamline (B21). The research presented new insights into colloidal materials that had been developed to store heat reversibly through a physical transformation in their structure, providing an efficient method to store energy when it is freely available – for example from the sun on a bright day – and release it when required.

Diamond continued to highlight the fascinating research achieved throughout the year. One example, high resolution imaging obtained on the Joint Engineering, Environmental and Processing (JEEP) beamline (I12), is helping scientists from the University of Kentucky to develop an image-enhancing computational technique. This aims to develop a method to distinguish carbon-based ink from carbonised papyri of 2,000 year old scrolls from the Herculaneum collection held by the Institut de France. The prospect of being able to read the writing hidden inside these exceptionally precious and fragile artefacts gripped the public's imagination, with over 700 pieces of news coverage being generated globally to date.

The lifeblood of Diamond is the staff we employ, the students we train and the users we attract. Diamond is finding it increasingly difficult to recruit into some positions, particularly senior scientists, who have stopped applying for posts at Diamond from the rest of Europe – formerly our most fertile recruiting ground for recruitment, with compelling evidence that BREXIT is a major factor. Recruitment into IT posts is also proving difficult. In both cases we are exploring new approaches, including through the recently-established Diamond Apprenticeship Scheme, whereby a total of 19 people have begun an apprenticeship with us in the past 3 years. Apprentices are accepted either from external applications or through internal development programmes that involve staff taking diplomas or degrees; we are also increasingly exploring more internal development of scientific staff to fill some senior positions, and accelerated graduate training schemes for IT staff, all of which are showing new shoots of growth.

In the last financial year, we received 2,138 proposals for experiments on our instruments via peer reviewed access routes, requesting a total of 26,543 shifts. After peer review, 1,232 proposals were awarded beamtime. This resulted in 13,462 experimental shifts being awarded across 32 beamlines and nine electron microscopes. We welcomed 6,454 onsite user visits from academia across all instruments, with an additional 5,851 remote user visits. The machine continues to perform to the highest standard with 98.1% uptime and 104.7 hours mean time between failures (MTBF). Diamond also provides services critical to industry in the UK, with over 170 companies paying for proprietorial access in fields ranging from high-value materials for aerospace and the automotive industry, to drugs to treat infectious disease and depression. The past year has seen record income from such sources, boosted in particular by an expansion of Cryo-EM services, in partnership with Thermo Fisher, and the XChem fragment screening facility which aids drug discovery.

A key challenge for Diamond for the year to come will be to adapt our user operations under the ongoing COVID-19 restrictions, as well as the way in which we deliver some technical projects, to a world in which frequent travel and work in teams of people who are physically close will be limited. Diamond must adopt new working methods and new ways to support its users on beamlines that have traditionally not been used to remote access.

2020 will be a year like no other, where resilience and perseverance from our staff will help us shape the future.

Prof Andrew Harrison
CEO Diamond Light Source

[1] The *h*-index is defined as the maximum value of *h* such that the given author/journal has published *h* papers that have each been cited at least *h* times. To calculate the facility *h*-index for Diamond we have used all articles published by our scientists and user community.

Beamline Development and Technical Summary

In its thirteenth year of experiments, Diamond is now operating with 32 beamlines and 11 electron microscopes. This year saw the completion of the latest phase of construction and the DIAD beamline will hopefully welcome first users in early 2021. Of the electron microscopes, nine are cryo-electron microscopes specialising in life sciences and make up eBIC (electron Bio-Imaging Centre), with two provided for industry use in partnership with Thermo Fisher Scientific. The two remaining microscopes dedicated to advanced materials research are supplied by Johnson Matthey and the University of Oxford. These microscopes form ePSIC (electron Physical Science Imaging Centre) and are operated under strategic collaboration agreements to provide for substantial dedicated peer reviewed user access. Both eBIC and ePSIC are next to the Hard X-ray Nanoprobe beamline (I14). Along with eBIC and ePSIC, the UK X-ray Free Electron Laser (XFEL) Hub, the Membrane Protein Laboratory and the XChem facility make up the complimentary integrated facilities available at Diamond. For academic research, Diamond instruments (beamlines and microscopes) are free at the point of access through peer review. For proprietary research, access can be secured through Diamond's industry team.

Following a restructure and subsequent internal changes, the instruments and beamlines are organised into eight science groups as described below.

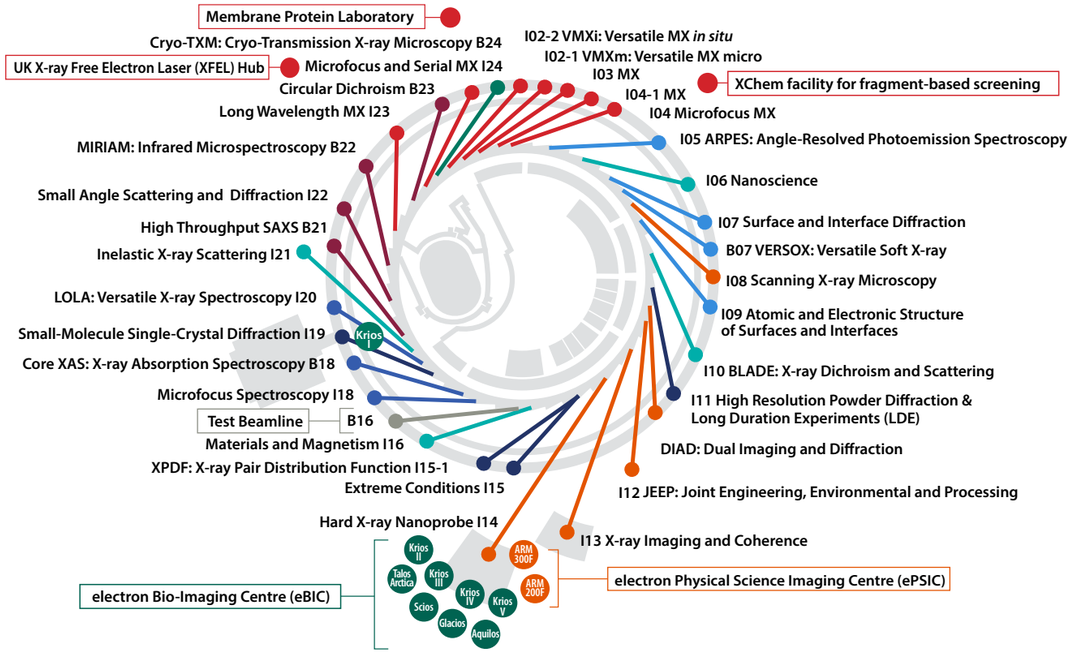

Macromolecular Crystallography | **Structures and Surfaces** | **Magnetic Materials** | **Imaging and Microscopy**

Crystallography | **Biological Cryo-Imaging** | **Spectroscopy** | **Soft Condensed Matter**

Electron Microscopes

Microscope	Main Capabilities	Accelerating Voltages	Operational Status
Titan Krios I	Cryo-EM, Cryo-ET	80, 120, 200, 300 kV	Operational since 2015
Titan Krios II	Cryo-EM, Cryo-ET	80, 120, 200, 300 kV	Operational since 2016
Titan Krios III	Cryo-EM, Cryo-ET	80, 120, 200, 300 kV	Operational since 2017
Titan Krios IV	Cryo-EM, Cryo-ET	80, 120, 200, 300 kV	Operational since 2017
Titan Krios V	Cryo-EM, Cryo-ET	80, 120, 200, 300 kV	Operational since 2018
Talos Arctica	Cryo-EM, Cryo-ET	200 kV	Operational since 2016
Glacios	Cryo-EM, Cryo-ET	200 kV	Installed, March 2019
Scios	Cryo-SEM, Cryo-FIB	3 to 30 kV	Operational since 2017
Aquilos	Cryo-SEM, Cryo-FIB	3 to 30 kV	Operational since 2019
JEOL ARM200F	Atomic scale STEM imaging, EELS, EDX, electron diffraction	80, 200 kV	Operational since 2017
JEOL ARM300F	Atomic scale TEM and STEM imaging, electron diffraction, 4D-STEM, EDX	30, 60, 80, 160, 200, 300 kV	Operational since 2017

Diamond's beamlines: current operational status April 2020

Beamline Name and Number	Main Techniques	Energy / Wavelength Range	Status
I02-1 - Versatile MX micro (VMXm)	Micro- and nano-focus in vacuum cryo-macromolecular crystallography (VMXm)	7 - 28 keV	Commissioning
I02-2 - Versatile MX *in situ* (VMXi)	*In situ* microfocus macromolecular crystallography, Serial Synchrotron Crystallography	10 - 25 keV	Commissioning
I03 - MX	Macromolecular crystallography (MX), Multiwavelength Anomalous Diffraction (MAD)	5 - 25 keV	Operational
I04 - Microfocus MX	MX, MAD	6 - 18 keV	Operational
I04-1 - Monochromatic MX	MX, XChem fragment screening	13.53 keV (fixed wavelength)	Operational
I05 - ARPES	Angle-Resolved PhotoEmission Spectroscopy (ARPES) and nano-ARPES	18 - 240 eV; 500 eV	Operational
I06 - Nanoscience	X-ray Absorption Spectroscopy (XAS), X-ray photoemission microscopy and X-ray magnetic circular and linear dichroism	80eV - 2200eV	Operational
I07 - Surface and Interface Diffraction	Surface X-ray diffraction, Grazing Incidence X-ray Diffraction (GIXD), Grazing Incidence Small Angle X-ray Scattering (GISAXS), X-ray Reflectivity (XRR)	6 - 30 keV	Operational
B07 - VERSOX: Versatile Soft X-ray	Ambient Pressure XPS and NEXAFS	250 - 2800 eV	Operational
	NEXAFS and High-Throughput XPS	50 - 2200 eV	Commissioning
I08 - Scanning X-ray Microscopy	Scanning X-ray microscopy, NEXAFS/ XANES, X-ray fluorescence	I08 branch: 250 eV - 4.4 keV	Operational
		J08 - Soft and Tender X-ray Ptychography branch: 250 - 2000 eV	Construction
I09 - Atomic and Electronic Structure of Surfaces and Interfaces	XPS (including HAXPES), X-ray Standing Waves (XSW), Near Edge X-ray Absorption Fine Structure (NEXAFS), energy-scanned photoelectron diffraction	Hard X-rays: 2.1 - 18+ keV Soft X-rays: 0.1 - 2.1 keV (currently 0.1 - 1.9 keV)	Operational
I10 - BLADE: Beamline for Advanced Dichroism Experiments	Soft X-ray resonant scattering, XAS and X-ray magnetic circular and linear dichroism	Circular: 400-1600eV; Linear Horizontal: 250-1600eV; Linear Vertical: 480-1600eV	Operational
I11 - High Resolution Powder Diffraction	X-ray powder diffraction	6 - 25keV (0.5 - 2.1 Å)	Operational
DIAD: Dual Imaging and Diffraction	Simultaneous imaging and diffraction	8 - 38 keV	Construction
I12 - JEEP: Joint Engineering, Environmental and Processing	Time-resolved imaging and tomography (phase- and attenuation-contrast), time-resolved powder diffraction, single crystal diffraction, diffuse scattering, energy dispersive X-ray diffraction (EDXD), high-energy small angle X-ray scattering (under development)	53 keV - 150 keV monochromatic or continuous white beam	Operational
I13 - X-ray Imaging and Coherence	Phase contrast imaging, tomography, full-field microscopy (under commissioning), coherent diffraction and imaging (CXRD,CDI), ptychography and photocorrelation spectroscopy (XPCS) (under commissioning), innovative microscopy and imaging	Imaging branch: 8 - 30keV	Operational
		Coherence branch: 7 - 20keV	
I14 - Hard X-ray Nanoprobe	Scanning X-ray fluorescence, X-ray spectroscopy, ptychography and transmission diffraction	5 - 23 keV	Operational
I15 - Extreme Conditions	Powder diffraction, single crystal diffraction	Monochromatic and focused 20 - 80 keV White beam	Operational
I15-1 - XPDF	X-ray Pair Distribution Function (XPDF)	40, 65, and 76 keV	Operational
I16 - Materials and Magnetism	Resonant and magnetic single crystal diffraction, fundamental X-ray physics	2.5 - 15 keV	Operational
B16 - Test beamline	Diffraction, imaging and tomography, topography, reflectometry	4 - 20 keV monochromatic focused 4 - 45 keV monochromatic unfocused White beam	Operational
I18 - Microfocus Spectroscopy	Micro XAS, micro Extended X-ray Absorption Fine Structure (EXAFS), micro fluorescence tomography, micro XRD	2.05 - 20.5 keV	Operational
B18 - Core XAS	X-ray Absorption Spectroscopy (XAS)	2.05 - 35 keV	Operational
I19 - Small-Molecule Single-Crystal Diffraction	Small-molecule single-crystal diffraction	5 to 25 keV / 0.5 to 2.5 Å	Operational
I20 - LOLA: Versatile X-ray Spectroscopy	X-ray Absorption Spectroscopy (XAS), X-ray Emission Spectroscopy (XES) and Energy Dispersive EXAFS (EDE)	Dispersive branch: 6 - 26 keV	Optimisation
		Scanning branch: 4 - 20 keV	Operational
I21 - Inelastic X-ray Scattering	Resonant Inelastic X-ray Scattering (RIXS), X-ray Absorption Spectroscopy (XAS)	Currently 250 - 1500 eV (to be upgraded to 250 - 3000 eV)	Optimisation
B21 - High Throughput SAXS	BioSAXS, solution state small angle X-ray scattering	8 - 15 keV (set to 13.1 keV by default)	Operational
I22 - Small Angle Scattering and Diffraction	Small angle X-ray scattering and diffraction: SAXS, WAXS, USAXS, GISAXS. Micro-focus.	7 - 20 keV	Operational
B22 - MIRIAM: Multimode InfraRed Imaging And Mircrospectroscopy	IR micro- & nano-spectroscopy THz spectroscopy IR imaging (under commissioning)	nanoFTIR : 4000-900 cm^{-1} (2.5-11 μm) microFTIR: 10,000-100 cm^{-1} (1-100 μm) Spectroscopy (FTIR):10,000-10 cm^{-1} (1-1000 μm) Imaging (FPA): 10,000-900 cm^{-1} (1-11 μm)	Operational
I23 - Long Wavelength MX	Long wavelength macromolecular crystallography	3 - 8 keV (1.5 - 4.1 Å)	Optimisation
B23 - Circular Dichroism	Circular Dichroism (CD)	125-500 nm & 165-650 nm for CD Imaging at 50 µm resolution, 96-cell High-Throughput CD (HTCD) and High-Pressure CD up to 200 MPa	Operational
I24 - Microfocus and Serial MX	Macromolecular crystallography, MAD, Serial Crystallography	6.5 - 25.0 keV	Operational
B24 - Cryo Transmission X-ray Microscopy (TXM)	Full field X-ray imaging	200eV - 2600eV	Optimisation

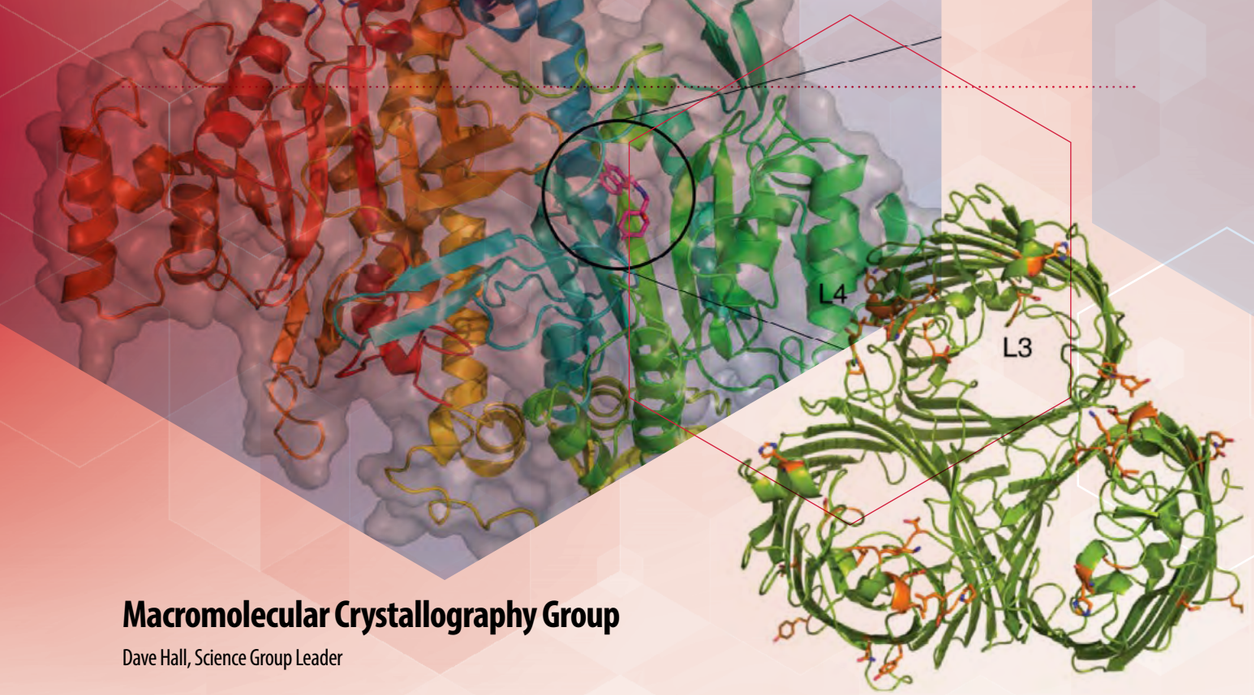

Macromolecular Crystallography Group

Dave Hall, Science Group Leader

Macromolecular crystallography (MX) remains at the forefront of understanding the form and function of biologically relevant molecules by revealing their shape and interactions at atomic resolution. The information derived from MX experiments can be complemented by many other life science techniques at Diamond (see in particular the Soft Condensed Matter and Imaging and Microscopy sections of this review) and coupled with experiments in the researcher's lab to give deeper insight by employing an integrated structural biology approach.

At Diamond seven beamlines (I03, I04, I04-1, I23, I24, VMXi and VMXm), alongside the XChem fragment screening facility, the UK XFEL Hub and the Membrane Protein Facility (see the Integrated Facilities and Collaborations section) are dedicated to exploiting the technique of MX for the benefit of the UK structural biology community and researchers from Europe and further afield.

Serial Synchrotron Crystallography (SSX) is available to users now on the Microfocus and Serial MX beamline (I24). In this relatively new area, sample delivery is continuously evolving but fixed targets and the lipidic cubic phase (LCP) extruder are now routine. The first successful light activated experiments for SSX have been carried out using Diamond's portable laser system, *PORTO*. Over the course of 2020 further *PORTO* commissioning will take place and this, coupled with other techniques, will enable dynamic crystallography at Diamond. The sample requirements for serial experiments can often be daunting; with this in mind some protocols for successful sample preparation have recently been published[1] and we are actively developing approaches that significantly reduce sample consumption by exploiting acoustic drop ejection[2].

Two significant upgrades will take place on I24 in the near future; the current insertion device will be replaced by a cryo-cooled permanent magnet undulator (CPMU), and an Eiger2 detector, equipped with a cadmium telluride (CdTe) sensor, will be installed to complement the existing detector. Biological crystals are radiation sensitive, however,the combination of the CPMU and the CdTe Eiger2 detector will facilitate efficient data collection at higher X-ray energies (more than 20 keV). Operating at higher X-ray energies, in turn, allows significantly more data to be collected from microcrystals due to photoelectron escape[3].

The Long-Wavelength MX beamline (I23) has continued to successfully operate in its unique wavelength range. Native phasing, where the intrinsic anomalous signal from, for example, sulphur, for experimental phasing is exploited, is now becoming a routine experiment with an increasing number of successful structure determinations. Access to the potassium absorption edge has provided further insight into the ribosome, one of the fundamental cellular machineries (see I23 highlight). While most ribosome work is now performed by single particle cryo-electron microscopy, this study needed the long wavelength X-rays only available at beamline I23 to unambiguously identify metal ions. Recent updates to the cryogenic sample transfer system and the software user interface, GDA, have increased the robustness and usability of the beamline, which will finally enable users to independently operate the beamline from spring 2020.

VMXm, the Versatile MX micro beamline, following first user experiments in late 2018 has been consolidating and undertaking further user experiments. A permanent liquid nitrogen distribution system has been installed in the experimental hutch, which is particularly useful for the sample transfer system. In conjunction with Diamond's Optics and Metrology Group, microfocus mirror optimisation is ongoing. To date a sub-400 nm vertical X-ray beam at the sample position has been achieved and the functionality of the novel, variable beam size vertical mirror[4] has been confirmed. In parallel, controls and acquisition systems continue to be developed, again to bring functionality and practicality for the final end-users. This work will continue through 2020 to support the transition to a full user programme.

Diamond's I03 and I04 MX beamlines continue to stay at the forefront of detector technologies. The first Eiger2 XE 16M detector was installed on I04 in December 2018. The move from the previously installed detector resulted in a step change for the users and the beamline. Most notably the increase in data acquisition frequency from 25 Hz to 133 Hz initially and then to higher frequencies. I03 installed an identical detector in April 2019. Since early summer 2019, both detectors can operate at 400 Hz in continuous mode and can acquire bursts of more than 28,000 images at 500 Hz. Peak acquisition rates can reach 560 Hz.

The significantly smaller pixel size (75 microns versus 172 microns) of the Eiger2 XE 16M in combination with the (almost) zero readout time leads to a noticeable improvement in data quality and allows for better spot separation, which is particularly useful when resolving long unit cells. In combination with the SMARGON multi-axis goniometer, operating on both I03 and I04, the Eiger2 XE detector also allows for even faster grid scans. This ability to carry out fast grid scans is used, for example, in automated X-ray centring where the 4M detector region of interest (ROI) is applied. This allows faster collection, processing, analysis and display of results. All processing pipelines have been adapted to deal with the new .h5 file format and new processing hardware has been implemented in order to deal with the heightened computing demand presented by the increased number of pixels. This upgrade has already enabled more efficient use of beamlines I03 and I04, increasing throughput significantly. Moreover, this upgrade also paves the way for new modes of data collection, especially serial approaches.

During 2019, unattended data collection protocols and procedures were developed further, resulting in high quality data being collected, fully autonomously, for cryo-cooled samples with no user interaction with the beamlines. Testing with Diamond users has been undertaken on I03 to benefit from their feedback and thus improve upon the systems in place. To manage fully autonomous data collection across four beamlines (I03, I04, I04-1 and I24), for thousands of potential users, for hundreds of thousands of samples, including from our XChem lab and from around the world, a robust system is required. Data collection through this system is rapid, in particular when exploiting the new Eiger2 detector properties, as exemplified by the collection this year from virus crystals at very high resolution (>1.7 Å) in around 30s[5]. Unattended data collection will be rolled out to the full user programme through 2020.

Staying with the theme of fully automated collection, the room temperature beamline, Versatile MX *in situ* (VMXi), has continued to mature and develop in conjunction with users from academia and industry. New hardware has been installed, robustness testing undertaken, development of and support for SSX carried out, and pre experiment support for beamtime at the European XFEL provided. The beamline routinely uses its double multilayer monochromator to provide extremely high flux photons. This is exploited by collecting data at extremely high rates using its Eiger2 4M detector. Rotation data sets of 20-60° each from crystals in crystallisation plates are taken in 1s. Consequently, the beamline can collect thousands of data sets per day. This is opening up the opportunity to investigate biological structures at near physiological temperatures and enable comparison with data more conventionally collected at cryogenic temperatures. The user programme will develop further through 2020, expanding the opportunities presented by the beamline to a wider community.

Beamline I04-1 and the associated XChem facility have continued to offer a great service to the general user programme and the structure-based drug design fragment screening programme. A continued focus on robustness and sample throughput has seen several improvements over the last year. The beamline end-station has had its control system upgraded providing greater control and robustness. Data collection methodologies for fragment screening have improved with a 30% faster crystal-to-crystal turnaround. Together these upgrades help serve the growing throughput from the XChem lab and an increasingly in-demand user programme from both academia and industry, that is able to offer broader fragment libraries and investigate a larger chemical space for each target of interest.

SARS-CoV-2 Structural Work at Diamond

Diamond led the way with a specific call for rapid access proposals from the user community for access to its life science facilities in response to the urgent need to address the COVID-19 outbreak. Additionally, to contribute to the global effort to combat COVID-19, researchers at Diamond in early 2020 solved a structure of the SARS-CoV-2 main protease (M^{Pro}) at very high resolution (PDB ID 6Y84) and completed an extensive XChem crystallographic fragment screen against it (see I04-1 highlight). The data have been deposited in the Public Protein Database (PDB) and are also available on the dedicated Diamond COVID-19 website[6]. This work was made possible by the availability of world class MX instruments and the XChem facility – a unique set of capabilities.

The facilities, user programme and training opportunities would not exist without the dedicated beamline scientists, technicians, engineers, software developers, computing support and many other supporting teams at Diamond who make it all happen!

1. Beale J.H. *et al.* Successful sample preparation for serial crystallography experiments. *J. Appl. Cryst*. **52**, 1385-1396 (2019). DOI: doi.org/10.1107/S1600576719013517
2. Davy B. *et al.* Reducing sample consumption for serial crystallography using acoustic drop ejection. *J. Sync. Rad.* **26**, 1820-1825 (2019). DOI: doi.org/10.1107/S1600577519009329
3. Storm S. L. S. *et al.* Measuring energy-dependent photoelectron escape in microcrystals. *IUCrJ.* **7(1)**, 129-135 (2020). DOI: 10.1107/S2052252519016178
4. Laundy D. *et al.* Development of a multi-lane X-ray mirror providing variable beam sizes. *Rev. Sci. Instrum.* **87(5)**, 051802 (2016). DOI: http://dx.doi.org/10.1063/1.4950732
5. Duyvesteyn H. M. E. *et al.* Glutathione facilities enterovirus assembly by binding at a druggable pocket. *Commun. Biol.* **3**, 9 (2020). DOI: https://doi.org/10.1038/s42003-019-0722-x
6. https://www.diamond.ac.uk/covid-19/for-scientists.html

Diamond shines light on peptide antibiotic biosynthesis

Related publication: Ghilarov D., Stevenson C. E. M., Travin D.Y., Piskunova J., Serebryakova M., Maxwell A., Lawson D. M. & Severinov K. Architecture of microcin B17 synthetase: an octameric protein complex converting a ribosomally synthesized peptide into a DNA gyrase poison. *Mol. Cell.* **73**, 1-14 (2019). DOI: 10.1016/j.molcel.2018.11.032

Publication keywords: Antibiotic; Protein complex; Crystal structure; Escherichia coli; Microcin B17; DNA gyrase; Azole synthetase; Heterocyclase; Dehydrogenase; Topoisomerase

New antibiotics are urgently needed to counter the ongoing threat of antimicrobial resistance. One such potential antibiotic called microcin B17 (MccB17) has gained attention for its distinct mechanism of action that allows it to remain effective against certain resistant bacteria. It is a peptide-derived antibiotic that targets DNA gyrase to cause double-strand breaks in DNA within pathogenic bacteria.

MccB17 is produced by a large, multiprotein complex known as microcin B17 synthetase, which is found in *E.coli*. To fully understand how MccB17 and related antibiotics are made, a series of X-ray Macromolecular Crystallography (MX) datasets from crystals of the synthetase were collected at MX beamlines I02, I03, I04 and I24 at Diamond Light Source.

The crystal structures revealed that microcin B17 synthetase was made of eight protein subunits, which can be divided into two halves, each containing distinct active sites. Using these structural data, it was hypothesised that MccB17 flips from one active site to the other as it is modified from a harmless peptide into an antibiotic.

Although MccB17 has been shown to have properties that make it unsuitable for use as an antibiotic in humans, it is hoped that this increased understanding could inform future therapeutics. The modifications observed in MccB17 could be introduced to other peptides to produce a new generation of novel antibiotics.

DNA gyrase is an essential enzyme found in gram-negative bacteria and represents a well validated target for antibiotics[1]. However, the emergence of pathogenic strains that have developed resistance to clinically important compounds that target this enzyme, most notably the fluoroquinolones, has driven the search for new molecules with therapeutic potential. Microcin B17 (MccB17) is a peptide-derived inhibitor targeting DNA gyrase produced by *E. coli* to give it a selective advantage over competing enteric bacteria; the inhibition of DNA gyrase by MccB17 leads to the accumulation of double-stranded DNA breaks and cell death[2]. Whilst the details are not fully understood, the mechanism of action of MccB17 is distinct from that used by fluoroquinolones and it is therefore likely to remain effective against fluoroquinolone-resistant mutants of DNA gyrase. Whilst MccB17 itself is unlikely to find clinical use due to unfavourable pharmacokinetics, a detailed understanding of how it is made could inspire the generation of novel therapeutic leads.

The biosynthesis of MccB17 is encoded by the plasmid borne *mcbABCDEFG* cluster, where McbA is a 69-amino acid precursor peptide which is post-translationally modified through the concerted action of McbB, McbC and McbD, which are collectively described as the McbBCD synthetase complex. McbA is a serine- and cysteine-rich peptide, and these residues are transformed into five-membered oxazole and thiazole rings, respectively, via sequential heterocyclisation and oxidation reactions (Fig. 1). Thus, MccB17 belongs to the thiazole/oxazole-modified microcin (TOMM) class of natural products.

In vivo, the fully modified McbA peptide is liberated from the synthetase via proteolytic cleavage of a leader peptide by the TldDE protease, whose structure and mechanism were previously elucidated by the research group using data collected on beamlines[3] at Diamond Light Source. However, in a *tldD* deletion mutant, the modified peptide remains tethered to the complex. Through the attachment of an N-terminal hexahistidine tag to McbA, it was possible to affinity purify the whole complex when overexpressed in this deletion mutant. Following further purification, this sample was used for crystallisation trials. After optimisation of promising conditions, diffraction quality crystals were obtained through an iterative microseeding procedure. X-ray data to a maximum resolution of 1.85 Å were recorded on Diamond beamlines and the structure was resolved by the Single wavelength Anomalous Dispersion (SAD) method using a selenomethionine-substituted crystal.

Prior to this study, the stoichiometry was assumed to be 1:1:1 for McbBCD, but the structure revealed an additional copy of McbB in the asymmetric unit, giving a composition of $McbB_2CD$. Moreover, this assembly was closely associated with a two-fold crystallographic symmetry-related copy, largely through interactions between opposed McbC subunits, to yield a $McbB_4C_2D_2$ octamer (Fig. 2). The latter was confirmed as the biologically-relevant assembly through size exclusion chromatography. Within each half of the octamer, the pair of McbB subunits adopt different conformations and together form a clamp that tethers the leader peptide of the fully processed McbA peptide.

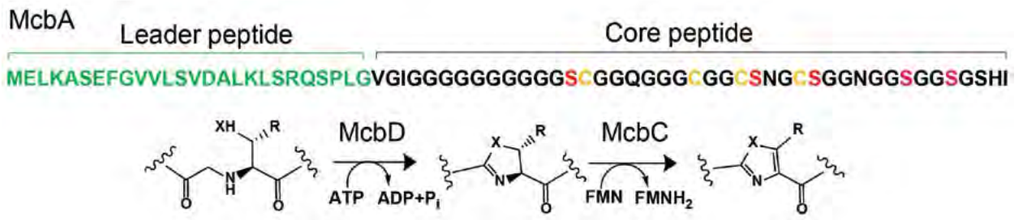

Figure 1: Sequence of McbA, the precursor for MccB17 biosynthesis. The leader peptide is indicated in green, and heterocyclisation sites are shown in red and yellow. Shown below are the two distinct catalytic activities of cyclisation and oxidation, associated with the McbD and McbC subunits, respectively.

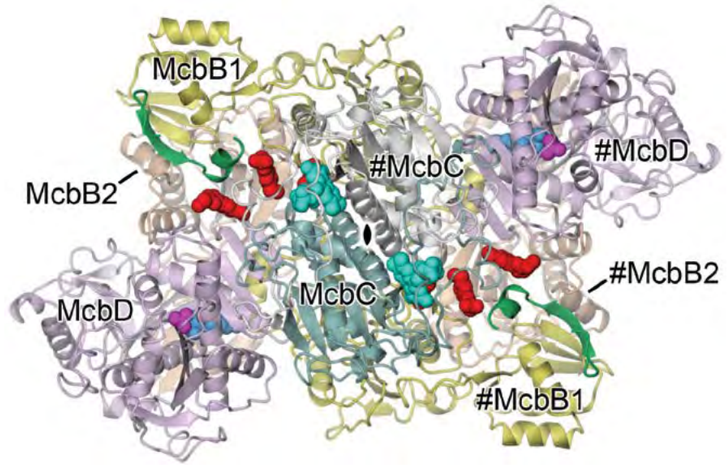

Figure 2: The full $McbB_4C_2D_2$ octamer in cartoon representation as viewed down the crystallographic two-fold axis (indicated by the black symbol) with individual subunits labelled, where those belonging to the right-hand asymmetric unit are preceded by the hash (#) symbol. Two copies of the leader peptide are shown in green cartoon representation, and as van der Waals spheres: ADP (blue), phosphate (magenta), FMN (cyan) and bound heterocycles (red).

Although, McbA is not fully resolved in electron density maps beyond the leader peptide, fragmentary electron density was apparent for a number of heterocycles, including the C-terminal oxazole group, bound at disparate locations in the complex, enabling speculation regarding the path taken by the peptide in the synthetase complex.

The ATP-dependent heterocyclase activity is associated with the McbD subunits (Fig. 1), which lie at opposite ends of the octamer (Fig. 2). A structure with ADP and phosphate bound enabled the delineation of the active site, leading to a proposed mechanism involving the phosphorylation of a hemiorthoamide intermediate, with the C-terminal proline residue acting as a general base, which was supported by *in vitro* experiments with selected site-directed mutants.

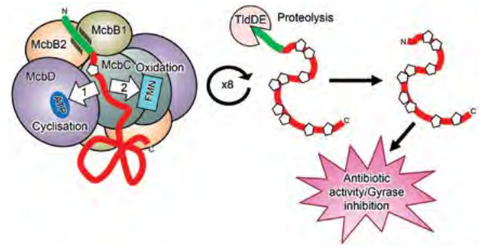

Figure 3: Schematic representation summarising the sequence of events leading to the production of mature MccB17. Firstly, the McbBCD synthetase binds the McbA precursor peptide via its leader peptide, between the two copies of McbB (McbB1 and McbB2) and then sequentially adds heterocycles. This involves the repeated shuttling of the precursor between McbD and McbC active centres. After the final modification, cleavage of the leader peptide by the TldDE protease yields the mature antibiotic, which is then released from the complex.

The FMN-dependent dehydrogenase activity resides within the McbC subunit (Fig. 1). Lying at the core of the complex (Fig. 2), each active site is comprised of amino acid residues from both McbC subunits. In addition to the tightly bound cofactor, the active site contains the terminal heterocycle of modified McbA, which stacks against the flavin moiety. Based on this arrangement, a mechanism involving the abstraction of a proton from the α-carbon of the azoline substrate by Lys201 and Tyr202 was proposed. However, the lack of a suitable general base in the vicinity of the N1 atom of FMN suggests that the cofactor is not fully reduced to $FMNH_2$, but that the negative charge that develops on N1 could be stabilised by a salt bridge to the adjacent Arg233 to yield a hydroquinone anion.

Despite the pair of McbC subunits at the core of the octamer being closely associated, it seems likely that each $McbB_2CD$ assembly functions independently of the other. Previous work has shown that heterocycles are introduced sequentially from the N- to the C-terminus of the McbA precursor peptide, with each one being fully formed before the next[4]. This observation necessitates the peptide to repeatedly flip between the heterocyclase (McbD) and dehydrogenase (McbC) active sites, which are separated by a distance of around 40 Å, whilst remaining tethered to the peptide clamp formed by the McbB subunit pair (Fig. 3).

Through this work, facilitated by access to the Diamond MX beamlines, almost 30 years of study on the biosynthesis of MccB17 has been reconciled, by shedding light on how the activities of the heterocyclase and dehydrogenase are temporarily and spatially coordinated during TOMM modification. More broadly, since oxazoles and thiazoles are found in a wide variety of bioactive natural products[5], this knowledge could enable the decoration of any given peptide with azoles following well-determined rules, towards the creation of new therapeutics.

References:

1. Collin F. *et al.* Exploiting bacterial DNA gyrase as a drug target: current state and perspectives. *Appl. Microbiol. Biotechnol.* **92**, 479-497 (2011). DOI: 10.1007/s00253-011-3557-z
2. Collin F. *et al.* The microbial toxin microcin B17: prospects for the development of new antibacterial agents. *J. Mol. Biol.* **431(18)**, 3400-3426 (2019). DOI: 10.1016/j.jmb.2019.05.050
3. Ghilarov D. *et al.* The origins of specificity in the microcin-processing protease TldD/E. *Structure* **25(10)**, 1549-1561.e5 (2017). DOI: 10.1016/j.str.2017.08.006
4. Milne J. C. *et al.* Cofactor requirements and reconstitution of microcin B17 synthetase: a multienzyme complex that catalyzes the formation of oxazoles and thiazoles in the antibiotic microcin B17. *Biochemistry*. **38(15)**, 4768-4781 (1999). DOI: 10.1021/bi982975q
5. Walsh C. T. *et al.* Three ring posttranslational circuses: insertion of oxazoles, thiazoles, and pyridines into protein-derived frameworks. *ACS Chem. Biol.* **7(3)**, 429-442 (2012). DOI: 10.1021/cb200518n

Funding acknowledgement: National Science Centre, Poland (UMO-2015/19/P/NZ1/03137); EU Horizon 2020 (665778); RFBR-Royal Society International Exchanges Scheme (KO165410043/IE160246); BBSRC BB/J004561/1 and BB/P012523/1).

Corresponding author:
Prof David Lawson, John Innes Centre, david.lawson@jic.ac.uk

On course for effective new vaccines to target malaria

Related publications: Rawlinson T. A., Barber N. M., Mohring F., Cho J. S., Kosaisavee V., Gérard S. F., Alanine D. G. W., Labbé G. M., Elias S. C., Silk S. E., Quinkert D., Jin J., Marshall J. M., Payne R. O., Minassian A. M., Russell B., Rénia L., Nosten F. H., Moon R. W., Higgins M. K. & Draper S. J. Structural basis for inhibition of Plasmodium vivax invasion by a broadly neutralizing vaccine-induced human antibody. *Nat. Microbiol.* **4**, 1497 (2019). DOI: 10.1038/s41564-019-0462-1

Alanine D. G. W., Quinkert D., Kumarasingha R., Mehmood S., Donnellan F. R., Minkah N. K., Dadonaite B., Diouf A., Galaway F., Silk S. E., Jamwal A., Marshall J. M., Miura K., Foquet L., Elias S. C., Labbé G. M., Douglas A. D., Jin J., Payne R. O., Illingworth J. J., Pattinson D. J., Pulido D., Williams B. G., de Jongh W. A., Wright G. J., Kappe S. H. I., Robinson C. V., Long C. A., Crabb B. S., Gilson P. R., Higgins M. K. & Draper S. J. Human antibodies that slow erythrocyte invasion potentiate malaria-neutralizing antibodies. *Cell* **178**, 216 (2019). DOI: 10.1016/j.cell.2019.05.025

Publication keywords: Malaria; Vaccine development; Erythrocyte invasion; Antibodies

Malaria is the most deadly parasitic disease to affect humans, causing hundreds of millions of severe cases and hundreds of thousands of deaths each year. Developing effective vaccines to prevent the disease has been hugely challenging. To guide the design of next-generation vaccines, researchers set out to understand the human antibody responses to vaccination with two promising vaccines.

When volunteers are vaccinated, they generate a broad antibody response. Some of these antibodies are effective at neutralising the parasite, while others are not. The research team used Macromolecular Crystallography (MX) beamlines I03 and I04 to collect data from crystals of the human antibodies bound to their malaria surface protein targets. Their aim was to characterise the structure of the most effective antibodies, allowing us to understand how they work.

Their results showed that some antibodies directly interfere with the function of malaria surface proteins, preventing them from binding to human red blood cell receptors. They also revealed that this inhibition can be indirect, most likely by stopping the parasite from getting close enough to the red blood cell to allow the interaction to happen.

Understanding these molecular details allows us to design new vaccines. The goal is now to use structure-guided methods ('structural vaccinology') to develop more effective vaccines.

Malaria is still the deadliest parasitic disease to affect humans, causing hundreds of thousands of deaths and hundreds of millions of cases each year. Two parasites cause the majority of human malaria, with *Plasmodium falciparum* responsible for most fatalities and *Plasmodium vivax* also causing widespread disease. There is a pressing need to tackle this scourge and an effective vaccine would be of huge benefit[1].

Malaria parasites live and divide within human blood cells and if can we prevent blood cell invasion we will stop the symptoms of the disease and prevent its transmission. Immunisation of human volunteers with components of the machinery used by parasites to invade blood cells generates an antibody response. However, the quality of these antibodies is variable. Some are highly effective at preventing invasion, while others have no effect. Some antibodies can even interfere with the function of effective inhibitory antibodies. How do we design a vaccine which only generates the most effective, protective antibodies?

In two studies published this year we characterised the human antibody responses to blood-stage malaria vaccines[2,3]. Human volunteers in Oxford were immunised with two vaccines as they took part in early-phase clinical trials and the antibodies that they generated were assessed for their protective potential. The beamlines at Diamond Light Source were used to visualise the epitopes of the most effective antibodies, revealing details which will guide future vaccine design.

The first study focused on the PvDBP molecule from *Plasmodium vivax*. PvDBP is used by the parasite to interact with the human receptor, DARC, in a process essential for blood cell invasion[4]. People in Africa with lower levels of DARC receptor are protected from vivax malaria. Antibodies targeting PvDBP would also be effective but variation in PvDBP across different strains of *Plasmodium vivax* makes this a challenge. Could we track down an antibody with broadly inhibitory effects?

A panel of antibodies was isolated from vaccinated volunteers and these were screened for efficacy using three different assays. One antibody in particular, DB9, stood out as it was effective in all three assays. By inhibiting blood cell invasion by a panel of parasites with different PvDBP sequences found in naturally infected Thai hospital patients, DB9 showed the desired broadly neutralising effects. However, the presence of other antibodies from the panel reduced the efficacy of DB9, interfering with its neutralising activity. How can we design a vaccine which generates DB9-like antibodies but not those which antagonise its function?

To guide this design process, we generated crystals of the antigen-binding fragment of DB9 bound to the DARC-binding domain of PvDBP and, using data collected at beamline I03, determined the structure. The epitope for DB9 was found in a region of PvDBP known as subdomain 3. This was surprising as the binding site on PvDBP for DARC has been mapped to a different region of PvDBP. However, we hypothesise, based on the structure, that DB9 will sterically block the parasite from getting close enough to the blood cell membrane for PvDBP to bind DARC. It was also interesting to find that the antibodies which interfere with the function of DB9 do not bind to subdomain 3 of DARC. This opens the way to design of future vaccines which induce antibodies resembling DB9 without generating antibodies that interfere with their function.

A similar approach was used to study antibody responses against the RH5 protein of *Plasmodium falciparum*. RH5 makes an interaction with basigin on the surface of red blood cells, which is essential for the parasite to invade[5].

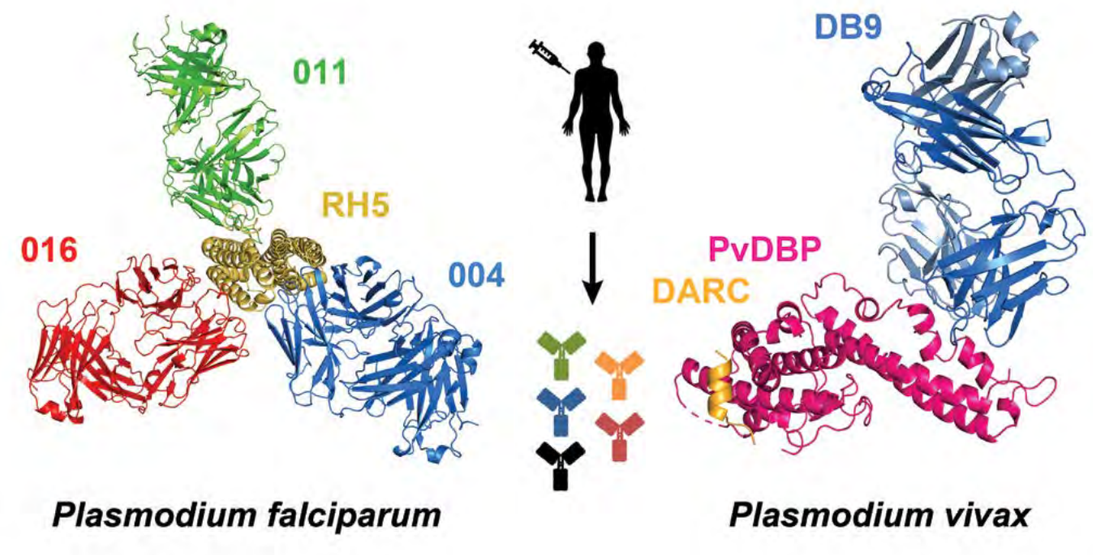

Structural insights into human antibodies which prevent blood cell invasion by the malaria parasite. The central panel illustrates the strategy of isolating human antibodies from vaccinated human volunteers. The left-hand panel shows the RH5 protein, essential for blood cell invasion by Plasmodium falciparum (yellow) bound to growth inhibitory antibodies 004 (blue) and 016 (red) and to potentiating antibody 011 (green). The right-hand panel shows a domain from the PvDBP protein (pink) required for blood cell invasion by Plasmodium vivax bound to part of the DARC receptor (orange) and growth inhibitory antibody DB9 (blue).

Antibodies were isolated from human volunteers vaccinated with RH5, and were assessed for the ability to inhibit parasite growth. In this case, there were two groups of inhibitory antibodies, represented by 004 and 016, which bind to different epitope sites. Data from beamline I04 allowed us to understand the nature of their epitopes on RH5, revealing that 004-like antibodies bind to a site which directly blocks basigin binding, while 016-like antibodies bind close to the basigin-binding site, most likely sterically blocking the RH5-basigin interaction when both RH5 and basigin are membrane associated.

In this case, antibody characterisation also gave an interesting surprise. A fascinating class of antibody represented by 011 showed no inhibitory activity alone. However, the presence of 011 increased the potency of inhibitory antibodies such as 004 and 016, allowing them to function at lower concentrations. The crystal structure of 011 revealed a novel epitope on the side of the RH5 molecule, while video microscopy of parasite invasion by Paul Gilson in Melbourne, showed that 011 slows the process of invasion. It only takes around 20 seconds for a malaria parasite to get inside a red blood cell and so we hypothesise that, by slowing invasion, 011 gives inhibitory antibodies more time to act.

In summary, structural mapping of the epitopes of the most effective antibodies at Diamond by Protein Crystallography has proved an important part of the characterisation of the antibody response to malaria vaccination. It has allowed us to understand the nature of the epitopes of inhibitory antibodies, revealing where they bind and how they act. These studies are guiding the design of next-generation vaccine immunogens, in which we aim to produce effective neutralising antibodies without generating antibody responses which interfere with their action. These immunogens will be included in the malaria vaccines of the future.

References

1. Draper S. J. *et al.* Malaria vaccines: recent advances and new horizons. *Cell Host Microbe.* **24**, 43 (2018). DOI: 30001524
2. Rawlinson T. A. *et al.* Structural basis for inhibition of Plasmodium vivax invasion by a broadly neutralising vaccine-induced human antibody. *Nat. Microbiol.* **4**, 1497 (2019). DOI: 31133755
3. Alanine D. G. W. *et al.* Human antibodies that slow erythrocyte invasion potentiate malaria-neutralising antibodies. *Cell* **178**, 216 (2019). DOI: 31204103
4. Chitnis C. E. *et al*. Targeting the Plasmodium vivax Duffy-binding protein. *Trends in Parasitology* **24**, 29 (2007). DOI: 18023618
5. Crosnier C. *et al*. Basigin is a receptor essential for erythrocyte invasion by Plasmodium falciparum. *Nature* **480**, 7378 (2011). DOI: 22080952

Funding acknowledgement:
SJD is a Wellcome Trust Senior Research Fellow (106917/Z/15/Z) while MKH is a Wellcome Trust Investigator (101020/Z/13/Z).

Corresponding authors:
Prof Simon J. Draper, University of Oxford, simon.draper@ndm.ox.ac.uk and Prof Matthew K. Higgins, University of Oxford, matthew.higgins@bioch.ox.ac.uk

Investigating antibiotic resistance in *Klebsiella pneumoniae* bacteria

Related publication: Wong J. L. C., Romano M., Kerry L. E., Kwong H. -S., Low W. -W., Brett S. J., Clements A., Beis K. & Frankel G. OmpK36-mediated Carbapenem resistance attenuates ST258 Klebsiella pneumoniae in vivo. *Nat. Commun.* **10**, 3957 (2019). DOI: 10.1038/s41467-019-11756-y

Publication keywords: Carbapenem resistance; Minimum inhibitory concentration; Outer membrane porin; Pore constriction; Liposome swelling assays; Mouse infection model

***Klebsiella pneumoniae* are common gut bacteria that can cause severe infections in other areas of the body. Such infections are usually acquired in hospital, and antibiotic-resistant strains account for a 40% mortality rate in hospital settings. More than 20,000 *K. pneumoniae* infections were recorded in UK hospitals in the past year. Carbapenems are used as antibiotics in hospitals when others have failed or are ineffective. However, *K. pneumoniae* is becoming increasingly resistant to Carbapenems and other antibiotics.**

Researchers at Imperial College London used Macromolecular Crystallography (MX) beamlines I03, I04 and I24 at Diamond Light Source to uncover one mechanism of antibiotic resistance in *K. pneumoniae*. The key lies in surface doorways known as pores. Resistant bacteria have much smaller pores, which blocks antibiotics from entering the bacteria.

Understanding the molecular mechanism of Carbapenem resistance will be valuable to medicinal chemists, who can use this information to design more effective antibiotics.

Interestingly, having smaller pores also makes the bacteria weaker, by restricting the amount of nutrients they can absorb. The resistant bacteria grow more slowly, but this disadvantage is outweighed by being able to avoid antibiotics, allowing them to maintain a high level of infection.

These results suggest that the extensive use of Carbapenems in hospitals is a significant driver in the spread of these antibiotic-resistant 'superbugs'. The study suggests that doctors should be more cautious in prescribing broad-spectrum antibiotics such as Carbapenems.

Resistance to Carbapenems by *K. pneumoniae* and other Gram-negative bacteria is a global problem and hospital-acquired Carbapenem-resistant infection mortality is high[1]. Resistance to Carbapenems is a result of carbapenemase enzymes, which inactivate Carbapenems by hydrolysis. In addition to the enzymes, resistance can also emerge as a result of mutations to the outer membrane porins through which antibiotics diffuse to the bacterial periplasm.

Porins play important physiological roles including the influx of small hydrophilic nutrients. The two major porins on the outer membrane of *K. pneumoniae* are OmpK35 and OmpK36. A major pathogenic *K. pneumoniae* clade is ST258[2], which expresses a truncated / non-functional *ompK35* and mutations in *ompK36* which reduced solute diffusion inside the cell. In order to understand how the OmpK36 mutations (12 substitutions and 5 insertions) confer resistance to Carbapenems (Fig. 1), the crystal structures of the $OmpK36_{WT}$ and $OmpK36_{ST258}$ variant were determined at 1.9 and 3.2 Å resolution, respectively[3] (Fig. 2). The overall structure of OmpK36 resembles other porins; it is a trimer that is composed of 16-stranded β-barrels. The $OmpK36_{ST258}$ structure can be superimposed on $OmpK36_{WT}$ with an rmsd of 0.43 Å over 340 C_α atoms. Two important structural components in porins are loops 3 and 4 (L3 and L4). L3 is not exposed at the cell surface but folds back into the barrel, forming a constriction zone half way inside the channel that contributes to the permeability properties, such as size exclusion limit and ion selectivity of the pore. L4 lies away from the pore and is involved in monomer trimerisation and subsequent stability. Comparison of the $OmpK36_{WT}$ and $OmpK36_{ST258}$ revealed that a Gly-Asp insertion (at positions 113 and 114) in L3 has constricted the pore size by approximately 26% relative to the $OmpK36_{WT}$ (Fig. 3). This constriction is a result of a more extended L3 inside the barrel that is stabilised by a salt-bridge between Asp114 and Arg127 at the barrel face of the pore (Fig. 2). To further validate the role of the Gly-Asp insertion in L3, a chimera was constructed, where the Gly-Asp insertion was introduced on the $OmpK36_{WT}$ background ($OmpK36_{WT+GD}$). The functional data, including minimum inhibitory concentration (MIC) and

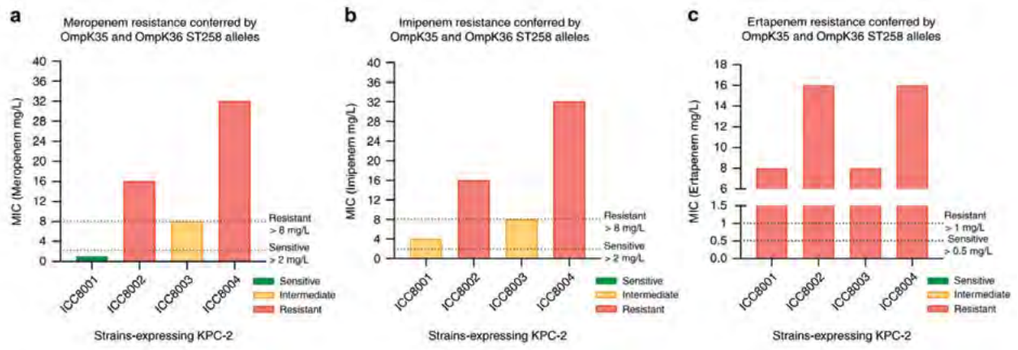

Figure 1: Minimum Inhibitory Concentration assays to assess the impact of mutations to antibiotics. OmpK35ST258 and OmpK36ST258 substitutions show increased resistance to several Carbapenems used to treat Gram-negative infections. Antibiotic key: IPM Imipenem, MEM Meropenem, ETP Ertapenem.

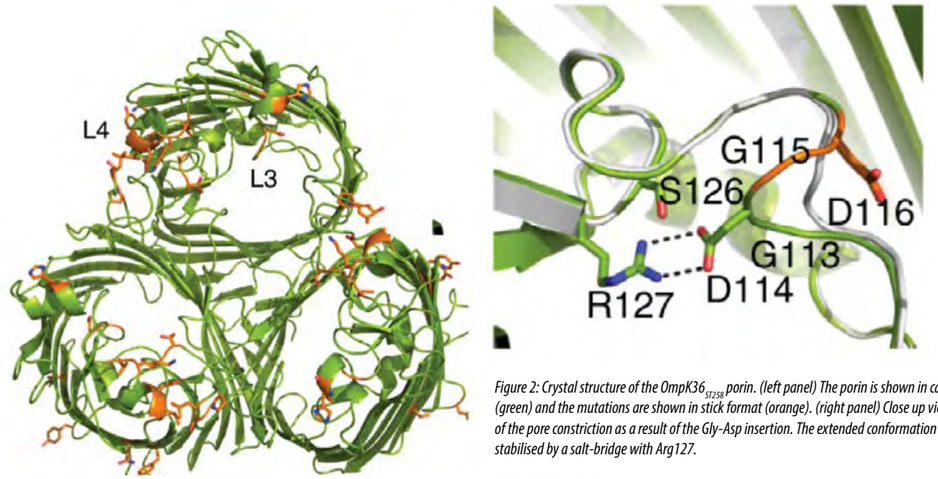

Figure 2: Crystal structure of the $OmpK36_{ST258}$ porin. (left panel) The porin is shown in cartoon (green) and the mutations are shown in stick format (orange). (right panel) Close up view of the pore constriction as a result of the Gly-Asp insertion. The extended conformation is stabilised by a salt-bridge with Arg127.

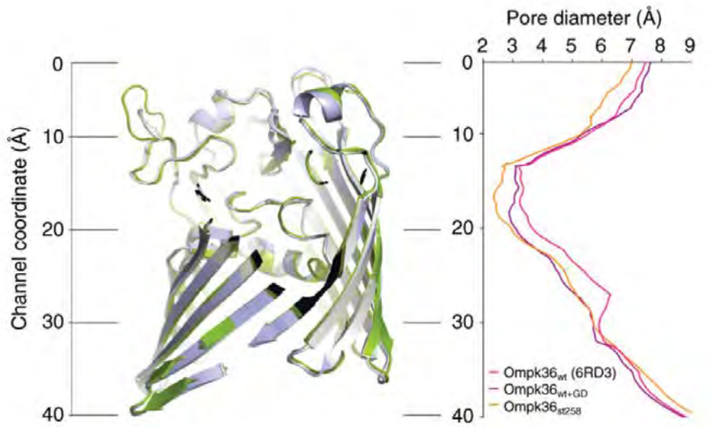

Figure 3: Pore diameter comparison. The OmpK36 monomer structure is shown as a cartoon. The face of the β-barrel has been removed to expose the pore and L3 (left panel). The minimal pore diameter graph (right panel) demonstrates a reduction in minimal pore diameter in both $OmpK36_{ST258}$ and $OmpK36_{WT+GD}$ compared to $OmpK36_{WT}$. The calculated pore diameter of the clinical $OmpK36_{ST258}$ is 2.37 Å and the $OmpK36_{WT+GD}$ chimera is 2.87 Å, whereas the $OmpK36_{WT}$ is 3.2 Å.

liposome swelling assays, revealed that the $OmpK36_{WT+GD}$ displays the same extent of resistance as the $OmpK36_{ST258}$ suggesting that the other mutations are not participating in the resistance mechanism. The crystal structure of the $OmpK36_{WT+GD}$ at 2.0 Å resolution revealed an identical L3 conformation and stabilisation as the $OmpK36_{ST258}$. The role of the salt-bridge in conferring carbapenem resistance was further investigated by generating an R127A substitution ($OmpK36_{ST258R127A}$). The MIC and liposome swelling assays indicated that stabilisation of L3 by the salt-bridge is not contributing towards the Carbapenem resistance but only by the Gly-Asp insertion.

Further functional data and mouse infection models showed that the L3 Gly-Asp insertion is detrimental to the fitness of the bacteria, potentially as a result of altered nutrient uptake. The functional and structural data have enabled the probing of the molecular mechanism of Carbapenem resistance mediated by outer membrane porins. Unlike other porins that display changes in their charge profile within the pore[4], thus repulsing antibiotics from influxing through them, the *K. pneumoniae* resistant bacteria utilise a unique mechanism of pore constriction alone that gives them the advantage of becoming resistant to several antibiotics without the need to alter their charge profile for each class of antibiotics. This mechanism very likely contributes to the high severity and mortality of hospital-acquired Carbapenem-resistant infections.

References:

1. Xu L. *et al.* Systematic review and meta-analysis of mortality of patients infected with carbapenem-resistant Klebsiella pneumoniae. *Ann. Clin. Microbiol. Antimicrob.* **6**, 18 (2017). DOI: 10.1186/s12941-017-0191-3
2. Peirano G. *et al.* Importance of clonal complex 258 and IncFK2-like plasmids among a global collection of Klebsiella pneumoniae with blaKPC. *Antimicrob. Agents Chemother.* **61**, e02610 (2017). DOI: 10.1128/AAC.02610-16
3. Wong, J. L. C. *et al.* OmpK36-mediated Carbapenem resistance attenuates ST258 Klebsiella pneumoniae in vivo. *Nat. Commun.* **10**, 3957 (2019). DOI: 10.1038/s41467-019-11756-y
4. Lou, H. *et al.* Altered antibiotic transport in OmpC mutants isolated from a series of clinical strains of multi-drug resistant E. coli. *PLoS One* **6**, e25825 (2011). DOI: 10.1371/journal.pone.0025825

Funding acknowledgements:

K.B. is supported by a grant for the Medical Research Council (MR/N020103/1). J.L.C.W. is supported by a clinical training programme from the MRC (MRC CMBI Studentship award MR/R502376/1). G.F. is supported by an Investigator grant from the Wellcome Trust.

Corresponding authors:

Prof Gad Frankel, Imperial College London, g.frankel@imperial.ac.uk and Dr Konstantinos Beis, Imperial College London, kbeis@imperial.ac.uk

Structure guided antiviral drug design against SARS-COV-2

Related publication: Douangamath A., Fearon D., Gehrtz P., Krojer T., Lukacik P., Owen C. D., Resmick E., Strain-Damerell C., Aimon A., Ábrányi-Balogh P., Brandão-Neto J., Carbery A., Davison G., Dias A., Downes T. D., Dunnett L., Fairhead M., Firth J. D., Jones S. P., Keeley A., Keserü G. M., Klein H. F., Martin M. P., Noble M. E. M., O'Brien P., Powell A., Reddi R. N., Skyner R., Snee M., Waring M. J., Wild C., London N., von Delft F. & Walsh M. A. Crystallographic and electrophilic fragment screening of the SARS-CoV-2 main protease. *Nat. Commun.* **11**, 5047 (2020). DOI: 10.1038/s41467-020-18709-w

Publication keywords: COVID-19; SARS-CoV-2 virus; Main protease; X-ray fragment based drug discovery; XChem; Antivirals; Protease inhibitors

At the end of 2019, a new coronavirus was identified as the cause of a disease outbreak in Wuhan, China. This disease now known as coronavirus disease 2019 (COVID-19) is caused by the highly contagious SARS-CoV-2 virus. As yet, we have no drugs against SARS-CoV-2 that have been verified in clinical trials and are limited to treating the disease symptoms.

There is a global race to produce a vaccine, but the vaccines in development may not provide long-lasting immunity. Vaccines are not suitable for all patients, including those whose immune systems are weakened by disease (e.g. cancer). It is therefore vital to develop new treatments that target the virus itself. Working towards this goal, researchers at Diamond Light Source explored interactions between drug-like molecules and a part of the virus known to be essential to its reproduction.

Researchers carried out the majority of this work on the Macromolecular Crystallography (MX) and XChem beamline (I04-1). Primarily I04-1 was used because it is embedded in the XChem pipeline, capable of handling the large numbers of samples quickly. Speed was vital, as researchers tested thousands of molecules to find promising candidates. Complementary experiments were carried out on other MX beamlines (I03, I04 and I24) to provide additional information. The XChem facility and the state-of-the-art structural biology labs in the Research Complex at Harwell were essential for rapid sample production and turn-around.

This rapid research allowed the team to solve the structure of a protein essential to the reproduction of the virus. They have also identified more than 90 compounds worthy of further investigation for development of antivirals for SARS-CoV-2. There is no certainty that the project will succeed, but by working in a fully open source approach to harness expertise across the world, the project aims to do as much as it can to help accelerate the discovery of antiviral therapies effective against COVID-19.

A novel coronavirus (CoV) belonging to the β-coronavirus cluster, SARS-CoV-2, has rapidly spread across the globe from an initial outbreak in Wuhan, China, in late 2019[1]. This is the third coronavirus to escape the animal population and cause human disease, following Severe Acute Respiratory Syndrome (SARS) in 2002 and Middle Eastern Respiratory Syndrome (MERS) in 2012[2-3]. SARS-CoV-2 is an enveloped, non- segmented, positive-sense RNA virus and as for other coronaviruses it possesses a large RNA genome of over 30 kb. The genome contains a 5' cap structure along with a 3' poly (A) tail, so it can act as an mRNA for translation of the replicase polyproteins. The replicase gene encodes the non-structural proteins (nsps) and takes up approximately 20 kb of the genome, with the remaining 10 kb encoding the structural and accessory proteins.

The SARS-CoV-2 replicase is expressed in the form of two polyproteins pp1a and pp1ab containing the nsps 1-11 and 1-16, respectively. SARS-CoV-2 encodes two cysteine proteases that cleave the replicase polyproteins; a papain-like protease (PL^{pro}), encoded within nsp 3, and a 3C-like or main protease (M^{pro}), encoded by nsp 5. PL^{pro} cleaves at three sites releasing nsp 1-3, while the M^{pro} is responsible for the remaining 11 cleavage events, releasing nsp 4-16. Several of the nsps then assemble into the replicase-transcriptase complex (RTC) which is responsible for RNA replication and transcription of the viral sub-genomic RNA.

To date, there are no antivirals that specifically target SARS-CoV-2. The SARS and MERS outbreaks have generated some research and much of this has been directed to validating a number of suitable antiviral targets, such as the viral proteases, polymerases, and entry proteins (the spike protein). However, significant work remains to develop drugs that target these processes effectively to inhibit viral replication. Furthermore, although vaccine research and development is proceeding at pace, it is not guaranteed that durable high level immunity will be induced. Pursuing novel avenues of innovation leading to chemical entities specifically and rationally designed to target the virus may therefore prove essential.

At the start of the SARS-CoV-2 outbreak, many groups in China immediately focused their research efforts on understanding the novel coronavirus in detail. The groups of Zihe Rao and Haitao Yang at Shanghai Tech were able to solve the X-ray structure of M^{pro} in early January 2020 which was an incredible feat, and they were keen to accelerate their work. Having worked with Diamond Light Source in the past, they were keen to apply a high-throughput structure based drug discovery approach to M^{pro} here. In discussion with the Rao and Yang groups, we were able to rapidly apply the methods they used to overproduce M^{pro} in sufficient quantities for structural work at Diamond.

Using the XChem platform at Diamond, experiments to explore interactions made between M^{pro} and hundreds of low molecular weight organic molecules ('fragments') in just tens of hours at beamline I04-1 commenced. The small size and varied functional groups and chemical properties of these fragments allowed us to probe the surface of the enzyme – particularly the enzyme's active site, the location at which it performs chemistry – for new binding interactions. Then, by merging and growing fragments with useful properties we could iteratively improve the binding of these compounds that can potentially lead to drugs that will bind tightly to the targeted protein, stopping it working. Finding a molecule with useful properties is a low probability event, but the high throughput capabilities of the XChem platform and the I04-1 beamline were leveraged to allow M^{pro} to be screened against thousands of different molecules over several days. Additionally, in collaboration with the London research group at the Weizmann Institute of Science in Rehovot, Israel, mechanistic inhibitors have been designed specifically to target and form a covalent bond with a cysteine residue in the active site and these were also assessed. These molecules

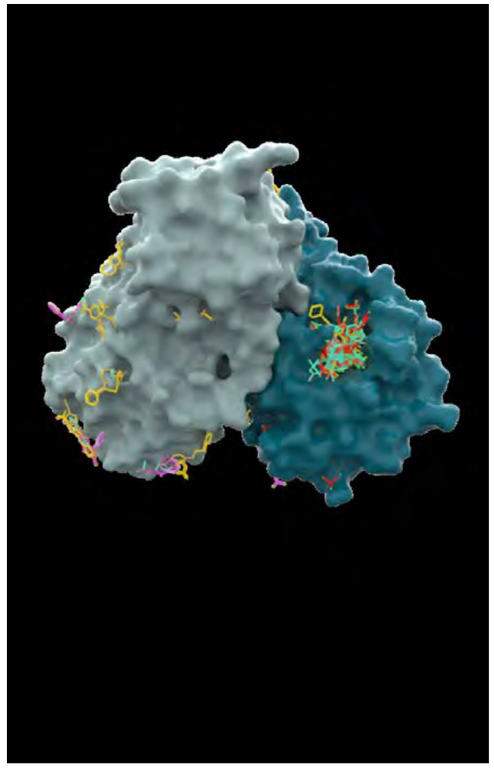

Figure 1: The dimar protease showing fragments bound at active site and other target areas.

form a covalent bond with the enzyme and were first identified by incubating the protein and ligand then performing intact protein mass spectrometry (MS). If the mass of the protein increased then it indicated that the molecule had bound. Large numbers of potential covalent inhibitors could be screened rapidly by MS and those found bound to M^{pro} could be followed up crystallographically at I04-1 to visualise how and where they bound to M^{pro}.

Escherichia coli bacteria were used to produce milligram quantities of M^{pro} protein that was then purified to crystallisation standard. The construct for M^{pro} protein expression has been shared with other groups in the UK and around the world, allowing multiple inhibitor studies to be carried out by many methods including nuclear magnetic resonance, surface plasmon resonance and mass spectrometry, to accelerate progress. The sample was crystallised using the crystallisation facility at Harwell, which is a joint venture between Diamond, the Research Complex at Harwell and the Rosalind Franklin Institute. The quality of the initial crystals was poor but they appeared over a matter of hours. Using this to our advantage, multiple cycles of optimisation were applied to improve the crystal quality in a rapid fashion. The crystal structure of M^{pro} was solved to high resolution (1.25 Å) on the Microfocus MX beamline (I04) at Diamond providing a high precision ground state structure for comparison with liganded structures. Crystal structures of the protein were solved for more than one thousand fragment binding experiments, and over one hundred binding molecules have been discovered. The average resolution of all datasets was 2.1 Å, allowing mechanisms of binding and changes in protein conformation to be described with confidence. The majority of fragments bind in the active site of the protein, and additional high value fragments have been found that bind at the dimerisation interface of the protein (Fig. 1). As dimerisation is essential for M^{pro} activity, this site is worthy of particular attention. As of the end of March 2020, 68 binding events have been structurally characterised, and based on these hits, screening for improved fragments is ongoing.

Based on the screens, one series of promising mechanistic covalent binding inhibitors has been progressed to find improved binders with greater potency. It remains a challenge to transform weakly binding fragments into clinical candidates. Due to the time-sensitive nature of the current COVID-19 outbreak, and to accelerate progress in drug development, the data have been made immediately available to the wider community through regular structure depositions in the protein data bank via the fragalysis platform at Diamond and through a crowd sourced drug design programme, Covid-Moonshot. However, time is of the essence to combat the pandemic and developing antivirals or vaccines typically takes a decade or more of research. A potential strategy for accelerating the discovery of antivirals for SARS-CoV-2 is to repurpose existing drugs approved for other diseases. So, in parallel to starting from scratch using the X-ray fragment-based approach (albeit in a high-throughput way never before realised through the Covid-Moonshot approach), we have established a joint initiative with Exscientia Ltd, an AI drug discovery start-up based in Oxford Science Park to screen almost every known approved and investigational drug – 15,000 clinical molecules – against the SARS-CoV-2 proteases. At the time of writing these screens are near to completion. The hope is that by being able to start with clinically-approved drug molecules we can move more rapidly to clinical trials and potentially provide treatment for patients.

This is not your normal Diamond Annual Review highlight, but a snapshot of the rapidly moving open-source approach to accelerated drug discovery in a time of crisis. Science is typically a competitive environment and achieving academic recognition through the publication of work is a well-defined process. However, this has led in modern science to a research culture that cares exclusively about what is achieved and not about how it is achieved. The completely open approach being pursued here, and by other scientific groups who have dropped everything to focus on COVID-19 to work selflessly and openly, releasing results and sharing them with the world as soon as they are produced, will help us respond to Wellcome's call[4] for how we can all reimagine how we conduct research. The work in progress highlighted here has been a truly open and collaborative effort involving the Walsh and von Delft teams at Diamond and collaborators at the Weizmann (London group), Exscientia Ltd, the University of Oxford (Schofield and Vakonnakis groups), Rosalind Franklin Institute (Owens group) and the University of Newcastle (Kawamura, Noble and Waring groups).

References:

1. Zhu N. *et al.* A Novel Coronavirus from Patients with Pneumonia in China, 2019. *N. Engl. J. Med.* **382**, 727–733 (2020). DOI: 10.1056/NEJMoa2001017
2. Kuiken T. *et al.* Newly discovered coronavirus as the primary cause of severe acute respiratory syndrome. *Lancet* **362**, 263–270 (2003). DOI: 10.1016/S0140-6736(03)13967-0
3. Bermingham A. *et al.* Severe respiratory illness caused by a novel coronavirus, in a patient transferred to the United Kingdom from the Middle East, September 2012. *Euro Surveill.* **17(40)**, 20290 (2012)
4. Farrar J. Why we need to reimagine how we do research. *Wellcome* (2019) https://wellcome.ac.uk/news/why-we-need-reimagine-how-we-do-research (accessed March 2020)

Funding acknowledgement:
This work has been made possible by repurposing of funding from Diamond Light Source, Weizmann Institute, Rosalind Frankin Institute, Universities of Oxford & Newcastle.

Corresponding author:
Dr Martin Walsh, Diamond Light Source, martin.walsh@diamond.ac.uk

There is a letter K in ribosome

Related publication: Rozov A., Khusainov I., El Omari K., Duman R., Mykhaylyk V., Yusupov M., Westhof E., Wagner A. & Yusupova G. Importance of potassium ions for ribosome structure and function revealed by long-wavelength X-ray diffraction. *Nat. Commun.* **10**, 2519 (2019). DOI: 10.1038/s41467-019-10409-4

Publication keywords: X-ray crystallography; Ribosome; Translation

Ribosomes are giant protein factories, found in the cells of all lifeforms. They are responsible for the accurate conversion of genetic information into proteins. The most complex RNA-protein assemblies in the cell, they require metal ions to maintain their structure and function. Until recently, the exact type and location of these metal ions had not been determined.

An international team of researchers used the long wavelength macromolecular crystallography beamline, I23 (the only beamline in the world allowing access to the required X-ray wavelength), to pinpoint hundreds of potassium ions within bacterial ribosomes. Using this cutting-edge technique, they were able to demonstrate - for the first time - that potassium ions are not only involved in the overall formation of the structure of ribosomal RNA (rRNA) and ribosomal proteins, but also play an essential role in its function.

These results fill a considerable gap in our knowledge and could potentially lead to therapeutic applications. Ribosomes and associated molecules, collectively known as the *translational apparatus,* are the primary target for more than half of current antibiotics. Problems with the translation process are also implicated in a number of human diseases.

A greater understanding of the structure of ribosomes will, therefore, be a vital asset for drug discovery. Having increased the precision of our ribosome model, the research team hopes to increase the efficiency of drug design and offer targets for the development of new classes of antibiotics.

The ribosome is the largest (~2.5 MDa and 70 Svedberg units (70S) in bacteria and up to ~4 MDa and 80 Svedberg units (80S) in higher eukaryotes) and the most abundant RNA-containing macromolecular complex in cells. Ribosomes are conserved in all kingdoms of life; they are composed of ribosomal RNA (rRNA) and proteins unequally distributed among two asymmetric subunits (small and large subunits, called 30S and 50S respectively in bacteria). Generally, the folding of nucleic acid structures, especially larger ones, requires the presence of counter ions, hence, large macromolecular complexes which contain nucleic acids necessitate correspondingly large numbers of various metal ions. Overall improvement of data collection methods in X-ray crystallography and cryo-electron microscopy (cryo-EM) over the last decades has led to more detailed maps of 70S ribosomes, revealing multiple density peaks tentatively attributed to metal ions. A multitude of technical limitations has prevented empirical identification of the nature of these ions and they were generally assigned as magnesium. Magnesium was chosen since it is the best-known RNA stabilizing counter ion, and ribosomes tolerate only a very narrow concentration range during purification and in vitro translation experiments. At the same time the presence of potassium (the most abundant intracellular ion) has also been shown to be essential for these experiments, however its role might have been understated due to a wider range of concentration tolerance[1].

The universal method of localisation of metal ions in macromolecular structures is the geometrical analysis of ion coordination and solvent environment; albeit, this method is subject to severe limitations and does not provide unambiguous assignment even in the case of atomic resolution structures. Moreover, the structures of large macromolecular dynamic complexes generally have poor resolution statistics; the issue is compounded by the simultaneous presence of various ions that can be either co-purified or introduced from the solvent. Taking into account the corresponding values of coordinate errors and atomic displacement parameters, except at very high resolution, it appears almost impossible to distinguish between e.g. Mg^{2+}, Na^{+} or K^{+}, based only on average M. ….O coordination distances (2.1 Å, 2.4 Å and 2.8 Å respectively) and geometry, both by means of manual inspection or automated modelling software protocols. In addition, even at high resolution, the experimentally deduced electron density maps are time-averages and, thus, it is not straightforward to assess the simultaneous presence of ions when in proximity. Very few experimental approaches allow tackling such problems. Anomalous X-ray diffraction is a very well-established tool to determine and localise ions in three-dimensional structures[2]. Data collection in the vicinity of the absorption edge of the specific element allows rather precise determination of the element atoms positioning in the structure. The majority of synchrotron beamlines for macromolecular crystallography are optimised for the 6–17.5 keV X-ray range[3]. However, to detect and measure the anomalous signal from potassium around its K-edge (E=3.608 keV) access to lower energies is necessary. I23 at Diamond Light Source is currently the only synchrotron beamline for macromolecular crystallography covering the energy range around the potassium K-edge.

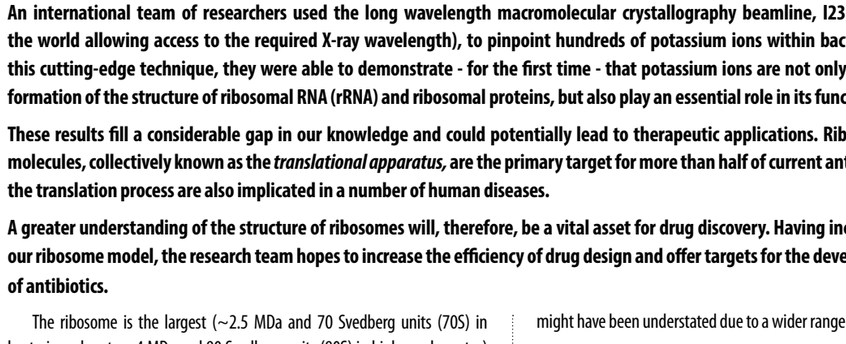

Figure 1: Structural rearrangements of the decoding centre upon binding of A-tRNA. In the initiation complex (left), only one K^{+} ion conserves the architecture of decoding centre through coordination with C518 and G529 of helix 18 (h18) and amino acids Pro45 and Asn46 of protein uS12. The mRNA in the absence of A-tRNA is shifted away from h18, while G530 adopts syn conformation. In the elongation complex (right), mRNA moves towards h18 in order to form base pairing with the A-tRNA. A second K^{+} ion is involved in the codon–anticodon interaction via coordination through C518, G530, Pro45 and U(+6) ribose.

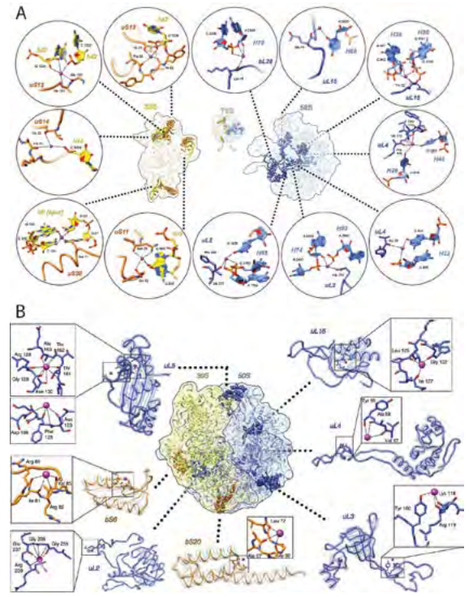

Figure 2: (A) Potassium ions (magenta) that mediate interaction of 30S subunit r-proteins (orange) with 16S rRNA (yellow) and 50S subunit r-proteins (blue) with 23S rRNA (light blue). tRNAs and mRNA are omitted from the figure. (B) Interaction of K^{+} ions with the ribosomal proteins from 30S subunit and from 50S subunit. K^{+} ions are shown as magenta spheres, 30S proteins in orange, 50S proteins in blue.

We have achieved the direct experimental assignment of K^{+} ions in the full 70S ribosome structure by long-wavelength X-ray crystallography. Registering long-wavelength diffraction from ribosome crystals became possible thanks solely to the novel long-wavelength beamline at Diamond. Experiments at long wavelengths have a number of obstacles to overcome: mainly large diffraction angles and absorption from air in the beam path, the sample mount, solvent around the crystal and the crystal itself. Beamline I23 has been designed to address these challenges by operating in a vacuum environment with a multi-axis goniometer and a large semi-cylindrical area detector[4]. The experimental setup has allowed us to mitigate the strong absorption of X-rays from the crystals, the surrounding mother liquor and sample mounts, limiting the resolution of collected datasets. In the end, our data allowed us to unambiguously assign about 30% of the metal sites as K^{+}.

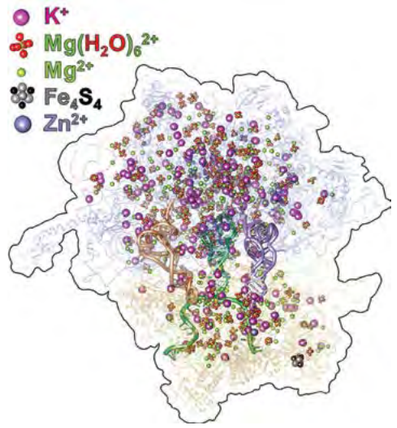

Figure 3: Thermus thermophilus 70S elongation complex model contains 211 experimentally distinguished K^{+} ions, 334 Mg^{2+}, 251 $Mg(H2O)_6^{2+}$, 1 Zn^{2+} and 1 Fe_4S_4 cluster.

We have managed to solve crystal structures of two 70S ribosomal functional complexes with bound messenger RNA (mRNA) and transfer RNAs (tRNAs), representing two distinct stages of translation: initiation and elongation. Our findings provide insights into the role of metal ions in two ribosome active sites, the decoding and peptidyl transferase centers. We demonstrate how K^{+} (but not Mg^{2+}) coordinates mRNA within the decoding center in order to maintain correct frame position during the elongation state (Fig.1). We also localise potassium ions that are required for subunits association and stabilisation of tRNAs, rRNAs, and r-proteins (Fig. 2). These results shed light on the role of metal ions for the ribosome architecture and function, thereby expanding our view on fundamental aspects of protein synthesis.

We have managed to elucidate the role of K^{+} in protein synthesis at the three-dimensional level. The distribution of K^{+} ions over the whole mass of the ribosome indicates that this ion is as important as Mg^{2+} (Fig. 3). We show that potassium ions are involved in the stabilisation of main functional ligands such as mRNA and tRNAs, as well as ribosomal RNAs and ribosomal proteins, via the interaction with nitrogen and oxygen atoms of side chain residues, nucleotide bases, polypeptide or sugar-phosphate backbones. These observations suggest more global and general functions of K^{+} ions in ribosomal organisation rather than its role as a stabiliser of particular regions of the ribosome or particular type of interactions.

Our work adds deeper insights into the mechanism of protein synthesis and opens another dimension in understanding of ribosome organisation. We show that some regions (e.g. the decoding center) require very precise localisation, coordination and nature of metal ions. Our observations display contrasting behaviours for the interactions of potassium and magnesium ions with ribosomal complexes. While magnesium ions tend to bind in pockets around anionic phosphate oxygen atoms with tight geometrical constraints[5], potassium ions interact with backbone carbonyl groups in protein bending folds and hydroxyl group of riboses or carbonyl groups on bases, especially guanine nucleotides, with a variable number of ligands and larger distance variations.

References

1. Nierhaus K. H. Mg^{2+}, K^{+}, and the ribosome. *J. Bacteriol.* **196**, 3817 (2014). DOI: 10.1128/JB.02297-14 JB.02297-14
2. Handing K. B. *et al.* Characterizing metal-binding sites in proteins with X-ray crystallography. *Nat Protoc.* **13** 1062 (2018). DOI: 10.1038/nprot.2018.018 nprot.2018.018
3. Djinovic Carugo K. *et al.* Softer and soft X-rays in macromolecular crystallography. *J. Synchrotron Rad.* **12**, 410 (2005). DOI: 10.1107/S0909049504025762
4. Wagner A. *et al.* In-vacuum long-wavelength macromolecular crystallography. *Acta Cryst.* **D72**, 430 (2016). DOI: 10.1107/S2059798316001078
5. Leonarski F. *et al.* Mg^{2+} ions: do they bind to nucleobase nitrogens? *Nucleic Acids Research* **45**, 987 (2017) DOI: 10.1093/nar/gkw1175 gkw1175

Funding acknowledgement:
This work was supported by the French National Research Agency grants ANR-15-CE11-0021-01, ANR-16-CE11-0007-01, a grant DBF20160635745 from "La Fondation pour la Recherche Médicale", and the Russian Government Program of Competitive Growth of Kazan Federal University. This study was also supported by the grant ANR-10-LABX-0030-INRT under the frame program Investissements d'Avenir ANR-10-IDEX-0002-02.

Corresponding authors:
Dr Alexey Rozov, Urania Therapeutics, arozov@uraniatx.com and Dr Gulnara Yusupova, Institute of Genetics, Molecular and Cellular Biology, gula@igbmc.fr

A new target for malaria research

Related publication: Baragaña B., Forte B., Choi R., Hewitt S. N., Bueren-Calabuig J. A., Pisco J. P., Peet C., Dranow D. M., Robinson D. A., Jansen C., Norcross N. R., Vinayak S., Anderson M., Brooks C. F., Cooper C. A., Damerow S., Delves M., Dowers K., Duffy J., Edwards T. E., Hallyburton I., Horst B. G., Hulverson M. A., Ferguson L., Jiménez-Díaz M. B., Jumani R. S., Lorimer D. D., Love M. S., Maher S., Matthews H., McNamara C. W., Miller P., O'Neill S., Ojo K. K., Osuna-Cabello M., Pinto E., Post J., Riley J., Rottmann M., Sanz L. M., Scullion P., Sharma A., Shepherd S. M., Shishikura Y., Simeons F. R. C., Stebbins E. E., Stojanovski L., Straschill U., Tamaki F.K., Tamjar J., Torrie L. S., Vantaux A., Witkowski B., Wittlin S., Yogavel M., Zuccotto F., Angulo-Barturen I., Sinden R., Baum J., Gamo F-J., Mäser P., Kyle D. E., Winzeler E. A., Myler P. J., Wyatt P. G., Floyd D., Matthews D., Sharma A., Striepen B., Huston C. D., Gray D. W., Fairlamb A. H., Pisliakov A. V., Walpole C., Read K. D., Van Voorhis W. C. & Gilbert I. H. Lysyl-tRNA synthetase as a drug target in malaria and cryptosporidiosis. *P. Natl. Acad. Sci. USA* **116**(14) 7015-7020 (2019). DOI:10.1073/pnas.1814685116

Publication keywords: Malaria; Cryptosporidiosis; tRNA synthetase; Target based drug discovery

New drugs are needed to treat malaria, which caused more than 400,000 deaths worldwide in 2017. A related parasite causes the gastrointestinal disease cryptosporidiosis, which spreads through contact with human or animal faeces (often via dirty water). Although symptoms generally subside in a couple of weeks in healthy individuals, the disease can be fatal in patients with compromised immune systems. Estimates suggest that cryptosporidiosis causes more than 200,000 deaths each year, with malnourished children particularly at risk. At present, there is no effective treatment for infected children.

Target-based screening is a focused approach to drug design, which looks for compounds that bind to, or inhibit, enzymes critical to disease. While it has been a successful approach for many other diseases, a lack of validated targets for the malaria parasite has hampered the use of target-based screening.

A team of researchers at the University of Dundee, together with many collaborators, used Macromolecular Crystallography (MX) on the Microfocus and Serial MX beamline (I24), together with complementary techniques, to validate a novel biological target critical to both malaria and cryptosporidiosis and an exciting new compound series that shows activity against this target.

Having identified a drug target for both malaria and cryptosporidiosis, and a series of compounds that inhibit it, the team's focus now is on improving the properties of the compound series. It's early days, but the goal is to deliver a drug candidate that can pass all the safety milestones required to advance to clinical development.

Malaria and cryptosporidiosis are major burdens to both global health and economic development in many countries. Malaria caused more than 400,000 deaths in 2017, and cryptosporidiosis is estimated to cause more than 200,000 deaths a year. The spread of drug resistance is a growing concern for malaria treatment, and there is no effective treatment for malnourished or immunocompromised children infected with cryptosporidium. New treatments with novel mechanisms of action are needed for both diseases.

However, at present there are few validated targets for drug discovery in malaria and even less for cryptosporidiosis. The natural product cladosporin is active against blood- and liver-stage *Plasmodium falciparum*. Target deconvolution in *P. falciparum* has shown that cladosporin inhibits lysyl-tRNA synthetase (*Pf*KRS1)[1]. Unfortunately, cladosporin is not amenable to development as a drug lead itself due to its high metabolic instability and lack of oral bioavailability.

To identify new inhibitors of this promising target, as a collaboration with the University of Washington in Seattle, under the auspices of the Structure-guided Drug Discovery Coalition, recombinant *Pf*KRS1 was produced, assays developed and a biochemical screen of the GlaxoSmithKline malaria actives set of about 13,000 compounds was carried out (the Tres Cantos Antimalarial Set). The most promising hit for the screen showed similar levels of inhibition of *Pf*KRS1 and *P. falciparum* asexual blood stage as cladosporin. This hit also suffers from low metabolic stability like cladosporin but had the advantage of being synthetically tractable allowing rapid compound development. Thus, a hit optimisation project was started with the aim of developing analogues with improved metabolic stability and similar potency capable of clearing parasites from mouse models of malaria.

The structural information gained using the beamline facilities at Diamond Light Source, to understand how the hit compound and analogues interact within the active site of the enzyme, has played a key role in the optimisation process. MX revealed the shape of molecules and insights into their function, and the crystallographers in the team worked at facilities in Seattle and New Delhi as well as at Diamond. The Dundee team have BAG (Block Allocation Group) access to Diamond, an access route specially designed for groups of users who require regular access, and who can coordinate different short experiments to fill a beamtime shift of eight hours. For this particular work, beamline I24 at Diamond was used.

A published structure of cladosporin bound to *Pf*KRS1 showed that cladosporin binds within the ATP binding pocket[2]. The screening hit was co-crystallised with *Pf*KRS1 and also binds in the ATP binding pocket. The core of the hit occupies the same space as the adenine ring of ATP and the cyclohexyl moiety projects into the pocket where the ribose ring of ATP binds. This pocket is completed by the substrate lysine.

Several rounds of compound design, aided by the structural information and computational models, followed by synthesis and testing led to the identification of a lead molecule with similar potency and selectivity and excellent metabolic stability. The complex of the lead bound to the enzyme showed that the changes introduced to improve metabolic stability had minimal effect upon the position of the ligand within the binding site with respect to hit compound (Fig. 1).

The lead compound was active against both *Pf*KRS1 (IC_{50} = 0.015 µM) and whole-cell bloodstream *P. falciparum* 3D7 (EC_{50} = 0.27 µM) and was selective compared with both the *Hs*KRS (IC_{50} = 1.8 µM) and HepG2 cells (EC_{50} = 49 µM).

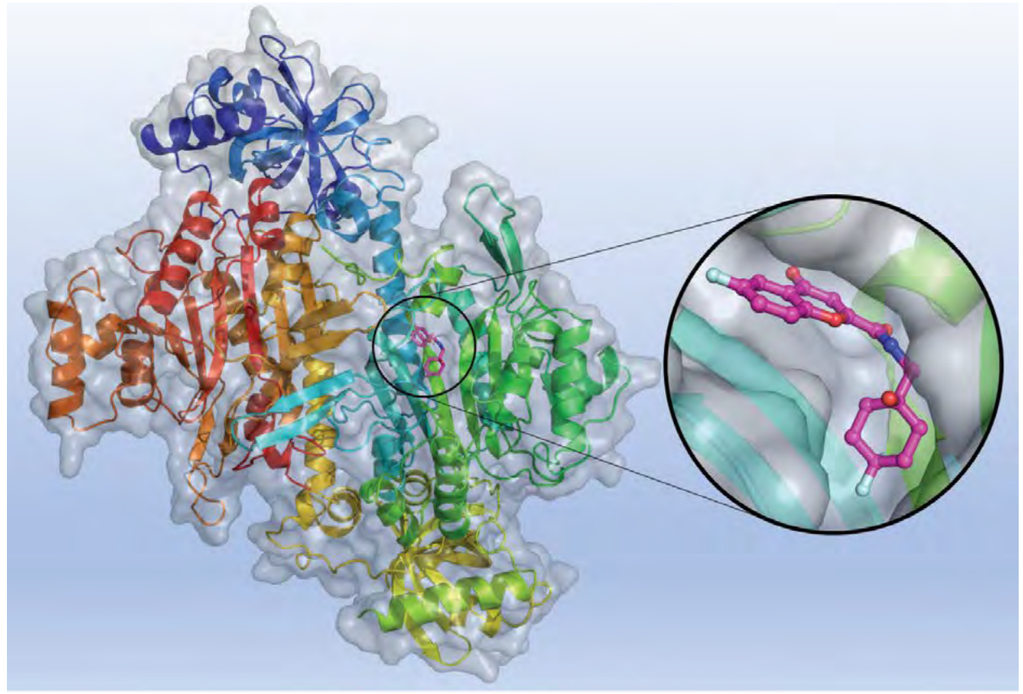

Figure 1: A co-crystal structure of the lead compound with P. falciparum lysysl-tRNA synthetase.

The biological and pharmacokinetic profile was sufficient to justify a rodent efficacy study. The lead was evaluated *in vivo* in a mouse model of malaria, which showed a reduction of the number of malaria parasites in blood by 90% at day 5 of the study.

There is a high level of sequence identity within the active-site regions of *Pf*KRS1 and *Cp*KRS. Therefore, cladosporin, the screening hit, and the lead compound were tested in a cellular assay against *C. parvum*. The three compounds showed inhibition of parasite growth. Several structures of *C. parvum* enzyme bound to our inhibitors showed retention of the ligand binding mode compared with the malaria enzyme. These results prompted the researchers to progress the lead compound to *in vivo* efficacy in two different *Cryptosporidium* mouse models. A reduction of parasite burden by two orders of magnitude with the lead compound in both disease models was observed.

Furthermore, X-ray crystallography and molecular dynamics simulations were used to rationalise the selectivity of the compounds for *Pf*KRS1 and *Cp*KRS compared to (human) *Hs*KRS. MD simulations suggest that the selectivity observed for the lead is due to a combination of a more favourable configuration of the binding site and a higher degree of stabilisation upon ligand binding in the parasite enzymes.

These results offer a strong validation of lysyl-tRNA synthetase as a drug target for malaria and cryptosporidiosis.

References:

1. Hoepfner D. *et al*. Selective and specific inhibition of the plasmodium falciparum lysyl-tRNA synthetase by the fungal secondary metabolite cladosporin. *Cell Host Microbe* **11**(6), 654-663 (2012). DOI: 10.1016/j.chom.2012.04.015

2. Khan S. *et al*. Structural basis of malaria parasite lysyl-tRNA synthetase inhibition by cladosporin. *J. Struct. Funct. Genomics.* **15**(2), 63-71 (2014). DOI: 10.1007/s10969-014-9182-1

Funding acknowledgement:
We thank the European Synchrotron Radiation Facility for beamtime, highlighting the staff of beamlines BM14 and ID29; Diamond Light Source for beamtime (proposal mx10071); the staff of beamline I24 for assistance with crystal testing and data collection; the entire Seattle Structural Genomics Center for Infectious Disease team; the Division of Biological Chemistry and Drug Discovery Protein Production Team; GlaxoSmithKline for the Tres Campos Antimalarial screening set; the Scottish Blood Transfusion Centre (Ninewells Hospital, Dundee) for providing human erythrocytes; Christoph Fischli and Sibylle Sax at the SwissTPH for technical assistance with the SCID mouse model; and Anja Schäfer for technical assistance with the in vitro antimalarial activity testing. The Art of Discovery thanks Dr. Cristina Eguizabal and the Basque Center of Transfusion and Human Tissues (Galdakao, Spain) and the Bank of Blood and Tissues (Barcelona, Spain) for providing human blood. The University of California, San Diego thanks Jenya Antonova-Koch for help. This work was supported by the Bill and Melinda Gates Foundation through Grant OPP1032548 to the Structure-Guided Drug Discovery Coalition and OPP1134302 (to B.S.). This work was also supported in part from federal funds, from the NIH/National Institute of Allergy and Infectious Diseases Grant R21AI123690 (to K.K.O.) and Contracts HHSN272201200025C and HHSN272201700059C (to P.J.M.); Medicines for Malaria Venture (through access to assays to I.H.G. and through RD/08/2800 to J.B.); Wellcome Trust for support of the X-ray Crystallography Facility 094090, IT support Grant 105021 (to I.H.G.), and Institutional Strategic Support Fund 204816 (to A.V.P.), all at the University of Dundee and for Investigator Award 100993 (to J.B.).

Corresponding authors:
Prof Ian H. Gilbert, University of Dundee, i.h.gilbert@dundee.ac.uk;
Dr Beatriz Baragana, University of Dundee, b.baragana@dundee.ac.uk

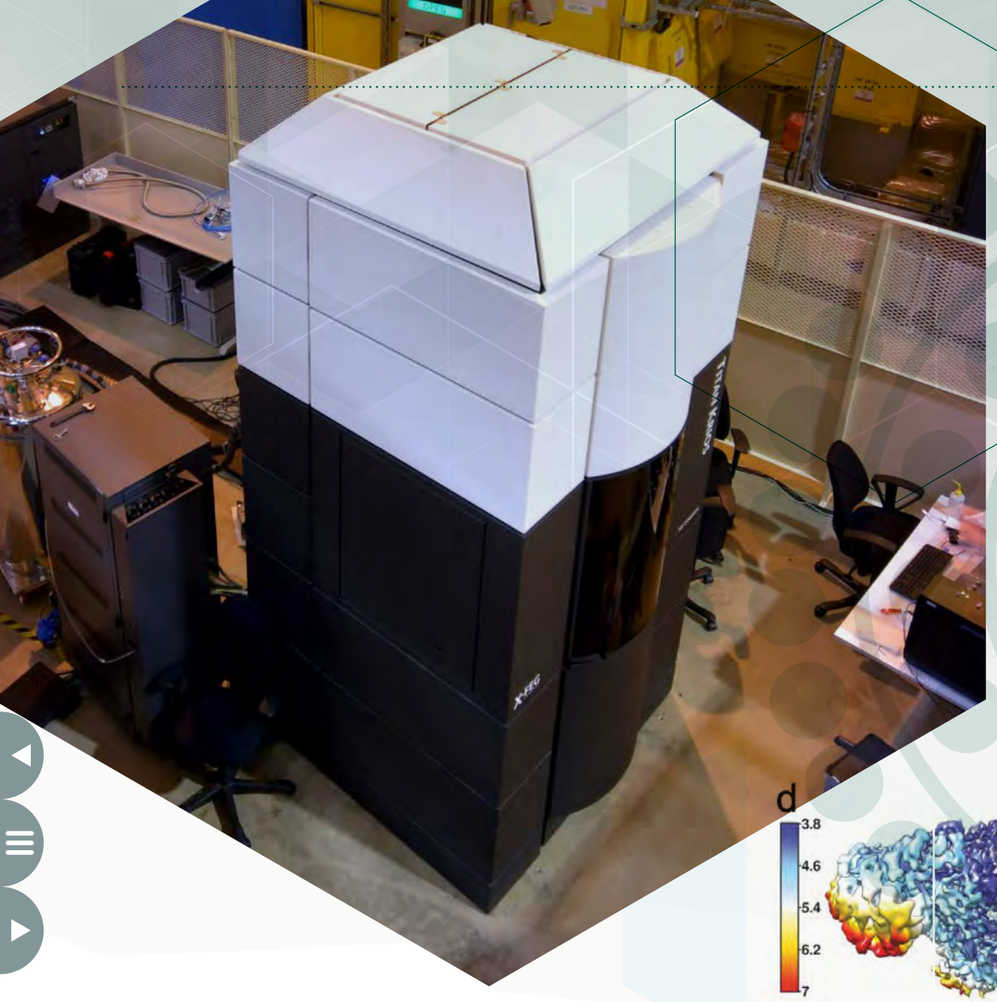

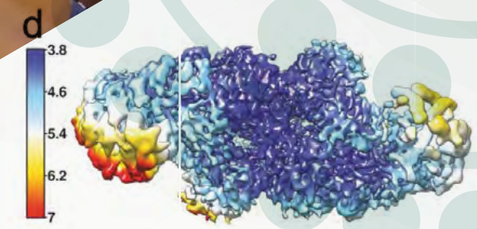

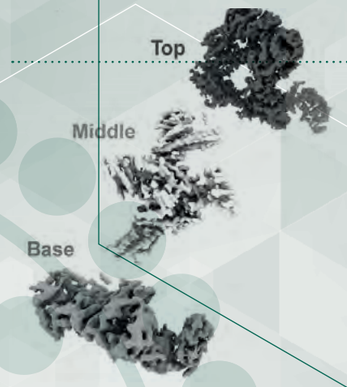

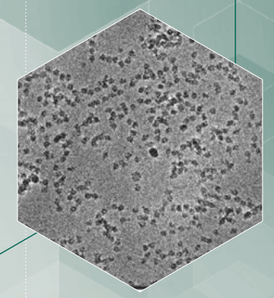

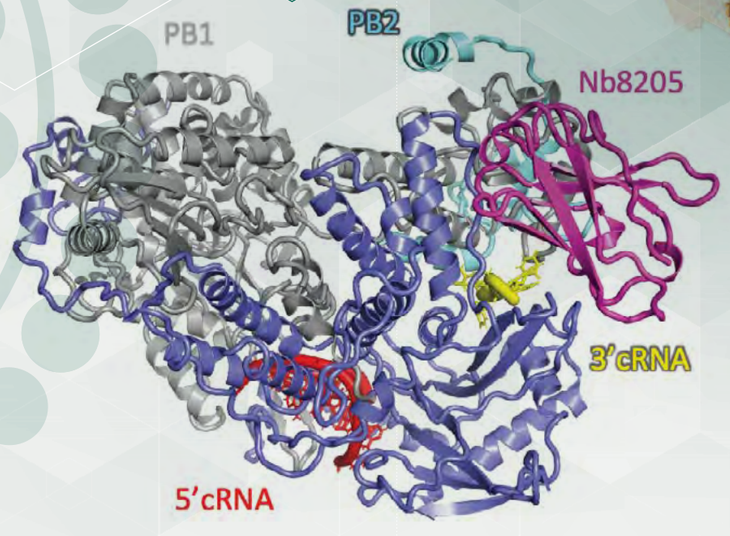

Biological Cryo-Imaging

Martin Walsh, Deputy Director of Life Sciences and Science Group Leader

The Biological Cryo-Imaging Group at Diamond brings together dedicated facilities for X-ray, light and electron microscopy. B24 is a cryo-TXM (full field cryo-transmission X-ray microscopy) beamline dedicated to biological X-ray imaging, which has established a cryo-super-resolution fluorescence microscopy facility in a joint venture between Diamond and the University of Oxford. Exploiting electrons for imaging, the electron Bio-Imaging Centre (eBIC) is the national centre for cryo-electron microscopy (cryo-EM) in the UK and provides a range of capabilities and supporting facilities for cryo-EM.

Following on from our jam-packed first full year, the Biological Cryo-Imaging Group continues to grow and introduce new capabilities and ways of working. It has been a busy year, with both B24 and eBIC developing and expanding their capabilities. This has meant that installation, commissioning of new instrumentation and associated recruitment has remained our major focus.

At eBIC during 2019, we finalised upgrades to all our Titan Krios' with the installation and commissioning of the K3™ direct electron counting detector from Gatan. The Thermo Fisher Aquilos™ cryofocused ion beam (cryo-FIB) and scanning electron microscope has been fully commissioned and integrated into the eBIC user programme. As part of an extensive collaboration with Thermo Fisher and the Rosalind Franklin Institute, a cryo-capable Helios Hydra dual-beam has also been installed and commissioned. To facilitate and grow the user community, two modes of access to the cryo-FIB instruments (Scios™ and Aquilos™) are now in place. A rapid access route provides users with a day for cryo-FIB milling of samples, which they then take back to their home laboratory for imaging. This is followed by a standard access route, which provides three days of cryo-FIB milling and two days of microscope time (Titan Krios) for cryo-electron tomography (cryo-ET) data collection.

At B24, upgrades to the X-ray microscope in order to allow acquisition of data at higher energies and exploit phase contrast imaging at the beamline are progressing well with installation of phase contrast optics completed and currently under commissioning. The collection of dual-axis X-ray data collection leading to the reduction of missing wedge artefacts has also been successfully demonstrated and workflows continued to be improved e.g. samples can now be accepted on both conventional EM grids and autogrids. A great deal of the software focus has been towards improving correlative workflows in, for example, automation of image registration between cryo-structured illumination microscopy (cryo-SIM) and cryo-soft X-ray tomography (cryo-SXT) through development of new algorithms. Correlative Light X-ray Microscopy (CLXM) has been enthusiastically taken up by the user community and is in high demand. In addition, we were delighted to perform our first Correlative Light and Electron Microscopy (CLEM) experiment with external users.

Training for users continues to be a major activity at B24 and eBIC. Over the summer of 2019, B24 organised and delivered a Cryo-Imaging Correlative Image Data Analysis Workshop at the University of Okayama, Japan and also hosted a Super-Resolution Fluorescence Microscopy Developers Symposium at Diamond. At eBIC, hands-on workshops continue to be the primary focus, and these remain highly popular and heavily oversubscribed. The well-established Cryo-EM Sample Preparation Workshop continues to be offered bi-annually and a Micro-ED (Micro-Electron Diffraction) Workshop was held to introduce the technique to structural biologists. A series of lectures covering theoretical background and practical considerations together with hands on data collection at eBIC using EPU-D and tutorials on data reduction and analysis again created a high demand for places by participants. eBIC's central role in training the EM community is exemplified by a recently funded extensive collaborative grant with the Astbury Centre in Leeds and other institutions. This five year grant for EM training, funded by the Wellcome Trust and MRC, will enable a significant uplift in both training courses and hands-on instrument use. Software training at eBIC continues to be carried out in collaboration with CCP-EM, although the programme has been disrupted by the COVID-19 pandemic. However, eBIC microscopes were involved in the rapid response to COVID-19 provided by Diamond and continued operations focused on SARS-Cov-2 research in spite of the UK lockdown.

Finally, following on from the success of iNEXT (Infrastructure for NMR, Electron microscopy, and X-rays for Translational research), which was funded by the European Commission H2020 programme to provide access to structural biology infrastructure, an extended and enhanced programme - iNEXT-Discovery[1] - has been funded and commenced on the 1st February 2020. The overall aim of these networks is to aid the opening and integration of existing national and regional research infrastructures to the wider European science user community. iNEXT provided state-of-the-art access to Macromolecular Crystallography (MX), Biological Solution Small Angle X-ray Scattering (BioSAXS), Nuclear Magnetic Resonance (NMR) and cryo-EM. Support for access to MX, BioSAXS and cryo-EM at Diamond has allowed us to assist users from across Europe to access our facilities and to, also, fund a number of joint research activities to further enhance and develop methods and capabilities. iNEXT-Discovery brings X-ray imaging into the fold with instrument access to both B24 at Diamond and Mistral at ALBA, Spain. B24 and Mistral are currently collaborating on developing correlative workflows for CLXM. eBIC will provide access to cryo-FIB milling, in addition to instrument access for single particle and tomography experiments, and lead the training programme for cryo-EM within iNEXT-Discovery.

Although progress in the first quarter of 2020 has been impacted by the COVID-19 pandemic, we are continuing to work hard to further expand our bio-imaging capabilities in 2020 and look forward to growing our user community and increasing our impact in the field of 3D bio-imaging.

1. https://inext-discovery.eu/network/inext-d/home

Visualising a DNA repair machine

Related publication: Shakeel S., Rajendra E., Alcón P., O'Reilly F., Chorev D. S., Maslen S., Degliesposti G., Russo C. J., He S., Hill C. H., Skehel J. M., Scheres S. H. W., Patel K. J., Rappsilber J., Robinson C. V. & Passmore L. A. Structure of the Fanconi anemia monoubiquitin ligase complex. *Nature* **575**, 234-237 (2019). DOI: 10.1038/s41586-019-1703-4

Publication keywords: DNA repair; DNA crosslink; E3 ubiquitin ligase; Cryo-EM; Mass spectrometry; Cancer

The human genetic illness Fanconi Anaemia (FA) causes abnormal development, bone marrow failure and a lifetime risk of developing cancer. FA is known to deactivate one of more than 20 genes that code for proteins that function collectively to repair damaged DNA and are known as the FA repair pathway.

The FA pathway repairs crosslinks within and between strands of DNA. The multi-protein FA core complex acts at the centre of this pathway to identify and signal the site of DNA crosslinks. When the FA pathway is defective, it results in human disease. Although the FA core complex had been characterised in cells, it had not been fully reconstituted in the lab.

Researchers isolated an FA core complex and determined its structure, using Cryogenic Electron Microscopy (cryo-EM) at the Electron Bio-Imaging Centre (eBIC) to image the complex at high resolution. They created 3D reconstructions from the images and used them to build models for how the FA core complex assembles and functions.

Using the models, researchers can now make new hypotheses for how the FA core complex functions and begin to define this DNA repair pathway in molecular terms. This will allow them to explain why specific patient mutations inactivate the pathway – and in the future, we may be able to predict whether certain changes might cause disease.

This was a long-term investigation, which took ten years to go from project conception to structure determination. The success of the project in the final stage was dependent on the excellent support from eBIC.

DNA crosslinks occur during normal cellular metabolism, or after exposure to chemicals such as chemotherapeutic drugs or alcohol. Crosslinks block the replication of DNA and transcription, and therefore they must be repaired to maintain genome integrity. Defects in the ability to repair DNA crosslinks result in Fanconi Anaemia (FA), a human disorder characterised by developmental defects, bone marrow failure, and predisposition to cancer[1]. FA patients harbour mutations in any one of 22 FANC (FA complementation group) genes, and these genes encode proteins that function in DNA crosslink repair[2].

At the heart of the FA DNA repair pathway is a megadalton, multi-protein E3 ubiquitin ligase, the FA core complex. This complex monoubiquitinates its substrate proteins at the site of DNA crosslinks, creating a signal that recruits other repair factors to excise and repair the DNA lesions. X-ray crystal structures of the RING finger subunit (FANCL) had been previously determined[3] and these provided important insights into how FANCL binds to its cognate E2 enzyme. A native FA core complex had previously been purified from cells[4], showing that the catalytic module of the complex is comprised of three subunits (FANCL, FANCB and FAAP100). This catalytic module is a more specific and more efficient E3 ligase than FANCL alone. Studies using negative stain electron microscopy indicated that the catalytic module is a dimer of heterotrimers[5]. Still, progress in understanding the mechanistic basis of ubiquitination by the FA core complex had been slowed by the challenges in obtaining FA core complex in sufficient quantity and purity, an incomplete description of subunit functions and interactions, and a lack of high-resolution structures.

In the present study, methods were developed to isolate an active FA core complex by simultaneously over-expressing all eight subunits in insect cells, allowing purification of milligram quantities of a pure recombinant complex. This sample, as well as a subcomplex containing a subset of the subunits, was imaged using cryo-EM and 3D structures were obtained (Fig. 1). Computational methods were used to reduce blurring in peripheral parts of the complex (multi-body refinement and particle subtraction followed by focussed classification and refinement), and new methods were developed for local symmetry averaging. Together, these methods increased the resolution of the 3D reconstructions, allowing visualisation of the FA core complex for the first time.

Previously determined structures accounted for only 12% of the mass of

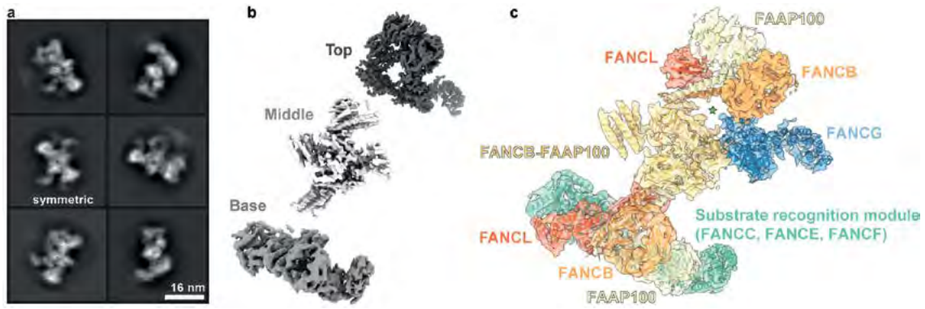

Figure 1: (a) Selected 2D class averages of the FA core complex. One class appears to be symmetric (labelled). (b) Focused classification and refinement (top, base) or multibody refinement (middle) resulted in three independent cryo-EM maps that are shown separately. (c) Model of FA core complex subunits (cartoon) fitted into the EM density (isosurface), coloured by assigned subunits. The green star marks a channel with a diameter of approximately 23 Å. Figure panels reproduced from Shakeel et al. (2019).

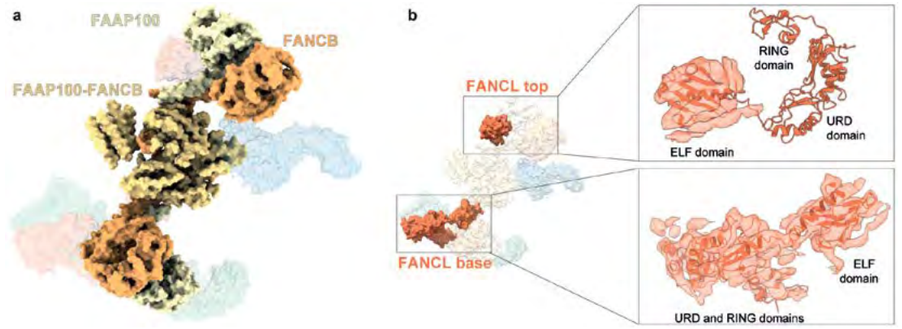

Figure 2: (a) Surface representation of the FA core complex model, highlighting FANCB and FAAP100, which act as a molecular scaffold. FANCB, orange; FAAP100, yellow; regions where we are unable to distinguish FANCB and FAAP100, yellow–orange. (b) Surface representation of the FA core complex model, highlighting the two copies of FANCL (left). On the right, the two models of FANCL are shown in cartoon representation, fitted in the cryo-EM map. Density for the URD and RING domains is not well defined in the top copy. Figure panels reproduced from Shakeel et al. (2019).

the FA core complex, and the sequences of many subunits did not resemble proteins of known structure, making it difficult to interpret the cryo-EM data at 4.2 Å resolution. Thus, the sample was also studied using complementary methods including native mass spectrometry, crosslinking mass spectrometry and biochemical reconstitution. By integrating these data, models for seven of the eight subunits could be built into the cryo-EM maps (Fig. 1c).

The three subunits of the catalytic module were each present in two copies within the FA core complex, resulting in a pseudosymmetry in the centre of the complex (Fig. 2). Interestingly, the structure showed that FANCB, FANCL and FAAP100 not only act as the catalytic module, but they are also the structural core of the complex, providing a scaffold to assemble the remaining five subunits. Only one copy of each of the remaining subunits could be identified in the maps.

Examination of the models showed that two subunits (FANCB and FAAP100) have strikingly similar structures despite no apparent sequence similarity. The

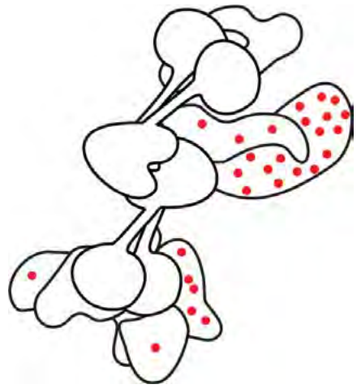

Figure 3: Distribution of patient mutations per subunit are indicated on the FA core complex by red dots. Most mutations are found in the structural periphery of the complex.

models also showed that there are two RING finger subunits (FANCL), located at opposite ends of the FA core complex (Fig. 2b). RING fingers are critical for the E3 ligase function. The two copies of FANCL are asymmetrically positioned – one is located in the base and is surrounded by the subunits of the substrate recognition module. All three domains of FANCL are visible in the base of the cryo-EM map. In contrast, the second FANCL is at the top of the complex and the RING domain is not visible. It is likely that this domain is flexible and therefore blurred out in the maps. The different conformations of the two FANCL subunits suggest that they play distinct roles within the complex, and extensive interactions with other subunits likely explain why the catalytic module is a better E3 ligase than FANCL alone[4]. Asymmetric dimerisation has been observed for other RING fingers and therefore may be a general feature of E3 ligases.

Finally, the distribution of patient mutations were mapped onto the overall structure (Fig. 3). Intriguingly, almost all of the patient mutations are found in the structural periphery of the FA core complex. This suggests that mutations are not well tolerated in the central core of the complex because they would likely compromise its structural integrity, thereby abrogating ubiquitin ligase activity. In agreement with this, the few patients that have mutations within the structural core of the complex (in FANCB or FANCL) are severely afflicted. On the other hand, mutations in the periphery would not disrupt the structural integrity of the complex and are therefore more tolerated.

The new structural model of the FA core complex provides insights into monoubiquitination by this large, multi-subunit E3 ligase in DNA repair. The structure and the reconstituted monoubiquitination system will be used in future studies to understand the mechanisms and regulation of FA-mediated DNA repair.

References:

1. Kottemann M. C. *et al.* Fanconi anaemia and the repair of Watson and Crick DNA crosslinks. *Nature* **493**, 356-363 (2013). DOI: 10.1038/nature11863
2. Walden H. *et al.* The Fanconi Anemia DNA repair pathway: structural and functional insights into a complex disorder. *Annu. Rev. Biophys.* **43**, 257-278 (2014). DOI:10.1146/annurev-biophys-051013-022737
3. Hodson C. *et al.* Structure of the human FANCL RING-Ube2T complex reveals determinants of cognate E3-E2 selection. *Structure* **22(2)**, 337-344 (2014). DOI: 10.1016/j.str.2013.12.004
4. Rajendra E. *et al.* The genetic and biochemical basis of FANCD2 monoubiquitination. *Mol. Cell.* **54(5)**, 858-869 (2014). DOI: 10.1016/j.molcel.2014.05.001
5. Swuec P. *et al.* The FA core complex contains a homo-dimeric catalytic module for the symmetric mono-ubiquitination of FANCI-FANCD2. *Cell. Rep.* **18(3)**, 611-623 (2017). DOI: 10.1016/j.celrep.2016.11.013

Funding acknowledgement:
Medical Research Council MC_U105192715

Corresponding author:
Dr Lori A Passmore, MRC Laboratory of Molecular Biology,
passmore@mrc-lmb.cam.ac.uk

Structural studies offer details of flu virus replication

Related publication: Fan H., Walker A. P., Carrique L., Keown J. R., Serna Martin I., Karia D., Sharps J., Hengrung N., Pardon E., Steyaert J., Grimes J. M. & Fodor E. Structures of influenza A virus RNA polymerase offer insight into viral genome replication. *Nature* **573**, 287-290 (2019). DOI: doi.org/10.1038/s41586-019-1530-7

Publication keywords: Influenza virus; RNA polymerase; Virus replication

Influenza (commonly known as the flu) is an acute respiratory infection responsible for over three million cases of severe illness each year. In order to stay one step ahead of flu outbreaks, scientists are trying to decipher the structure and mechanisms of influenza A viruses.

When the virus infects host cells, it makes many copies of its RNA genome to produce new virus particles. The enzyme responsible for this genome replication is called RNA-dependent RNA polymerase, or FluPolA.

A team of researchers from the University of Oxford used Cryogenic Electron Microscopy (cryo-EM) imaging at the Electron Bio-Imaging Centre (eBIC) to analyse the influenza virus polymerase. They also used the Macromolecular Crystallography (MX) beamlines I03, I04, I24 to analyse crystals of the polymerase.

Using X-ray crystallography, they were able to obtain the first, high-resolution structures of FluPolA of human and avian influenza viruses, revealing crucial details of how the structure of FluPolA is vital in initiating RNA synthesis. Using cryo-EM allowed them to study the protein binding to an RNA template.

Their results suggest a target by which virus reproduction might be inhibited. In the future, this could lead to the development of antiviral drugs against the flu. This is a compelling example of integrative structural biology, with scientists using complementary techniques (including nanobody technology from Instruct-BE) to gain new insights into the replication mechanisms of FluPolA.

Influenza is an acute respiratory infection, caused by influenza A viruses, which are responsible for seasonal pandemics. The major host species of influenza A virus are aquatic birds, but occasionally the virus can cause zoonotic infections in humans and other animals[1]. All viruses need to infect and replicate within cells for their continued existence. This involves replicating new copies of the viral genome, which for influenza is negative sense single-stranded ribonucleic acid. Like other similar viruses, influenza carries its own polymerase (FluPol), which catalyses the synthesis of this new viral RNA. The molecular mechanisms by which FluPol replicates the viral RNA (vRNA) through a complementary RNA (cRNA) intermediate remain largely unknown. In addition, FluPol is multi-functional and not only replicates the viral genome but transcribes capped viral messenger RNA (mRNA). It does this by binding to cellular PolII and cleaving off the cap structure from newly synthesised cellular mRNA, which it uses to prime transcription. How the polymerase switches between transcription and genome replication is not well understood and is an area of active study.

As such, FluPol lies at the heart of the influenza virus lifecycle and has been the focus of a prolonged research effort to understand its structure and mechanisms. Ultimately, this may facilitate the development of antiviral compounds that target the polymerase.

FluPol comprises a complex of three viral proteins: PA, PB1 and PB2, known together as a heterotrimer. PB1 is the RNA polymerase and has the canonical right-hand-like fold, with subdomains known as fingers, palm and thumb. PB2 is involved in the binding of the cap of cellular mRNA, and PA has an endonuclease domain that cleaves the cap structure away from the cellular RNA. The FluPol trimer binds the conserved 5′ and 3′ ends of the viral RNA segment, known as the vRNA promotor, which form a partially dsRNA panhandle structure.

Previous structural work on FluPol from different influenza viruses had revealed that the molecule is highly dynamic and can take up strikingly different poses[2,3]. Though the fold of each of the domains within the FluPol trimer is identical, the arrangement of domains within PB2 and PA are dramatically altered between the unbound (apo) form and promotor RNA-bound complexes. This is thought to reflect the balance between transcription and replication.

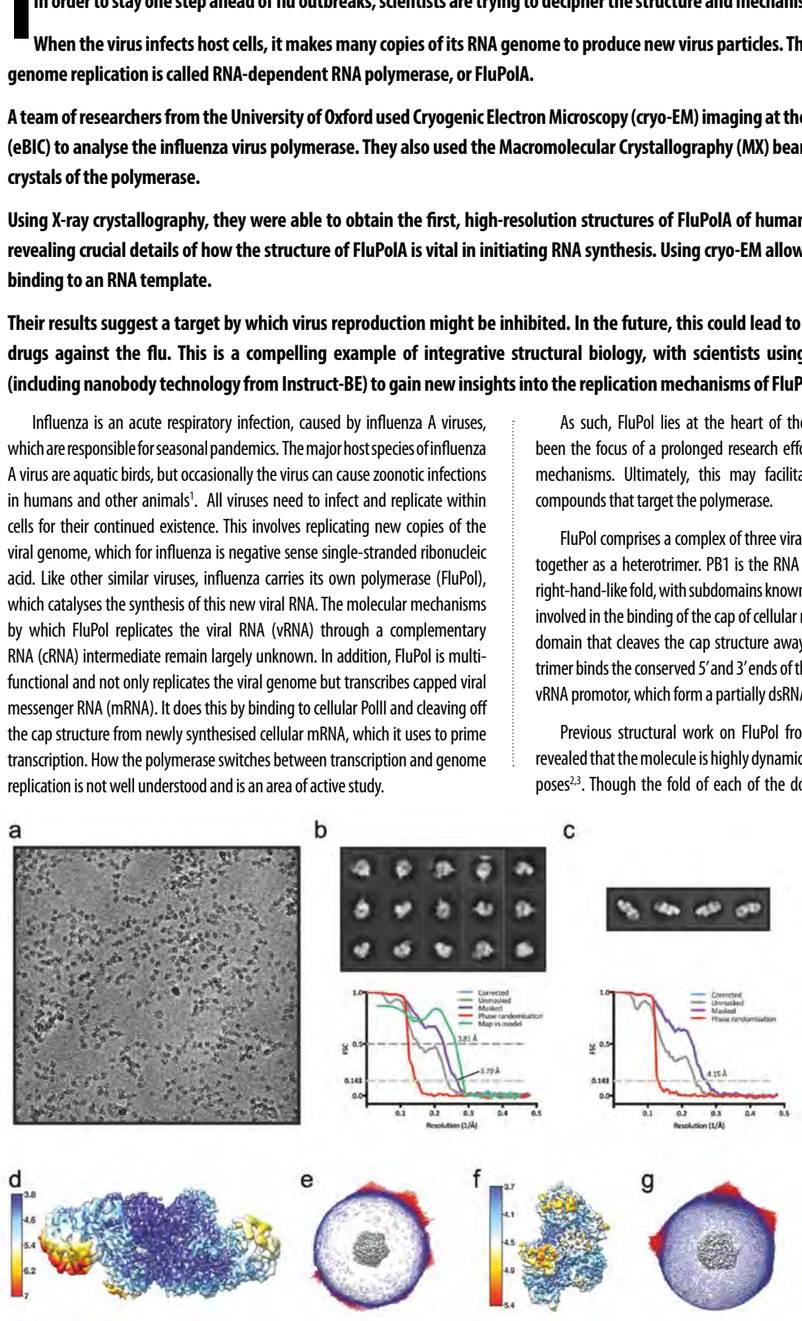

Figure 1: Single particle cryo-EM analysis of monomeric and dimeric cRNA-bound human H3N2 FluPolA heterotrimer in complex with Nb8205. (a) Representative micrograph of cRNA-bound FluPolA in complex with Nb8205, embedded in vitreous ice. (b) Representative 2D class averages. (c) Forward Scatter Curves (FCS) for the 3D reconstruction using gold-standard refinement in RELION, indicating an overall map resolution of 3.79 Å and 4.15 Å for the monomeric and dimeric FluPolA form, respectively, and the model-to-map FSC. Curves are shown for phase-randomisation, unmasked, masked and phaserandomisation-corrected masked maps. (d) and (f) The 3D reconstructions, locally filtered and coloured according to RELION local resolution, for the dimeric (d) and monomeric (f) form. (e) and (g) Angular distribution of particle projections for the dimeric (e) and monomeric (g) form, with the cryo-EM map shown in grey.

Using X-ray crystallography, this paper describes the first, high-resolution structures of FluPol of human and avian influenza viruses. Intriguingly the structures showed that the heterotrimeric FluPol forms dimers in the crystals. FluPol was then solved by Single Particle Analysis (SPA) cryo-EM, using the microscopes at eBIC, which confirmed that this dimer interface of FluPol was retained in solution and revealed that the 5′-end of the RNA template was bound to FluPol in a hook conformation in an RNA binding pocket, whilst the 3′-end was disordered.

To determine whether the dimeric FluPol structure was important to enzyme activity, mutations were introduced to destabilise the dimer interface. The viral transcription and replication by FluPol mutants were measured using a mini-replicon assay, showing that the dimeric structure of FluPol was important for the initiation of vRNA synthesis from the cRNA template.

It was clear from analysis of the protein in solution that FluPol is in dynamic equilibrium between monomeric and dimeric forms. To gain further insight into FluPol dimerisation and cRNA binding, a nanobody was used that reduces FluPol dimerisation. The use of nanobodies in structural analyses is well established but, in this work, they were of great use in probing function. Again, SPA cryo-EM was used to solve the structures of monomeric and dimeric FluPol bound to the nanobody and cRNA promoter. The structure of FluPol dimers with and without nanobody are essentially identical, with the same ordered 5′ and dynamic 3′ cRNA. However, the monomeric FluPol bound to nanobody revealed the binding of both 5′ and 3′ cRNA. Intriguingly the 3′ cRNA bound at a site previously unobserved and in a groove close to the dimer interface and could represent a parking site for 3′ RNA during replication and transcription. Further evidence comes from the observation that RNA binding is seen in a similar site of the RNA polymerase of La Crosse orthobunyavirus[4].

By comparing the structures of monomeric and dimeric FluPol-nanobody complexes it was found that dimerisation induces a movement of a helical bundle that is formed by the thumb subdomain of PB1 and the N1 subdomain of PB2. This movement results in an opening of the binding site for the 3' cRNA, which explains the absence of 3' cRNA at this site in the dimeric structure. Furthermore, dimerisation leads to rearrangements in the polymerase active site, specifically the retraction of the priming loop (part of the thumb subdomain) and could destabilise binding of the 3' cRNA in the active site.

To show that the nanobody affected the function of FluPol, a cellular mini-replicon assay was used with co-expression of the nanobody, which showed the severe inhibition of replication and transcription, whereas another nanobody that does not affect FluPol dimerisation had no significant effect. Furthermore, viral infectivity assays with the nanobody caused a significant reduction in virus titre.

In this paper, using an integrative structural and functional biology approach, it was shown that dimerisation of FluPol is required for the initiation of vRNA synthesis from the cRNA viral template. The dependency on dimerisation for replication of vRNA from cRNA template is consistent with previous observations that vRNA synthesis requires a trans-activating polymerase[5]. It is interesting to note that a requirement for trans-activation through polymerase dimerisation provides a mechanism for tuning the amount of vRNA synthesised, where vRNA production is initiated only when a sufficient level of newly made free polymerase is available in the cell. This would help ensure that the virus does not trigger an antiviral response through recognition by pathogen-recognition receptors by producing vRNA that cannot be assembled into viral ribonucleoprotein complexes (vRNPs).

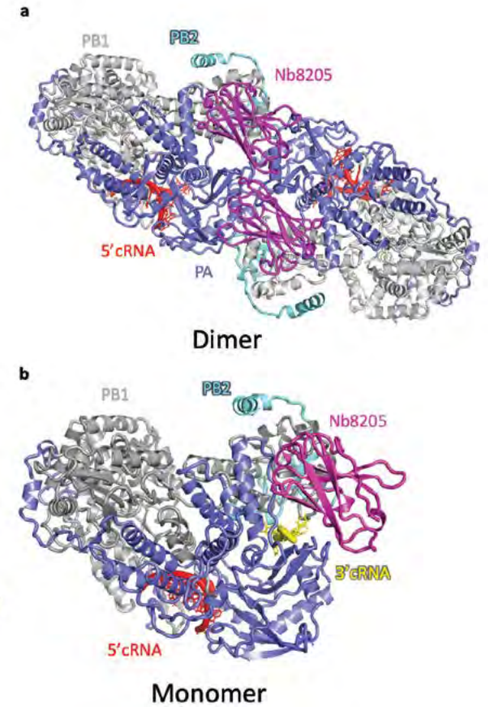

Figure 2: Structures of (a) dimeric and (b) monomeric cRNA-bound human H3N2 FluPol heterotrimer in complex with nanobody solved by single particle cryo-EM analysis. In the monomeric structure 3′ cRNA (coloured yellow) binds in a narrow groove, that in the dimeric form of FluPol is opened up and is not able to accommodate 3′ cRNA. The structures in panels (a) and (b) are in the same orientation but are not drawn to scale.

References:

1. Mostafa A. *et al.* Zoonotic potential of influenza A viruses: a comprehensive overview. *Viruses* 10, 497 (2018). DOI: 10.3390/v10090497
2. Hengrung N. *et al.* Crystal structure of the RNA-dependent RNA polymerase from influenza C virus. *Nature* **527**, 114-117 (2015). DOI: 10.1038/nature15525
3. Pflug A *et al.* Structure of influenza A polymerase bound to the viral RNA promoter. *Nature* **516**, 355-360 (2014). DOI: 10.1038/nature14008
4. Gerlach P. *et al.* Structural insights into bunyavirus replication and its regulation by the vRNA promoter. *Cell* **161**, 1267-1279 (2015). DOI: 10.1016/j.cell.2015.05.006
5. York A. *et al.* Isolation and characterization of the positive-sense replicative intermediate of a negative-strand RNA virus. *P. Natl. Acad. Sci.* **110**, E4238–45 (2013). DOI: 10.1073/pnas.1315068110

Funding acknowledgement: This work was supported by the Medical Research Council, the Wellcome Trust and by Instruct-ERIC, part of the European Strategy Forum on Research Infrastructures (ESFRI). Computation used the Oxford Biomedical Research Computing (BMRC) facility, a joint development between the Wellcome Centre for Human Genetics and the Big Data Institute, supported by Health Data Research UK and the NIHR Oxford Biomedical Research Centre.

Corresponding author: Dr Jonathan Grimes, University of Oxford, jonathan@strubi.ox.ac.uk

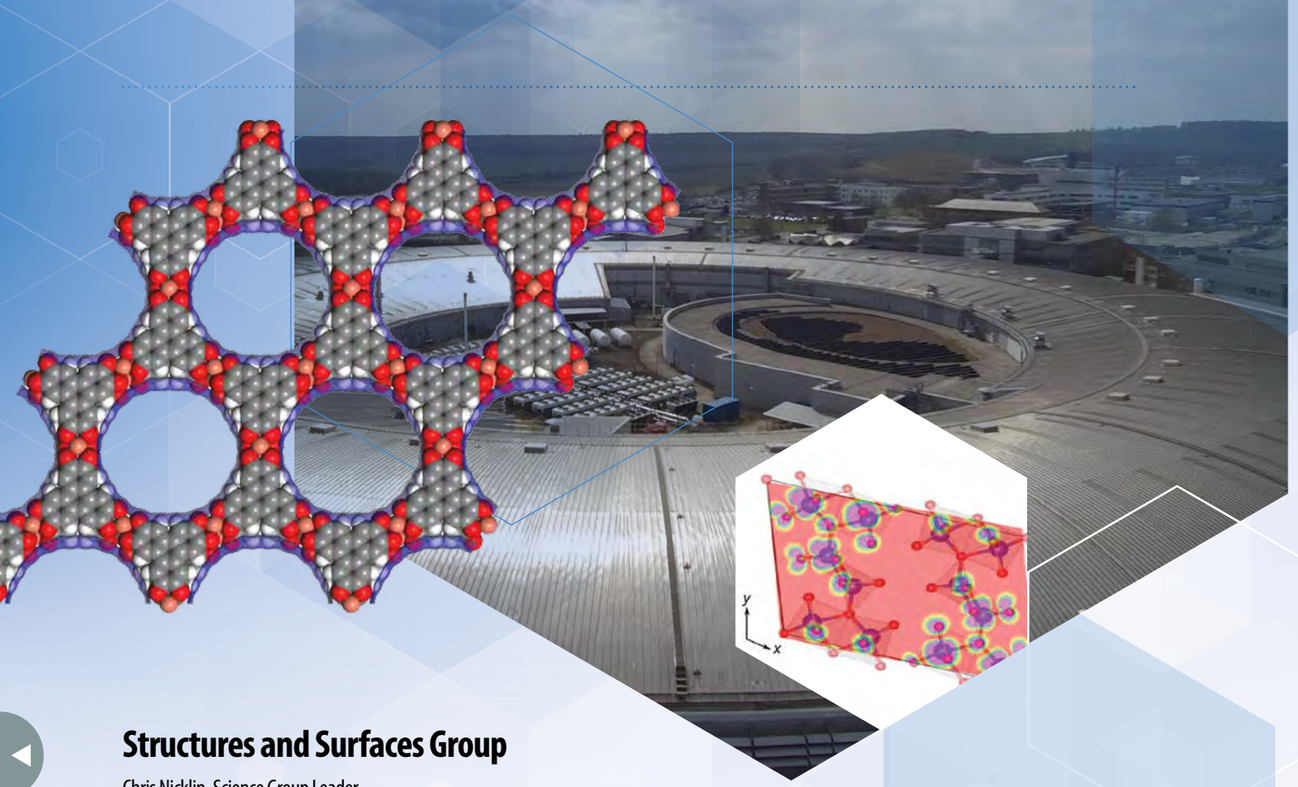

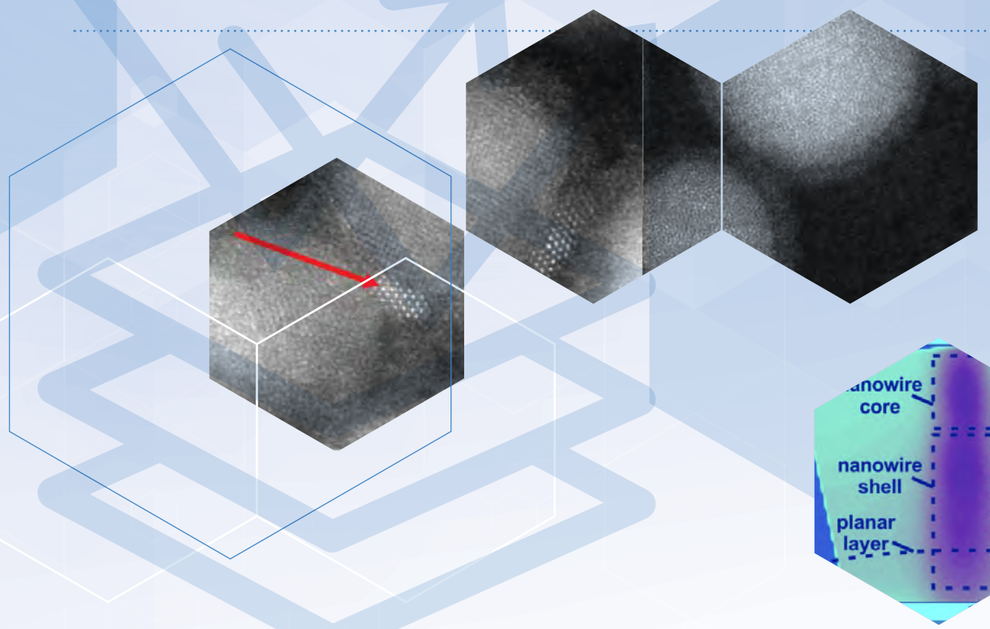

Structures and Surfaces Group

Chris Nicklin, Science Group Leader

The Structures and Surfaces Group comprises four beamlines: I05 (Angle Resolved Photoemission Spectroscopy – ARPES), I07 (Surface and Interface X-ray Diffraction), B07 (Versatile Soft X-ray Scattering – VERSOX), and I09 (Atomic and Electronic Structure of Surfaces and Interfaces). These offer a variety of techniques to examine the atomic-scale structure, chemical nature and electronic states at buried interfaces or the surfaces of materials, and in novel quantum materials. Developments are increasingly enabling the studies to be performed under *operando* conditions or during sample biasing, extending the range of scientific questions that can be explored. The group is continuing to expand the capabilities of the beamlines whilst also taking a strategic view for the future, through the development of a long-term roadmap of major upgrades, additional technique developments and potential new beamlines based on the workshop held last year. The Diamond-II science case highlighted, in particular, the important role that surfaces and interfaces play in broader research areas such as battery technology, photovoltaic structures, electronic devices (e.g. transistors) and catalytic/electrochemical systems under *operando* conditions. Expanding the techniques to these communities remains a key aim for the group.

Beamline I05 successfully completed its first beamline review by an expert panel that reports to the Scientific Advisory Committee (SAC). The quality of the research output, the impact (quality of the papers and citations generated) and the expertise and support of the beamline team were all highlighted as helping to make I05 a world-leading ARPES facility. The high-resolution branch is completing its upgrades to the gratings and electron energy analyser, whilst the NanoARPES end station will deliver improved flux through the incorporation of a capillary mirror. The team welcomed Matthew Watson, who had previously been a post-doctoral researcher at Diamond, back to the beamline as a beamline scientist. The group have ambitious plans for developing photoelectron spectroscopy at Diamond to complement the high-resolution facilities available on I05, the arrival of a soft X-ray ARPES system (momentum microscope) this year on I09, the hard X-ray (HAXPES) station also on I09 and the near ambient pressure (NAP-XPS) capability on B07.

The surface and interface diffraction facilities on beamline I07 are being upgraded to enhance the capabilities. This includes integrating continuous scanning of the diffractometer to improve the data collection efficiency and developing automated, fast attenuators to enable fast measurement of X-ray reflectivity and crystal truncation rods that cover many orders of magnitude changes in intensity. A new Excalibur detector is also being commissioned to replace the Pilatus P100K detectors mounted in the first experimental hutch. The diffractometer is being adapted to increase the range of one of the circles whilst a new hexapod will increase the reliability and speed of experiments and allow the use of heavier sample environments (up to 200 kg). There is a long term plan to revisit the optics layout of the beamline with the ambition of reducing the beam size and increasing the flux at the sample. This may include use of a multilayer monochromator, new mirrors or compound refractive lenses and upgraded double crystal deflector system for liquids studies and improved beam intensity monitoring.

This year, the second branch of beamline B07 (VERSOX) will open to users, initially enabling Near Edge X-ray Absorption Fine Structure (NEXAFS) studies using soft X-rays to study processes such as molecular adsorption or catalysis. This will be complemented by a high throughput XPS/NEXAFS system that will allow chemical state analysis of many samples where the tuneable photon energy from the synchrotron source can be utilised to measure and/or enhance the signal from low atomic number elements. As the two branchlines work independently, this will bring additional capability and supplement the techniques offered by the group. The near-ambient pressure XPS system available on Branch C of the beamline continues to work well with the first user publications coming out at the end of 2019. The possibility of measuring XPS spectra up to pressures of 50 mbar is opening up new avenues of research, particularly with the focus on understanding catalytic processes in greater detail. In addition, the relatively wide photon energy range (180 eV to 2800 eV) enables experiments which are not possible at many other beamlines (e.g. Boron, Sulphur K-edge NEXAFS). Different end stations are available depending on the requirements of the experiment. The gas handling capability of the beamline is being improved through the installation of an automated gas delivery system to enable accurate control of the sample environment in terms of gas composition and pressure. The beamline team have ambitious plans to expand the facilities offered to enhance studies on solid-liquid interfaces and nano-clustered samples.

Beamline I09 has had several years of major upgrades whilst maintaining an exceptionally active user programme. This year saw the hard X-ray (HAXPES) system move to its final location on the hard X-ray branch, and with-beam commissioning is underway whilst the next large end station for soft X-ray ARPES (also known as a momentum microscope) is expected to be delivered this year. The unique design of the beamline means that the hard and soft branches can operate independently or be combined into end station 2, where the majority of the work has been undertaken since the beamline opened to users. Smaller scale upgrades have continued to add to the capabilities of the beamline, notably, a new manipulator that enables sample biasing, cooling and heating whilst still allowing sample transfer has been built and installed in end station 2. Future plans include replacing the simple (three fixed energy) monochromator with a fully tuneable version to enhance the HAXPES studies and an upgraded plane grating monochromator to improve the resolving power (energy resolution) of the soft X-ray branch.

The group are aiming to enhance the associated infrastructure available for surface science research, including the design of a new offline ultrahigh vacuum system to characterise samples that could then be studied on the beamlines. This will position Diamond to be able to rapidly study new samples and enhance the link between laboratory-based and synchrotron-based studies. We aim for this capability to be at the core of many of the joint PhD studentships that we support. The proposal was well received by the SAC and design work will start on the system in 2020.

The range of science undertaken at the beamlines continues to be a combination of detailed surface science characterisation through to the application of the methods to novel samples, as outlined in the contributions from a selection of our users. There is also a shift towards many more multi-modal experiments that make use of several techniques to answer a scientific question. This is shown in the science contribution from Rosa Arrigo who has used B07, together with electron microscopy, diffraction and spectroscopy to understand the nature of the preferential formation of one chiral enantiomer by catalysis using nanoparticles. The report by the group of Emmanouil Dimakis highlighting work on I07 to understand the in-plane strain in core-shell nanowires of GaAs/InGaAs also combines the diffraction measurements with electron microscopy and compositional information. The application of the techniques to different types of samples or processes continues to grow as exemplified in the contribution by Louis Piper who studied samples relevant to the production of hydrogen via photocatalysis of water for clean energy through optimisation of the sample composition. Fundamental scientific studies form a large part of our portfolio and particularly noteworthy this year has been the discovery of a Weyl fermion in a magnetic compound by the group of Yulin Chen. The angle resolved photoemission data recorded on beamline I05 displayed the key characteristics predicted by the theoretical calculations and details of the dispersion of the features were also measured, adding to the evidence of this quasiparticle.

The members of the Structures and Surfaces Group are committed to continuing to offer the best support to our users, to ensure the highest quality scientific output from the beamlines. The combination of strong interactions and collaborations, together with continuous improvements to the instrumentation and technique development is key to our success. Please contact us if you would like to discuss any of the possibilities that we offer and how such synchrotron-based studies could help in your research.

Discovery of the Weyl fermion in a ferromagnetic crystal

Related publication: Liu D. F., Liang A. J., Liu E. K., Xu Q. N., Li Y. W., Chen C., Pei D., Shi W. J., Mo S. K., Dudin P., Kim T., Cacho C., Li G., Sun Y., Yang L. X., Liu Z. K., Parkin S. S. P., Felser C. & Chen Y. L. Magnetic Weyl semimetal phase in a Kagomé crystal. *Science* **365**, 1282 (2019). DOI: 10.1126/science.aav2873

Publication keywords: Magnetic Weyl semimetal; Weyl fermion; Fermi-arcs; Angle-Resolved Photoemission Spectroscopy (ARPES)

Condensed matter systems, such as crystalline solids, can serve as a platform for the study of phenomena in other fields of physics, including high energy physics. In some ways, a crystal can be viewed as a 'mini-universe'. An international team of researchers were intrigued by the search for a massless chiral particle – the Weyl fermion – in a magnetic compound.

The existence of the Weyl fermion was initially proposed in 1929, but never proven. In 2011, there was a prediction that a magnetic crystal can host Weyl fermions, and the unique electronic structures in a crystal with Weyl fermions could give rise to many intriguing physical phenomena.

The research team used the Angle-Resolved PhotoEmission Spectroscopy (ARPES) beamline (I05) to investigate the electronic structures of the crystal. They successfully found both the bulk Weyl fermions and the unique surface Fermi-arcs that connect them.

The exotic Weyl fermions in this compound have many interesting and useful properties. Their enormous electron mobility means that they could be used for fast electronic devices. A large magnetoresistance makes them a candidate for large density magnetic storage devices. With spin-polarised surface electrons, this compound could be used in spintronics devices, and the bulk-surface electron correlation could be useful for unique optoelectronic applications.

Weyl semimetals (WSMs) represent a novel type of topological matter that hosts emergent Weyl fermions in the bulk of a crystal and associated surface electrons that form an exotic unclosed surface Fermi surface (called the surface Fermi-arcs, or SFAs). The unique electronic structures in the WSM can give rise to many intriguing physical phenomena such as chiral magnetic effects, unusually large anomalous Hall effect and quantum anomalous Hall effect[1].

In solids, WSMs can exist in crystals that break the time-reversal symmetry (TRS) or inversion symmetry (IS), or both. The TRS-broken (i.e. magnetic) WSMs were first proposed in 2011[2] and have many preferred properties over the IS-breaking WSMs[3]. However, despite the many candidates predicted over the years, experimental confirmation that they exist had remained elusive. In this work, Angle-Resolved PhotoEmission Spectroscopy (ARPES) was used to systematically study the electronic structures of a Kagomé crystal $Co_3Sn_2S_2$ and directly observe the characteristic Weyl fermions and the associated SFAs, thus confirming the existence of magnetic WSMs[3].

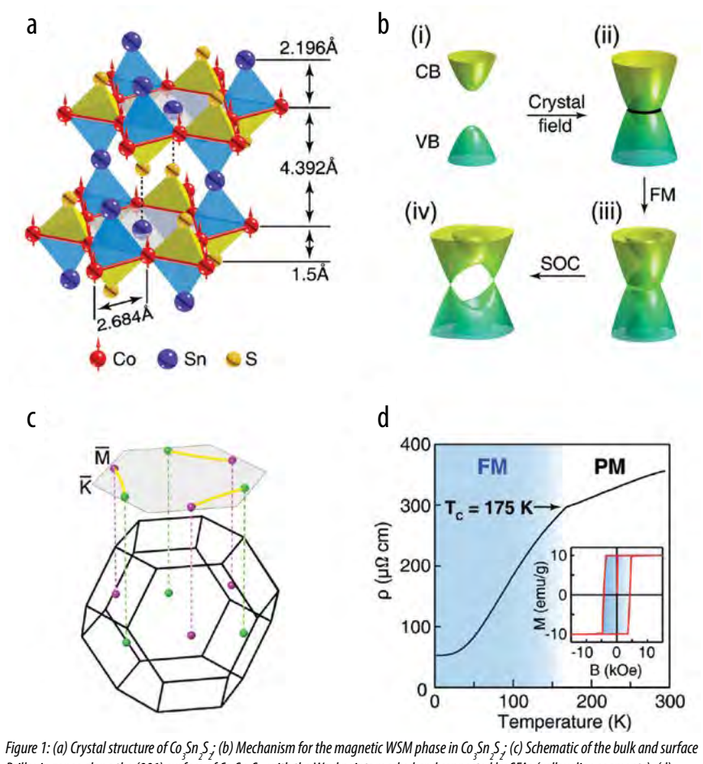

Figure 1: (a) Crystal structure of $Co_3Sn_2S_2$; (b) Mechanism for the magnetic WSM phase in $Co_3Sn_2S_2$; (c) Schematic of the bulk and surface Brillouin zones along the (001) surface of $Co_3Sn_2S_2$ with the Weyl points marked and connected by SFAs (yellow line segments); (d) Temperature dependences of longitudinal electric resistivity. Inset: Hystersis loop of the magnetisation (external magnetic field is along the z axis) measured at T= 2 K, showing a typical ferromagnetic behaviour.

The crystal structure of $Co_3Sn_2S_2$ is composed of stacked ...-Sn-[S-(Co_3-Sn)-S]-... layers (Fig. 1a). In each Sn-[S-(Co_3-Sn)-S] layer group, the central Co layer forms a two-dimensional Kagomé lattice with an Sn atom at the centre of the hexagon; S atoms are located alternately above and below the triangles formed by the Co atoms, with the adjacent Sn-[S-(Co_3-Sn)-S] layer groups linked by layer-sharing Sn atoms. The TRS-breaking WSM phase in $Co_3Sn_2S_2$ (Fig. 1b) is caused by the joint effects of crystal field, ferromagnetism (FM), and spin-orbital coupling (SOC). The crystal field first mixes the valence band (VB) and conduction band (CB) to form four-fold degenerate nodal lines (Fig. 1b (ii), black curve); subsequently, the degeneracy of the nodal line is lifted (Fig. 1b (iii), green curve) by the FM transition that breaks the TRS; finally, SOC splits the doubly degenerate nodal line in Fig. 1b (iii) into a pair of Weyl points with opposite chirality (Fig. 1b (iv)). According to

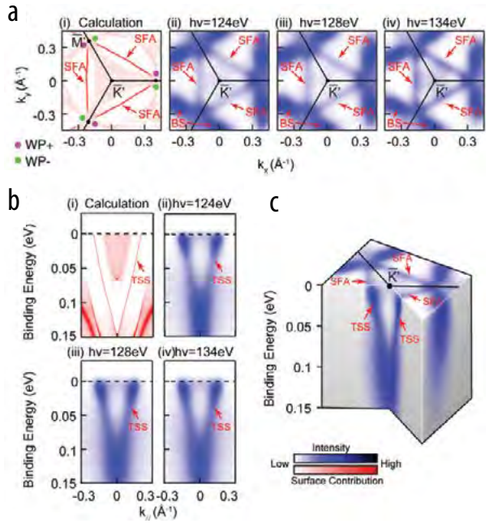

Figure 2: (a) Comparison of (i) the calculated FS from both bulk and surface states and (ii)-(iv) the experimental FSs under different photon energies. The magenta and green dots in (i) represent the Weyl points with opposite chirality and the SFAs are indicated by red arrows; (b) Comparison of the dispersion from (i) calculated TSS along the high Γ-K'-Γ direction and (ii)-(iv) the experimental TSSs; (c) 3D intensity plot of the experimental band structure near the K' point.

ab initio calculations for this material[4], there are three pairs of Weyl points within each bulk Brillouin zone (BZ) connected by the SFAs (Fig. 1c). The temperature-dependent transport (Fig. 1d) and magnetisation measurements (Fig. 1d, inset) clearly illustrate that an FM transition occurs at a critical temperature T_c = 175 K with a hysteresis loop.

According to the calculations, the SFAs in $Co_3Sn_2S_2$ are located around the K' of the BZ (Fig. 2a (i)), formed by a line segment that connects one pair of Weyl points with opposite chirality in each BZ. These line segments from three adjacent BZs can form a triangle-shaped surface Fermi surface (FS) piece. This unusual surface FS topology was indeed observed experimentally (Fig. 2a (ii)-(iii)), where the unchanged shape of these line-segment FS pieces from different photon energies indicates their surface origin (Fig. 2a (ii)-(iii)). Notably, each line-segment FS piece merges into the bulk FS pockets near the M' point of the BZ (Fig. 2a (i)), in excellent agreement with the calculations. In addition to the FS topology, the dispersions of the topological surface states (TSSs) that result in the SFAs from different photon energies are also in good agreement with calculations (Fig. 2b, c).

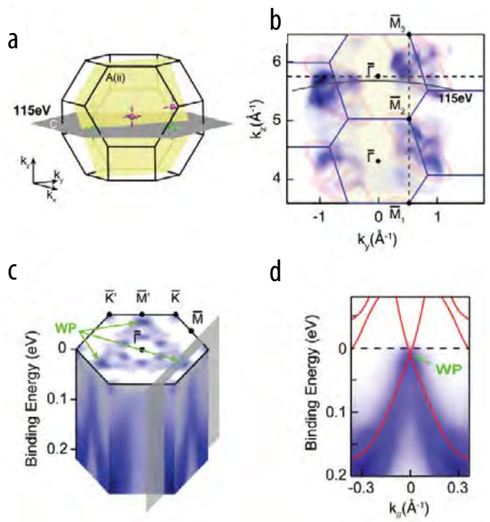

Figure 3: (a) Schematic of the measurement k_y-k_z plane (vertical yellow plane) in 3b. Weyl points are also illustrated; (b) Photoemission intensity plot along the k_y-k_z plane (yellow plane in 3a) near Fermi level. Overlaid red contours are calculated bulk FSs; (c) 3D ARPES spectra intensity plot measured with 115 eV photon energy, showing both the FS (top surface) and the band dispersions (side surfaces). The grey plane indicates the location of the band dispersion cut in 3d. (d) Band dispersion showing linear Weyl dispersion, in agreement with the calculations (red curves overlaid).

With the SFAs identified, a search was undertaken for the characteristic bulk Weyl fermion dispersion. For this purpose, broad range (50 to 150 eV) photon energy dependent ARPES measurements were performed to precisely identify the k_z momentum locations of the Weyl points (Fig. 3b). The bulk bands with strong k_z dispersion can be seen in the k_y–k_z spectra intensity map (Fig. 3b), agreeing well with the calculations (overlaid in red in Fig. 3b).

The agreement between experiments and calculations (Fig. 3b), allows the identification of the bulk Weyl points in $Co_3Sn_2S_2$, which lie at $k_z = \pm 0.086$ Å^{-1} planes (Fig. 3a) and can be accessed by using 115 eV photons (corresponding to $k_z = -0.086$ Å^{-1} in Fig. 3a). To precisely locate the in-plane momentum loci of the Weyl points, k_x-k_y FS mapping (Fig. 3c) of the band structures across the surface BZ were performed first, then with a focus on band dispersions that cut through the Weyl point (see the cutting plane in Fig. 3c). Indeed, point-like FSs (the Weyl points) were observed as illustrated in Fig. 3c. The band dispersions in Fig. 3d also show the linear crossing of the bands at the Weyl point, in good agreement with the calculations. The observation of the distinctive SFAs and bulk Weyl points with linear dispersions, together with the overall agreement of the measurements with theoretical calculations, establishes $Co_3Sn_2S_2$ as a magnetic WSM. This finding extends the possibilities for the exploration of other exotic phenomena associated with TRS-breaking WSMs (such as the unusually large anomalous Hall conductivity and quantum anomalous Hall effects at the 2D limit) and potential applications.

References:

1. Armitage N. P. *et al.* Weyl and Dirac semimetals in three-dimensional solids. *Rev. Mod. Phys.* **90**, 015001 (2018). DOI:10.1103/RevModPhys.90.015001
2. Wan X. *et al*. Topological semimetal and Fermi-arc surface states in the electronic structure of pyrochlore iridates. *Phys. Rev. B* **83**, 205101 (2011). DOI:10.1103/PhysRevB.83.205101
3. Liu D. F. *et al.* Magnetic Weyl semimetal phase in a Kagomé crystal. *Science* **365**, 1282 (2019). DOI:10.1126/science.aav2873
4. Xu Q. *et al.* Topological surface Fermi arcs in the magnetic Weyl semimetal $Co_3Sn_2S_2$. *Phys. Rev. B* **97**, 235416 (2018). DOI:10.1103/PhysRevB.97.235416

Funding acknowledgement:
This work was supported by the Shanghai Municipal Science and Technology Major Project (grant no. 2018SHZDZX02), the Alexander von Humboldt Foundation, the National Natural Science Foundation of China (grant nos. 11774190, 11634009, 11674229, and 11974394), the National Key R&D Program of China (grant nos. 2017YFA0305400 and 2017YFA0206303), the Tsinghua University Initiative Scientific Research Program, and the Wurzburg-Dresden Cluster of Excellence on Complexity and Topology in Quantum Matter (EXC 2147, no. 39085490).

Corresponding author:
Prof Yulin Chen, University of Oxford, yulin.chen@physics.ox.ac.uk

Insights into the structure and reactivity of Ni nanoparticles for catalytic asymmetric hydrogenation

Related publication title and DOI: Arrigo R., Gallarati S., Schuster M. E., Seymour J. M., Gianolio D., da Silva I., Callison J., Feng H., Proctor J. E., Ferrer P., Venturini F. & Held G. Influence of synthesis conditions on the structure of nickel nanoparticles and their reactivity in selective asymmetric hydrogenation, *ChemCatChem* **12**, 1491-1503 (2019). DOI: 10.1002/cctc.201901955

Publication keywords: Nanoparticles; Ni phosphides; Hot-injection synthesis; hydrogenation; XPS ; XAFS; HRTEM

Chiral organic molecules occur in two different enantiomeric (mirror image) forms. In pharmaceutical applications, these two forms can have different effects. To maximise the effectiveness of a drug, and to reduce side effects, it is essential to synthesise only the desired form. A team of researchers studied the synthesis of methyl-3-hydroxybutyrate (MHB), an important intermediate step in the synthesis of a treatment for the eye disease glaucoma, using a nickel (Ni) catalyst. The biggest challenge of this reaction is selecting the (*R*)-MHB form. Understanding how enantioselectivity is realised over nickel catalysts is paramount to tackle this challenge.

The team studied the impact of synthesis conditions on the size, shape and electronic structure of the Ni nanoparticles on their catalytic performance. To achieve this goal, the researchers used the Versatile Soft X-ray (VERSOX) beamline, also known as B07, at Diamond Light Source to perform surface sensitive X-ray photoelectron and absorption spectroscopy to determine the electronic structure of the Ni nanoparticles, and electron microscopy at the electron Physical Science Imaging Centre (ePSIC) to determine the size and shape of the nanoparticles.

Their results are relevant for asymmetric hydrogenation reactions and for the catalysis over Ni nanoparticles in general.

The enantioselective asymmetric hydrogenation of unsaturated molecules is broadly applied for the synthesis of pharmaceuticals and fine chemicals, where the biggest challenge is attaining total selectivity to one enantiomer[1]. One of the most studied examples of such reactions is the hydrogenation of the carbonyl double bond of methyl acetoacetate (MAA) to methyl-3-hydroxybutyrate (MHB) over nickel catalysts (Fig. 1). This reaction can be carried out with high enantiomeric selectivity towards the desired (*R*)-MHB product if the surface of the nickel catalyst is modified with a chiral molecule, typically (*R,R*)-tartaric acid (TA). However, the long-term stability of heterogeneous Ni catalysts for this reaction is poor. Understanding of the much-debated mechanism by which enantioselectivity is realised at the Ni surface aided by modifiers is beneficial for the design of improved catalysts[2]. Three possible pathways have been proposed: a) a one-to-one molecular interaction of adsorbed TA controls the adsorption geometry of MAA[3] such that H_2 is delivered to the desired side of the carbonyl double bond; b) TA molecules form a supramolecular chiral arrangement on the Ni surface which desorb leaving a chiral enantioselective Ni surface[4]; c) the interaction of TA with oxidised Ni particles facilitates etching of Ni cations from the surface leaving chiral Ni kink sites[5]. In this work we explore whether achiral round-like small nanoparticles (NPs) with high-index surface sites enable more opportunities for the generation of enantioselective surface ensembles upon chiral modification.

Herein, supported and unsupported nickel nanoparticles are synthesised by means of hot-injection colloidal synthesis. The impact of the synthesis conditions on the physicochemical properties, such as morphology, size and structure are investigated using synchrotron-based X-ray Photoelectron Spectroscopy (XPS), high angle annual dark field scanning transmission electron microscopy (HAADF-STEM) and X-ray diffraction (XRD). The reactivity of these NPs in enantioselective hydrogenation is investigated to determine a structure-activity correlation, which will enable new mechanistic insights into the selective chiral function of the catalytic system and the structural transformations responsible for performance degradation.

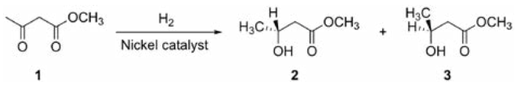

Figure 1: Hydrogenation of pro-chiral methyl acetoacetate (1) gives two enantiomers, (R)- and (S)-methyl-3-hydroxybutyrate (2 and 3, respectively). When the surface of the nickel catalyst is modified with (R,R)-tartaric acid (also in combination with an inorganic salt such as NaBr), the (R)-enantiomer is preferably obtained.

To control the size of the NPs the ratio between the reducing (oleylamine, OAm) and protecting agents (trioctylphosphine, TOP) was changed (in the sample notations used later on x and y correspond to the relative amounts of OAm and TOP, respectively). While OAm is expected to control the nucleation rate and growth, TOP acts as capping agent and provides surface stabilisation through coordination with the Ni surface, thus hindering the growth of the NPs.

The HAADF-STEM image of Ni_5x1.5y (Fig. 2a) shows a core shell crystalline Ni NP_s composed of a metallic core encapsulated within a shell of lower contrast, presumably of organic nature. Moreover, Ni nanocrystallites are embedded in this organic shell (Fig. 2b). Twinned metallic Ni nanoparticles are formed when the amount of the reducing agent (x) is 5 and above (Fig. 2a and 2b). However, when the amount of OAm (x) is relatively lower (Ni_2.5x1.5y), round amorphous core-shell NPs are obtained (Fig. 2c). Average particle sizes as determined by statistical analysis of the HAADF-TEM are 8.0±1.4 nm, 7.0±1.3 nm and 10.6±1.9 nm for Ni_2.5x1.5y, Ni_5x1.5y, Ni_10x1.5y, respectively. The trend in particle size observed for Ni_5x1.5y and Ni_10x1.5y is consistent with the expectation: the smaller NPs in the Ni_5x1.5y catalyst are due to the relatively more abundant capping agent TOP which hinders aggregation and growth.

The Ni2p XPS spectra of the as synthesised samples recorded using the ambient pressure end station of beamline B07 (VERSOX) are also reported in Fig. 2d-f. XPS was particularly useful in this study to identify not only the electronic structure of Ni in these nanoparticulate systems but also to clarify the nature of the Ni amorphous phase in the sample Ni_2.5x1.5y. The XPS spectra were characterised by a main metallic Ni $2p_{3/2}$ peak at the binding energy of 852.6 eV (Ni1), a relatively less abundant component Ni2 at 853.7 eV due to Ni(II) in NiO, and a more abundant component Ni3 at 856.1 eV due to a mixed Ni(II)/Ni(III) oxy-hydroxide phase. A closer inspection of the spectrum of the Ni_2.5x1.5y sample reveals the presence of an additional $Ni^{\delta+}$ component Ni4 at 852.95 eV attributed to Ni phosphides. The presence of a phosphide phase was also confirmed by energy dispersive X-ray elemental mapping and Raman spectroscopy. Therefore, under the synthesis conditions realised during the Ni_2.5x1.5y synthesis, the large amount of TOP not only acts as capping agent to prevent NPs' growth but also as a source of phosphorous.

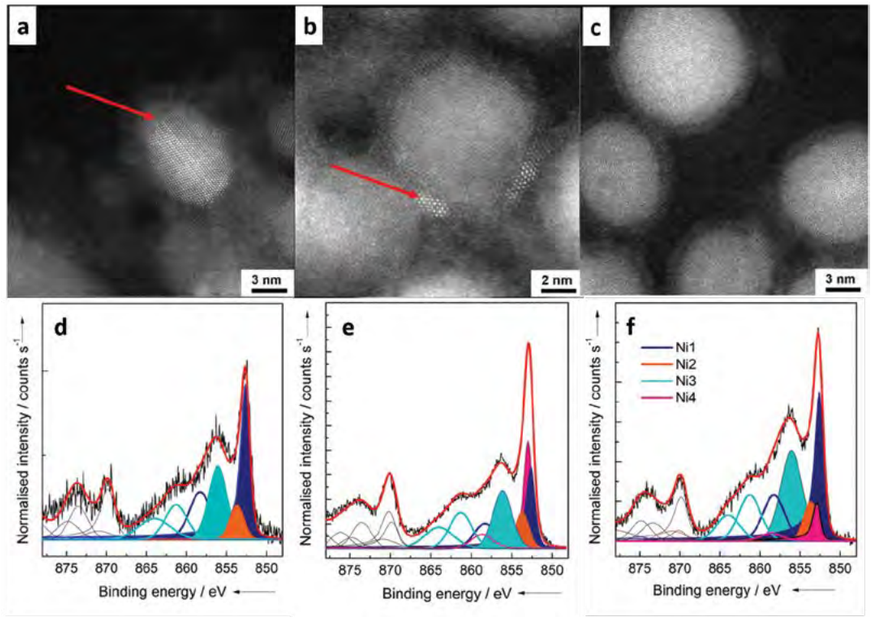

Figure 2: (a) and (b): HR-HAADF-STEM characterisation of Ni_5x1.5y. The arrow indicates the twinned lamellae of the NPs in (a) and a smaller Ni NPs embedded in the organic shell in (b); (c) HR-HAADF-STEM characterisation of Ni_2.5x1.5y; Fitted Ni 2p XP spectra (KE 570 eV) for Ni_10x1.5y (d); Ni_2.5x1.5y (e) and Ni_5x1.5y (f). Fitting: Ni1 (852.6 eV) is Ni^0; Ni2 (853.7 3 V) is Ni^{2+} and Ni3 (856.1 eV) is Ni^{2+}/Ni^{3+} in oxide and oxyhydroxide, Ni4 (852.9 eV) is NiP; respectively.

Fig. 3a and 3b report the instantaneous conversion of MAA and selectivity as a function of the reaction time for the TA modified unsupported and SiO2-supported NPs, respectively. The activities of the catalysts are steadily increasing for the unsupported Ni NP_s indicating that new surface is continuously exposed during the reaction due to the detachment of the C overlayer. However, the increase of the activity is not reflected in an increase of the selectivity towards the (*R*)-MHB. Particularly, for the unsupported Ni_5x1.5y and Ni_10x1.5y the selectivity towards the (*R*)-MHB is maintained constant within the time frame investigated regardless of the MAA conversion achieved.

Interestingly, the unsupported Ni_2.5x1.5y is highly selectivity towards the (*R*)-MHB at the beginning of the reaction but deteriorates very rapidly to reach a similar value characteristic for these unsupported NPs systems, for which the TA modification appears to no longer exist. Amongst the SiO_2-supported Ni NP_s, Ni/SiO_2_5x0.75y shows interesting results. This sample is initially present as a NiO phase which explain the low conversion achieved, since the active hydrogenation Ni surface is metallic. However, this catalyst shows also the highest selectivity towards (*R*)-MHB observed in this study. These results allow to draw a structure function correlation according to which high selectivity towards (*R*)-MHB is obtained when cationic Ni species are present which can strongly bind carboxylate groups of TA. It is therefore evident that to design highly active and (*R*)-selective hydrogenation catalysts, a combination of large Ni metallic surface domains is needed, together with the existence of Ni cationic islands where the chiral modifier can strongly chemisorb to assist the side-by-side selective hydrogenation of MAA.

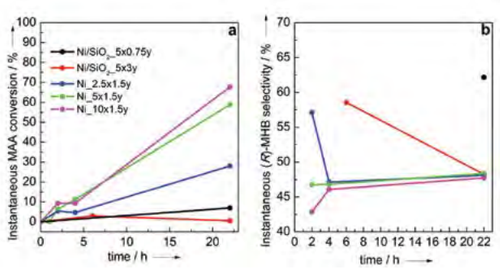

Figure 3: Instantaneous conversion of MAA vs. time of reaction (a) and corresponding instantaneous selectivity to (R)-MHB (b).

References:

1. Kyriakou G. *et al.* Aspects of Heterogeneous Enantioselective Catalysis by Metals. *Langmuir.* **27**, 9687-9695 (2011).DOI: 10.1021/la200009w
2. Tsaousis P. *et al.* Combined Experimental and Theoretical Study of Methyl Acetoacetate Adsorption on Ni{100}. *J. Phys. Chem. C.* **122**, 6186-6194 (2018). DOI:10.1021/acs.jpcc.8b00204
3. Humblot V. *et al.* From Local Adsorption Stresses to Chiral Surfaces: (*R,R*)-Tartaric Acid on Ni(110). *J. Am. Chrm. Soc.* **124**, 503-510 (2002). DOI: 10.1021/ja012021e
4. Baddeley C. J. *et al.* Fundamental Investigations of Enantioselective Heterogeneous Catalysis. *Top. Catal.* **54**, 1348-1356 (2011). DOI: 10.1007/s11244-011-9761-3
5. Keane M. A. *et al.* Asymmetric hydrogenation of methyl acetoacetate using Ni/SiO_2 modified with tartaric acid and alanine. *J. Mol. Catal.* **73**, 91-95 (1992). DOI: 10.1016/0304-5102(92)80064-N

Funding acknowledgement:
Simone Gallarati acknowledges fellowship from the Year in Industry placement scheme at Diamond Light Source (2017-18, "Chirally modified catalyst nanoparticles" project). Haosheng Feng is grateful for the Summer Placement student program at Diamond Light Source. The UK Catalysis Hub is kindly thanked for resources and support provided via our membership of the UK Catalysis Hub Consortium and funded by EPSRC (portfolio grants EP/K014706/1, EP/K014668/1, EP/K014854/1, EP/K014714/1 and EP/I019693/1).

Corresponding author:
Dr Rosa Arrigo, University of Salford, r.arrigo@salford.ac.uk

Tuning the optoelectronic properties of semiconductor nanowires

Related publication: Balaghi L., Bussone G., Grifone R., Hübner R., Grenzer J., Ghorbani-Asl M., Krasheninnikov A. V., Schneider H., Helm M. & Dimakis E. Widely tunable GaAs bandgap via strain engineering in core/shell nanowires with large lattice mismatch. *Nat Commun* **10**, 2793 (2019). DOI: 10.1038/s41467-019-10654-7

Publication keywords: III-V semiconductors; Core/shell nanowires; Strain engineering; Telecommunication bands

The functionality of all advanced semiconductor electronic and optoelectronic devices relies on combinations of materials with different electronic properties. As these materials have different crystal lattice parameters, it is not always possible to combine them. A team of researchers investigated using nanowires to host combinations of materials with a significant mismatch in their lattice parameters, and how this affects the fundamental semiconductor properties.

They carried out their experiments on the Surface and Interface Diffraction beamline (I07). Due to the combination of the diffractometer, the operating energy range and the X-ray beam dimension, I07 offered the ideal environment for the investigation of ensembles of nanowires in grazing incidence X-ray beam geometry.

The research teams findings about the widely tunable electronic properties of gallium arsenide nanowires open up new possibilities for photonics and electronics. Different devices (lasers, photodiodes, photovoltaic cells, high electron mobility transistors, etc.) could be made of the same material system, ensuring process compatibility. Fabrication costs would be minimised, due to the absence of cross-contamination issues, and no requirement for different processing temperatures or different thermal budget limits.

III-V semiconductor nanowires of high structural quality can be grown epitaxially on Si substrates despite the large lattice mismatch, paving the way to the monolithic integration of various nano-devices, such as high electron mobility transistors, lasers, light-emitting diodes, photovoltaic cells, and on-demand emitters of single photons or entangled photon pairs, in CMOS platforms. The technological importance of III-V semiconductors originates from their high electron mobility and direct bandgap[1]. The nanowire geometry also provides the advantage that core/shell heterostructures with large lattice mismatch can be grown without the appearance of misfit dislocations[2], beyond what is possible with conventional thin film heterostructures. The lattice mismatch is accommodated by the elastic deformation of not only the shell, but also the core[3], with the actual strain profile being dependent on the relative thicknesses of the core and the shell.

In this work, it is demonstrated that GaAs/$In_xGa_{1-x}As$ and GaAs/$In_xAl_{1-x}As$ core/shell nanowires with very large lattice mismatch (up to 4%) can be grown on Si substrates without any dislocations and morphological instabilities. In appropriately designed heterostructures, a hydrostatic tensile strain as high as 7% can be achieved in the GaAs core, leading to a dramatic narrowing of its bandgap by up to 40%. These findings render GaAs nanowires a versatile material system for photonic devices across the near-infrared range, including telecom photonics at 1.3 µm, with the additional possibility of monolithic integration in Si-CMOS chips.

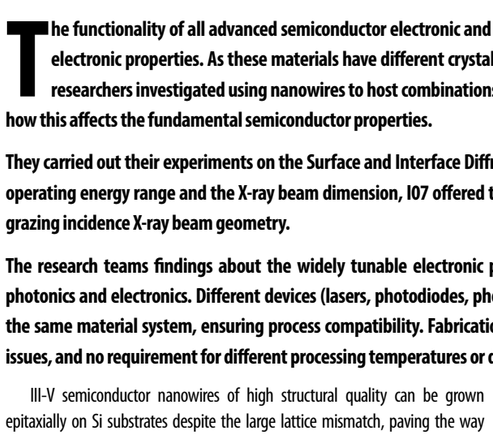

Figure 1: Morphology, composition, and strain of GaAs/$In_{0.20}Ga_{0.80}As$ core/shell nanowires. (a) Side-view SEM image of as-grown nanowires with a shell thickness of 40 nm. (b) EDXS compositional map perpendicular to the axis of one nanowire from the sample shown in (a). (c) Hydrostatic strain measured by Raman scattering spectroscopy in the core (blue data points) and the shell (red data points) as a function of the shell thickness. The star symbols correspond to XRD results.

Vertical GaAs/$In_xGa_{1-x}As$ and GaAs/$In_xAl_{1-x}As$ core/shell nanowires were grown on Si(111) substrates by molecular beam epitaxy[4]. The GaAs core was 20 – 25 nm in diameter and 2 µm in length. Conformal growth of the shells around the GaAs cores was achieved under growth conditions that ensured limited surface diffusivity of the indium adatoms along the nanowire sidewalls. The thickness and the composition of the ternary shell were varied systematically in order to investigate their effect on the strain. Transmission electron microscopy (TEM) showed that the shell adopted the crystal structure of the core, i.e. zinc-blende structure with rotational twins only at the two ends of the nanowires, without any misfit dislocations. An example of GaAs/$In_{0.20}Ga_{0.80}As$ nanowires is shown in the scanning electron microscopy (SEM) image in Fig. 1a. The corresponding compositional map perpendicular to the axis of one nanowire, as measured by energy-dispersive X-ray spectroscopy (EDXS), is shown in Fig. 1b. The hydrostatic strain in the GaAs core and the $In_{0.20}Ga_{0.80}As$ shell was first measured by micro-Raman scattering spectroscopy ($\lambda = 532$ nm) at 300 K on single nanowires. The results (Fig. 1c) showed that the compressive strain in the shell decreased with increasing the shell thickness and became almost equal to zero for shells thicker than 40 nm. On the other hand, the tensile strain in the core increased with increasing the shell thickness and saturated at 3.2% for shells thicker than 40 nm. This indicates that the strain is gradually transferred from the shell to the core with increasing the shell thickness.

The lattice parameters of the core and the shell along the three orthogonal crystallographic directions x, y, z (z-axis is parallel to the nanowire axis, whereas x- and y- axes are perpendicular to it) and the corresponding strain components ε_{xx}, ε_{yy} and ε_{zz} were measured using X-ray diffraction (XRD) at Diamond Light Source. The Surface and Interface Diffraction beamline (I07) offered an ideal non-destructive experimental configuration for the measurement of the in-plane strain state of as-grown nanowire ensembles in non-coplanar grazing incidence X-ray geometry (GID). With a few hundreds of µm large X-ray beam, reciprocal space maps of the in-plane (20-2) and (22-4) reflections were collected in GID geometry at an energy of 9 keV, using a 100 K Pilatus detector. In addition, a constant He flux was kept around the sample within a Kapton® dome to limit possible radiation damage. According to the penetration depth profile of X-rays for the material under investigation, an incident angle of 0.2° close to the critical angle of total external reflection ensured a depth sensitivity of only a few nanometers below the surface. This reduced the diffracted contribution significantly from the growth substrate. It is worth mentioning that the final beam size in the vertical direction corresponded to a several-mm-long footprint of the X-ray beam impinging on the substrate surface. This strongly influenced the resulting resolution in reciprocal space. As an example, Fig. 2a shows a two-dimensional reciprocal space map of reflection (22-4) for a sample with 10 nm shell thickness. Here, three signals at different $Q_{[11\text{-}2]}$ values are visible along the vertical direction; they are attributed, from top to bottom, to the GaAs core, the $In_{0.20}Ga_{0.80}As$ shell, and a planar polycrystalline $In_{0.20}Ga_{0.80}As$ layer that grew unintentionally on the Si substrate. From the position of the diffracted signals, the lattice parameters in x and y directions were determined. The lattice parameter in z direction was determined from measurements of the out-of-plane (-1-1-1) reflection that were performed at the High Resolution X-ray Diffraction beamline P08 at the PETRA III synchrotron in Hamburg.

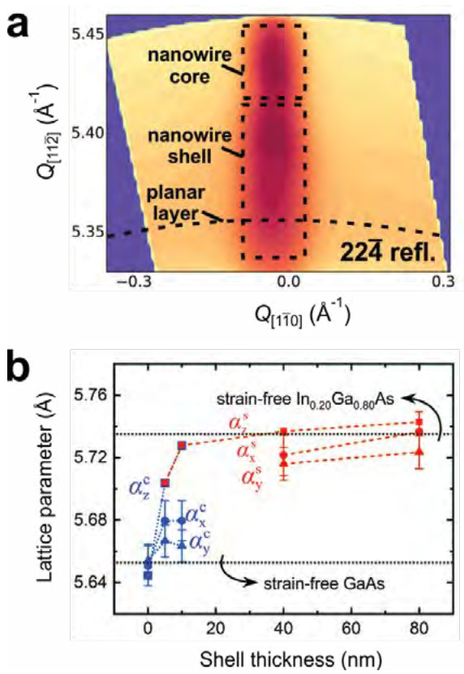

Figure 2: Measurements of the lattice parameters in GaAs/$In_{0.20}Ga_{0.80}As$ core/shell nanowires as a function of shell thickness by high-resolution XRD. The measurements were performed on ensembles of as-grown nanowires. (a) An example of a 2D reciprocal space map of the (22-4) reflection for nanowires with a shell thickness of 10 nm. The contributions from the core, the shell and the planar polycrystalline layer are indicated. (b) XRD-measured average lattice parameters a of the core (blue data points) and the shell (red data points) along the three orthogonal directions x, y, z (z parallel to nanowire axis) as a function of the shell thickness.

The XRD results (Fig. 2b) show that the GaAs crystal expands in all three dimensions with increasing the $In_{0.20}Ga_{0.80}As$ shell thickness up to 10 nm (the XRD signal from the core could not be resolved for thicker shells). Furthermore, the shell becomes almost strain-free when its thickness is at least 40 nm. The strain components ε_{xx}, ε_{yy} and ε_{zz} in the core are calculated as the relative change of the corresponding lattice parameters (i.e. $\varepsilon_{xx} = \Delta a_x^c / a_x^c$, etc). Finally, the hydrostatic strain in the core $\Delta V/V = \varepsilon_{xx} + \varepsilon_{yy} + \varepsilon_{zz}$ (star symbols in Fig. 1c) was found to be in good agreement with the Raman scattering measurements.

The strain in the GaAs core became even higher when 40–80 nm thick $In_xGa_{1-x}As$ or $In_xAl_{1-x}As$ shells with higher x were employed (Fig. 3a). This had a tremendous effect on the bandgap of GaAs, which decreased by up to 40% (Fig. 3b), as measured by photoluminescence (PL) spectroscopy, making it possible to reach the 1.3 µm (O-) telecom band.

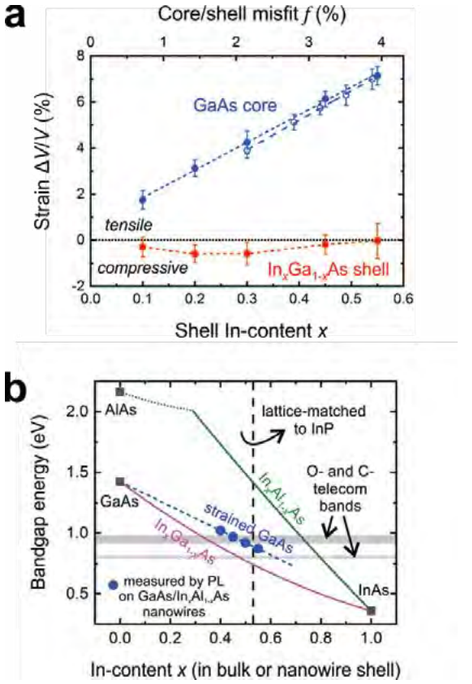

Figure 3: Strain and bandgap of GaAs/$In_xGa_{1-x}As$ and GaAs/$In_xAl_{1-x}As$ core/shell nanowires. (a) Hydrostatic strain measured by Raman scattering spectroscopy in the core (blue data points) and the shell (red data points) as a function of the $In_xGa_{1-x}As$ (closed symbols) or $In_xAl_{1-x}As$ (open symbols) shell composition x and the corresponding core/shell misfit f. (b) Bandgap energy of the strained GaAs core in $In_xAl_{1-x}As$ core/shell nanowires (measured by PL at 300 K) as a function of the shell composition x. The blue dashed line is a linear fit. The bandgaps of strain-free III-As ternary alloys are shown for comparison.

References:

1. Vurgaftman I. *et al.* Band parameters for III-V compound semiconductors and their alloys. *J. Appl. Phys.* **89**, 5815 (2001). DOI: 10.1063/1.1368156
2. Glas F., Strain in nanowires and nanowire heterostructures. Semiconductors and semimetals **93**, 79-123 (2015). DOI: 10.1016/bs.semsem.2015.09.004
3. Grönqvist J., Strain in semiconductor core-shell nanowires. *J. Appl. Phys.* **106,** 053508 (2009). DOI: 10.1063/1.3207838
4. Tauchnitz T., Decoupling the two roles of Ga droplets in the self-catalyzed growth of GaAs nanowires on SiOx/Si(111) substrates, *Cryst. Growth Des.* **17**, 5276-5282 (2017). DOI: 10.1021/acs.cgd.7b00797

Funding acknowledgement:
We are grateful to Diamond Light Source for the allocated beamtime SI15923 and financial support, as well as to the German Synchrotron DESY, PETRA III for the allocated beamtime I-20160337. Finally, we are thankful for the support by the Structural Characterization Facilities Rossendorf at Ion Beam Center, the computational support from the HZDR Computing Cluster, and the funding of TEM Talos by the German Federal Ministry of Education of Research (BMBF), Grant No. 03SF0451 in the framework of HEMCP.

Corresponding authors:
Dr Genziana Bussone, Deutsches Elektronen-Synchrotron (DESY), genziana.bussone@desy.de and Dr Emmanouil Dimakis, Institute of Ion Beam Physics and Materials Research, Helmholtz-Zentrum Dresden-Rossendorf, e.dimakis@hzdr.de

Engineering a new class of photocatalysts for clean fuel production

Related publication: Andrews J. L., Cho J., Wangoh L., Suwandaratne N., Sheng A., Chauhan S., Nieto K., Mohr A., Kadassery K. J., Popeil M. R., Thakur P. K., Sfeir M., Lacy D. C., Lee T. L., Zhang P., Watson D. F., Piper L. F. J. & Banarjee S. Hole extraction by design in photocatalytic architectures interfacing CdSe quantum dots with topochemically-stabilized tin vanadium oxide. *J. Am. Chem. Soc.* **140,** 17163-17174 (2018).
DOI: 10.1021/jacs.8b09924

Publication keywords: Photocatalyst; metal oxide; X-ray Photoelectron Spectroscopy; Electronic Structure

The generation and storage of clean energy is one of the grand challenges of the 21st century. Water splitting, using sunlight to split water into hydrogen and oxygen, is a promising strategy for clean hydrogen generation. However, it requires the concerted action of absorption of photons, separation of excitons and charge diffusion to catalytic sites and catalysis of redox processes. A new generation of photocatalysts will be needed that employ hybrid systems, where different components perform light-harvesting, charge separation and catalysis in synergy.

Chalcogenide materials contain one or more chalcogen elements (e.g. sulfur, selenium or tellurium). Quantum dots (QDs) are semiconductor particles just a few nanometres in size, which have different optical and electronic properties to larger particles of the same material. Chalcogenide QDs have high absorption coefficients that can be easily optimised in the visible spectrum for efficient light harvesting. However, they suffer from photo-corrosion due to the build-up of photo-generated holes.

Researchers developing a new class of hybrid photocatalyst for hydrogen generation used Hard X-ray Photoelectron Spectroscopy (HAXPES) measurements at the Surface and Interface Structural Analysis beamline (I09). The high energy HAXPES enabled them to detect new states induced by intercalating ('doping') post-transition metal ions in V_2O_5 semiconductors nanorods interfaced to the QDs. The added ions facilitated rapid, efficient hole transfer from the quantum dot to suppress photo-corrosion and enhance hydrogen generation.

In 1972, Fujishima and Honda first demonstrated photolysis with UV light using a wide band gap semiconductor, TiO_2, to generate photoexcited holes to oxidise the water[1]. The corresponding electrons were transferred to a platinum electrode for the hydrogen evolution. For TiO_2, the filled O 2p shell is situated at a very negative potential compared to the oxidation potential of water therefore requiring an undesirable 2 V over-potential. Since then there has been considerable research efforts towards developing cheaper platinum-free systems using visible light. From a materials perspective these activities have focused largely on reducing the band gap of the semiconductor i.e. band gap engineering, by modifying the electronic structure by altering the composition.

One promising route to band engineer the semiconductor photocatalyst is to combine d^0 transition metals (e.g. V^{5+}) with lone pair-active post-transition N-2 metal ions e.g. Bi^{3+} e.g. $BiVO_4$. Post-transition metal oxide incorporating N-2 ions can exhibit lone pair distortions where the lone pair s^2 electrons are mediated by hybridising with oxygen 2p orbitals[2]. The oxygen-mediated lone pair orbital raises the ionisation potential closer to the elusive H_2O/O_2, while reducing the hole effective band-edge mass. A synthetic lone pair active metal oxide was first demonstrated in 2014, where Pb^{2+} was intercalated into the tunnel framework of metastable ζ-phase polymorph of V_2O_5 [3]. When the lone pair active ion is inserted into tunnels of the ζ-V_2O_5 structure the oxygen mediated lone pair states push out from the void, as illustrated in Fig. 1a, b. The intercalation of the lone pair active ions reduces the band gap and ionisation potential by 0.8 eV compared to the parent ζ-V_2O_5.

The rich playground afforded by the topochemical synthesis of $M_xV_2O_5$ enables the rational design of p-type metal oxide semiconductors that can be interfaced with efficient visible-light QDs[4]. The ζ-V_2O_5 nanowires decorated with CdSe QDs exhibit a staggered band gap or type II band offset, Fig. 1c. The photogenerated electrons from the CdSe migrate to the unoccupied conduction band and can be used to reduce protons to hydrogen if a sacrificial agent is used to address the buildup on holes on the quantum dot. By screening $M_xV_2O_5$ candidates with lone pair active ions, it was possible to band engineer the interfacial alignment to promote hydrogen evolution at the preferred QD site and hole transfer to the nanowire at energies close to the H_2O/O_2 redox level, Fig. 1d.[4,5]

The HAXPES measurements at I09 were critical for both screening the $M_xV_2O_5$ candidates and measuring the band offset at the nanowire/QD hybrid photocatalysts. As the photon energy is increased the relative orbital cross-sections of the ejected photoelectrons varies to increase the sensitivity of metal s orbitals compared to oxygen p orbitals. As a result, the measured valence band spectra from HAXPES can more easily identify the lone pair states than traditional photoemission spectroscopy. Meanwhile, the increased kinetic energy of the escaping photoelectrons afforded by HAXPES increased the effective probing depth of the technique and facilitates the detection of signals from deeper within the solid compared to transitional photoemission studies. As a result, the band offset of the buried nanowire/QD interface could be measured. From our studies we identified β-$Sn_{0.23}V_2O_5$, where the hole barrier height with the quantum dot could be reduced to zero, thereby facilitating fast (< ps) hole transfer[5]. In addition, the reduction of the vanadium resulted in the partial filling of the conduction band states suppressing electron transfer and promoting the hydrogen evolution at the preferred QD site.

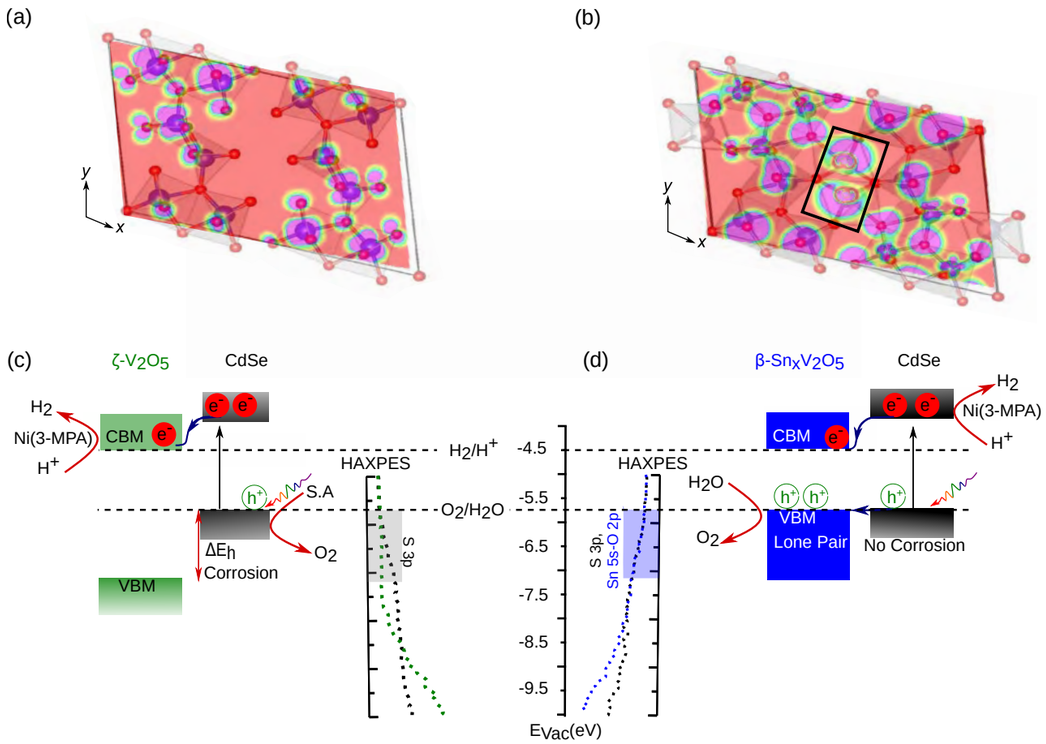

Figure 1: The calculated spatial distribution of topmost filled orbitals of (a) ζ-V_2O_5 and (b) β-$Sn_{0.23}V_2O_5$, highlighting the lone pair states formed by the intercalation of Sn^{2+} ions (black box). (c-d) The measured band offsets of the engineered hybrid photocatalysts formed by decorating the metal oxide nanowires with CdSe quantum dots. The HAXPES data is shown alongside the band diagrams on a common energy scale (w.r.t. vacuum level), the shaded regions highlight the difference in valence band edge alignment for decorated and undecorated nanowires. The intercalated Sn^{2+} is responsible for both suppressing photo-corrosion and inducing hydrogen generation at the preferred quantum dot. A sacrificial agent (SA) was required for ζ-V2O5/CdSe (reproduced from Razek et al., 2020).

References

1. Fujishima A. *et al.* Electrochemical photolysis of water at a semiconductor electrode. *Nature* **238**, 37-38 (1972). DOI: 10.1038/238037a0
2. Walsh A. *et al.* Stereochemistry of post-transition metal oxides: revision of the classical lone pair model. *Chem. Soc. Rev.* **40**, 4455-4463 (2011). DOI: 10.1039/C1CS15098G
3. Wangoh L. *et al.* Electron lone pair distortion facilitated metal-insulator transition in β-$Pb_{0.33}V_2O_5$ nanowires. *Appl. Phys. Lett.* **104**, 182108 (2014). DOI: 10.1063/1.4875747
4. Razek, S. A. *et al*., Designing catalysts for water splitting based on electronic structure considerations *Electron. Struct*. **2** 023001 (2020). DOI: 10.1088/2516-1075/ab7d86
5. Andrews J. L. *et al*. Hole extraction by design in photocatalytic architectures interfacing CdSe quantum dots with topochemically stabilized tin vanadium oxide. *J. Am. Chem. Soc.* **140**, 17163-17174 (2018). DOI: 10.1021/jacs.8b09924

Funding contribution:
This research was supported from the National Science Foundation under DMREF grants 1626967, 1627583 and 1627197. We thank Diamond Light Source for access to beamline I09 (SI12764 and SI16005) that contributed to the results presented here.

Corresponding authors:
Dr Louis Piper, Binghamton University State University of New York, lpiper@binghamton.edu

Ms Sara Abdel Razek, Binghamton University State University of New York, smohame7@binghamton.edu

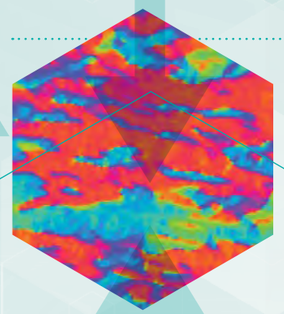

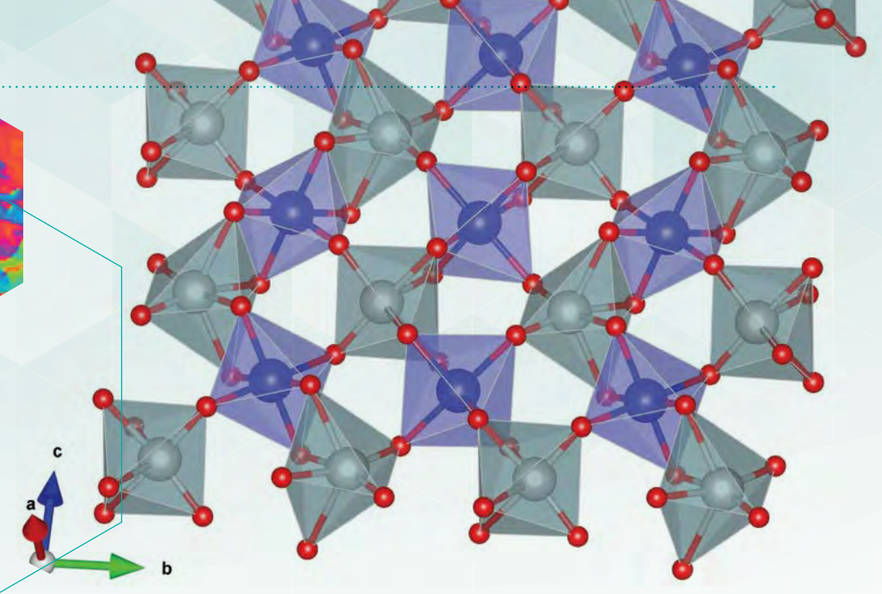

Magnetic Materials Group

Sarnjeet Dhesi, Science Group Leader

The Magnetic Materials Group comprises scientists, engineers and technicians, working across beamlines I06, I10, I16 and I21, developing and exploiting a diverse range of sensitive polarised X-ray probes including resonant X-ray scattering, PhotoEmission Electron Microscopy (PEEM), X-ray Absorption Spectroscopy (XAS) and Resonant Inelastic X-ray Scattering (RIXS). Over the last year, our research community has investigated a wide range of new materials to gain fundamental insights into the electronic and magnetic degrees of freedom underpinning their physical properties. In this contribution, we present research from the beamlines demonstrating how X-ray Magnetic Circular Dichroism (XMCD) can isolate surface magnetism in topological insulators and how nanoscale X-ray magnetic imaging can reveal localised shear strain effects that remain hidden in macroscopic measurements. We also present the first results from a new nickelate superconducting material demonstrating hybridisation between two-dimensional (2D) and three-dimensional (3D) electronic states and X-ray scattering work that hints at covalency in uranium sesquinitride. The results, demonstrate how polarised X-rays can uncover a wealth of electronic and magnetic detail to aid the development of advanced materials in applications ranging from low-power consumption electronics to nuclear fuels.

Nickelates have long held the promise of superconductivity, so that its recent discovery in an infinite-layer nickelate has created considerable interest. There are a number of similarities between the nickelates and other 2D transition-metal oxide superconductors, such as the cuprates for which superconductivity was first observed in the 1980s. However, there are a number of differences that are expected to lead to a distinctly different mechanism for superconductivity in the nickelates. Firstly, the O to Ni charge transfer energy in nickelates is ~3 times that of the O to Cu charge transfer energy in the cuprates which leads to a much weaker hybridisation between the O and Ni electronic states. The large charge transfer energy also implies that the Ni to Ni super-exchange energy, mediated by the O sites, is lower in the nickelates. These two effects then have immediate consequences for the electronic and magnetic structure of the infinite-layer nickelate. On the Inelastic X-ray Scattering beamline (I21), Hepting and co-workers have used XAS and RIXS to build a detailed picture of the underlying electronic structure at the O and Ni sites of an infinite-layer nickelate thin film. The results demonstrate the similarity of Ni valence to the Cu sites in cuprates case, but with negligible hybridisation between the oxygen 2*p* states and the Ni 3*d* states and much stronger hybridisation between the Nd 5*d* states and the Ni 3*d* states leading to electron pockets at specific points in the 3D Brillouin zone and a self-doping effect. This first study was performed in the normal state of the material and future studies will have to address how superconductivity emerges by introducing doped charge carriers via Ni-Nd hybridisation. The high-efficiency collection geometry and spectral resolution on I21 have also enabled many-body spin-flip excitations in anti-ferromagnet NiO to be explored for the first time. Double spin-flip excitations have been known to be present in NiO for some time, but the distinction between double magnons arisings from two excitations on two single sites or on the same site has proved difficult to determine. On I21, RIXS at the Ni L_3 edge combined with theoretical calculations has now shown that the double-magnon excitations arise mainly from spin-flip excitations on the same magnetic site (Fig. 1).

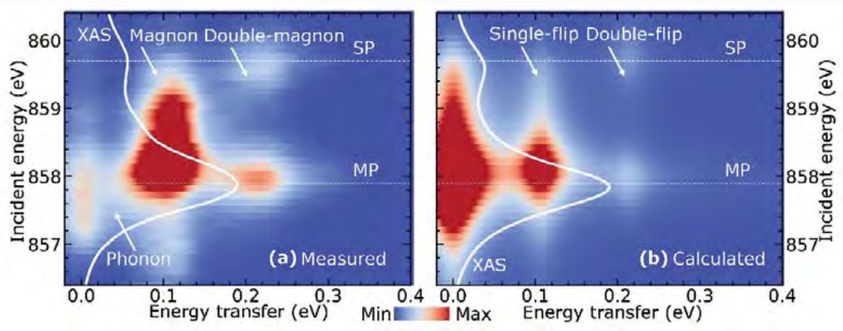

Figure 1 (a) *Experimental and (b) calculated low energy-transfer RIXS maps showing the spin-flip excitations. The solid white lines represent the NiO XAS spectrum. The main peak (MP) and satellite peak (SP), at which the RIXS spectra show the single and double magnon structure with a maximum intensity, are indicated by the broken lines*[1].

Uranium dioxide is commonly used in nuclear reactor rods, but uranium mononitride could be the material of choice due to its higher thermal conductivity and strength. Unfortunately, U_2N_3 is known to form on the surface of UN and its solubility in water hinders safe disposal of any spent fuel. On the Materials and Magnetism beamline (I16), hints on the formation of U_2N_3 have been gained by understanding its magnetic properties using resonant X-ray scattering. In general, diffraction peaks from U_2N_3 contain contributions from two different U sites with different symmetries, but by a judicious choice of reflections and experimental geometry one of the sites could be proposed to have no 5*f* contribution implying the presence of a U(VI) valent ion. The high valence at one of the U sites can then be directly related to the rapid rate of corrosion in U_2N_3 and its solubility in water.

Topological insulators are well known for an insulating bulk phase with topologically protected surface states that resist any perturbation by disorder. Introducing magnetic impurities in the surface region can result in the opening of a tuneable band gap, but little is known about the change in the properties of magnetic topological insulators close to the surface. On BLADE: X-ray Dichroism and Scattering beamline (I10), XMCD has been used to measure the magnetic properties of Cr doped Bi_2Se_3 sheets inserted at different depths in a thin film. The results show that the surface maintains an ordered magnetic phase, even though the bulk becomes non-magnetic, with a Curie temperature ~15K higher than the bulk.

The magnetoelectric effect was predicted and discovered over half a century ago, but only recently have composite materials with large effects been realised. The control of the local magnetisation vector in ferromagnetic thin films grown on ferroelectric substrates has therefore been an area of intense study, but recently PEEM studies of Ni films grown on PMN-PT has unveiled a new twist to the story. Through a nanoscale analysis of the changes in the local magnetisation vector of the Ni film, after applying a strain via the PMN-PT, a picture emerges in which both the normal and shear components of the strain have to be taken into account to understand the ~62° rotation of the magnetisation vector. The discovery then opens up the possibility of independently storing non-volatile binary information using up to six possible states.

The Magnetic Materials Group has continued to innovate and develop the capabilities of its X-ray research facilities. The new 1.6 T electromagnet, operating at a sample temperature less than 8 K, is available for the user community on I10 with proposals being accepted via standard and rapid access modes. This latest addition to the suite of instruments of the group is specifically designed for rapid characterisation of samples using XMCD as well as X-ray magnetic linear dichroism. I16 has added further polarisation control of the incoming X-rays, using a double-bounce phase retarder system, and also implemented a versatile polarisation analysis system for the scattered X-rays. I21 has had an upgrade of the monochromator optics to maintain a world-leading throughput and energy resolution and is currently implementing polarisation analysis. In the coming year, the Nanoscience beamline (I06) will have a major upgrade of the PEEM facility to an aberration-corrected PEEM with additional *in situ* sample storage and sample magnetisation facilities.

The Magnetic Materials Group is dedicated to continually improving its facilities and would welcome further input from our user community. We organise regular workshops to explore new scientific and technical opportunities together with our user community. Our objective is to operate a suite of state-of-the-art polarised X-ray beamlines with leading edge data acquisition, data logging and data analysis software.

1. Nag A. *et al.* Many-Body Physics of Single and Double Spin-Flip Excitations in NiO. *Phys. Rev. Lett.* **124**, 067202 (2020). DOI: 10.1103/PhysRevLett.124.067202

A new slant on magnetoelectrics

Related publication: Ghidini M., Mansell R., Maccherozzi F., Moya X., Phillips L. C., Yan W., Pesquera D., Barnes C. H. W., Cowburn R. P., Hu J. -M., Dhesi S. S. & Mathur N. D. Shear-strain-mediated magnetoelectric effects revealed by imaging. *Nat. Mater.* **18**, 840–845 (2019).
DOI: 10.1038/s41563-019-0374-8

Publication keywords: Piezoelectric effect; X-ray Magnetic Circular Dichrosim (XMCD); PhotoEmission Electron Microscopy (PEEM); Magnetoelectric effect

When an international team of researchers used Diamond Light Source's Nanoscience beamline (I06) to investigate the piezoelectric properties of a ceramic material, PMN-PT, they made an unexpected discovery. Some solids develop electrical charge in response to an applied mechanical stress, which is called the piezoelectric effect. Piezoelectric crystals can convert mechanical energy into electricity or vice-versa. One example of an application is the automatic focusing of mobile phone cameras. In this application, the strain varies continuously with applied voltage. However, cycling the applied voltage can lead to discontinuous changes of strain that can be used to drive magnetic switching in a thin ferromagnet film, meaning that data can be written electrically, and stored magnetically.

The researchers were using a ferromagnetic film of nickel as a sensitive strain gauge for single PMN-PT crystal. By combining PhotoEmission Electron Microscopy (PEEM) with X-ray Magnetic Circular Dichroism (XMCD) while varying the voltage across the crystal, they were able to produce a magnetic vector map.

The initial measurements showed magnetic domains that seemingly rotated by 90° due to ferroelectric domain switching, which was what the team were expecting to see. However, the high-resolution data from I06 offered the opportunity to dig a little deeper, and to carry out a pixel-by-pixel comparison of the XMCD-PEEM images.

This revealed the magnetic switching angles typically fell well short of 90°. Although unexpected, this result could be explained by considering a shear component. This discovery should be applicable to other materials and will inform the development and miniaturisation of devices based on magnetoelectric materials.

Controlling magnetic materials with a voltage could lead to low-power spintronic logic and memory devices. Recent research on beamline I06 has revealed a new twist on the mechanism behind this control.

Using a voltage to control magnetic materials could be key to developing the next-generation of spintronic devices, where information can be processed and stored by flipping spins instead of moving charge. It is widely believed that the impact of spintronics on information technology could be huge, as reducing the movement of charge would reduce Joule heat, thus leading to more energy efficient computers that work faster.

Voltage-controlled magnetism is known as the converse magnetoelectric effect (CME), whereas magnetic control of electrical polarisation is known as the direct magnetoelectric effect. The CME was first described in 1958 by Landau and Lifshitz[1] to explain the curious observation that certain crystals develop a magnetic moment when subjected to an applied electric field. An elegant theoretical paper by Dzialozinski[2] identified antiferromagnetic Cr_2O_3 (the most thermodynamically stable oxide of chromium) as a suitable candidate for CMEs, and the first measurements were performed on this material by Astrov in 1962[3]. However, the CME was so small that magnetoelectrics were almost completely forgotten until the beginning of this century, when they went mainstream by throwing together people with expertise in magnetism and people with expertise in ferroelectricity.

The renewed interest in magnetoelectrics was driven by the discovery of new materials, which unlike Cr_2O_3 show long-range charge order as well as long-range spin order. These 'multiferroic' materials tend to show intrinsic magnetoelectric coupling between the two types of order, but they are not suitable for applications. This is because they only show large CMEs at low temperature. By contrast, large CMEs at room temperature can be found in multiferroic systems in which ferromagnetic films are addressed via strain from an underlying piezoelectric material. This piezoelectric material is typically drawn from the subset of piezoelectric materials that are ferroelectric, such that long-range charge order is manifested as an electrical polarisation that is spontaneous, stable and electrically switchable.

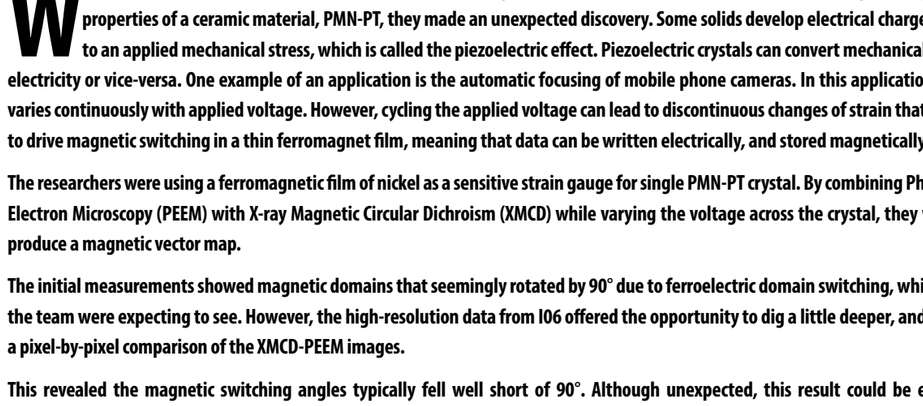

Figure 1: Magnetic vector maps of a ferromagnetic Ni film[4], obtained (a) before and (b) after applying an electric field across the ferroelectric substrate of PMN-PT. Visual inspection suggests that the local magnetisation rotates by the hitherto expected value of 90°, but quantitative analysis (Fig. 2) reveals that this is not the case. Any resemblance between (a) and a map of the world is purely coincidental.

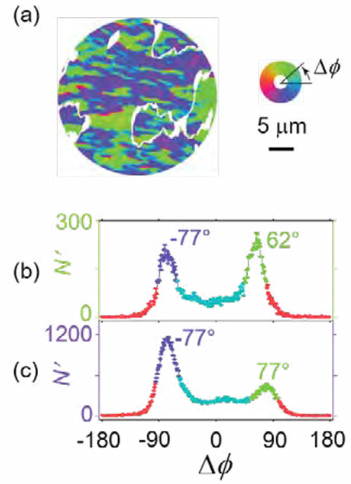

Figure 2: Detailed comparison of the two magnetic vector maps in Fig. 1[4]. (a) Map of the magnetic changes between Fig. 1a and Fig. 1b; (b) Histogram showing these magnetic changes for pixels that started green in Fig. 1a; (c) Histogram showing these magnetic changes for pixels that started purple in Fig. 1a. (Data are filtered by colour to identify peaks.) Pixel magnetisations typically switched by angles that fall short of 90°.

The converse piezoelectric effect permits a material to convert a voltage into a mechanical deformation, e.g. to focus cameras in mobile telephones. By contrast, the direct piezoelectric effect permits a material to convert mechanical deformations into a change of electrical polarisation and thus electrical current, e.g. for microphones and energy harvesting. The piezoelectric material of choice is typically a ferroelectric oxide with the perovskite crystal structure, e.g. PZT $[Pb(Zr_xTi_{1x})O_3]$ and PMN-PT $[(1\text{-}x)Pb(Mg_{1/3}Nb_{2/3})O_3\text{–}xPbTiO_3]$. The transduction is linear under normal service conditions, but a sufficiently large voltage can switch the ferroelectric domains to produce large changes of strain that are discontinuous and nonvolatile. In an overlying thin film, the resulting magnetic changes are also large, discontinuous and nonvolatile, as required for magnetoelectric memory elements.

Work recently published in *Nature Materials*[4] exploited beamline I06 at Diamond to reveal a novel type of magnetoelectric effect in a multiferroic system. This system comprised a thin polycrystalline film of ferromagnetic nickel on a ferroelectric substrate of PMN-PT with an (011) surface. CMEs of record magnitude were initially recorded in a vibrating sample magnetometer, whose probe was wired for electrical access to the sample. From these data, it appeared that electrically switching ferroelectric domains in the PMN-PT substrate produced 90° rotations of Ni magnetisation via strain, as expected. However, PhotoEmission Electron Microscopy (PEEM) data obtained on I06, with magnetic contrast from X-ray Magnetic Circular Dichroism (XMCD), told a different story about the magnetoelectric effects on a shorter lengthscale. For different voltages across the substrate, XMCD-PEEM images were obtained for orthogonal azimuthal sample orientations, and combined to form magnetic vector maps of in-plane magnetisation (as done previously by the same team when reporting extrinsic magnetocaloric effects in *Nature Materials*[5]).

Visual inspection of the vector maps permits one to believe that the expected 90° magnetic rotations took place when an electric field switched the underlying ferroelectric domains (Fig. 1). However, the apparent resolution of the colour wheel is only accurate to a few tens of degrees. Instead, a pixel-by-pixel comparison revealed that the magnetic rotations typically fell short of 90° (Fig. 2). The shortfall arose due to a shear strain that accompanies the well-known normal strain associated with ferroelectric domain switching in PMN-PT. This shear strain had not been hitherto considered, even though it follows directly from knowlege of the PMN-PT unit cell. (The predicted magnetic rotation of 62.6° is not modal due to long-range strain between different ferroelectric domains.) Moreover, the effect of this shear strain was missed in previous magnetoelectric measurements because clockwise and anticlockwise magnetic rotations serve to cancel its signature.

The high-resolution vector maps of magnetisation were key to the discovery of the shear strain, as was the pixel-by-pixel comparison. Although high-resolution vector maps of magnetisation are rarely found in the literature, they have become standard for the team with PEEM available on beamline I06, as will pixel-by-pixel comparisons. The observation of sub-90° magnetic switching has immediate implications for the performance of proposed magnetoelectric random access memory devices. The shear strain tends to compromise the magnetoresistive read-out of the magnetic information[6,7], but only slightly, and it offers an exciting opportunity to write data both electrically and magnetically in the same bit. More generally, the magnetically soft nickel film acted as a sensitive strain gauge, and it revealed an unexpected twist in a well-known ferroelectric material. This method of studying local strain could now become a standard technique for mapping strain, and it could, moreover, yield yet more surprises in the future.

References:

1. L. D. Landau and E. M. Lifshitz, Electrodynamics of Continuous Media, *Pergamon Press* **1st ed**, (1958).
2. Dzyaloshinskii I. E. On the magneto-electrical effect in antiferromagnets. *J. Exptl. Theoret. Phys. (U.S.S.R.)* **37**, 881-882 (1959).
3. Astrov D. N. Magnetoelectric effect in chromium oxide. *J. Exptl. Theoret. Phys. (U.S.S.R.)* **13 (4)**, 729 (1961).
4. Ghidini M. *et al.* Shear-strain-mediated magnetoelectric effects revealed by imaging. *Nat. Mater.* **18**, 840–845 (2019). DOI: 10.1038/s41563-019-0374-8
5. Moya X. *et al.* Giant and reversible extrinsic magnetocaloric effects in $La_{0.7}Ca_{0.3}MnO_3$ films due to strain. *Nat. Mater.* **12**, 52-58 (2013). DOI: 10.1038/nmat3463
6. Bibes M. *et al.* Towards a magnetoelectric memory. *Nat. Mater.* **7**, 425-426 (2008). DOI: 10.1038/nmat2189
7. Hu J.-M. *et al.* High-density magnetoresistive random access memory operating at ultralow voltage at room temperature. *Nat. Commun.* **2**, 553 (2011). DOI: 10.1038/ncomms1564

Funding acknowledgement:
This work was funded by Isaac Newton Trust grants 10.26(u) and 11.35(u), UK EPSRC grant EP/G031509/1, the Royal Society (X.M.) and a start-up fund from the University of Wisconsin-Madison (J.-M.H.). D.P. acknowledges funding from the Agència de Gestió d'Ajuts Universitaris i de Recerca – Generalitat de Catalunya (grant 2014 BP-A 00079). We thank Diamond Light Source for time on beamline I06 (proposal SI-8876), and we thank S. Zhang for discussions.

Corresponding author:
Massimo Ghidini, University of Parma, massimo.ghidini@fis.unipr.it

The extraordinary magnetic transition in topological matters

Related publication: Liu W., Xu Y., He L., van der Laan G., Zhang R. & Wang K. Experimental observation of dual magnetic states in topological insulators. *Sci. Adv.* **5**, eaav2088 (2019). DOI: 10.1126/sciadv.aav2088

Publication keywords: X-ray magnetic circular dichroism (XMCD); Topological insulator; Surface magnetism

The recently discovered topological phase offers new possibilities for condensed matter and spintronics. Three-dimensional (3D) topological insulators (TIs) exhibit novel phases of quantum matter, and sharp transitions, in the electronic structure near their surfaces. Because these can give rise to an anomalous quantum Hall effect and other coherent spin transport phenomena that minimise heat dissipation, 3D TIs have potential uses for next-generation energy-efficient electronics. Although the metallic surface states of TIs have been extensively studied, there has been less direct comparison of their surface and bulk magnetic properties.

Researchers used the X-ray Magnetic Circular Dichroism (XMCD) technique at BLADE (Beamline for Advanced Dichroism Experiments), also known as I10, to investigate prototype magnetic TIs. XMCD is one of the most powerful tools for the study of surface phenomena, offering unique elemental selectivity and atomic-scale high sensitivity.

They were able to quantitatively address the different magnetic moments and transition temperatures, respectively, for the surface and the bulk of the TI. The researchers demonstrated a 'three-steps' transition model, with a temperature window of around 15 K where the surface of the TI is magnetically ordered while the bulk is not.

These surface states of magnetic TIs are immune to material disorders. As a result, they have substantial implications for emerging technologies such as dissipationless transport and quantum computing. Understanding the dual magnetisation process will aid in defining the physical model of magnetic TIs and lays the foundation for making use of them in information technology.

Three-dimensional (3D) TIs feature novel phases of quantum matter with sharp transitions in the electronic structure near their surfaces. It is well known the different electronic properties of the surface and the bulk universally exist in all solids owing to the termination of the periodic lattice structure. In addition, however, TIs present a new class of nontrivial surface states arising from the intrinsic strong spin-orbit coupling and characterised by a Rashban spin texture[1-3]. These low-dimensional surface states are immune to localisation caused by disorders as long as the disorder potential is time-reversal invariant and therefore have strong implications for the emerging technologies such as dissipationless transport and quantum computation. Breaking the time-reversal invariance by introducing a magnetic perturbation (Fig. 1a), on the other hand, reveals a complex phenomenology associated with a tuneable excitation band gap of the surface spectrum. Such a magnetic TI system resembles that of a massive Dirac fermion, which represents an ideal laboratory to study the interplay between magnetism and topology.

While the presence of the metallic surface state has been well studied, experimental evidence on the magnetic properties of the TI surface is far from conclusive. It is possible to distinguish the surface moment of a magnetic TI from that of the bulk using the synchrotron-based X-ray absorption technique, X-ray Magnetic Circular Dichroism (XMCD). This is on the basis of the modified surface band structure, i.e. surface-atom core-level shift, which is reflected in a different surface valence state of metallic elements and can be experimentally observed in their characteristic X-ray absorption spectra. Tuning the absorption to the magnetic resonant edges, XMCD can be obtained for the surface and bulk dopants, respectively, revealing the magnetic ground state and temperature dependence in an unambiguous surface-bulk-resolved manner. Using the absorption end station of I10 at Diamond Light Source, this was successfully demonstrated with a set of modulation-doped Bi_2Se_3, a prototype magnetic TI. This has been achieved by accurately controlling the dopant distribution profiles along the growth direction using the slow-deposition molecular beam epitaxy technique (Fig. 1b).

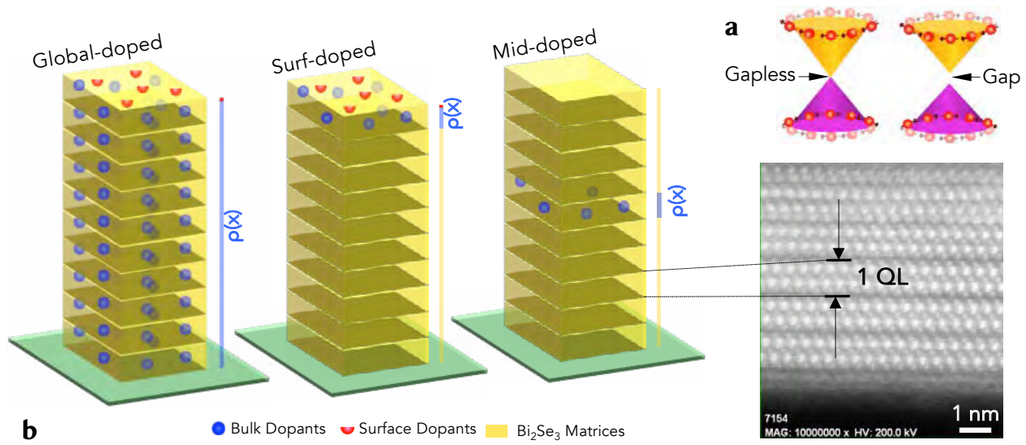

Figure 1: (a) Conceptual illustration of the Dirac fermion states of Bi_2Se_3. (b) Sample configuration of the global-, surf-, and mid-doped Bi_2Se_3.

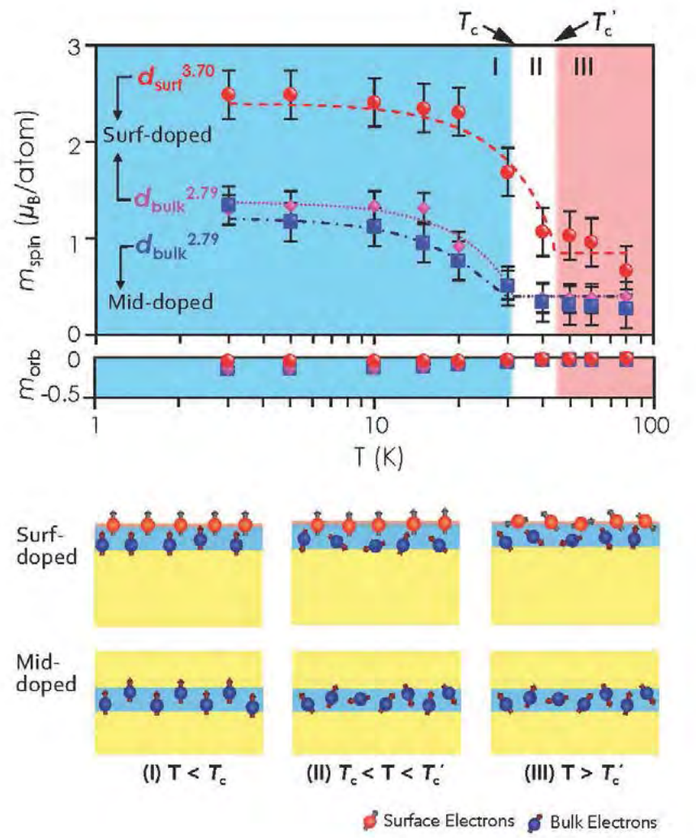

Figure 2: M-T relationships. Upper row: The XMCD-derived m_{spin} and m_{orb} versus temperature. Lower rows: schematic illustration of the 'three-steps' transition.

We performed temperature-dependent XMCD measurements at the Cr $L_{2,3}$ absorption edges of the $Bi_{2-x}Cr_xSe_3$ thin films on I10. Circularly polarized X-rays with ~100% polarization were used in normal incidence with respect to the sample plane and parallel to the applied magnetic field. The XMCD was obtained by taking the difference of the absorption spectra by flipping the X-ray helicity at a fixed magnetic field. Atomic multiplet theory was used to calculate the electric-dipole transitions, which reveals two deconvoluted Cr spectra uniquely representing the surface and the bulk properties of the $Bi_{2-x}Cr_xSe_3$, respectively. In line with the electrical magneto-transport measurements, the XMCD-derived spin moment exhibits a Curie-like behaviour, pointing to a ferromagnetic phase of the Bi_2Se_3 thin films at low temperatures. Remarkably, the fact that the spin moment of the surface and the bulk electrons show distinct temperature dependencies points to the presence of dual magnetic states simultaneously existing within one sample. With careful comparison of the respective magnetisation modes of the bulk and the surface, a 'three-steps' transition model was concluded for the magnetic TIs against temperature (Fig. 2). During phase I both the surface and bulk are magnetically ordered below T_c; between T_c and T_c' (phase II) the surface retains magnetisation whilst the bulk does not any longer; eventually above T_c' (phase III), both the surface and the bulk lose their magnetic ordering.

To conclude, an experiential approach to determine the magnetic ground state in a 'surface-specific' manner using the synchrotron-based X-ray technique has been defined and validated. An enhanced surface magnetic ordering of the $Bi_{2-x}Cr_xSe_3$ systems with a significantly large surface magnetic moment and high ordering temperature has been unambiguously observed. A 'three-steps-transition' model has been demonstrated, in which a temperature 'window' of ~15 K exists where the surface of the TI is magnetically ordered but the bulk is not. Future work to explore the tuning of this 'window' and understand the dual magnetization process will provide important information to refine the physical model of magnetic TIs and lays the foundation for making use of them in the emerging spintronic technologies.

References:

1. Liu C. X. *et al.* Quantum anomalous Hall effect in $Hg_{1-y}Mn_yTe$ quantum wells. *Phys. Rev. Lett.* **101**, 146802 (2008). DOI: 10.1103/PhysRevLett.101.146802
2. Hsieh D. *et al.* A tunable topological insulator in the spin helical Dirac transport regime. *Nature* **460**, 1101 (2009). DOI: 10.1038/nature08234
3. Chen Y. L. *et al.* Massive Dirac fermion on the surface of a magnetically doped topological insulator. *Science* **329**, 659 (2010). DOI: 10.1126/science.1189924

Funding acknowledgement:
UK EPSRC (EP/S010246/1), Royal Society (IEC\NSFC\181680), and Leverhulme Trust (LTSRF1819\15\12).

Corresponding author:
Dr Wenqing Liu, Royal Holloway University of London, wenqing.liu@rhul.ac.uk

Understanding the structure of uranium nitride

Related publication: Lawrence Bright E., Springell R., Porter D. G., Collins S. P. & Lander G. H. Synchrotron X-ray scattering of magnetic and electronic structure of UN and U_2N_3 epitaxial films. *Phys. Rev. B* **100**, 134426 (2019). DOI: 10.1103/PhysRevB.100.134426

Publication keywords: Actinides; Thin films; Single crystals; Resonant elastic X-ray diffraction

Uranium mononitride (UN) has many possible advantages over uranium dioxide as a nuclear fuel, including being safer, stronger and more thermally conductive and having a higher temperature tolerance. Further fundamental research on UN and uranium sesquinitride (U_2N_3) is required to understand their potential as advanced nuclear fuels.

Formed on the surface of UN, U_2N_3 dissolves in water. This has serious implications for the safe disposal of spent fuel, but what causes the dissolution? A possible reason is the presence of the highly soluble U(VI) valent state in U_2N_3.

Researchers used a technique called Resonant X-ray Scattering to investigate U_2N_3. The Materials and Magnetism beamline (I16) combines X-ray diffraction to study atomic structure with spectroscopy to observe electronic structure. Its combination of high X-ray flux and low background detectors allows for the detection of weak signals in the energy range of interest for this experiment.

Their results indicate that one of the uranium sites in U_2N_3 might be U(VI) valent, which is known to be highly soluble in water. In addition, they found strong evidence for covalency involving the 5*f* states in uranium. The specific signal of covalency has not been observed in actinides previously, so may open new avenues for the better characterisation of these materials. Developing theoretical models to explain these experimental results should lead to a deeper understanding of the properties of the materials.

Uranium nitride is a possible 'accident tolerant fuel' that has many characteristics, such as a higher uranium density and a high thermal conductivity, making it a better choice than the conventional fuel UO_2. However, the oxidation of UN progresses through the formation of a surface layer of U_2N_3, and that material has been found to corrode some 25 times more rapidly than UN itself[1]. Our experiments have endeavoured to find some fundamental reasons for this large difference in the corrosion rates of the two materials. At Bristol University epitaxial films of both UN and U_2N_3 with a thickness of ~ 200 nm were grown[2] for the experiments on I16 at Diamond Light Source.

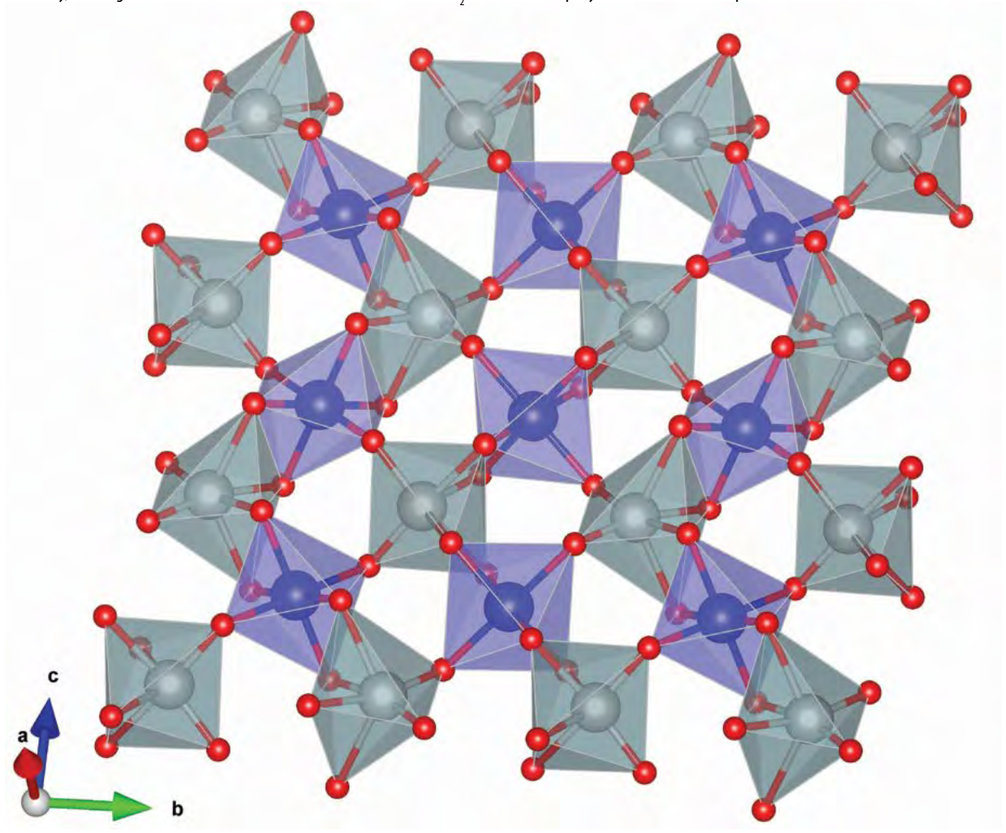

Figure 1: A projection of the bixbyite structure of U_2N_3 which has a cubic unit cell with $a_0 = 10.67$ Å and space group #206 with 32 uranium atoms in the unit cell. The nitrogen atoms are shown in red. 8 of these called U_1 (in blue) have C_{3i} symmetry and 24 uranium atoms, called U_2 (in grey) have C_2 symmetry. Both U atoms have a non-centrosymmetric local environment, but this is more exaggerated (as can be seen from the figure) in the case of the U_2 (grey) atoms.

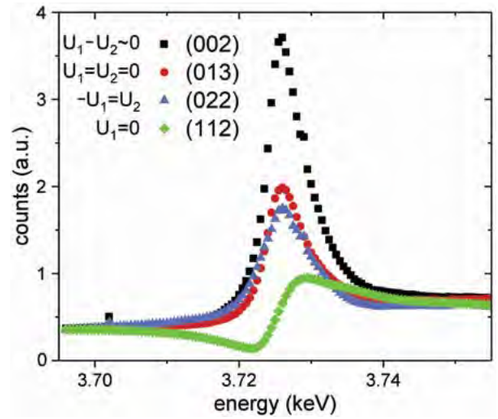

Figure 2: Energy profiles of various Bragg reflections from the U_2N_3 film. The profiles are independent of temperature. A normal "energy dispersive" curve is shown in green from the (112) reflection. The other profiles represent reflections in which the strong (spherical) Thomson scattering from the two uranium sites cancels, or almost cancel. They represent so-called anisotropic resonant X-ray scattering[4] and show that there is an aspherical charge density associated with the U_2 sites. Such a charge density is almost certainly due to covalency between the uranium 5f electrons and the 2p states of nitrogen.

Whereas the crystal structure of UN is the simple rocksalt structure, that of U_2N_3 is considerably more complicated, being the so-called 'bixbyite structure', and a perspective on this is shown in Fig. 1. There are *two* independent sites for the uranium atom (U_1 and U_2), whereas only one exists in UN. A number of methods, including photoemission experiments[2], have been used to estimate the valency of these materials, and for UN this is ~ 3+, i.e. U(III), but for U_2N_3 the valency is higher. Such methods are not site selective, so leave open the question of the valency at each individual site. This is important as the U(VI) valent state is highly soluble in water, so if that is present in at least one of the sites of U_2N_3, this could explain its high corrosion rates.

The magnetic properties give one clue to the valency; for example, U(VI) has no 5*f* electrons so cannot be magnetic. Resonant X-ray Diffraction with the beam energy tuned to the uranium M_4 edge at 3.726 keV showed that U_2N_3 is antiferromagnetic and the magnetic wave-vector was determined for the first time (no single crystals of U_2N_3 have been prepared previously), but the precise magnetic configuration remains ambiguous. Neutrons from the ISIS spallation source were used to try and answer this question – the use of neutrons and resonant X-rays being a powerful combination[3].

In an effort to extract further information on the valency and bonding of the two separate uranium sites 'Diffraction absorption experiments' were performed at the U M_4 edge on a number of Bragg reflections of the U_2N_3 film. The reflections have different contributions from the two independent uranium atoms, as the atomic sites have different symmetries. For strong Bragg reflections, in which the scattering from both the U_1 and U_2 atoms are in-phase, or one set is absent, the expected result is a dispersive curve that reflects the combined effect of both the real ($f_0 + f'$) and imaginary (f'') parts of the uranium scattering factor. Such a curve is shown in the green curve in Fig. 2 for the (112) reflection, in which only the U_2 atoms participate. (Scattering from nitrogen is neglected, as it is far weaker than that from uranium; in addition, there is no edge sensitive to nitrogen in the energy range covered).

However, for reflections in which the strong Thomson scattering (from the 86 core electrons of uranium) is reduced by the cancellation between the two separate uranium atoms, a very interesting profile is shown in Fig. 2 that is precisely the energy profile at the M_4 edge of the imaginary part (f'') from the uranium atoms. This profile reflects the fact that around one of the uranium sites is an *aspherical charge density*, which involves the uranium 5*f* electrons. For example, for the (013) reflection, which is forbidden and has no contribution from the Thomson (spherical) charge density, this aspherical part is the only contribution to the scattering intensity. Similarly, for the (002) and (022), in which the strong spherical charge density contributions almost cancel, the aspherical part is also observed. From the pattern of the intensities in Fig. 2, it becomes clear that any aspherical contribution from the U_1 sites must be small, suggesting that these sites may possibly have the U(VI) valency, in which there are no occupied 5*f* states.

This effect has been observed before, mainly at the *K* edge of the transition metals[4]. However, at the *K* edge with the *d* transition metals there is the possibility of both dipole and quadrupolar transitions, making the identification of the underlying physics complicated. For the U M_4 edge this ambiguity is removed; the transition is definitely of dipole symmetry illuminating an aspherical shape known as a *charge quadrupole*. The non-centrosymmetric coordination of this distribution around the uranium nucleus then couples to the imaginary scattering factor (f'') giving rise to scattered intensity, with a distinctive energy profile, at the Bragg position. Such charge quadrupoles have been observed previously in the actinides, but they are associated with effects related to the magnetism[5]. In this case, the charge quadrupoles are temperature independent, and so not related to the magnetic order at ~ 75 K. They are certainly induced by covalency, probably mixing between the uranium 5*f* states and the nitrogen 2*p* states.

In conclusion, these experiments strongly suggest that the U_1 site may have a significantly higher valency, quite possibly U(VI), and this is responsible for the rapid corrosion rates of U_2N_3. In addition, these experiments have opened the way for more quantitative modelling in such systems, based on the observation of an aspherical 5*f* charge distribution around the U_2 atom

References:

1. Lawrence Bright E. *et al.* Comparing the corrosion of uranium nitride and uranium dioxide surfaces with H_2O_2. *J. Nucl. Mater.* **518**, 202-207 (2019). DOI: 10.1016/j.jnucmat.2019.03.006
2. Lawrence Bright E. *et al.* Epitaxial UN and α-U_2N_3 thin films. *Thin Solid Films* **661**, 71-77 (2018). DOI: 10.1016/j.tsf.2018.07.018
3. Wadley P. *et al.* Antiferromagnetic structure in tetragonal CuMnAs thin films. *Sci. Rep.* **5**, 17079 (2015). DOI: 10.1038/srep17079
4. Kokubun J. *et al.* Anisotropic resonant X-ray scattering: Beauty of forbidden reflections. *The European Physical Journal Special Topics* **208**, 39 (2012). DOI: 10.1140/epjst/e2012-01605-4
5. Santini P. *et al.* Multipolar interactions in f-electron systems: The paradigm of actinide dioxides. *Rev. Mod. Phys.* **81**, 807 (2009). DOI: 10.1103/RevModPhys.81.807

Funding acknowledgement:
EPSRC Grant No. 1652612

Corresponding author:
Gerard Lander, Institute Laue Langevin, Grenoble, lander@ill.fr

Revealing the electronic structures of nickelate superconductors

Related publication: Hepting M., Li D., Jia C. J., Lu H., Paris E., Tseng Y., Feng X., Osada M., Been E., Hikita Y., Chuang Y.-D., Hussain Z., Zhou K. J., Nag A., Garcia-Fernandez M., Rossi M., Huang H. Y., Huang D. J., Shen Z. X., Schmitt T., Hwang H. Y., Moritz B., Zaanen J., Devereaux T. P. & Lee W. S. Electronic structure of the parent compound of superconducting infinite-layer nickelates. *Nature Mater.* **19**, 381-385 (2020).
DOI: 10.1038/s41563-019-0585-z

Publication keywords: High Tc superconductor; Strongly correlated electronic system; Nickelate; XAS; RIXS

Since the 1986 discovery of high-temperature superconducting copper oxides (cuprates), researchers have been trying to engineer nickelate oxides (nickelates) to produce another high-temperature superconductor. With the recent discovery of the first nickelate superconductor, there is a renewed push to uncover the electronic structures of the nickelate.

Revealing the electronic structure allows us to characterise its similarities and differences to cuprates. This information is crucial to understand the mechanism of superconductivity in nickelates and cuprates. It is also useful to synthesise other unconventional high-temperature superconductors.

Researchers set out to determine the electronic structure of nickelates, using theoretical calculations and data taken at several synchrotrons. They used the Resonant Inelastic X-ray Scattering (RIXS) beamline (I21) at Diamond Light Source. Both RIXS and X-ray Absorption Spectroscopy (XAS) can uncover how the electrons of constituent ions hybridise to form the low energy electronic states from which superconductivity emerges. In particular, the RIXS beamline at I21 possesses the high resolution and high efficiency required for this work.

Their results showed that the rare-earth layers in the nickelate provide a 3D metallic state which couples with the electrons in the 2D nickel oxide planes. This is very different from the case of cuprates, in which the rare-earth layer is insulating, and not actively involved in the low energy electronic states. The microscopic electronic structures of the nickelate can now be used to in the design and synthesis of new unconventional superconductors.

Since the discovery of high temperature superconducting copper oxide (cuprates), search for another transition metal oxide superconductor has debuted. In particular, nickel oxides have been proposed to be a material that could be engineered to mimic the electronic structures of cuprates[1-3]. Recently, the first nickelate superconductor has finally been discovered[4]. It is a Sr-doped infinite-layer $NdNiO_2$, which is produced by removing the apical oxygen atoms from the perovskite nickelate $NdNiO_3$ using a metal hydride-based soft chemistry reduction process. The undoped infinite nickelates appears to be a close sibling of cuprates, it is isostructural to the infinite-layer cuprates with monovalent Ni^{1+} cations and possesses the same $3d^9$ electron count as that of Cu^{2+} cations in undoped cuprates. Yet, as discovered in this work, the electronic structure of the undoped $RNiO_2$ (R = La and Nd) remains distinct from the Mott, or charge-transfer, compounds of undoped cuprates, and even other nickelates.

To uncover the electronic structure of the infinite-layer cuprates, X-ray absorption spectroscopy (XAS) and Resonant Inelastic X-ray Scattering (RIXS) across oxygen (O) K-edge and nickel (Ni) L-edges were conducted. The O K-edge XAS of infinite-layer nickelates has first uncovered a major difference from cuprates and other nickelates. In the latter systems, such as NiO and $RNiO_3$, a pre-edge peak exists in the oxygen K-edge XAS, a signature of strong hybridisation between oxygen 2*p* ligand states and the Ni(Cu) 3*d* states, making them the so-called charge-transfer compounds (Fig. 1a). Interestingly, such pre-peak in O K-edge XAS is absent in the infinite nickelates (Fig. 1a), indicating that the oxygen 2*p* ligands states are much less involved in the low energy electronic structures. Therefore, its electronic structure is different from that of charge transfer compounds, including cuprates and other nickelates.

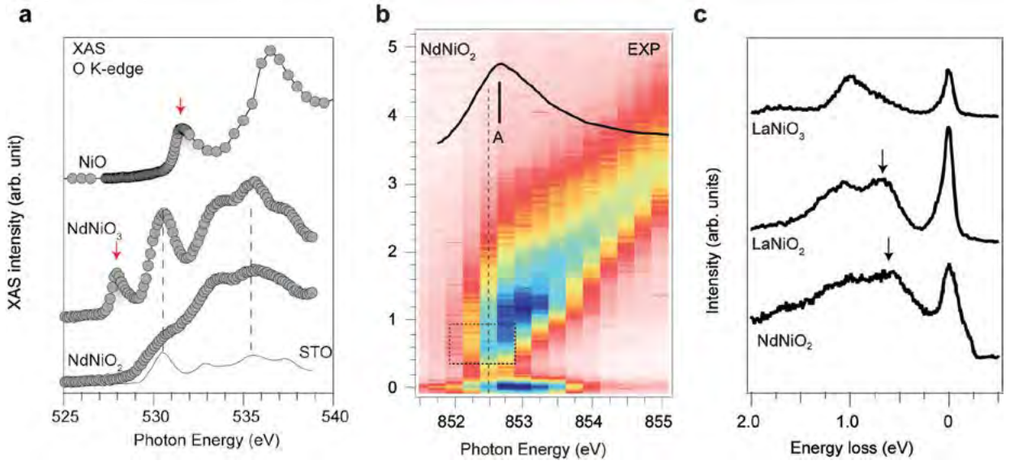

Figure 1: Representative XAS and RIXS Data (a) O K-edge XAS for nickelates. The red arrows indicate the pre-edge peak, which is a signature of oxygen ligand hybridisation. This pre-edge peak is absent in $NdNiO_2$. (b) RIXS map of $NdNiO_2$ across the Ni L-edge. The XAS is superimposed as black curve. The dashed box indicates the 0.6 eV feature attributed to the hybridisation of rare-earth 5d states and Ni 3d state. (c) RIXS spectrum at a fixed incident photon energy to highlight the 0.6 eV feature in La- and Nd-NiO_2. Such feature is absent in the $LaNiO_3$.

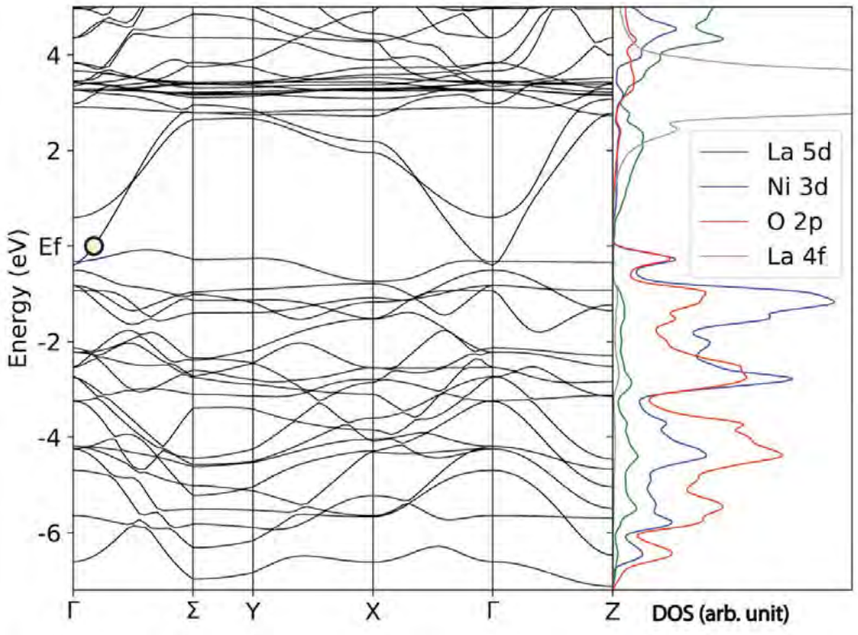

Figure 2: LDA + U calculation for $LaNiO_2$. The orbital-projected density of states is shown in the right panel. The band structure for $NdNiO_2$ is qualitative the same as those of $LaNiO_2$.

The XAS and RIXS across the Ni L-edge has further revealed the electronic structures of the Ni cation in the $RNiO_2$. As shown in the black curve of Fig. 1b, the XAS for infinite-layer nickelates shows one main absorption peak (denoted A), which is distinct from those of NiO and $RNiO_3$, but closely resembles the single peak associated with the $2p^63d^9$–$2p^53d^{10}$ transition in cuprates. Further information about the electronic states of Ni cation is revealed by RIXS. In Fig. 1b, RIXS intensity map as a function of energy loss and incident energy across the Ni L-edge were shown. The ~1 eV and ~1.8 eV features resemble the *dd* excitations seen in $LaNiO_3$ and $NdNiO_3$ except that they are broader and exhibit a dispersion with incident photon energy. This suggests that the Ni 3*d* states in $NdNiO_2$ are mixed with delocalised states. Interestingly, an additional 0.6 eV feature appears, which is absent in the $RNiO_3$ (R = La, Nd) compounds (Fig. 1c). Using exact diagonalisation calculation, we reproduce the general features from XAS and RIXS, including the 0.6 eV features, which highlights the hybridisation between the Ni $3d_{x^2-y^2}$ and R 5*d* orbitals. Thus, in configuration interaction, the Ni state can be expressed as a combination of $|3d^9>$ and $|3d^8\underline{R}>$ where $\underline{R}$ denotes a charge transfer to the rare-earth cation. Note that as also shown in the paper, the RIXS map of $LaNiO_2$ is qualitatively similar to that shown in $NdNiO_2$, except that the resonant energy for the 0.6 eV peak shifts to lower energy.

To further analyse the electronic structure, we turn to LDA+*U* calculations. It is found that oxygen 2*p* bands lie significantly further away from the Fermi energy, signalling reduced oxidation and implying a charge-transfer energy that exceeds *U*. As shown in Fig. 2, the density of states near Fermi energy is dominated by the half-filled Ni $3d_{x^2-y^2}$ states, which appear isolated from the occupied Ni 3*d* bands and exhibit a single-band Hubbard model-like separation, all but confirming that the Ni cation should be in a nearly monovalent $3d^9$ state, consistent with the Ni L-edge XAS and RIXS (Fig. 1). Furthermore, the density of states at Fermi energy is actually finite, but small. Near the zone point, a Fermi surface pocket forms of mainly La 5*d* character; it is quite extended and three-dimensional (3D). This contrasts with the two-dimensional (2D) nature of the correlated $3d_{x^2-y^2}$ Ni states. In other words, the electronic structure of the infinite layer nickelate consists of a low density 3D metallic rare-earth band coupled to a 2D Mott system. This electronic structure resembles the Anderson-lattice (or Kondo-lattice) model for the rare-earth intermetallics, but with the notable addition of a weakly hybridised single-band Hubbard-like model for the Ni layer, rather than strongly interacting *4f* states (or localised spin moments). In this work, an effective model Hamiltonian is derived via downfolding the aforementioned LDA+*U* calculation, severing as a starting point to further theoretically investigate emergent phenomena in infinite-layer nickelate system.

The results reported in this work provide a glimpse into the remarkable electronic structure of the parent compound of the infinite-layer nickelates, urging for further theoretical and experimental investigations, particularly about the Fermi surface and elementary excitations, such as spin, charge, and phonon excitations.

References:

1. Anisimov V. I. *et al.* Electronic structure of possible nickelate analogy to the cuprates. *Phys. Rev. B* **59**, 7901 (1999). DOI: 10.1103/PhysRevB.59.7901
2. Lee K.-W. *et al.* Infinite-layer $LaNiO_2$: Ni^{1+} is not Cu^{2+}. *Phys. Rev. B* **70**, 165109 (2004). DOI:10.1103/PhysRevB.70.165109
3. Hansmann P. *et al.* Turning a Nickelate Fermi Surface into a Cuprate-like One through Heterostructuring. *Phys. Rev. Lett.* **103**, 016401 (2009). DOI: 10.1103/PhysRevLett.103.016401
4. Li D. *et al.* Superconductivity in an infinite-layer nickelate. *Nature* **572**, 624 (2019). DOI: 10.1038/s41586-019-1496-5
5. Bisogni V. *et al.* Ground-state oxygen holes and the metal-insulator transition in the negative charge-transfer rare-earth nickelates. *Nat. Commun.* **7**, 13017 (2016). DOI: 10.1038/ncomms13017

Funding acknowledgement:
This work is supported by the U.S. Department of Energy (DOE), Office of Science, Basic Energy Sciences, Materials Sciences and Engineering Division, under contract DE-AC02-76SF00515. X. F. and D. L. acknowledge partial support from the Gordon and Betty Moore Foundation's EPiQS Initiative through Grant GBMF4415. Part of the synchrotron experiments have been performed at the ADRESS beamline of the Swiss Light Source (SLS) at the Paul Scherrer Institut (PSI). The work at PSI is supported by the Swiss National Science Foundation through the NCCR MARVEL (Research Grant 51NF40_141828) and the Sinergia network Mott Physics Beyond the Heisenberg Model - MPBH (Research Grant CRSII2_160765/1). Part of research was conducted at the Advanced Light Source, which is a DOE Office of Science User Facility under contract DE-AC02-05CH11231.

Corresponding author:
Dr Wei-Sheng Lee, SLAC National Accelerator Lab., leews@stanford.edu

Imaging and Microscopy Group

Paul Quinn, Science Group Leader

The Imaging and Microscopy Group brings together eight experimental facilities (I08, J08, DIAD, I12, I13-1, I13-2, I14 and ePSIC) which use electrons and X-rays to image samples under different experimental conditions across a diverse range of length scales and time scales. Different contrast mechanisms allow for imaging of sample properties such as elemental composition, density and structure. This ability to extract image sample properties in minute detail lends itself to a wide range of scientific areas, from chemistry and catalysis to environmental science, materials science, biology, medicine and cultural heritage.

This year has seen considerable progress in cross-group activities. Ptychography is an area of active development and we are leveraging the considerable expertise in the group to enable new activities such as low-dose electron microscopy and higher resolution imaging across the instruments. These shared activities have also extended to sample preparation with improvements in sample sectioning, using focused ion-beams or laser machining, and transferable sample mounts to enable multi-scale imaging across the x-ray and electron instruments in the group. Software packages developed by the electron microscopy community for image, diffraction and composition analysis are also being expanded to incorporate x-ray modalities to combine the knowledge and tools of both communities.

The Scanning X-ray Microscopy (SXM) beamline (I08) is for morphological, elemental and chemical speciation on a broad range of organic-inorganic interactions in a 250 - 4400 eV photon energy range, and sample investigations under ambient or cryogenic conditions. I08 has a range of applications including biological and biomedical sciences, earth and environmental science, geochemistry and materials science. I08 improved and partially automated and simplified User operation. The new soft X-ray spectro- and tomo-ptychography branchline (J08) optimised for the 250 - 2000 eV photon energy range is approaching the end of its commissioning and testing phase and a call for first experiments is expected for the second half of 2020, providing a step change in imaging and spectro-microscopic performance for soft X-ray imaging at Diamond.

The DIAD beamline for Dual Imaging And Diffraction will be a beamline to offer two X-ray techniques used on the same sample quasi-synchronously. This enables *in situ* characterisation of the 3D microstructure of a material at the same time as its crystallographic phase and/or strain state. Next to a standard tomography setup, a mechanical test rig for diffraction and tomography will be one of the main instruments to allow *in situ* experiments for a variety of scientific disciplines such as engineering and materials science, biomaterials and hard tissues, geology and mineralogy and soil-plant interactions. DIAD uses light from a ten pole permanent magnet wiggler. Power diffraction studies are conducted using monochromatic light. For radiography and tomography, a choice between monochromatic or pink imaging is available. The X-ray energy for each technique can be chosen independently in an energy range from 8 - 38 keV. DIAD is part-funded by the University of Birmingham through a collaboration that was set up in 2016. The beamline took first light into the Optics Hutch in December 2018. The hardware installation is now in its final stages and early X-ray commissioning has commenced. DIAD is expected to take First Users in friendly commissioning mode in early 2021.

The Joint Engineering, Environmental and Processing (JEEP) beamline (I12) uses a 4.2 T superconducting wiggler to provide polychromatic and monochromatic X-rays in the energy range 53 - 150 keV. These high photon energies provide good penetration through large or dense samples. The beamline offers beam sizes ranging from 50 x 50 μm^2 for diffraction, up to 90 x 25 mm^2 for imaging. The beam characteristics enable the study of macro-scale samples that are representative of bulk materials and processes. Another feature of I12 is the ability to use complex, enclosed sample environments without unacceptable attenuation of the beam. X-ray techniques available are radiography, tomography, energy-dispersive diffraction, monochromatic 2D diffraction and scattering. I12 has a diverse user community (materials science and engineering; chemical processing; biomedical engineering; geoscience; environmental science; physics; palaeontology) who make full use of the beamline's capabilities. The beamline's two flexible experimental hutches allow users to bring their own rigs and sample chambers. I12 continues to support a wide range of *in situ*, time resolved experiments, notably in additive manufacturing, materials property testing and chemical processing. It is common for users to combine imaging and diffraction in the same experiment. Working with Diamond's Controls, Data Acquisition and Data Analysis teams, I12 has improved time resolved tomography reliability, and increased utilisation of the Large Field of View camera for tomography of large objects, some over 100 mm in diameter. Since 2019 the Pilatus 2M CdTe detector is the beamline's main diffraction detector, while the Energy-Dispersive X-ray Diffraction (EDXD), present on the beamline since Day 1, is still performing well for academic and industrial users. 2019 was a particularly busy and varied year for the I12 team, and we look forward to some exciting publications from our users in the coming months.

The I13 Imaging and Coherence beamline is for multi-scale imaging in the energy range of 6 - 30 keV. The achievable resolution ranges from several microns to some tens of nanometers with two branchlines operating independently for this purpose. The 'Diamond Light Source - The University of Manchester Collaboration' Imaging Branchline performs mainly in-line phase contrast tomography with a strong emphasis on dedicated sample environments. A new full-field microscope using Zernike phase contrast imaging over a field of view of 50 - 100 µm and a resolution of 50 - 100 nm is now in operation, with a growing user community, allowing us to identify nano-sized structures under dynamic conditions. The highest spatial resolution, of 30 nm, is achieved on the coherence branch with ptychographic imaging. Continuous improvements such as a new Eiger detector, have reduced ptycho-tomography scans from days to a few hours, and ongoing fly-scanning developments aim to reduce this even further. Ptychography has now become a standard user friendly experiment. Instrumental upgrades for Bragg-CDI (new detector robot software) have expanded the experimental capabilities for studying nano-crystalline structures and have been applied successfully in combination with ptychography.

I14, the Hard X-ray Nanoprobe beamline, offers a small beam of 50 – 100 nm for high resolution imaging. I14 has entered its third year of operation and has developed and expanded its capabilities in X-ray fluorescence, diffraction, X-ray Absorption Near Edge Structure (XANES), differential phase contrast and ptychography for mapping inhomogeneities in a wide range of samples. For XANES mapping, there have been a few advances in automated drift correction to improve data quality. Battery materials, metallic particles in cells and photovoltaic films are just a sample of the many science areas and successful experiments conducted. The beamline is approaching the end of its optimisation phase with new techniques and facilities such as ptychography and tomography being made available to users. An increasing emphasis on *in situ* studies is also driving several exciting developments.

The electron Physical Science Imaging Centre (ePSIC) at Diamond consists of two transmission electron microscopes, a JEOL ARM 200 and a JEOL GRAND ARM 300, which were brought to Diamond through a collaboration with Johnson Matthey and the University of Oxford respectively. The ARM 200 is a state of the art probe-corrected analytical microscope capable of atomic resolution electron energy loss and X-ray spectroscopy. The ARM 300 is a dedicated imaging instrument aligned across a wide range of accelerating voltages (30 - 300 keV). It is both probe- and imaging-corrected and has numerous detectors, including a fast direct electron detector (operating at up to 2000 fps). These combined capabilities make this a unique resource for electron microscopy within the UK. With *in situ* sample holders, users at ePSIC can perform variable temperature measurements from 100 to 1600 K to directly image the atomic structure of materials during thermally driven transitions. An Oxford Instruments Energy Dispersive X-ray (EDX) detector has been added to the ARM 300 to allow combined X-ray spectroscopy and high-resolution imaging. The state of the art instrumentation available at ePSIC attracts both established electron microscopists looking to develop new techniques, and scientists with limited previous electron microscopy experience interested in the atomic structure of their samples. The collaboration of the expert staff at ePSIC with this range of users is helping to bring cutting-edge microscopy techniques to the wider material science community. Over the last twelve months ePSIC users have made notable breakthroughs in fields such as catalysis and low dimensional materials as well as important contributions to the development of electron ptychography and scanning diffraction imaging.

Investigating the formation and healing of defects in 2D semiconductors

Related publication: Hopkinson D. G., Zólyomi V., Rooney A. P., Clark N., Terry D. J., Hamer M., Lewis D. J., Allen C. S., Kirkland A. I., Andreev Y., Kudrynskyi Z., Kovalyuk Z., Patanè A., Fal'ko V., Gorbachev R. & Haigh S. J. Formation and healing of defects in atomically thin GaSe and InSe. *ACS Nano* **13**, 5112 (2019). DOI: 10.1021/acsnano.8b08253

Publication keywords: 2D materials; Point defects; III-VI semiconductors

The amazing electrical and mechanical properties of graphene have attracted huge interest. They have also prompted worldwide efforts to investigate other 2D materials, crystalline materials consisting of a single layer of atoms.

2D III-VI semiconductors, including gallium selenide (GaSe) and indium selenide (InSe), have excellent optoelectronic properties when reduced to 'monolayers' just four atoms thick. Such materials are easily damaged by air and water vapour, with atomic point defects at the selenium sites in the crystal considered key to their instability.

To improve our understanding of the presence and nature of defects in these materials, researchers conducted the first study of defects in monolayer crystals of GaSe and InSe. They used the E02 microscope at ePSIC to image samples at atomic resolution with annular dark-field scanning transmission electron microscopy (ADF-STEM).

Their work identified several different defect types in both GaSe and InSe monolayers. They observed point defects (missing or additional atoms) moving from atomic site to atomic site under the electron beam, with the perfect crystal structure able to recover during imaging. In thicker crystals (two layers or more), they observed extended defects, such as lines of missing atoms and changes in layer stacking order.

2D III-VI semiconductors are a very new class of material, and we are only just beginning to explore their vast potential. This research suggests that heating or laser annealing may provide a route to improving the crystal quality of atomically thin 2D III-VI semiconductors.

III-VI semiconductors are layered compounds with each constituent monolayer comprised of two atomic sublayers of group III post transition metals, such as gallium (Ga) or indium (In) sandwiched between sublayers of group VI chalcogenides, such as sulphur (S), selenium (Se), or tellurium (Te) (Fig. 1a). The layers are held together by weak, van der Waals forces allowing them to be separated to produce atomically thin sheets via 'scotch-tape' mechanical exfoliation; this being the same technique that drew enormous attention as a key method for isolating high quality monolayer graphene from graphite. In particular, InSe has attracted considerable interest for having extremely high electron mobility, comparable to graphene, which has the highest known electron mobility of any material. However, unlike graphene, an almost perfect conductor, InSe is a semiconductor with a thickness-dependent bandgap in the optical range[1]. Furthermore, when atomic layers of InSe are stacked together with other III-VI semiconductors, and graphene or boron nitride (a 2D insulator) to form so-called 'van der Waals heterostructures', fully tuneable optical activity from infrared up to violet is possible[2]. This platform has the potential to revolutionise low power optoelectronic devices for high speed applications, such as sensing, optical fibre waveguides, photodetectors, single photon emission devices, and ring lasers.

A key challenge for the commercial exploitation of atomically thin III-VI semiconductors is maintaining their crystal quality when the materials are made atomically thin. The materials properties are found to degrade in humid and oxygen-rich environments and this has often been assigned to poor environmental stability. Despite the suggested importance of crystal defects, no experimental studies of point defects existed prior to the current study. The objective was therefore to understand and propose strategies to mitigate this behaviour. In particular, missing Se atoms (termed Se vacancies, V_{Se}), were predicted to drastically

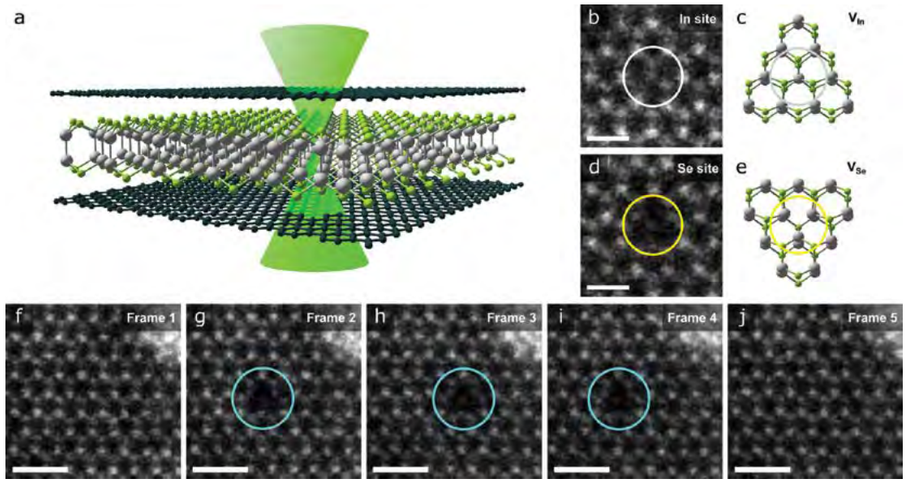

Figure 1: ADF imaging of point defects in monolayer InSe. (a) Cartoon showing the principle of imaging graphene-encapsulated monolayer InSe. In atoms are grey, Se atoms are gold, C atoms are black. (b, d) ADF image of (b) In vacnancy, VIn, and (d) Se vacancy, VSe, with (c, e) their corresponding DFT-relaxed structural models, tilted slightly to aid visualisation of the defect. (f – j) Time series of defect (g) formation, (h – i) migration, and (j) healing. All scale bars: 1 nm. Adapted with permission from the Related Publication. Copyright 2019 American Chemical Society.

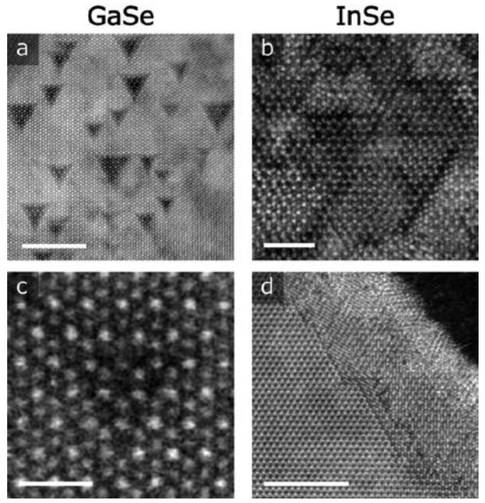

Figure 2: Comparison of extended defects observed in GaSe and InSe. (a) Time averaged image of stable trigonal defects in thick (>10 layer) GaSe. Scale bar: 5 nm. (b) Dense networks of line defects in bilayer InSe. Scale bar: 2 nm. (c) Detail of a trigonal defect in bilayer GaSe. Scale bar: 1 nm. (d) Atomically sharp crystalline-amorphous transition towards the edge of a few layer InSe. Scale bar: 5 nm. Adapted with permission from the Related Publication. Copyright 2019 American Chemical Society.

reduce the crystal's stability, as they provide reactive sites for the dissociation of oxygen (O)[3]. In this work, in an attempt to preserve the pristine quality of the bulk crystal, the GaSe and InSe sheets were exfoliated in an argon glove box and sandwiched between graphene for protection (as graphene is completely impermeable to air and moisture) (shown in the cartoon in Fig. 1a). Imaging of the atomically thin GaSe and InSe, was performed using state-of-the-art, low voltage, annular dark field scanning transmission electron microscopy (ADF-STEM) at the ePSIC facility, Diamond Light Source. Low voltage STEM, operating at 60–80 kV acceleration voltage instead of the typical 200–300 kV range, minimises electron beam-induced damage to the sample and graphene encapsulation. In most STEM instruments these imaging conditions would severely limit the achievable spatial resolution, but the advanced aberration correcting optics and highly stable environment allow atomic resolution imaging to be routinely achievable, even at low acceleration voltage.

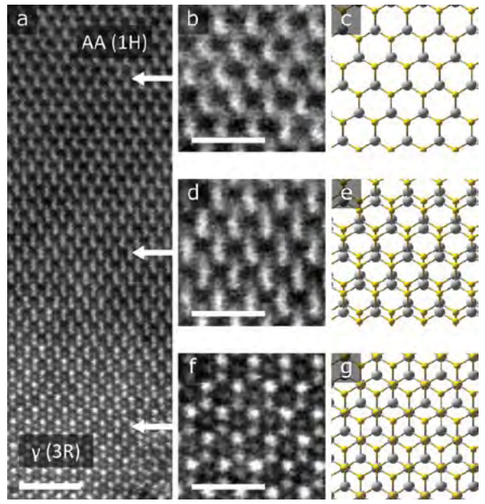

Figure 3: Strain-induced changes in stacking order in bilayer InSe. (a) Transition from stable γ stacking (bottom) to AA stacking (top) in InSe. Scale bar: 2 nm. Detail of (b) AA, (d) intermediate, and (f) γ stacking, with (c, e, g) corresponding structural models. Scale bars: 1 nm. Adapted with permission from the Related Publication. Copyright 2019 American Chemical Society.

Both pristine and defective regions of monolayer were observed (examples for InSe given in Fig. 1). From the effect of the electron beam, new defects were also observed to form, move, and heal, returning to their original pristine state (Fig. 1f–j). Image simulations were performed matching the experimental parameters of the microscope, using atomic structures containing candidate defects, relaxed using density functional theory (DFT). When compared with the experimental data, these simulations enabled the identification of the point defects in the crystal, such as the substitution of O to a Se site in GaSe (see Related Publication) and single In and Se vacancies in InSe (Fig. 1b–c, and d–e, respectively).

Point defects were also observed to have coalesced to form extended defects in few layer materials and these also appeared morphologically different in isostructural GaSe and InSe. GaSe typically formed trigonal faceted defects, believed to consist of regions where both Ga and Se atoms have been equally lost from the crystal (Fig. 2a, c). In contrast, InSe was observed to predominantly form networks of line defects, suggested to comprise of mainly Se vacancies (Fig. 2b). InSe, in addition, showed interesting damage structures at the edges of the crystal, where a sharp transition was seen from pristine crystal to a semi-crystalline and amorphous edge (Fig. 2d). In addition to vacancies, large areas of altered stacking of layers were observed in both GaSe and InSe were seen, where the crystal stacking deviated from the most energetically stable phase (named ε and γ for GaSe and InSe, respectively), to the unexpected AA sequence, where both metal and chalcogen atoms are vertically aligned. Fig. 3 demonstrates this for InSe, where the transition from γ to AA stacking is seen to extend over 4 nm.

Given the excellent properties of devices carefully produced in the same controlled argon environment, the abundant presence of defects found in these materials suggests that preparing 2D III-VI semiconductors in ultra-high vacuum may produce even better properties yet. Furthermore, the observed changes in stacking were found to have only a small energy penalty but could have significant effects on the electronic structure, motivating further work to explore the potential of engineered restacking for optoelectronic device applications.

References:

1. Bandurin D. A. *et al.* High electron mobility, quantum Hall effect and anomalous optical response in atomically thin InSe. *Nat. Nanotechnol.* **12**, 223–227 (2017). DOI: 10.1038/nnano.2016.242
2. Terry D. J. *et al.* Infrared-to-violet tunable optical activity in atomic films of GaSe, InSe, and their heterostructures. *2D Mater.* **5**, 041009 (2018). DOI: 10.1088/2053-1583/aadfc3
3. Kistanov A. A. *et al.* Atomic-scale mechanisms of defect- and light-induced oxidation and degradation of InSe. *J. Mater. Chem. C* **6**, 518–525 (2018). DOI: 10.1039/C7TC04738J

Funding acknowledgement:
Engineering and Physical Sciences Research Council (EPSRC) U.K Grants EP/K016946/1, EP/M010619/ 1, EP/R031711/1, EP/P009050/1, EP/S019367/1, EP/N010345/1, and EP/P026850/1, EPSRC Graphene NoWNano CDT, Defense Threat Reduction Agency Grant HDTRA1-12-1-0013, European Union Horizon 2020 research and innovation program (European Research Council Grant Agreement ERC-2016-STG-EvoluTEM-715502, the Hetero2D Synergy grant, and the European Graphene Flagship Project), National Academy of Sciences of Ukraine, the Leverhulme Trust.

Corresponding authors:
David G. Hopkinson, National Graphene Institute and Department of Materials, The University of Manchester, david.hopkinson@postgrad.manchester.ac.uk
Prof Sarah J. Haigh, National Graphene Institute and Department of Materials, The University of Manchester, sarah.haigh@manchester.ac.uk

Identifying the earliest known fungi

Related publication: Bonneville S., Delpomdor F., Préat A., Chevalier C., Araki T., Kazemian M., Steele A., Schreiber A., Wirth R., & Benning L. G. Molecular identification of fungi microfossils in a Neoproterozoic shale rock. *Sci. Adv.* **6**, eaax7599 (2020). DOI: 10.1126/sciadv.aax7599

Publication keywords: Fungi fossils; Neoproterozoic; Chitin

Fossils of fungi are scarce and hard to tell apart from other microorganisms, and only two percent of species in the kingdom Fungi have been identified. Until now, the oldest confirmed mushroom fossil was 460 million years old.

With no method to distinguish fungi fossils from the remains of other organisms, identification had to be based on morphological criteria - the size and shape of the fossil. This has hindered our understanding of the early evolution of fungi and the beginnings of more complex life forms.

Researchers used synchrotron techniques to investigate fossilised filamentous networks in rocks formed between 715 and 810 million years ago. They were looking for traces of chitin, a constituent of fungal cell walls. Using X-ray absorption near-edge spectroscopy (XANES) on the Scanning X-ray Microscopy beamline (I08), they investigated ultrathin sections of the fossilised filaments. They combined these results with complementary µFTIR spectroscopy on the Multimode InfraRed Imaging And Microspectroscopy (MIRIAM) beamline (B22).

Their results clearly show that traces of chitin are present in the filamentous fossils, meaning that they have chemically identified the oldest known fossil fungi. These early fungi were already present on Earth between 715 and 810 million years ago, almost 300 million years earlier than previously thought.

In that era, fungi would have been a crucial partner for the first plant to grow on land. The fungi fossils examined were preserved in rocks deposited in the transition zone between land and sea. As such, those fungi could have participated in the establishment of the first land plants.

Fungi form vast microscopic filamentous networks in symbiosis with plant roots that facilitate nutrient uptake from soil particles[1]. Because of these unique capabilities, ancient fungi are thought to have been crucial partners of early plants involved in terrestrial invasion[2]. However, the timing of this major evolutionary transition is largely unknown because of the notorious scarcity and ambiguous nature of the Precambrian fossil record for fungi. A number of Precambrian remains (e.g., *Hurionospora*, *Shuiyousphaeridium*, *Tappania)*, filaments and spores from 0.9-1 Ga in Arctic Canada, in Siberia (Lakhanda microbiota) or even older structures in 2.4-billion-year-old basalt were inferred to be of fungal nature, yet their conclusive attribution to Fungi remains problematic[3,4]. In this study, we report the discovery of fungi fossils in a dolomitic shale from the Mbuji-Mayi Supergroup (MMS) from the Sankuru-Mbuji-Mayi-Lomami-Lovoy Basin (SMMLL), south-central of the Democratic Republic of Congo (DRC). This shale (BIIc8 unit) was deposited in a coastal, perennial lacustrine pond between 715 and 810 million-years ago. The remains are dark, cylindrical filaments typically between 3.5 µm to 11.5 µm in width, extending over hundreds of microns in length and sometimes forming a dense network (Fig. 1). The size of the fossils fits well with fungal hypha dimensions; however, size alone cannot be a criterion as prokaryotes also form filaments and networks of similar dimensions. In order to determine whether those filamentous networks represent Neoproterozoic fungal or cyanobacterial remains, an in-depth chemical characterisation is required.

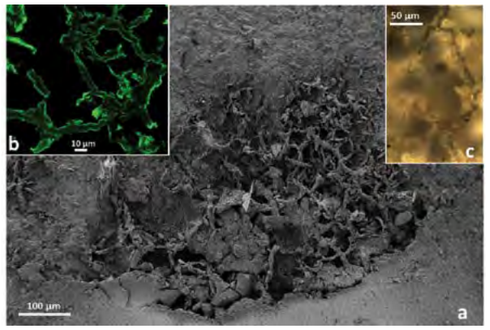

Figure 1: Textures and structures observed via (a) scanning electron and (b) light microscopy of a thin section from the fossiliferous dolomitic shale rock from BIIc8 (Mbuji-Mayi Supergroup). (c) Confocal laser scanning fluorescence microscopy using WGA-FITC of mycelium-like structure.

Chitin is a biopolymer of N-acetyl-glucosamine which is abundant in fungal cell walls and more generally in animal taxa (i.e., ciliates, arthropods, chrysophytes, diatoms) yet absent in prokaryotic organisms. The chitin-producing organisms listed above are morphologically distinct from our fossils, thus finding chitin in the filament would be a strong argument for a fungal affinity. We detected chitin using Wheat Germ Agglutinin conjugated with Fluorescein IsothyoCyanate (WGA-FITC), a highly specific dye of N-acetyl glucosamine trimers. We observed that the WGA-FITC binds to extensive portions of the mycelial structure (Fig. 1) whereas staining was negative when WGA-FITC was exposed to inclusions of "non-fungal" organic matter. Considering the fungus-like morphology, the binding of the WGA-FITC to the cell wall, we assert that this positive staining can be used as a clear indicator of chitinous remnants and thus that those filamentous fossils are of fungal origin.

Synchrotron radiation Fourier Transformed InfraRed spectroscopy (SR-µFTIR) performed on B22 revealed important information about the functional groups in the fossil filaments (Fig. 2). First, the kerogenization is evidenced by (i) the aromatic bands (1597 cm^{-1}, 3070 cm^{-1} and 1270 cm^{-1}) and (ii) the strong aliphatic peaks (~2800~-3000 cm^{-1}) and at lower wavenumber 1458 cm^{-1}, 1408 cm^{-1} and 727 cm^{-1}. As kerogen matures, aromaticity tends to increase relative to the aliphatic character, with fully aromatic graphite being the ultimate end member. Here, this process is far from complete as the aliphatic vibrations are still preeminent. Those long aliphatic chains result from the alteration of the protein-chitin complex of the fungal cell wall which produce free aliphatic groups and unsaturated carbon which then polymerise into long polymethylenic chains[5]. Here, even though the aliphatic signal is strong, the degradation of the protein-chitin complex appears incomplete as we found sharp vibrations characteristic of amide at 1651 and 1540 cm^{-1} assigned to amide I (v C=O), amide II (δ N-H). As for carbohydrates (950-1200 cm^{-1}), although depleted, we could still detect a pyranose peak at 1170 cm^{-1}. The fact

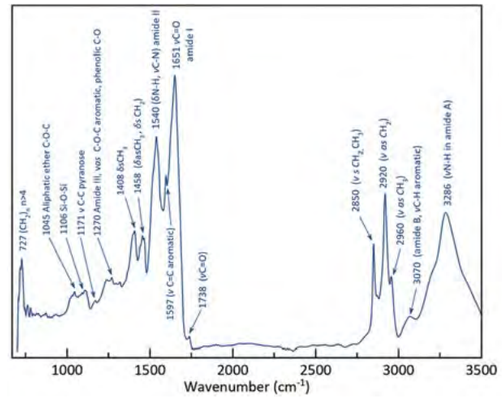

Figure 2: Synchrotron-µFTIR (average over 31 10 by 10 µm areas) of fragments of fossilised filaments. Assignments of absorption bands and vibration modes (δ=deformation; v=stretching; s=symmetric; as=asymmetric) are indicated in parentheses.

that, in addition to the aromatic and aliphatic vibrations, amide and pyranose peaks are present is a testimony of the exceptional preservation of those fossils and is also consistent with the presence of vestigial 'chitin'.

Ultrathin sections were sampled across filaments by Focus Ion Beam (FIB) and analysed by X-ray Absorption Near Edge spectroscopy (XANES) at the C and N K-edge on I08 (Fig. 3). We detected two characteristic peaks of chitin at 285.1 eV (C=C 1s-π* transition in aromatic carbon) and at 288.6 eV (1s-π* transition of amide carbonyl and C-N bonds). Compared to pure chitin, the strengthening of the aromatic carbon peak (285.1 eV) and the occurrence of two additional features in the filament spectra (286.7 eV C=O/C=N bonds and 287.5 eV for aliphatic carbon) are consistent with the SR- µFTIR results and illustrate the incomplete degradation of the fossil. Our N-XANES data confirmed the presence of amydil N (401.3 eV), which corresponds to the main spectral feature of chitin, while the 398.7 and 399.7 eV peaks are associated with pyridine and its derivatives, which are known alteration-products of chitinous tissues. When compared to modern fungi, our XANES data exhibit the same trend as when it is compared to chitin, i.e., more intense aromatic/olefinic and imine/ketone/phenolic peaks (at 285.1/398.8-399.9 eV and 286-287.2 eV) and reduced amide/carboxylic peaks (at 288.6 eV/401.3 eV). Equivalent C- and N-XANES trends were observed in a recent study simulating burial-induced maturation of various modern microorganisms[6]. This difference in C-XANES is particularly marked for (*Aspergillus fumigatus,* not shown here), but also visible C and N-XANES for *Parmelia saxatalis* although to a lesser extent (Fig. 3). The latter fungal species exhibit significant aromatic/olefinic peak and generally have C-XANES spectra close to the one of our fossil filaments. Although not directly diagnostic, the fossil filaments exhibit C- and N-XANES spectral features consistent with the presence of vestigial chitin, and also share some similarities with modern fungal species.

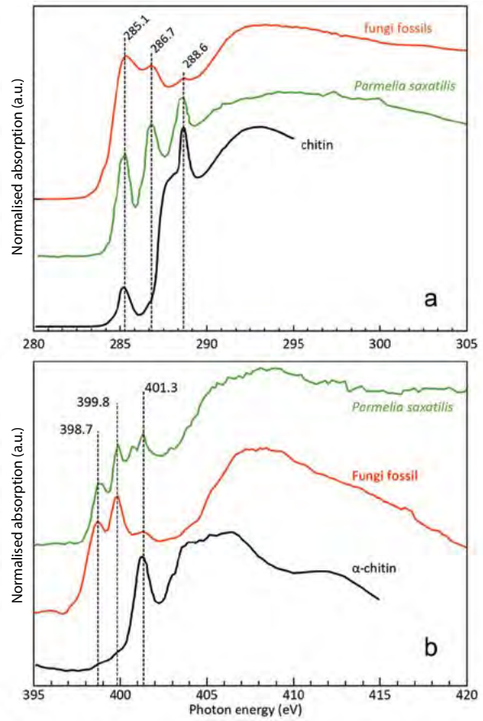

Figure 3: (a) C-XANES spectra for fungal hypha in lichen (Parmelia saxatalis), chitin and fossil filament. For the fossil, the main peaks are centered at 285.1 eV (aromatic C=C), 286.7 eV (ketone and phenol C) and a shoulder in amide/carboxylic acids energy bands (288–288.7 eV). (b) N-XANES spectra of the above-mentioned samples. The fossilised filament exhibits spectral features at 398.7 eV (imine), at 399.8 eV related to pyridine and a shoulder at 401.3 eV which corresponds well with the main spectral feature of the chitin (N 1s-3p/σ transition in amide). Note that all those features are visible in the spectra of P. saxatalis.*

Using an array of microscopic (SEM and TEM - and confocal laser scanning fluorescence microscopy) and spectroscopic techniques (Raman, FTIR, XANES), we demonstrated the presence of vestigial chitin in these fossil filaments. Based on the combined evidences of presence of vestigial chitin, syngenicity, size and morphology, those fossil filaments and mycelium-like structures are identified as remnants of fungal networks and represent the oldest, molecularly identified remains of Fungi. As such, this discovery pushes well into the Neoproterozoic the possibility that fungi helped to colonise land surface, almost 300 million years prior to the first evidence of land plants.

References:

1. Bonneville B. *et al.* Tree-mycorrhiza symbiosis accelerate mineral weathering: evidences from nanometer-scale elemental fluxes at the hypha–mineral interface. *Geochim. Cosmochim. Acta* **75**, 6988 (2011). DOI: 10.1016/j.gca.2011.08.041
2. Selosse M. -A *et al.* Origins of the terrestrial flora: a symbiosis with fungi? *BIO Web of Conferences* **4**, 00009 (2015). DOI: 10.1051/bioconf/20150400009
3. Butterfield N. J. Probable Proterozoic fungi. *Paleobiology* **31**, 165 (2005). DOI: 10.1666/0094-8373(2005)031<0165:PPF>2.0.CO;2
4. Cody G. D. *et al.* Molecular signature of chitin-protein complex in Paleozoic arthropods. *Geology* **39**, 255 (2011). DOI: 10.1130/G31648.1
5. Alleon J. *et al.* Organic molecular heterogeneities can withstand diagenesis. *Sci. Rep.* **7**, 1508 (2017). DOI: 10.1038/s41598-017-01612-8

Funding acknowledgement:
This research was supported by the "Van Buren" funds from ULB and the Fonds National de la Recherche Scientifique (FRS-FNRS PDR T.1012.14). We thank Diamond Light Source and their beamline scientists for access to beamline B22 (SM15050) and I08 (SP14953) that contributed to the results presented here.

Corresponding author:
Dr Steeve Bonneville, Biogéochimie et Modélisation du Système Terre, steeve.bonneville@ulb.ac.be

Internal flow in melt pools during arc welding and additive manufacturing of metals

Related publication: Aucott L., Dong H., Mirihanage W., Atwood R., Kidess A., Gao S., Wen S., Marsden J., Feng S., Tong M., Connolley T., Drakopoulos M., Kleijn C. R., Richardson I. M., Browne D. J., Mathiesen R. H. & Atkinson H. V. Revealing internal flow behaviour in arc welding and additive manufacturing of metals. *Nat. Commun.* **9**, 5414 (2018). DOI: 10.1038/s41467-018-07900-9

Publication keywords: Synchrotron X-ray; Fluid flow; Welding; Additive manufacturing

During advanced manufacturing processes, such as fusion welding and additive manufacturing, metallic alloys undergo rapid transitions in state between liquid and solid. Fluid flow inside the melt pool significantly influences the properties of the manufactured component.

The dynamic nature of the flow and the high temperature and opaque nature of molten metal make the direct experimental observation of the flow evolution inside the melt pool challenging.

Researchers were able to achieve direct time-resolved imaging of melt pool flow dynamics using synchrotron radiation on beamline I12, which has a high enough energy to penetrate through metal.

They were able, for the first time, to track internal flow streams during arc welding of steel. Their measurements showed instantaneous flow velocities ranging from 0.1 m/s to 0.5 m/s.

The results showed that when the temperature-dependent surface tension coefficient is negative, bulk turbulence is the main flow mechanism and the critical velocity for surface turbulence is below the limits identified in previous theoretical studies.

When the alloy exhibits a positive temperature-dependent surface tension coefficient, surface turbulence occurs, and damaging oxides can be trapped within the subsequent solid as a result of higher flow velocities.

These findings provide insights into internal melt pool flow during arc melting. They demonstrate that controlling internal melt flow through adjusting surface-active elements can optimise both the widely used arc welding and the emerging wire arc additive manufacturing routes.

In welding and additive manufacturing, metal is melted to form a molten pool that upon solidification can form high integrity products for applications such as automobiles, ships and other large metallic structures. Correct control of the melt pool is essential in manufacturing processes to avoid catastrophic failures[1]. Several fundamental physical phenomena govern the flow in the melt pool, including convection, plasma drag, electromagnetic forces and surface tension effects[2,3]. For steels, surface tension driven Marangoni forces dominate the melt pool flow, and are key to determining the shape and properties of the solidified structures[4,5]. Direct experimental observation of the flow evolution inside melt pools has been hindered by the dynamic nature of the flow as well as the high temperature and opaque nature of molten metal.

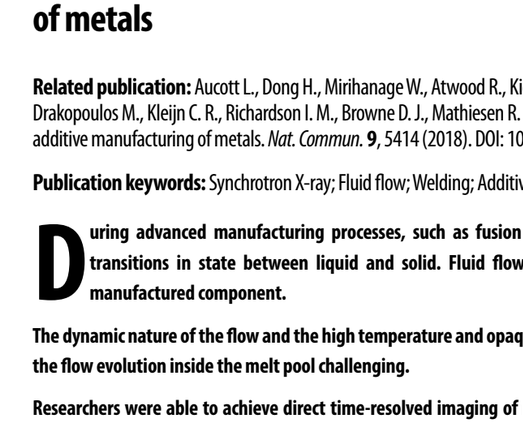

Figure 1: (a) Schematic diagram of the experimental setup and (b) an example radiograph annotated to show the key elements under observation during the experiment. A white beam of ~ 50–150 keV was used and the beam size was 12x50 mm² (H x W) and was transmitted through the entire melt pool. The detector was a Vision Research Phantom v7.3 CMOS camera, lens-coupled to cadmium tungstate or caesium iodide scintillators. With an optical magnification of 1.8x, the linear resolution was 13 µm/pixel. Imaging was acquired at frame rates up to 2 kHz at 800x600 pixels per frame.

In this study, a high-energy synchrotron micro-radiography technique at I12 has been employed to observe melt pool formation and flow dynamics *in situ* during advanced manufacturing of metallic alloys in a time-resolved way. These novel experimental observations have allowed the development of understanding of how the melt pool forms and evolves under realistic fusion welding conditions or wire arc additive manufacturing of metal.

The experimental setup, illustrated in Fig. 1, was positioned to transmit the incoming high-flux synchrotron white beam through the molten metal pool. Melt pools were created in solid steel bars using an electric arc. X-ray radiographs of the molten region, illustrated in Fig. 1b, were captured by employing a scintillator coupled fast CMOS camera, at 2 kHz frame rate, covering the whole molten region. Tungsten (W) particles, approximately 50 µm in size, were used as tracers to visualise the flow in the pool. In comparison to the iron and other constituting elements of the sample material, W particles exhibit significantly higher X-ray attenuation. W particles in the melt pool appear darker than the surrounding liquid metal in the projected images. Therefore, the trajectories of the W particles can be tracked to reveal the internal flow in the melt pool.

The morphological evolution of melt pools in low sulphur (S) (0.0005 wt%) and high S (0.3 wt%) steels are presented in Fig. 2. Both melt pools were created using exactly the same process parameters and sample dimensions. The images represent three instances to assess the overall geometric evolution in respect to time, until the melt pools grow to their maximum size. Quantitative

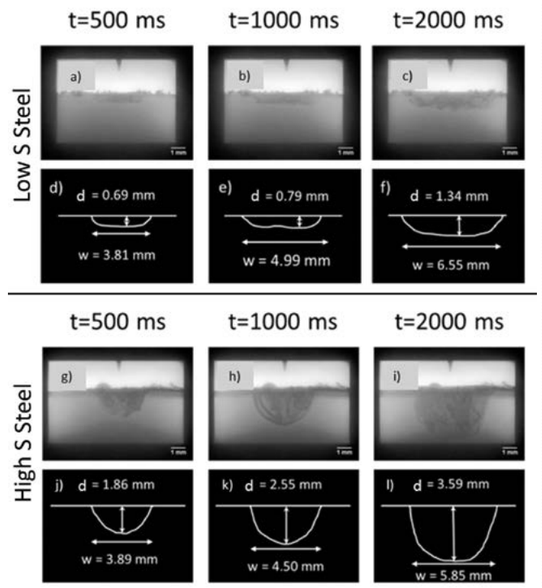

Figure 2: Synchrotron X-ray radiographs of the evolving melt pool for low S and high S steels at three time instances. The corresponding measured geometries are below the respective radiographs. The melt pools are created using the same melting parameters and sample dimensions. (a–f) are from a low S steel melt pool, while (g-l) are from a high S steel, showing that the high S melt pool favours downward growth to penetrate deeper than the low S melt pool. All scale bars=1 mm.

measurements of melt pool width evolution show that in the initial 500 ms the width evolution is nearly identical. After 500 ms, the low S sample begins to grow wider than the high S sample. The difference in the shape of the weld pool is radical and the high S sample immediately grows at a higher rate than the low S sample. The melt pool of the low S sample reached only 1.34 mm depth after 2000 ms. The high S steel melt pool appears to favour downward growth to penetrate a depth of 3.59 mm.

Melt pool shape evolution is mainly determined by the internal flow. As illustrated in the measured instantaneous flow (Fig. 3), for low S steel, the tracer particles follow anti-clockwise paths in the left-half of the melt pool and therefore there is an outward flow in the upper part of the pool. Consequently, the highest temperature liquid metal under the heat source is being convectively transported horizontally away from the melt pool centre towards its lateral extremities. This leads to the development of the shallow, wide melt pool. The flow in the high S steel melt pool is in the opposite direction. The flow tracked by tracer particles reveals inward flow in the upper part of the melt pool. Therefore, the highest temperature liquid metal in the upper centre region of the melt pool is transported vertically downwards to the centre bottom. The bottom of the melt pool receives more heat load, which stimulates further melting of the solid substrate at the bottom of the pool. As a result, the melt pool in the high S steel is deeper than that in low S steel. Instantaneous particle (flow) velocities for low and high S steel melt pools are presented in Fig 3. The flow velocities can exceed 0.5 m s^{-1} in high S steel, whereas, in low S steel, flow velocities do not exceed 0.3 m s^{-1}.

Observations allow us to comprehend how melt pool formation and evolution progress under realistic manufacturing conditions. The widely used arc welding and the emerging wire arc additive manufacturing routes can be optimised by controlling internal melt flow through adjusting surface-active elements such as sulphur.

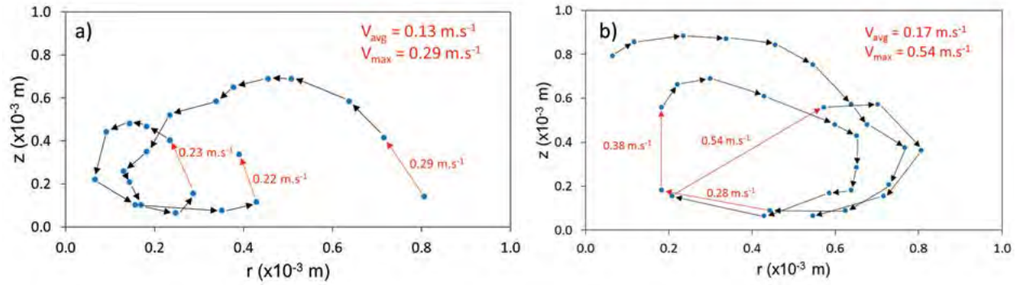

Figure 3: Measured flow direction and instantaneous velocity in (a) low S steel, and (b) high S steel in 2 seconds (s) after the inception of melting. r and z denote the distance in the radial and vertical axis, respectively.

References

1. Bonnín Roca J. *et al.* Policy needed for additive manufacturing. *Nature Mat.* **15**, 815 (2016). DOI: 10.1038/nmat4658
2. David S. A. *et al.* Current issues and problems in welding science. *Science* **257**, 497 (1992). DOI: 10.1126/science.257.5069.497
3. Tong M. *et al.* Multiphysics numerical modeling of fusion welding with experimental characterization and validation. *JOM* **65**, 99 (2013). DOI: 10.1007/s11837-012-0499-6
4. Wang Y. *et al.* Effects of surface active elements on weld pool fluid flow and weld penetration in gas metal arc welding. *Metallurgical and Materials Transactions B* **32**, 501 (2001). DOI: 10.1007/s11663-001-0035-5
5. Aucott L. *et al.* Initiation and growth kinetics of solidification cracking during welding of steel. *Sci. Rep.* **7**, 40255 (2017). DOI: 10.1038/srep40255

Funding acknowledgement:
This research work was supported by the European Commission as part of the FP7 program, as the project, Modelling of Interface Evolution in Advanced Welding, Contract No. NMP3-SL-2009-229108.

Corresponding authors:
Prof Helen Atkinson CBE FREng, Cranfield University, helen.atkinson@cranfield.ac.uk, Prof Hongbiao Dong, University of Leicester, h.dong@leicester.ac.uk

Understanding the environmental implications of the Fukushima nuclear accident

Related publications: Martin P. G., Louvel M., Cipiccia S., Jones C. P., Batey D. J., Hallam K. R., Yang I. A. X., Satou Y., Rau C., Mosselmans J. F. W., Richards D. A. & Scott T. B. Provenance of uranium particulate contained within Fukushima Daiichi Nuclear Power Plant Unit 1 ejecta material. *Nat. Commun.* **10**, 2801 (2019). DOI: 10.1038/s41467-019-10937-z

Martin P. G., Jones C. P., Cipiccia S., Batey D. J., Hallam K. R., Satou Y., Griffiths I., Rau C., Richards D. A., Sueki K., Ishii T. & Scott T. B. Compositional and structural analysis of Fukushima-derived particulates using high-resolution x-ray imaging and synchrotron characterisation techniques. *Sci Rep.* **10**, 1636 (2020). DOI: 10.1038/s41598-020-58545-y

Publication keywords: Fukushima; Uranium; Nuclear; Contamination; Radiation; SIMS; Synchrotron; Tomography

The Fukushima Daiichi Nuclear Power Plant accident released a large number of radioactive particulates into the environment. To understand the environmental and health hazards this material poses, scientists from the University of Bristol studied the physical form and chemical composition of small (sub-mm) released particles. The plant operators also needed to know what exactly happened in the reactors, and how the physical properties of the material would affect removal and reprocessing/waste storage operations.

Diamond Light Source's X-ray Imaging and Coherence Beamline (I13-1) was the ideal platform through which to perform high-resolution imaging to examine the fine internal structure of the particulates and to perform elemental mapping to determine the material's composition. The results show that the particulates have a glassy composition that is likely to be stable in the environment. Uranium in the samples demonstrates that fuel was released from the reactor core.

The researchers were able to establish a chronology of the release events, providing information on the likely state of the 'fuel debris' – facts critical for retrieval and reactor decommissioning.

Experiments at Diamond have analysed two of the three particulate types released from Fukushima, and an upcoming investigation on the Microfocus Beamline (I18) will examine the third. Such is the impact of this work that this Bristol and Diamond team have been asked to analyse material released obtained from the Chernobyl exclusion zone – the first work to do so in nearly 20 years.

The accident at Japan's Fukushima Daiichi Nuclear Power Plant (FDNPP) in March 2011 is one of only two International Nuclear Event Scale (INES) Level 7 incidents – the most severe, to have ever occurred (the only other being Chernobyl). Initiated by the Magnitude 9.0 Great Tohoku earthquake off the countries eastern coast, the ensuing 15 m high tsunami subsequently crippled the plants routine and emergency systems that provided core cooling to each of the sites four operational reactors. Despite the efforts of the plants operators, the Tokyo Electric Power Company (TEPCO), to bring the reactors under control through emergency seawater injection, the decay heat in each of the reactors progressively rose over the following week to dangerous levels.

Eventually, the heat and gaseous build-up in each of the reactors and reactor buildings became too great, with a series of explosions (Unit 1 and Unit 3) and discrete releases (Unit 2) occurring up to 10 days after the initial event. Although approximately 80% of the 520 PBq of radioactivity[1] (approximately 10% of Chernobyl) released from Fukushima was dispersed out into the Pacific Ocean[2], a considerable inventory of radioactive material was deposited over the Japanese land area. This contamination existed as a number of isotopically distinct yet spatially mixed plumes, composed primarily of the volatile fission product caesium (Cs). While the vast majority of the work to-date has focused on quantifying the distribution and environmental implications of this easy to detect ionic (gaseous) radiocaesium release, work at the University of Bristol and Diamond has sought to study the particulate input into environment and the elements (e.g. actinides) more commonly overlooked as they are much harder to detect. Such knowledge will allow for a greater understanding of the potential health implications associated with other material released into the environment in addition to crucial insight into the release dynamics and the current state of material in the reactor – essential for the soon to commence fuel debris retrieval operations.

X-ray tomography (XRT) combined with elemental distribution information derived from X-ray fluorescence (XRF) is capable of detailing both the internal structure of the sub-mm particulate collected from the land surrounding the plant. The bright, strongly coherent and highly focused beam of X-rays produced by the synchrotron enables rapid data collection from short exposure times, with the unique optical configuration on I13-1 allowing for image resolutions not attainable on other beamlines. Following their collection and isolation from bulk sediments by collaborators at the Japan Atomic Energy Agency (JAEA)[3], the radioactive particulate was encapsulated within a special X-ray transparent kapton tape. This would prevent the sample from being dislodged during the analysis and being lost on the beamline.

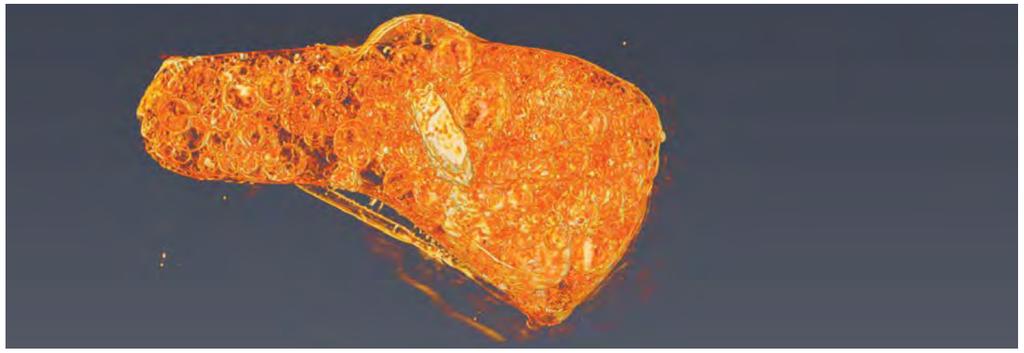

Figure 1: Tomographic reconstruction of one of the particulate samples analysed. A high-density iron-based fragment is observed embedded into the surface of the material. The particle is approximately 500 µm in length.

The suite of sub-mm particulate studied on I13-1 was sourced exclusively from reactor Unit 1 that sustained a large reactor building hydrogen explosion but dispersed radioactive material closer to the plant boundary than the smaller particles from Unit 2. For each particle, following the careful alignment of the beamline optics, an X-ray tomography (absorption contrast) scan was undertaken by taking an X-ray 'photo' as the sample was slowly rotated within the beam – producing an image like a hospital X-ray. By then using tomographic reconstruction algorithms, it was possible to produce an absorption 3D representation of each particle, detailing its internal form (Fig 1). The highly coherent X-rays produced on I13-1 also allowed for an enhanced examination of the samples fine structure using X-ray ptychography, which showed the highly porous and fibrous nature of the particulate samples. Following the physical structural analysis of each sample with XRT, an analysis of the composition was performed using XRF. Each particle was rastered through the beam path with an elemental spectrum obtained for each pixel 'step'. Reconstructions of the species distribution, paired with the XRT derived structure, were then performed using software developed in-house at Diamond[4].

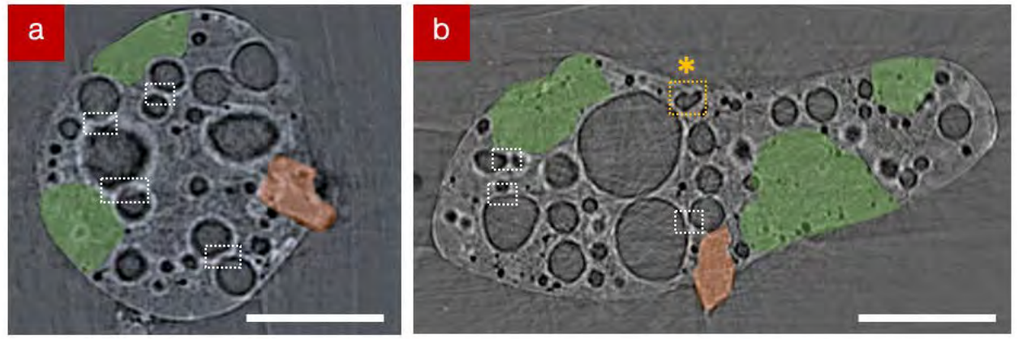

*Figure 2: Tomographic slice through the particle overlain with compositional data derived from XRF analysis. Orange = stainless-steel, Green = cement. Scale bars = 100 µm. White boxes = locations where voids connect, Yellow box and * = location at which two bubbles have likely fused.*

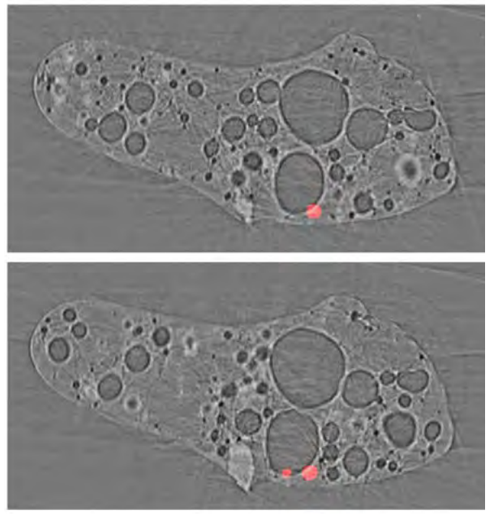

Figure 3: Tomographic sections through an FNDPP derived particle, with uranium inclusions identified using XRF overlain.

Using the combined XRT, ptychography and XRF analysis of the samples, it was possible to understand how the material from reactor Unit 1 at the FDNPP was formed and the conditions in the reactor at the time of its release. Most importantly, this work has shown for the first time that uranium derived from the reactor Unit 1 core was released during the accident – with core integrity and containment becoming sufficiently compromised during the accident. In fact, the presence of both cement and stainless-steel within some of the particles highlights the explosive nature of the release event (Fig. 2). This knowledge of the likely state of the current conditions in the reactor is important as the Japanese plan to shortly commence operations to remove the damaged core debris material in Units 1, 2 and 3 at the FDNPP.

The close collaboration between the University of Bristol, JAEA and Diamond has provided crucial information to guide Japanese authorities in the remediation of the contaminated environment and in on-site decommissioning activities. This forensic analysis has opened the door to future in-depth high resolution studies on radioactive particulate material derived from not just the FDNPP accident - from the mm to the nm scale.

References:

1. Steinhauser G. *et al.* Comparison of the Chernobyl and Fukushima nuclear accidents: a review of the environmental impacts. *Sci Total Environ.* **470-471**, 800-817 (2014). DOI: 10.1016/j.scitotenv.2013.10.029
2. Stohl A. *et al.* Xenon-133 and caesium-137 releases into the atmosphere from the Fukushima Dai-ichi nuclear power plant: determination of the source term, atmospheric dispersion, and deposition. *Atmos. Chem. Phys.* **12**, 2313-2343 (2012). DOI: 10.5194/acp-12-2313-2012
3. Satou Y. *et al.* First successful isolation of radioactive particles from soil near the Fukushima Daiichi Nuclear Power Plant. *Anthropocene* **14**, 71-76 (2016). DOI: 10.1016/j.ancene.2016.05.001
4. Cipiccia S. *et al.* An Iterative Self-Absorption Correction Algorithm for 3D Ptycho-Fluorescence Imaging. *Microsc. Microanal.* **24**(S2), 94-95 (2018). DOI: 10.1017/S1431927618012862

Funding acknowledgement:

Daiwa Anglo-Japanese Foundation (Grant Reference: 11424), Great Britain Sasakawa Foundation (Grant Reference: 5223), EPSRC (Reference: EP/S020659/1), EPSRC (Reference: EP/K040340/1)

Corresponding author:
Dr Peter Martin, University of Bristol, peter.martin@bristol.ac.uk

Working towards early detection of osteoarthritis

Related publication: Madi K., Staines K. A., Bay B. K., Javaheri B., Geng H., Bodey A. J., Cartmell S., Pitsillides A. A. & Lee P. D. In situ characterisation of nanoscale strains in loaded whole joints via synchrotron X-ray tomography. *Nat. Biomed. Eng.* **4**, 343 (2020). DOI: 10.1038/s41551-019-0477-1

Publication keywords: Biomedical engineering; Bone quality; Biomechanics, Nano-metre strain resolution; Osteoarthritis

There are no effective methods for the early detection of osteoarthritis (OA), a condition that affects a large part of the world's population. The subtleties of how early-stage OA affects the shape (morphology) and mechanical behaviour of different joint tissues are not well understood.

Researchers wanted to measure the morphology of the different tissues in 3D with cellular-level resolution, while the joint was under lifelike loading. They needed to measure the strains within these tissues at the level of 100's of nanometres, without using staining or too high a flux, both of which damage the tissue and change its mechanical behaviour.

Using the 'Diamond Light Source - The University of Manchester Collaboration' Imaging Branchline (I13-2), they were able to take time-resolved 3D images, which they then analysed to resolve the strains and displacements within the tissue with 100 nm resolution. They were able to image joint morphology at a cellular level and resolve strains with 100 nm accuracy in physiologically realistic loading conditions for the first time. Using a combination of three key advances (low dose, pink phase contrast imaging, a unique nano-precision loading device and bespoke Digital Volume Correlation analysis software) enabled them to characterise how the articular cartilage adapts to spread load during the early stages of OA.

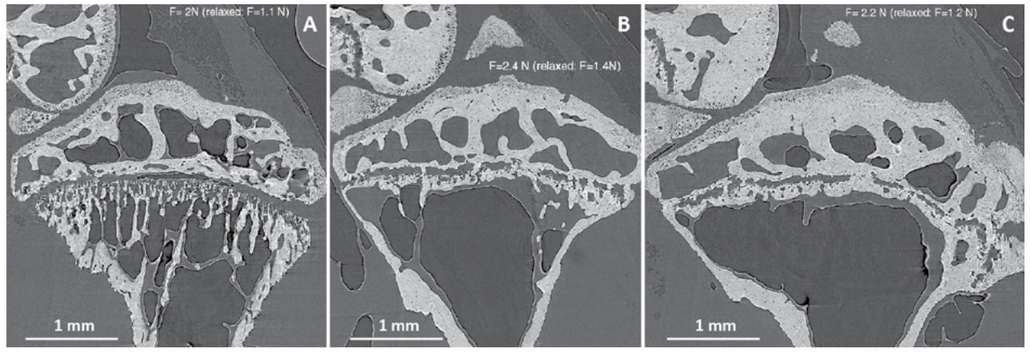

Figure 1: Vertical sections through tomography data of knee joints under load for (a) 8-week, (b) 36-week and (c) 60-week-old STR/Ort representing pre, incipient, and advanced stages of arthritis. Significant changes in overall joint morphology and mineralised tissue characteristics are readily apparent.

The technique developed may be used to determine the efficacy of new treatments for OA at very early stages.

Osteoarthritis is one of the largest contributors to global disability among all medical conditions, and the societal health care burden is increasing dramatically as populations age[1]. It is a pernicious medical condition with a host of contributing factors and comorbid conditions, and suitable treatment strategies have long been sought. But progression from initial disease identification through management of symptoms to eventual surgery (total joint replacement) remains common and is burdensome both in terms of years lived with disability and pain, and direct and indirect cost of care. A significant barrier to understanding of disease etiology and evaluation of treatment efficacy is the disparate perspectives taken by researchers and the variety of methodologies they employ. This study employed three key advances to help bridge those gaps: low dose, pink phase contrast imaging (on I13-2); a unique nano-precision loading device; and bespoke Digital Volume Correlation analysis software.

The behaviour of cells, the structure and composition of tissues, the organisation of tissues within bones, and the mechanical function of synovial joints are all relevant but involve very different spatial scales and research techniques. Without a consistent perspective and integrated research context it is difficult to unify results into a coherent picture. This project was organised around a classic medical research approach of small-animal disease models. The STR/Ort mouse strain exhibits age-related knee arthritis in a manner very similar to that seen in humans and is an established model of the disease[2]. Comparison with the healthy CBA control mouse strain as a function of animal age provides a basis for identifying key differences associated with the pathology.

A primary outcome of this study was attainment of high-resolution tomography data for native-state (fully hydrated, unfixed, unstained) intact knee joints subjected to compressive *in situ* loading (Fig. 1), at a resolution sufficient to reveal tissue and cellular levels of detail, enabling simultaneous functional and morphological evaluation. Study of intact joints is essential in establishing proper boundary conditions and maintaining the overall residual stress state of the mechanical system. Resolution to tissue and cellular levels of detail connects through to biological research that addresses tissue characteristics, calcified cartilage in particular, and microenvironments of the embedded chondrocytes and osteocytes.

The imaging challenges in achieving suitable tomography quality within this context were manifold. Load was applied through the robust, nano-precision P2R *in situ* system that allowed careful monitoring of sample relaxation before projection acquisition[3]. Customised sample grips were developed through additive manufacturing from laboratory tomography pre-scans of representative samples and positioned within the loading system with precision x-y stages. Beam configuration and scan parameters were critical in limiting acquisition time and minimising sample damage whilst maintaining suitable resolution. Efforts by scientists of the I13-2 branchline were essential in establishing the overall imaging protocol that proved effective.

Prior work with mouse bone samples produced excellent resolution of microstructural details using a monochromatic step-scan strategy, but estimated sample X-ray dose of 157 kGy was excessive, embrittling the tissue and hampering functional assessment. A shift to 20 keV 'pink beam', continuous acquisition and increased filtering (Carbon 950 µm, Aluminum 2 mm, Silver 75 µm, Platinum) to eliminate the more damaging low-energy X-rays, proved effective. Imaging of similar resolution to monochromatic scanning was produced but with dose reduced to approximately 100 kGy. A final adjustment - primarily a reduction in the number of projections from 2400 to 600 - reduced exposure to 27 kGy and total acquisition time to 1.1 minutes. Both of these factors, low dose and low scan time, were critical for project success. Resolution alone is not enough for *in situ* loading studies of biological samples as beam damage and sample motion must be controlled.

Functional assessment was conducted through digital volume correlation (DVC) analysis, which compares an initial unloaded tomography data volume with subsequent volumes generated under *in situ* loading to quantify deformation within the samples[4,5]. The full joint was evaluated in this way (Fig. 2), demonstrating internal deformation patterns within both the femur and tibia. The displacement measurement accuracy was assessed by correlating repeat image volumes in the unloaded state and was determined to be 240 – 480 nm for the full joint, and 80 – 160 nm for the articular calcified cartilage region.

An additional loading methodology using a 200 µm radius diamond tip indenter in place of the femur was employed to create uniform mechanical input to the medial condyle of the tibia. This allowed more spatially resolved deformation measurement and a closer association with microstructural detail (Fig. 3). Deformation localised within the articular calcified cartilage region of

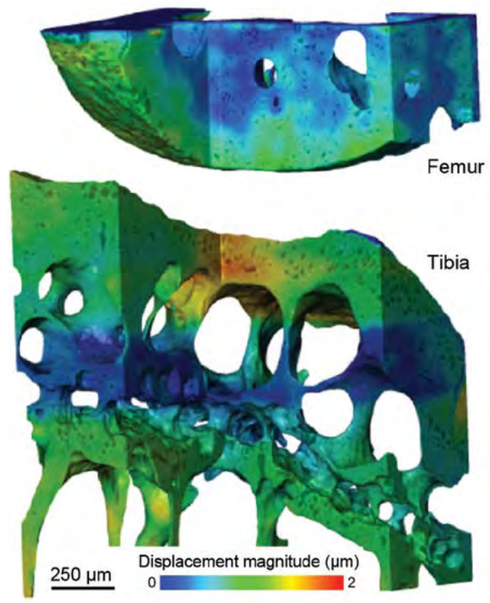

Figure 2: Digital Volume Correlation (DVC) generated, nanometre accuracy, displacement field for a 36-week old STR/Ort knee joint under compressive loading. Large-scale view reveals the influence of overall tissue structure on joint compliance.

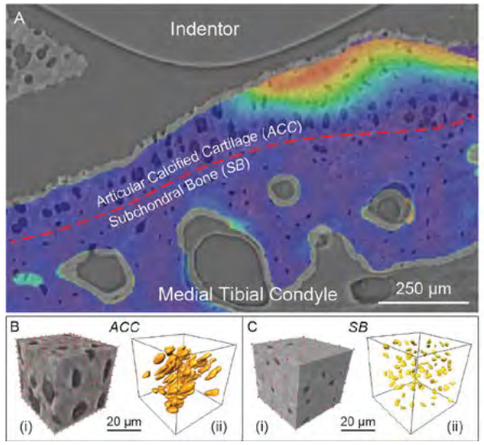

Figure 3: Combined morphological and functional assessment under indentation loading. Displacements concentrate within the articular calcified cartilage region (a). Hypertrophic chondrocyte lacunae (b(i)) provide texture for DVC tracking, and morphological analysis (b(ii)) quantifies pore volume, shape and orientation. Similar features arise from osteocyte lacunae within the subchondral bone region (c(i)), (c(ii)).

the articular surface is a key insight into joint function. The same imaging data allows visualisation and quantification of the small lacunae hosting individual cells within the tissue. While further study is required to fully elaborate the structure/functional relationships within this system, this synchrotron-based *in situ* imaging approach applied to intact bones and joints is a promising approach with no analogue within other existing research methodologies.

References:

1. Cross M. *et al.* The global burden of hip and knee osteoarthritis: estimates from the Global Burden of Disease 2010 study. *Ann. Rheum. Dis.* **73**, 1323 (2014). DOI: 10.1136/annrheumdis-2013-204763

2. Staines K.A. *et al.* The STR/ort mouse model of spontaneous osteoarthritis – an update. *Osteoarthritis and Cartilage* **25**, 802 (2017). DOI: 10.1016/j.joca.2016.12.014

3. Kareh K. *et al.* Revealing the micromechanisms behind semi-solid metal deformation with time-resolved X-ray tomography. *Nat. Commun.* **5**, 4464 (2014). DOI: 10.1038/ncomms5464

4. Bay B.K. *et al.* Digital volume correlation: Three-dimensional strain mapping using X-ray tomography. *Experimental Mechanics* **39**, 217 (1999). DOI: 10.1007/BF02323555

5. Bay B.K. Methods and applications of digital volume correlation. *Journal of Strain Analysis for Engineering Design* **43**, 745 (2008). DOI: 10.1243/03093247JSA436

Funding acknowledgement:

Engineering and Physical Sciences Research Council (grants EP/I02249X/1 and EP/M009688/1): Arthritis Research UK (grant 18768): MRC (grant MR/R025673/1). Facilities and research support were provided by the Diamond-Manchester Branchline (I13-2) at Diamond Light Source (Beamtimes MT13237-1, MT11076-1 and MT5003-1) and the Research Complex at Harwell.

Corresponding authors:
Prof Brian K. Bay, Oregon State University, brian.bay@oregonstate.edu and Prof Peter D. Lee, University College London, peter.lee@ucl.ac.uk

Evaluating the environmental impact of zinc oxide nanomaterials in municipal wastewater

Related publication: Gomez-Gonzalez M. A., Koronfel M. A., Goode A. E., Al-Ejji M., Voulvoulis N., Parker J. E., Quinn P. D., Scott T. B., Xie F., Yallop M. L., Porter A. E. & Ryan M. P. Spatially resolved dissolution and speciation changes of ZnO nanorods during short-term *in situ* incubation in a simulated wastewater environment. *ACS Nano* **13**, 11049 (2019). DOI: 10.1021/acsnano.9b02866

Publication keywords: ZnO nanomaterials; X-ray fluorescence microscopy; Scanning electron microscopy; Spatially resolved *in situ* ZnO transformations

Zinc oxide (ZnO) engineered nanomaterials are used in a wide range of consumer products, such as sunscreens, personal care products, and anti-bacterial agents. There are concerns about their potential impact as an environmental pollutant, with concentrations of ZnO nanomaterials in municipal water predicted to be of the order of milligrams per litre. ZnO nanomaterials may inhibit bacterial processes in urban wastewater treatment plants. They could also adversely affect the health of organisms in soils and waters once treated material is released back into the natural environment.

What effect the ZnO nanomaterials will have on the environment depends on how they are transformed by chemical reactions with (e.g.) sulphur or organic carbon in environmental systems. Researchers need spatially-resolved *in situ* methods to track transformations in real-time.

X-ray Fluorescence Microscopy (XFM) has emerged in recent years as a promising technique for imaging environmental samples due to its high spatial resolution and sensitivity to a wide range of elements.

Researchers used time-resolved hard X-ray Fluorescence Microscopy on the Hard X-ray Nanoprobe beamline (I14) to monitor dynamic changes to the nanomaterials *in situ*. They were able to make predictions about the rates at which ZnO nanomaterials transform during the first stages of the wastewater treatment process. Their results can be used to generate fundamental knowledge about the fate of ZnO nanomaterials in conventional municipal sewage systems.

Nanostructures of zinc oxide (ZnO) are at the forefront of application-driven nanotechnology because of their unique optical, piezoelectric, semiconducting and antibacterial properties. Their exceptional properties, such as nanometric size and high surface reactivity, which are utilised or engineered advantageously for many applications, may also increase their toxicity to the environment in the course of their synthesis, use, and disposal. Thus, there is an urgent need to understand their fate as transition from common usage to the environment via wastewater treatment and disposal plants, as well as any potential impact on the (micro)organisms. A methodology based on spatially resolved *in situ* X-ray Fluorescence Microscopy (XFM) was developed at I14, allowing observation of real-time dissolution and morphological and chemical evolution of synthetic template-grown ZnO nanorods (~ 725 nm length, ~ 140 nm diameter). An in-house liquid cell was designed by the I14 beamline staff, where the templated ZnO nanorods were aligned within the path of the X-ray beam, and subsequently incubated with ~ 200 µL of simulated sludge solution. Primary sludge, mainly formed by organic matter and humic substances, is one of the first physio-chemical barriers that influent or sewage waters encounter when entering the cleaning cycle of a regular wastewater treatment plants (WWTP) and, therefore, humic acid (10 mg L^{-1}) was selected as simplified aquatic medium for this study. It is only by applying this simplified system – instead of a more complex real sludge – that accurate proof-of-concept of the feasibility of the technique can be generated.

Consecutive XFM maps were acquired *in situ* during incubation of the ZnO nanorods for two short-time scales (1 hour and 3 hours), allowing evaluation of ZnO morphology changes within the initial stages of their release to sewage waters. A gradual decrease of the Zn fluorescence intensity was observed during the proposed *in situ* incubation periods. Over the 3-hours experiments, some of the Zn-hotspots dissolved extensively until they were no longer detectable. The expected ZnO nanorod dissolution favoured the release and transport of Zn^{2+} ions within the simulated sludge solution, as confirmed by Inductively Coupled Plasma Mass Spectroscopy (ICP-MS). This partial nanorod dissolution was further established by *ex situ* scanning electron microscopy, exhibiting thinner rod structures smaller than ~200 nm length and ~20 nm width.

To obtain chemical and speciation information along the Zn K-edge, further XFM image stacks were collected on the drained Zn-structures at different photon energies[1]. Nine energies (9-E) were selected as follows: i) three for background removal at Zn pre-edge; ii) five post-edge energies to differentiate between the distinctive features of the Zn-species; and iii) a spectrum image at the isosbestic point, where all the Zn-phases presented a similar fluorescence intensity irrespective of their speciation. Hence, speciation maps (SM) were calculated through fitting the absorption data from each pixel to the linear combination of the standard spectra after acquiring 9-E imaging scans (Fig. 1). Quantification maps (QM) were calculated by normalising the speciation maps to the isosbestic point, producing a visual estimation of the real extent of the Zn-species generation. A fluorescence map was also acquired at the maximum energy of the Zn K-edge X-ray Absorption Near Edge Structure (XANES) spectrum (E_{max} in Fig. 1) for total Zn intensity contribution. After 1 hour incubation of the ZnO nanorods in the simulated sludge (Fig. 1b), ZnS became the predominant species on the surface of the Zn-hotspot according to the SM, which was confirmed by the calculated QM. As expected, this differs from the spectra taken for the "as-synthesised" ZnO, which showed predominant ZnO contribution (Fig. 1a). After the 3 hours incubation, a different behaviour of the ZnO nanorods was found depending on the region analysed. In the first region (Fig. 1c), most of the Zn-hotspots remained as ZnO in the SM. The QM indicated a significant amount of ZnS species generated in areas depleted in ZnO. The second region analysed after 3 hours incubation (Fig. 1d) showed a more disperse variation in the Zn-species in the SM, with ZnS as the dominant species. Although ZnO was still a major component of the larger hotspots in the QM, trace amounts of diffuse Zn-phosphate ($Zn_3(PO_4)_2$) and Zn adsorbed to iron-oxyhydroxides (Zn-Fe(ox)) were also mapped after the 3 hours incubation, with different trends in their spatial variations. Le Bars *et al.*[2] showed that nano-ZnS is a major Zn species in raw liquid organic wastes, but it was a minority in solid and more processed organic-rich wastes. Furthermore, the formation of a ZnO-$Zn_3(PO_4)_2$ core-shell structure has been reported in phosphate-rich environments[3], where Zn^{2+} can be complexed with aqueous PO_4^{3-}, resulting in the formation of an amorphous zinc phosphate hydrate precipitate[4]. Although $Zn_3(PO_4)_2$ is the thermodynamically favoured species, the full transformation to these species is kinetically limited to longer reaction times (15 days)[3,4], which were not achieved here. The higher solubility reported by Ma *et al.*[5] for the ZnS-shell/ZnO nanomaterials than that expected for bulk ZnS (Ksp = $2 \cdot 10^{-25}$ yields a solubility of $3.7 \cdot 10^{-10}$ mM) would kinetically favour the transformation to ZnS phase rather than to $Zn_3(PO_4)_2$ under these conditions. To confirm the validity of the spectra extracted from the 9-energies speciation, a larger energy resolution image stack was acquired using 135-energies along the Zn K-edge. The generated XANES spectra were compared with the corresponding standards for the expected Zn-species, and subsequently analysed by linear combination fitting (LCF) analyses. An estimation of the ZnO composition of the samples was obtained by LCF, showing a decrease in the ZnO contribution after only 1-hour incubation in the simulated sludge to a ~27-41%, and a further significant decrease to an only ~12-17% of the total Zn content within 3-hours.

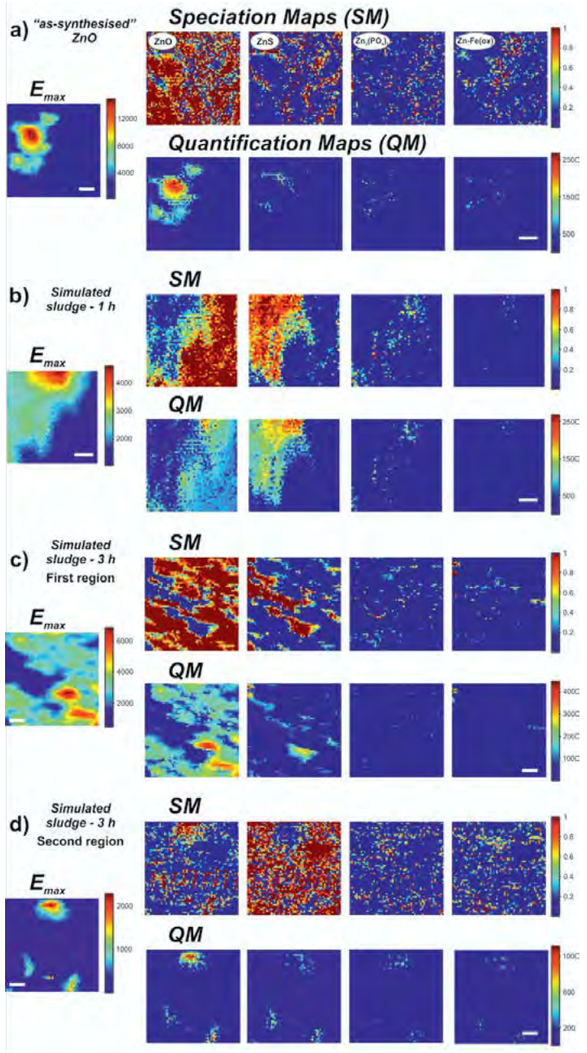

Figure 1: 9-Energy X-ray Fluorescence Microscopy (XFM) of: (a) "as-synthesised" ZnO, (b) sample after the 1-hour incubation in a simulated sludge and (c-d) two different regions analysed in the sample after the 3-hours incubation. [Left] Fluorescence map acquired at E_{max}=9669 eV. [Right] Speciation maps (SM) of the expected Zn-species, where the red colour equals a 100% compound contribution and the blue colour corresponds to 0%. Quantification maps (QM) for the same species were calculated after normalising the SM with the isosbestic point. The numbering on the scale bars on the QM provides an estimation of the Zn-species contribution. Scale bars = 750 nm.

In this work, spatially resolved maps of ZnO nanomaterial transformation within a simulated environmental medium have been acquired dynamically. These results demonstrated that: i) ZnO nanorods partially transformed to ZnS species predominantly within *in situ* short-time incubations (1 –3 hours) in a simulated primary sludge medium, ii) minor $Zn_3(PO_4)_2$ and Zn adsorbed to Fe-oxyhydroxides were also measured in some non-sterically impeded regions, iii) the ongoing ZnO dissolution and the humic acid presence have an influence in the preferential transformation of the remaining ZnO nanorods. As nanomaterials formulations become more complex, the XFM technique would offer the possibility to characterise chemical transformations of individual nanoparticles within complex mixtures and coupled behaviour between the particles. When studying the structural and functional impacts of transformed nanomaterials on organisms, this information could, in future, be used to generate mechanistically underpinned insight to predict nanomaterial behaviour, refine guidelines for safe use and to inform remediation strategies of engineered nanomaterials.

References:

1. Koronfel M. A. *et al.* Chemical evolution of CoCrMo wear particles: an *in situ* characterization study. *J. Phys. Chem. C* **123**, 9894 (2019). DOI: 10.1021/acs.jpcc.9b00745
2. Le Bars M. *et al.* Drastic change in zinc speciation during anaerobic digestion and composting: instability of nanosized zinc sulphide. *Environ. Sci. Technol.* **52**, 12987 (2018). DOI: 10.1021/acs.est.8b02697
3. Rathnayake S. *et al.* Multitechnique investigation of the pH dependence of phosphate induced transformations of ZnO nanoparticles. *Environ. Sci. Technol.* **48**, 4757 (2014). DOI: 10.1021/es404544w
4. Lv J., Dissolution and microstructural transformation of ZnO nanoparticles under the influence of phosphate. *Environ. Sci. Technol.* **46**, 7215 (2012). DOI: 10.1021/es301027a
5. Ma R., Sulfidation mechanism for zinc oxide nanoparticles and the effect of sulfidation on their solubility. *Environ. Sci. Technol.* **47**, 2527 (2013). DOI:10.1021/es3035347

Funding acknowledgement:
This work and Miguel Gomez-Gonzalez contract were supported by the Natural Environment Research Council project: NE/N006402/1. Mary Ryan acknowledges support from the RAEng/Shell via a Research Chair in Interfacial Nanoscience. Reprinted (adapted) with permission from ACS Nano 2019, 13, 10, 11049-11061, Spatially Resolved Dissolution and Speciation Changes of ZnO Nanorods during Short-Term *In Situ* Incubation in a Simulated Wastewater Environment. Copyright 2019 American Chemical Society.

Corresponding author:
Miguel A. Gomez-Gonzalez, Diamond Light Source Ltd., miguel.gomez-gonzalez@diamond.ac.uk

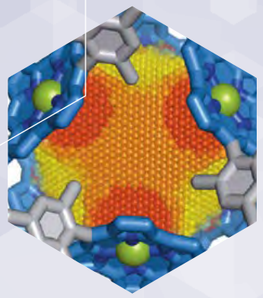

Crystallography Group

Joe Hriljac, Science Group Leader

The Crystallography Group comprises the High-Resolution Powder Diffraction beamline (I11), the Extreme Conditions beamline (I15), the X-ray Pair Distribution Function (XPDF) beamline (I15-1), and the Small-Molecule Single-Crystal Diffraction beamline (I19). Bringing these beamlines together into one science group means we can fully exploit the technical and scientific expertise within its teams to provide the basis for future development and pioneering experiments.

The coming year will see the continuation of many beamline upgrade projects, with the aim to further develop our tools, data analysis pipelines and strategic planning for the Diamond-II upgrade. 2019 was a particularly challenging year for everyone involved with I15 and I15-1 due to a failure of the cryocooling system for the superconducting wiggler in May. Extensive effort was put into the repair led by the Diamond Insertion Device team, and it is a relief to say that from January 2020, we were able to resume normal operations and our user program.

I11 update

The high brightness beamline uses monochromatic X-rays in the range of 6 - 25 keV for high-resolution and time-resolved powder diffraction experiments in the first Experimental Hutch (EH1) or for Long Duration Experiments in EH2. Thanks to our dedicated beamline staff, I11 has continued to efficiently deliver beamtime, facilitating experiments to the busy user programme throughout the year, in particular for non-ambient applications and experiments requiring unusual hardware setups such as toxic/corrosive gas absorption studies at cryogenic temperatures, resonant diffraction at high temperature and time-resolved *in operando* lithium-ion (Li-ion) battery work.

After running for ten years, many components such as the monochromator, diffractometer and Multi-analyser Crystal (MAC) detector began to show signs of wear. An upgrade plan, endorsed by the Scientific Advisory Committee (SAC) and the Diamond Industrial Science Committee (DISCo) at the end of 2017 to replace these components started in 2019. The construction and installation of a new high stability monochromator were completed during the June shutdown. A new Newport diffractometer has been delivered and installed and commissioning will finish in September 2020. A superconducting undulator to replace the original in-vacuum system and provide better flux at high energy has undergone extensive specification and early prototype testing, and this should be complete and ready for installation soon. Finally, an upgrade to the linear PSD in EH1 is planned, and it is anticipated that a next-generation detector should be available in 2021.

I15 update

The Extreme Conditions beamline, I15, employs high energy X-rays to explore the structure of materials at high pressures, high and low temperatures, as well as other *in situ* and *in operando* conditions. The beamline receives an X-ray continuum from the superconducting wiggler; this allows for experiments that require monochromatic X-rays between 20 and 80 keV, as well as polychromatic beam. I15 was originally designed to serve the mineral physics community, which it has, whilst also assisting material scientists, chemists and solid-state physicists with their structural investigations, at pressure or otherwise.

I15 continues to offer extensive capabilities and support to users to assist their high pressure studies. I15 users have pre-experiment access to bespoke assistance and training from our highly skilled staff in diamond anvil cell (DAC) preparation and loading, as well as the usage of beamline DACs for novice users for I15 experiments. The high-pressure gas loader available at I15 offers users the choice of many possible gases to use as their pressure transmitting media (PTM), allowing them to optimise for hydrostaticity with helium or neon, or choosing a PTM based on desired interactions with the sample at pressure. Work is underway to add hydrogen to our gas loading capabilities in 2020. The recent addition of the laser heating system adds a further unique capability – the I15 system is capable of quickly ramping the laser power to perturb a sample without delivering too much heat to the bulk. Several small upgrades started in 2019; these include improved network infrastructure and a better design of the laser system. In 2020 the low-temperature cryostat for DAC work will be commissioned and, significantly, the beamline is procuring a vastly improved detector – a DECTRIS PILATUS3 X CdTe 2M that will provide much greater sensitivity to high-energy X-rays and the capability for much faster data collections. Software and hardware improvements to take advantage of the speed and sensitivity offered by the new detector are being explored. Diffraction mapping with automated processing has been successfully tested with the existing Perkin Elmer detector - this functionality will be improved with the CdTe PILATUS3. Further upgrades to I15 to take full advantage of fast hardware-based scanning and mapping are planned.

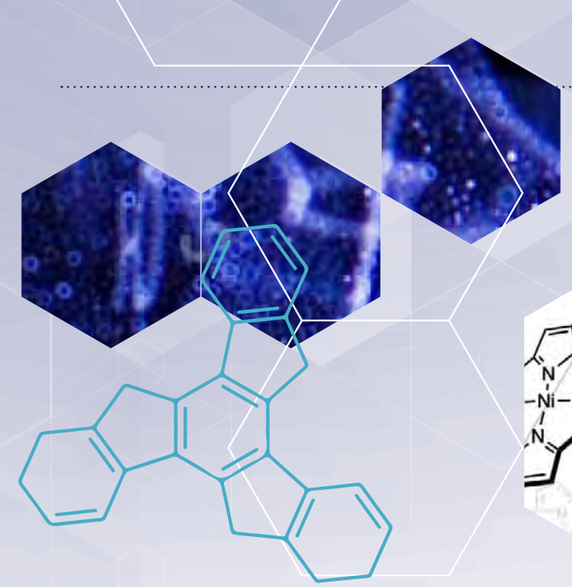

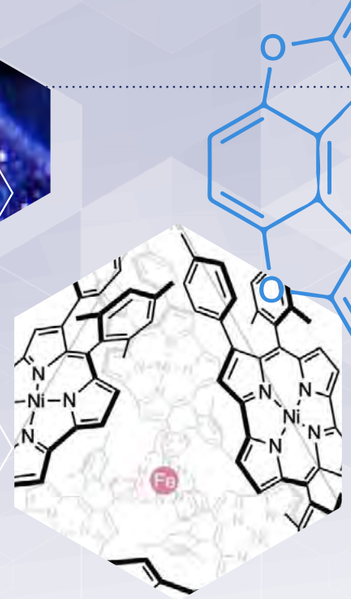

I15-1 update

The XPDF beamline, I15-1, is dedicated to producing high-quality X-ray scattering data for Pair Distribution Function (PDF) analysis. Operational since 2017, I15-1 has illuminated samples from diverse fields, from Earth sciences to pharmaceuticals, as well as material science and chemistry. XPDF receives X-rays from the inside edge of the wiggler fan, and this light is monochromated and directed to the end station in three energies: 40, 65 and 76 keV. PDF data are collected at high energies to produce the low sample absorption and high *Q*-range required for successful interpretation. Gaining structural information on amorphous samples is a primary goal of many XPDF experiments, but crystalline samples can also display local structure variations such as defects and disorder, which can be studied via PDF analysis. PDF data collections are rarely available at home institutions, so in order to allow more people to exploit this powerful technique I15-1 complements the standard proposal route with popular Rapid and Easy Access routes, where PDF data can be collected via a mail-in procedure.

Consisting of a sample position, with an optional sample-changing magazine, and two large area detectors, the end station is highly flexible and has been adapted to many *in situ* and *in operando* experiments, including variable temperature, gas flow, hydrothermal synthesis and electrochemical cycling. For more routine measurements, the 15-position sample changer has been a popular choice, allowing automatic data collection. Further upgrades including a new end station and a sample-changing robot are in progress, and both should be commissioned during 2020. The final aspect of the current upgrade is a new detector based on CdTe sensors that will be much more sensitive at high energy and with faster electronics for data readout.

These upgrades will be a synergistic addition to the existing auto-processing infrastructure and will allow users to collect better data with less manual intervention.

I19 update

The Small-Molecule Single-Crystal Diffraction beamline, I19, uses X-rays in the 5 – 25 keV energy range to determine the structures of small-molecule and extended three-dimensional systems, e.g. Metal-Organic Frameworks, with single-crystal diffraction techniques. These methods can be applied to the characterisation of novel materials or for investigating the variation in the structure of a crystalline material under an external physical influence such as a change in temperature, the exposure to a gas, photo-excitation or through the application of high-pressure.

The use of the robotic sample changer, and remote access, is now well established in Experimental Hutch 1 (EH1) of the beamline, where pre-mounted samples are sent to Diamond under cryogenic storage, and users then run their beamtime from their home institutions. This mode of operation makes it possible to carry out chemical crystallography studies in a more responsive manner as beamtime can be scheduled in more regular, and shorter, periods. We now schedule individual shifts, rather than whole one-day (three shifts) blocks of beamtime, for those wishing to run their beamtime via the remote access route. For Experimental Hutch 2 (EH2), we have recently developed a cell which allows a high static electric field to be applied to the sample crystal. The application of electric fields to materials can result in a variety of responses that may have important technological applications, spanning electronic and ionic conductivity to piezo- and ferro-electricity.

In 2019, the original monochromator was replaced with an upgraded one of a new design, and this now affords greater beam stability and ease of wavelength change.

The data collection software has also seen substantial work with greater integration of SynchWeb, ISPyB and dials/xia2, but also with local development more relevant to chemical crystallography in terms of optimising sample screening and choice of attenuation to minimise exposure times and subsequent beam damage. Overall, these have led to data collections at 2-4 times faster rates with equally good quality.

Investigating new electrode materials for sodium-ion batteries

Related publication: Wheeler S., Capone I., Day S., Tang C. & Pasta M. Low-Potential Prussian Blue Analogues for Sodium-Ion Batteries: Manganese Hexacyanochromate. *Chem. Mater.* **31**, 2619 (2019). DOI: 10.1021/acs.chemmater.9b00471

Publication keywords: Prussian blue analogues; Sodium-ion batteries

The lithium-ion (Li-ion) battery powers the modern world - our smartphones and other mobile devices, and even electric vehicles. As we transition to low-carbon transport and energy generation, we will rely more heavily on efficient battery technology. However, lithium is a costly and limited resource. In contrast, sodium is cheap and widely available. Sodium-ion batteries offer the prospect of cost-effective, environmentally-benign batteries, but their development will require new materials.

Prussian blue analogues (PBAs) have been identified as potential new battery materials. A team of researchers are investigating a new application for the PBA compound, manganese hexacyanochromate, that can be used as an anode material for sodium-ion batteries. They used the High Resolution Powder Diffraction beamline (I11) to run powder X-ray diffraction (XRD) on several manganese hexacyanochromate samples. XRD can be used to study the crystal structure and composition of materials.

Manganese hexacyanochromate is suited as electrode material in an aqueous electrolyte battery. In these experiments, the scientists dehydrated the samples at several different temperatures, to observe changes in structure and water content. They were able to distinguish water in two bonding environments clearly. They could selectively remove one and not the other by drying at a specified temperature.

These results will help us to understand the structure and composition of the candidate materials, an essential step in developing the efficient batteries of the future.

Prussian blue analogues (PBAs) are a family of materials that have an analogous structure but differ in composition. Their crystal structure (Fig. 1) is cubic and has two distinct transition metal sites, R and P, which are bridged by cyanide ligands. R is bonded to 6 carbons in an octahedral arrangement whereas P is bonded to 6 nitrogens in an octahedral arrangement. P and R can be Fe, Mn, Cr, Co among others, and when substituted the structure remains approximately the same. The PBA open-framework structure can host a number of alkali cations on interstitial sites including sodium and potassium, making them interesting as battery materials[1]. To store charge as an electrode material the transition metals change valence state (e.g. $Fe^{3+} + e^- \rightleftharpoons Fe^{2+}$) and alkali cations insert or are withdrawn from the structure to maintain charge neutrality. The PBA structure is particularly complex because, in addition to the range of composition, there are vacancies and water present within the material (Fig. 1b). These vacancies are the absence of the hexacyanometallate $[R(CN)_6]^{n-}$ complex and the fraction of vacancies can be as high as 1/3. Water molecules take two distinct bonding environments; 'coordinated' bonded to the P site within vacancies and 'interstitial' occupying interstitial sites.

Most PBA compounds researched for application in batteries have Fe in the R site and have reduction potentials (voltage at which the material reacts) that are high and suitable as cathode materials for sodium or potassium-ion batteries. They show excellent performance as cathode materials including exceptional cycle life (number of charge/discharge cycles) and rate capability (time to fully charge or discharge the battery)[2]. However, in the full battery they are coupled to an anode with inferior performance. In this project we are aiming to develop and characterise PBA compounds that have reduction potentials at low voltages that can be used as an anode material in combination with a PBA cathode[3,4]. The full cell voltage is the difference in voltage between the cathode and the anode.

Manganese hexacyanochromate (P = Mn, R = Cr) is a candidate low reduction potential PBA compound. It is easily synthesised in water at room temperature from manganese chloride and potassium hexacyanochromate. X-ray diffraction (XRD) is an essential technique to study the structure and composition of the material. Synchrotron powder XRD (I11) was performed on as-synthesised manganese hexacyanochromate and the model refined against the data using the whole-pattern fitting Reitveld method (Fig. 2). The material had a lattice parameter of 10.803920(13) Å. For the purpose of refinement, water molecules are treated as oxygen atoms only as hydrogen has negligible X-ray scattering. Positions of oxygen in the two bonding environments, coordinated and interstitial, could be distinguished and quantified. The occupancy value for the coordinated water was in good agreement with the hexacyanochromate vacancy fraction of 1/3. For the interstitial water position the refined atomic displacement value was relatively large at 0.19 $Å^2$. This is the case as there is not a single water position within the subcube but instead multiple positions that are indistinguishable by Reitveld refinement. These positions can be water molecules shifted off the centre position due to the presence of hexacyanochromate vacancies at one or more of the subcube corners, and also from hydrogen bonding within the material. Efforts to further refine these positions was unsuccessful.

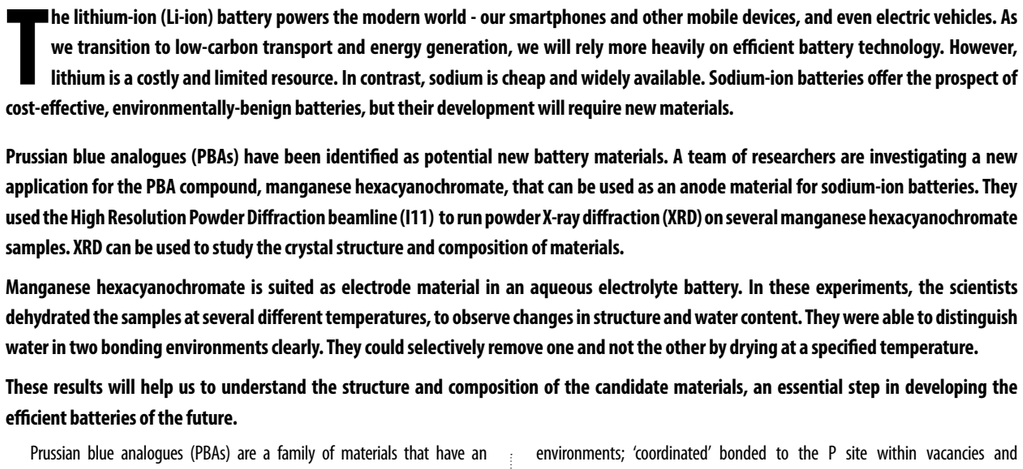

Figure 1: The cubic crystal structure of Prussian blue analogues (PBAs). (a) The crystal structure is composed of two transition metal sites (R and P) bridged by cyanide ligands. Within the open-framework structure are interstitial sites that can host alkali cations. (b) The structure contains hexacyanometallate ($R(CN)_6$) vacancies and type bonding environments for water, bonded to P site metals in vacancies and in interstitial sites.

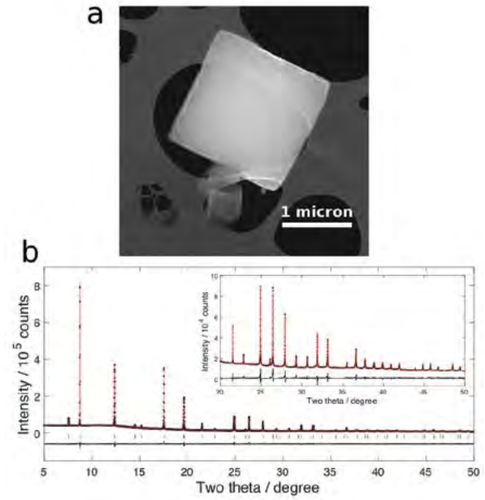

Figure 2: Physiochemical characterisation of manganese hexacyanochromate (P = Mn, R = Cr). (a) Scanning electron micrograph (SEM) and (b) synchrotron powder X-ray diffraction (XRD) of as-synthesised manganese hexacyanochromate (λ = 0.824525 Å). Experimental data (black dots), fitted (red curve) and difference (lower trace) are shown.

There is a significant difference in bonding strength between the two types of water. As the material is heated, the interstitial water, more loosely bound, leaves the material first and the coordinated water, more strongly bound, leaves the material at higher temperature. This was studied using thermal gravimetric analysis differential scanning calorimetry (TGA-DSC) coupled to a mass spectrometer (MS). Drying the material at 80 °C was found to remove most of the interstitial water but left most of the coordinated water. Synchrotron powder XRD found that the lattice parameter decreased to 10.660688(19) Å, a substantial change. Refined values for the quantity of water present show a decrease of 76% in interstitial water and a decrease of 41% in coordinated water. Drying the material at a higher temperature, 150 °C, resulted in a majority of both types of water being removed from the structure.

The electrochemical properties of manganese hexacyanochromate was subsequently characterised (Fig. 3). The material had a reduction potential of -0.86 V vs. SHE (standard hydrogen electrode), the lowest reported for any PBA material, and a specific capacity of 63 mAh g^{-1}. In an aqueous electrolyte the material exhibited extremely fast bulk diffusion of sodium ions, with a

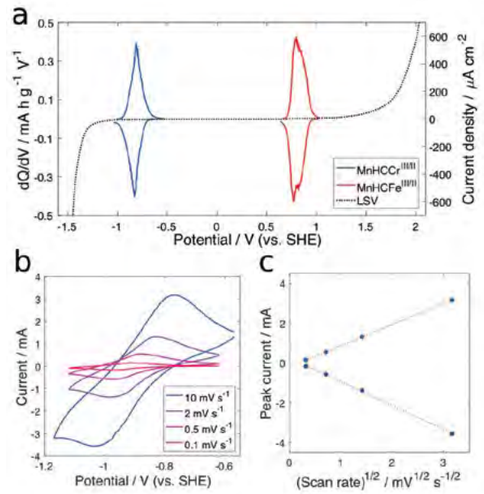

Figure 3: Electrochemical characterisation of manganese hexacyanochromate in an aqueous sodium-ion electrolyte. (a) Differential capacity plot of manganese hexacyanochromate and manganese hexacyanoferrate (for comparison), (b) and (c) cyclic voltammetry at a range of scan rates and peak current against root of scan rate.

calculated diffusion coefficient of 1.9 x10^{-6} $cm^2 s^{-1}$. Characterisation of the charge storage mechanism showed that the crystalline structure was maintained and there was reversible sodium insertion and chromium redox behaviour ($Na_{2/3}Mn^{II}[Cr^{II}(CN)_6]_{2/3} + 2/3Na^+ + 2/3e^- \rightleftharpoons Mn^{II}[Cr^{III}(CN)_6]_{2/3}$).

This study, for the first time, characterises a metal hexacyanochromate as an anode material for batteries. This is important as it identifies metal hexacyanochromates as a subset of PBAs for further investigation and improvement.

PBA materials are extremely diverse due to their wide composition space and number of tuneable parameters. They are also highly crystalline which makes synchrotron XRD an essential characterisation tool.

References:

1. Hurlbutt K. *et al.* Prussian Blue Analogs as Battery Materials. *Joule* **2**, 1950 (2018). DOI: 10.1016/j.joule.2018.07.017
2. Jiang L. *et al.* Building aqueous K-ion batteries for energy storage. *Nat. Energy* **4**, 495 (2019). DOI: 10.1038/s41560-019-0388-0
3. Pasta M. *et al.* Full open-framework batteries for stationary energy storage. *Nat. Commun.* **5**, 3007 (2014). DOI: 10.1038/ncomms4007
4. Firouzi A. *et al.* Monovalent manganese-based anodes and co-solvent electrolyte for stable low-cost high-rate sodium-ion batteries, *Nat. Commun.* **9**, 861 (2018). DOI: 10.1038/s41467-018-03257-1

Funding acknowledgement:
This publication arises from research funded by the John Fell Oxford University Press Research Fund. We acknowledge financial support from the Henry Royce Institute (through UK Engineering and Physical Science Research Council grant no. EP/ R010145/1) for capital equipment. I.C. S.W. acknowledges financial support from EPSRC. We thank Diamond Light Source for access to beamline I11 (proposal number EE14809-1)

Corresponding authors:
Dr Samuel Wheeler, Department of Materials, University of Oxford, samuel.wheeler@materials.ox.ac.uk and Prof Mauro Pasta, Department of Materials, University of Oxford, mauro.pasta@materials.ox.ac.uk

The fate of carbonate subducted into Earth's deep mantle

Related publication: Drewitt J. W. E., Walter M. J., Zhang H., Mcmahon S. C., Edwards D., Heinen B. J., Lord O. T., Anzellini S. & Kleppe A. K. The fate of carbonate in oceanic crust subducted into earth's lower mantle. *Earth Planet. Sci. Lett.* **511**, 213 (2019).
DOI: 10.1016/j.epsl.2019.01.041

Publication keywords: Carbonate; Subduction; Lower mantle; Decarbonation; Diamond formation; X-ray diffraction

The global carbon cycle is key to Earth's habitability, giving our planet a stable and hospitable climate, and an atmosphere relatively low in carbon dioxide. Carbonate can be transported into Earth's interior by subduction, fuelling surface volcanoes. Carbonate minerals may also be transported much deeper into the lower mantle, but what happens to these minerals under such high pressure and temperature conditions is uncertain. Researchers wanted to understand if carbonate remains stable in the lower mantle and if not, what reactions take place and hence what mineral form the carbonate takes.

Investigating the mineralogy of the deep Earth requires reproducing the extreme conditions of the Earth's interior. The team took synthetic carbonate rocks and subjected them to very high pressures (up to 90 GPa) and temperatures (2200 K), using a laser-heated diamond anvil cell. Because crystalline minerals have very specific diffraction pattern 'fingerprints', using synchrotron X-ray diffraction on I15 (the extreme conditions beamline) allowed them to identify precisely which minerals formed.

The results showed a barrier to subduction of carbonated minerals at a depth of 1000–1500 km, halfway to the core-mantle boundary. At these depths, carbonate in a subducted slab reacts with surrounding silica to form silicate minerals and solid carbon dioxide. As the slab temperature increases, the carbon dioxide releases pure carbon, which forms 'super-deep diamonds'. These super-deep diamonds may eventually return to the surface, providing the only direct evidence we have for the composition of Earth's deep interior.

The global carbon cycle is tightly connected to our planet's habitability. Compared to Earth's clement climate and low CO_2 atmosphere, the planet Venus is in a runaway greenhouse state, with high surface temperatures and a thick CO_2 atmosphere. One major difference between the planets is active plate tectonics, which has played a key role in making Earth's environment unique within our solar system. Carbon is transported into Earth's deep interior by subduction of carbonate-rich oceanic crust. Although much of this carbonate is re-released by volcanic activity as carbon dioxide (CO_2) into the atmosphere, the carbon isotope signature of so-called 'super-deep diamonds' and minerology of their inclusions reveal that crustal carbonate can reach the deep mantle[1,2]. Carbon and other volatiles in the deep mantle may promote chemical mass transfer through melting and may potentially have a large influence on the rheological properties of the mantle. However, despite its fundamental importance for understanding the evolution of the Earth, our knowledge of the minerology of carbonated rocks at the high pressure (*P*) and temperature (*T*) conditions of the lower mantle is extremely limited.

To investigate carbonate stability and reactions in the presence of silica (SiO_2), the building block of mantle minerals, synthetic carbonate rocks in the systems FeO-MgO-SiO_2-CO_2 or CaO-MgO-SiO_2-CO_2 were subjected to deep mantle *P-T* conditions of up to 90 GPa (≈ 900,000 atmospheres) and 2200 K using a laser-heated diamond anvil cell (LHDAC) setup at the University of Bristol. Sample compositions were designed to lie on the ternary plane between carbonate and SiO_2. In this way, the system will remain ternary if carbonate is stable, but will be non-ternary if decarbonation occurs. The key advantage of making systems on this ternary plane is that recognition of a decarbonation reaction requires only identification of the presence of non-ternary phases in the quenched run products (e.g. $FeSiO_3$, $CaSiO_3$, diamond, CO_2).

Angle dispersive synchrotron X-ray diffraction (XRD) measurements were made on the *P-T* quenched run products at beamline I15, where reaction products were identified from their crystalline Bragg diffraction peaks. A selection of typical XRD patterns obtained are shown in Fig. 1. At the lowest *P-T* conditions stishovite (SiO_2) and carbonate phases are identified. At *P* beyond ~ 40 to 70 GPa the XRD patterns reveal the formation of $(Mg,Fe)SiO_3$ (bridgmanite) or $CaSiO_3$ (Calcium perovskite) with a complete exhaustion of the carbonate phase. *In situ* confocal micro-Raman spectroscopy measurements on the *T*-quenched samples at high-*P* reveal the appearance of this silicate phase is accompanied by the formation of solid carbon dioxide (CO_2-V phase[3,4]). At *T* above ~ 1900 K diamond is detected in both XRD and Raman measurements of the run products.

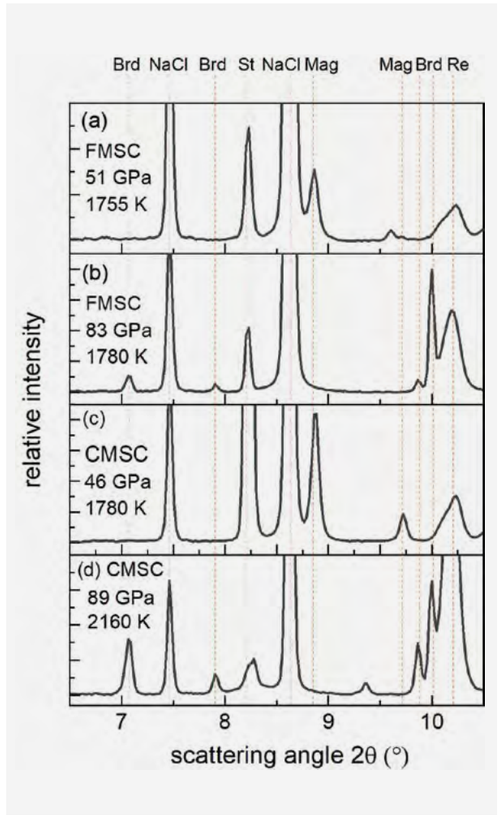

Figure 1: Selected X-ray diffraction patterns for the P-T quenched run products in the FeO-MgO-SiO_2-CO_2 (FMSC) system at (a) 51 GPa, 1755 K and (b) 83 GPa, 1780 K, and CaO-MgO-SiO_2-CO_2 (CMSC) system at (c) 46 GPa, 1780 K and (d) 89 GPa, 2160 K. The diffraction lines are labelled according to identified phases; Brd = bridgmanite, St = stishovite, Mag = magnesite, as well as the NaCl thermal insulation and Re gasket.

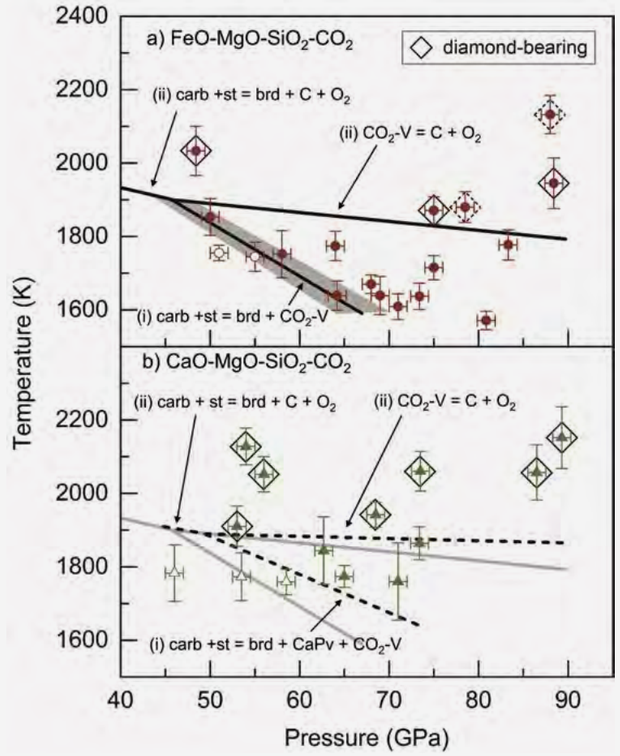

Figure 2: Pressure-temperature plots showing the decarbonation reaction boundaries in the systems (a) FeO-MgO-SiO_2-CO_2 (black lines) and (b) CaO-MgO-SiO_2-CO_2 (dashed lines with boundaries from (a) in grey). Open symbols denote experiments where carbonate and silica are stable. Filled symbols denote experiments where non-ternary phases formed in decarbonation reactions as labelled. Diamond symbols indicate the presence of diamond. Broken diamonds denote run products where the presence of diamond remains ambiguous. carb = carbonate; st = stishovite (SiO_2); brd = bridgmanite; CaPv = calcium perovskite.

The experimental results across the full *P-T* range shown in Fig. 2 reveal three general reactions common to both Fe- and Ca-bearing systems. Reaction boundary (i) with a negative Clapeyron slope is the breakdown of carbonate in the presence of SiO_2 to form bridgmanite ± Ca-perovskite + CO_2-V. Decarbonation reaction (ii) involves the formation of C (diamond) + O_2 directly from reaction of carbonate with SiO_2. Reaction (iii) is the breakdown of CO_2 formed in reaction (i) to diamond + O_2.

Seismic tomography surveys indicate that most subducting slabs eventually sink to the base of the mantle and reside there over long geological time-scales. This research reveals that these regions will be free from carbonate, since the carbonate phase cannot be transported to depths greater than 1500 km (halfway to the core-mantle boundary). At these depths, CO_2 will be released into the subducted slab in the form of its solid CO_2-V phase, where carbon and oxygen atoms are arranged in CO_4 tetrahedral units linked by oxygen atoms at each corner[5]. This is a structure very similar to that of silica suggesting the distinct possibility of rock-forming minerals consisting of solid CO_2 deep within Earth's lower mantle. However, as the temperature of the typically cooler subducting slab rises as it equilibrates with the ambient mantle at these depths, the CO_2 dissociates to form diamond, releasing oxygen into a nominally oxygen deficient lower mantle in the process. The ultimate fate of carbonate in the lower mantle therefore is diamond, which may be stored in the deep Earth over geological time-scales representing a long-term sink of carbon before eventually returning to the surface via upwelling mantle plumes. This process could represent one of the sources of super-deep diamonds found at the surface, providing the only direct evidence for the composition of the deep Earth.

References:

1. Walter M. J. *et al.* Primary carbonatite melt from deeply subducted oceanic crust. *Nature* **454**, 622–625 (2008). DOI: 10.1038/nature07132
2. Walter M. J. *et al.* Deep Mantle Cycling of Oceanic Crust: Evidence from Diamonds and Their Mineral Inclusions. *Science* **15**, 1209300 (2011). DOI: 10.1126/science.1209300
3. Litasov K. D. *et al.* Crossover from melting to dissociation of CO_2 under pressure: Implications for the lower mantle. *Earth Planet. Sci. Lett.* **309** 318–323 (2011). DOI: 10.1016/j.epsl.2011.07.006
4. Santoro M. *et al.* Partially collapsed cristobalite structure in the non molecular phase V in CO_2. *PNAS* (2012). DOI: 10.1073/pnas.1118791109
5. Datchi F. *et al.* Structure of Polymeric Carbon Dioxide CO_2-V. *Phys. Rev. Lett.* **108**, 125701 (2012). DOI: 10.1103/PhysRevLett.108.125701

Funding acknowledgement:
This work was funded by NERC grant NE/M000419/1 to M. J. Walter.

Corresponding author:
Dr James Drewitt, University of Bristol, james.drewitt@bristol.ac.uk

How nanoparticles influence their liquid environment

Related publication: Thomä S. L. J., Krauss S. W., Eckardt M., Chater P. & Zobel M. Atomic insight into hydration shells around facetted nanoparticles**.** *Nat. Commun.* **10**, 995 (2019). DOI: 10.1038/s41467-019-09007-1

Publication keywords: Pair distribution function (PDF); Hydration shell; Iron oxide nanoparticle; Liquid layering

There are many applications for nanoparticles in liquid suspensions, including cosmetic products, industrial catalysts and the contrast agents used in some medical imaging techniques. Previous research has shown that in these suspensions, liquid molecules group themselves around a nanoparticle like a shell. These "solvation shells" (or "hydration shells") were known to have from three to five layers, but were not fully understood. A research team from the University of Bayreuth in Germany used Diamond's I15-1 X-ray Pair Distribution Function (XPDF) beamline to take a closer look at the atomic and molecular structures of the layers.

Their research focused on magnetic nanoparticles, widely used for targeted drug release and magnetic resonance imaging (MRI). Using the pair distribution function (PDF) technique, they were able to precisely determine the relationships between magnetic nanoparticles and the surrounding liquid, down to the atomic level. Their results show that the crystalline structure of the nanoparticle has a significant influence on how nearby water molecules realign themselves. It has become clear that water molecules adhere to nanoparticles through dissociative bonds in some cases and molecular adsorption in others.

The knowledge gained could help to improve the self-assembly of nanoparticles and drive the understanding of nanoparticles with the environment.

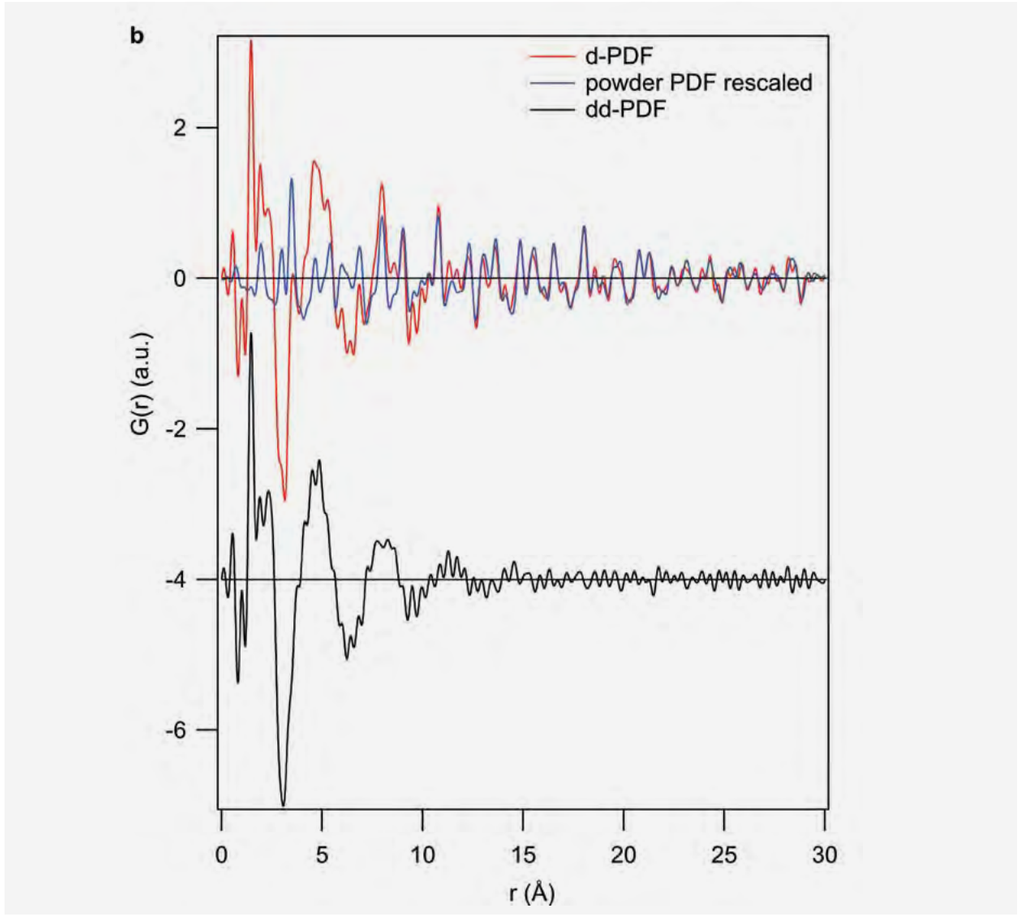

Figure 1: Extraction of hydration shell signal from experimental data: the PDF of the arginine-capped nanoparticle powder (blue) is scaled to the difference PDF (d-PDF, red) of the dispersion and bulk water in the range of 15–30 Å as only iron oxide nanoparticle peaks are present there. The hydration shell (black, in offset) remains and contains the structural information of the molecular arrangement of the water molecules around the iron oxide nanoparticles.

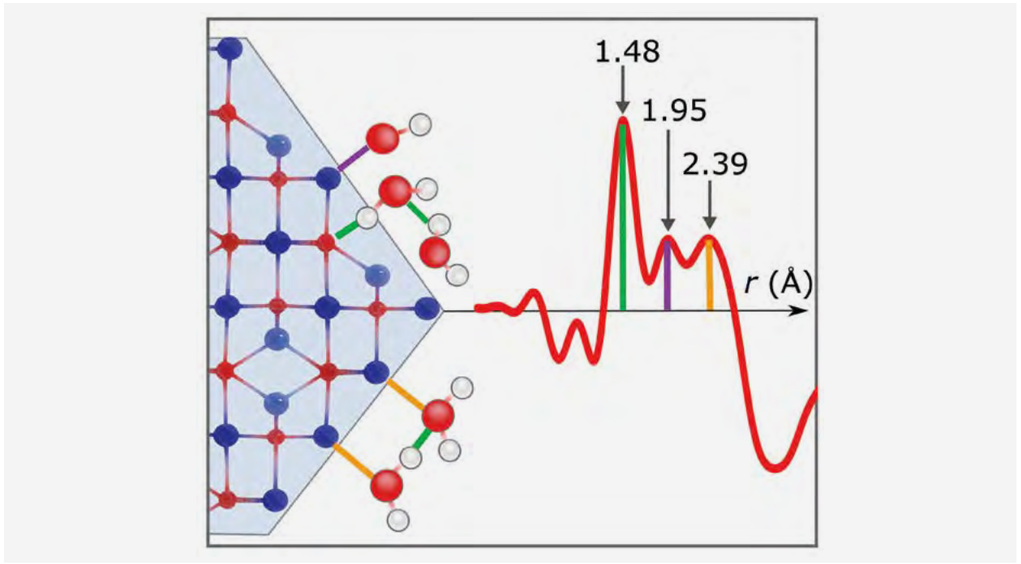

Figure 2: Schematic of two facets of iron oxide nanoparticle with dissociatively and molecularly adsorbed water molecules, together with experimental signal from hydration shell. Oxygen atoms are red, hydrogen white, Fe_{oct} dark blue and Fe_{tet} light blue. Bonds resulting in the peaks at 1.48, 1.95 and 2.39 Å are highlighted with solid lines in green, purple and yellow, respectively.

Nanoparticles in solution interact with their surroundings via hydration shells. Although the structure of these shells is used to explain nanoscopic properties, experimental structural insight is still missing. Water molecules are known to adsorb molecularly and dissociatively at surfaces of iron oxides. Now, for the first time, we could show with pair distribution function (PDF) experiments on aqueous dispersions of iron oxide nanoparticles that the water molecules adsorb and reorient at the particle surface. To our surprise, hydration shells around 7 and 15 nm sized magnetic iron oxide nanoparticles are comparable to shells on planar interfaces. The small organic capping agents used for particle stabilisation do not show a major impact on the water restructuring, whereas the interfacial structure is mainly dominated by the crystallinity of the particles. Individual interatomic distances of molecularly and dissociatively adsorbed water molecules directly at the particle surface could be identified, as predicted by theory[1,2].

During the experiment at beamline I15-1, we collected X-ray diffraction data of various sets of functionalised iron oxide nanoparticles, bulk water and a dispersion of the nanoparticles at ca. 0.3–0.5 weight %. The nanoparticles were synthesised via coprecipitation in basic solution at elevated temperature and functionalised with 13 different small organic capping agents at the end of the synthesis. The capping agents comprised dibutanoic acids, benzoic acids, basic amino acids, small α-hydroxy acids and some other bifunctional molecules. Stability of the dispersions has been confirmed with small angle X-ray scattering and zeta potential (surface charge) measurements. The zeta potential reflects the electrostatic repulsion between particles in the dispersion and the higher the modulus of its value, the better the colloidal stability. The nanoparticle size and faceting were determined with transmission electron microscopy. Thermogravimetric analysis showed that at least half of the particle surface was not covered and thus interacting with water.

In order to access the hydration shell signal, the scattering contribution from the bulk water and the dry nanoparticle powder were subtracted from the dispersion signal, see Fig. 1. The resulting double-difference PDF (dd-PDF) thus only contains information about the interfacial water structure which is different from the bulk water. The looser bound water layers at distances >3 Å create a sinusoidal oscillation with a wavelength of ca. 3 Å, in agreement with molecular dynamics simulations of water around hematite nanoparticles[3]. For distances <3 Å, three distinct peaks could be identified at 1.48, 1.95 and 2.39 Å, which correspond to different conformations of molecularly and dissociatively adsorbed water molecules, as predicted by density functional theory for water at magnetite facets[1,2]. Fig. 2 illustrates this first adsorbed layer and a more detailed discussion of the allocation of interatomic distances is found in the original publication.

In conclusion, this study provides a method of investigating the interfacial hydration structure around colloidal nanoparticles. The effects of edges and corners are expected to be significant only for even smaller particle diameters than the 7 nm investigated here. The size of the organic capping agents had minimal impact on the hydration shell structure, while the impact of concentration remains to be determined. This X-ray scattering based method of elucidating hydration shell structures bridges the structural gap between spectroscopy and theory.

References

1. Zhou C. *et al.* Density functional theory study of water dissociative chemisorption on the Fe_3O_4(111) surface. *J. Phys. Chem. C* **114**, 21405 (2010). DOI: 10.1021/jp105040v
2. Li X *et al*. Adsorption of water on the Fe_3O_4(111) surface: structures, stabilities, and vibrational properties studied by density functional theory. *J. Phys. Chem. C* **120**, 1056 (2016). DOI: 10.1021/acs.jpcc.5b10560
3. Spagnoli D. *et al.* Prediction of the effects of size and morphology on the structure of water around hematite. *Geochim. Cosmochim. Acta* **73**, 4023 (2009). DOI: 10.1016/j.gca.2009.04.005

Funding acknowledgement:
Deutsche Forschungsgemeinschaft (DFG, German Research Foundation) via SFB 840, scholarship of the Bavarian Academy of Sciences and Humanities; Bavarian Polymer Institute (BPI) for access to the keylabs 'Electron and Optical Microscopy' and 'Mesoscale Characterization: Scattering Techniques', Diamond Light Source for beamtime (EE17345–1).

Corresponding author:
Prof Mirijam Zobel, University of Bayreuth, Mirijam.Zobel@uni-bayreuth.de

The first nanocage with antiaromatic walls

Related publication: Yamashina M., Tanaka Y., Lavendomme R., Ronson T. K., Pittelkow M. & Nitschke J. R. An antiaromatic-walled nanospace. *Nature* **574**, 511 (2019). DOI: 10.1038/s41586-019-1661-x

Publication keywords: Supramolecular cage; Self-assembly; Antiaromaticity; Host-guest

Nanocages are complex, functional structures with nanometre-sized cavities. They already have a range of applications in chemistry, medicine and environmental science. Researchers have been working with large molecules with an inner cavity that can host a smaller 'guest' molecule. The nature of the host can modify the properties of the guest molecule – for example, neutralising a toxic compound. Although a wide range of molecular hosts have been investigated, until now none were made using 'antiaromatic' subunits, which are unusually unstable and difficult to isolate.

Researchers working in the Nitschke group at the University of Cambridge synthesised a host species from antiaromatic compounds in order to study the properties of guests nesting inside the unusual nanospace.

Using X-ray crystallography on the Small Molecule Single Crystal Diffraction beamline I19, they were able to determine the structure of the new host. Their work demonstrated the construction of an anti-aromatic-walled nanospace, the first of its kind, within a self-assembled nanocage, and the magnetic effects on guests nesting inside this nanospace. The experimental results agreed with theoretical models.

As this study describes the first host of its kind, more work is needed before we fully understand their potential applications.

Hollow molecular hosts can encapsulate smaller guests. These guest molecules can exhibit unusual reactivity and properties, in accordance with the properties of the "walls" that form the internal space[1]. Since the first report of a self-assembled nanocage held together using metal-ion coordination and capable of binding diverse guests in 1995[2], many research groups have reported molecular hosts having different sizes, shapes, and volumes.

The nanocages reported so far mostly have walls made up of aromatic molecules (e.g. single benzene rings, and multiple such rings fused together). Nanocages with antiaromatic (a cyclic molecule with 4n π electrons that is highly reactive and unstable) walls should have different properties to those of nanocages with aromatic walls. The magnetic properties of a nanospace with antiaromatic walls were hypothesised to be particularly intriguing, as antiaromaticity is predicted to enhance the local magnetic field inside the nanocage. Such an antiaromatic-walled nanospace has not been reported, and therefore their properties have never been experimentally clarified.

To utilise antiaromatic compounds as building blocks for nanocage construction, certain properties are desireable: (i) high stability, (ii) high symmetry, (iii) strong antiaromaticity, (iv) small molecular size but large antiaromatic surface, and (v) facile synthesis and functionalisation. In order to construct an antiaromatic-walled nanospace, Ni^{II}-dimesitylnorcorrole, first reported in 2012[3], was chosen as an antiaromatic porphyrin-like molecule. This norcorrole is a suitable building block for the construction of an antiaromatic-walled nanospace because it fully satisfies these requirements.

A di(aniline)-based subcomponent (Fig.1a) was synthesised from Ni^{II}-dimesitylnorcorrole in three steps. Then the antiaromatic cage was constructed using subcomponent self-assembly[4]. Di(aniline)-based subcomponent (6 equiv.), 2-formylpyridine (12 equiv.) and Fe^{II} bis(trifluoromethanesulfonyl) imide (NTf_2^-) (4 equiv.) were mixed in CH_3CN, resulting in the quantitative formation of the Fe_4L_6 cage as the uniquely observed product (Fig.1a).

Characterisation was carried out by nuclear magnetic resonance (NMR) spectroscopy, mass spectrometry (MS), and single crystal X-ray diffraction analyses. In organic chemistry, NMR and MS techniques are generally powerful tools for investigating chemical structures. However, these analyses are not sufficient for large and complicated compounds such as supramolecular cages since it is quite difficult to see their three-dimensional structural details. Single crystal X-ray diffraction analysis is the only way to determine their structure

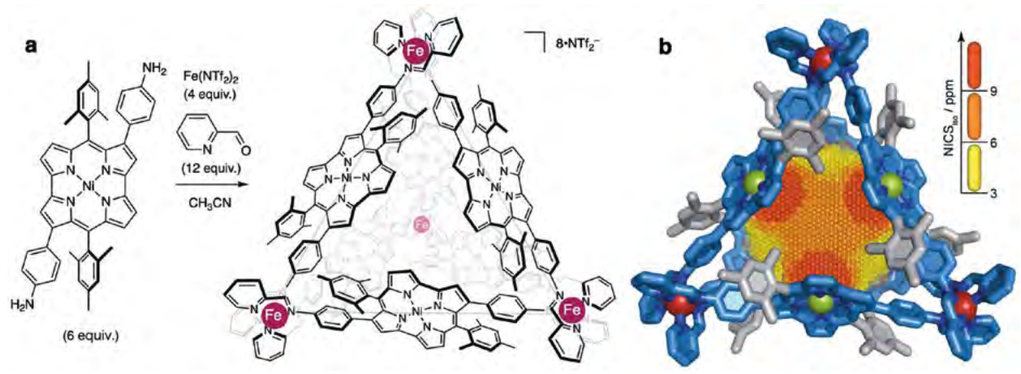

Figure 1: Chemical structure of an antiaromatic-walled nanospace; (a) construction of antiaromatic-walled nanospace. (b) X-ray crystal structure with a 3D NICS grid, showing magnetic deshielding experienced within the nanospace. Antiaromaticity effects becomes stronger in the order of yellow < orange < red color.

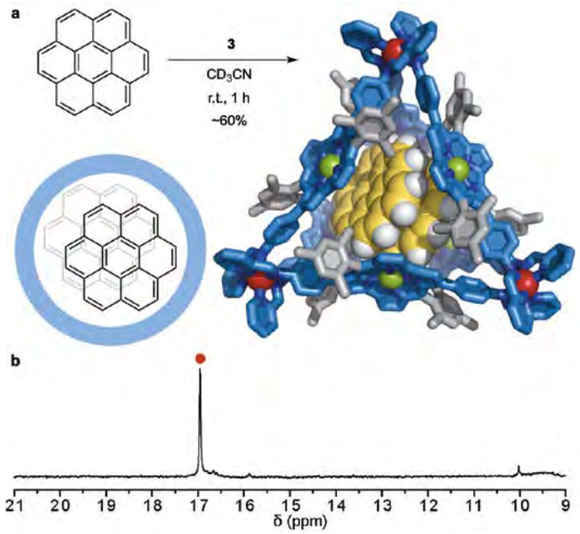

Figure 2: Host-guest study with antiaromatic nanocage; (a) Encapsulation of coronenes and an MM3-optimised structure of host-guest complex. (b) Partial 1H NMR spectrum of encapsulated coronene, showing a signal for the encapsulated guests in the downfield region.

precisely. When using our in-house diffractometer, structural refinement of the supramolecular cage reported in this study was not feasible, owing to the large size of the molecular cage (molecular weight = 8080.88 g/mol) containing large voids with disordered solvent molecules and counteranions.

Single crystal X-ray diffraction at the I19 beamline at Diamond Light Source was used to obtain unambiguous evidence for the formation of the supramolecular cage. According to the result from the I19 beamline, six ligands bridge four octahedral Fe^{II} centres to provide a *T*-symmetric tetrahedral cage having four apertures of ~3.3 Å on the faces. All Fe^{II} centres in each tetrahedron have the same Δ (right-handed) or Λ (left-handed) chiral configurations (Fig.1b). The metal–metal distances are 21.9 Å for Fe...Fe and 14.6 Å between Ni...Ni antipodes. Each norcorrole wall displays a 165.4(3)° bend inwards. As a result of this bending, the face aperture sizes are minimised via stacking between mesityl groups and the neighboring norcorrole edges in the crystal. The cavity volume for the X-ray crystal structure was estimated using the PLATON program to be 1150 $Å^3$, which is a suitable size for the encapsulation of organic molecules.

To investigate the extent of the antiaromaticity experienced within the void volume of cage, nucleus-independent chemical shift (NICS) calculations were carried out based on the X-ray crystal structure. The three-dimensional $NICS_{iso}$ grid of the cage revealed an enhanced antiaromaticity-induced magnetic field within the cavity (Fig.1b). The calculated NICS values around the centroid within the cage were consistently high, and the value at the centroid of the cage became approximately six times larger than the corresponding point above an unassembled norcorrole panel. This result indicates that the six norcorrole walls have an additive effect on the antiaromaticity experienced within the nanospace.

Host–guest studies were conducted to investigate experimentally the effect of guest binding within the antiaromatic-walled cavity of the cage. In the ^1H NMR spectrum, remarkably, the signal of encapsulated coronene was shifted downfield by 8.1 ppm compared to the free guest (Fig.2), as a result of the antiaromatic deshielding effect from the surrounding norcorrole walls. Similarly, six other polyaromatic molecules (e.g., a functionalised fullerene and a carbon nanobelt[5]) (Fig. 3) were successfully encapsulated within the nanospace, with chemical shift values moved up to 15 ppm downfield from their free values. This shift of 15 ppm from that of the free guest is the largest ^1H NMR chemical shift displacement resulting from an antiaromatic environment observed so far.

This cage may thus be considered as a new type of NMR shift reagent, moving guest signals well beyond the usual NMR frequency range and opening the way to further probing the effects of an antiaromatic environment on a nanospace.

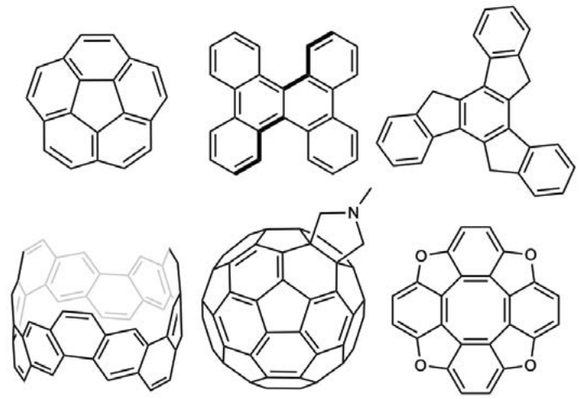

Figure 3: Molecules observed to bind within the nanocage.

References:

1. Cook T.R. *et al.* Metal-organic frameworks and self-assembled supramolecular coordination complexes: comparing and contrasting the design, synthesis, and functionality of metal-organic materials. *Chem Rev.* **113**, 734-77 (2013). DOI: 10.1021/cr3002824
2. Fujita M. *et al.*, Self-assembly of ten molecules into nanometre-sized organic host frameworks. *Nature* **378**, 469–471 (1995). DOI: 10.1038/378469a0
3. Ito, T. *et al.*, Gram-scale synthesis of nickel(II) norcorrole: the smallest antiaromatic porphyrinoid. *Angew. Chem. Int. Ed.* **51**, 8542-8545 (2012). DOI: 10.1002/anie.201204395
4. Zhang, D. *et al.*, Functional capsules via subcomponent self-assembly. *Acc. Chem. Res.* **51,** 2423-2436 (2018). DOI: 10.1021/acs.accounts.8b00303
5. Povie, G. *et al.*, Synthesis of a carbon nanobelt. *Science* **356**, 172-175 (2017) DOI: 10.1126/science.aam8158

Funding acknowledgement:

European Research Council (695009); UK Engineering and Physical Sciences Research Council (EPSRC, EP/P027067/1); Japan Society for the Promotion of Science (JSPS) for an Overseas Research Fellowship; Fondation Wiener-Anspach postdoctoral fellowship; Danish Council for Independent Research (DFF 4181-00206).

Corresponding author:

Prof Jonathan R. Nitschke, University of Cambridge, jrn34@cam.ac.uk

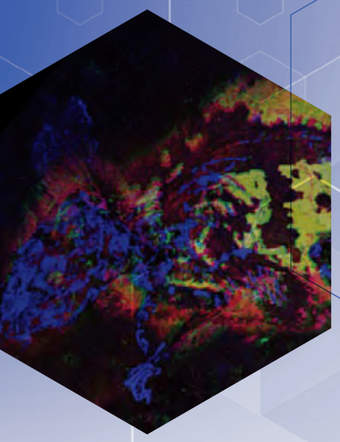

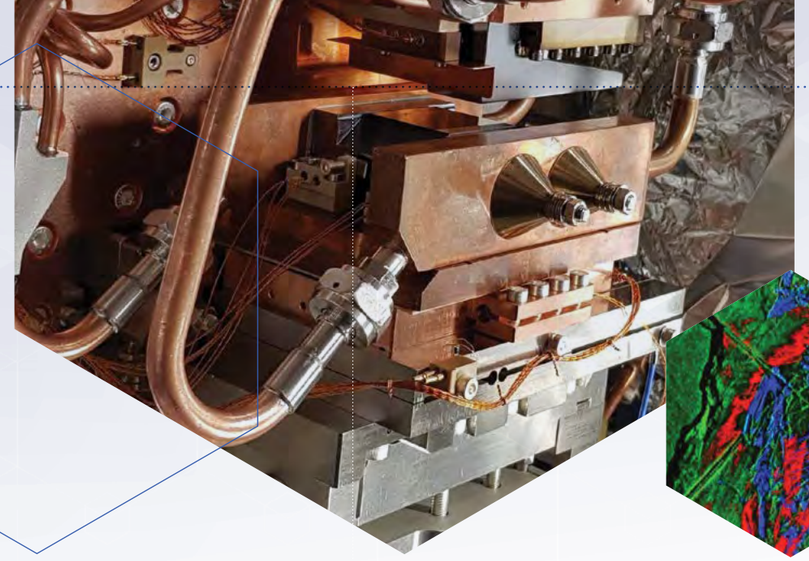

Spectroscopy Group

Sofia Díaz-Moreno, Science Group Leader

The Diamond Spectroscopy Group consists of four beamlines; the Microfocus Spectroscopy beamline (I18), the Core EXAFS beamline (B18), and the two independently operating branches of the Versatile X-ray Absorption Spectroscopy beamline (I20-Scanning and I20-EDE). These four spectrometers are complementary in the energy ranges they cover, the size of their focussed beam spots delivered to the sample and the time resolutions they are able to reach. This complementarity means that they can support research across many different scientific disciplines, from chemistry and catalysis through to materials science, condensed matter physics, environmental and life science, energy materials and cultural heritage.

Many technical developments have been implemented on the spectroscopy beamlines over the last year, aimed at improving the operational efficiency. Specific achievements include the integration of faster detectors and optimising the data collection and processing chains, and the implementation of automatic procedures to reduce experimental setup times. Additionally, new sample environment equipment for the study of energy materials has also been added to the beamline inventories, such as the multichannel potentiostat for B18.

I18 update

The Microfocus Spectroscopy beamline, I18, uses a finely focused X-ray beam to investigate heterogeneous materials on the micrometre scale using a variety of techniques, such as X-ray Fluorescence (XRF) mapping, X-ray Absorption Spectroscopy (XAS) and X-ray Diffraction (XRD).

In recent years, new techniques that required the processing of large amounts of data, such as fluorescence and diffraction computed tomography (CT) have been added to the techniques offered at I18. This has been possible thanks to advances in beamline data collection, both in software and hardware, enabling faster and more efficient measurements. These improvements include the development and implementation of the Diamond mapping project, a development to ease the use of fly scanning for 2D data collection, as well as the procurement and integration of the fast Excalibur detector used for XRD. In addition, the procurement of a second Vortex ME-4 energy resolving detector fitted with Cube pre-amplifiers allowed even faster collection rates for XRF and XAS measurements, as it can be used side by side with the existing unit.

These developments have been accompanied by improvements in the on-line data processing, so preliminary results can now be visualised within few minutes of the data collection. Currently it is possible to do full XRF and/or XRD CT reconstructions with a fully automated processing chain which starts immediately after the data is collected, and that requires no manual input. This makes the beamline ready for the future developments planned for 2020 that will further increase data collection speeds, such as the new sample stages. The stages have already been purchased and will become available in the second half of the year.

B18 update

The Core EXAFS beamline, B18, is optimised for the efficient collection of XAS data over all elements heavier than phosphorous. The focussing optics and the capability of the monochromator for continuous scanning, together with a flexible experimental space that supports a large range of sample environments, make this beamline ideal to perform experiments under *in situ* and *operando* conditions for catalysis and energy materials research. The latter science area has seen a substantial increase in the number of experiments performed in the last year. The intrinsic ability of XAS to provide element-specific, local and symmetry-selective information enables the elucidation of the mechanisms associated with mobile ion uptake and release during battery cycling. In response to this increased level of interest in this science area, a multi-channel potentiostat has been purchased for the beamline, and work is now progressing for the full integration of this system within the beamline data acquisition system. It is expected that the instrument will become available for the spectroscopy users for the second part of 2020.

The capabilities for fluorescence measurements in B18 have been enhanced by the upgrading of the von Hamos dispersive emission spectrometer to a four crystal cylindrical geometry from the initial one crystal prototype. The spectrometer is equipped with two interchangeable four-element Medipix position sensitive detectors and has been successfully used for three experiments during the last year, including a very demanding *in situ* catalysis study. Further efforts are being concentrated on making the system more user-friendly, including the data analysis pipeline.

The last year has also seen the integration of additional techniques at B18 that are complementary to XAS, such as the implementation of back-reflection energy-dispersive X-ray diffraction (EDXRD) with soft/tender X-rays in collaboration with the University of Leicester. This technique takes advantage of the broad energy range covered by the beamline, and has significant advantages in that it is a non-destructive technique and does not require any specific sample preparation. This makes the methodology ideal for applications in culture heritage, palaeontology and conservation science. The first experiments have shown the potential of this method, and regular access to B18 has now been granted for the next two years to develop the technique further.

I20-Scanning update

The Scanning branch of I20, I20-Scanning, exploits the high flux provided by the wiggler source through two different end stations. The XAS end station uses a 64 element monolithic germanium detector with the Xspress-4 read-out system to examine the structure of very low concentration samples. The X-ray Emission Spectroscopy (XES) end station uses a spectrometer based on a 1 m Rowland circle geometry to perform high-energy resolution studies of the electronic structure of samples.

A new first crystal cage with a wider first crystal for the four-bounce monochromator was installed in March 2019. The larger crystal shows no strain effects from clamping and gives a better beam profile than the previous crystal cage. This has enabled the closure of the wiggler gap for higher energy experiments, increasing significantly the available monochromatic flux. This upgrade will enhance the beamlines' capability in many scientific areas, such as the radionuclide research studies on novel uranium speciation under environmental conditions that is presented in this report.

This last year several experiments at cryogenic temperatures have been performed in the XES end station, either because the experiments required measurements at variable temperature, or to slow down the radiation damage that the high intensity beam at I20-Scanning often causes in sensitive samples during data collection. Some of these experiments have used the low profile closed cycle cryostat available at the beamline and that is specifically designed to fit in the limited space available in the XES end station. The liquid helium cryostat available in I18 has also been used as samples can be loaded into it under cryogenic conditions and this enables studies of short-lived species isolated from solution reactions.

I20-EDE update

The Energy Dispersive EXAFS (EDE) branch of I20 uses a polychromator to perform XAS experiments in a dispersive geometry. It is designed for *in situ* and *operando* studies with time resolutions ranging from seconds down to milliseconds or even microseconds. Many different sample environments are available at the beamline as illustrated in the scientific highlight on multimodal studies presented in this report.

The efficiency and usability of the beamline has been improved by several developments. The introduction of beampipes that can be moved in and out of the beam remotely to reduce air absorption when working at low energies is necessary when optimising the beamline optics and checking energy calibration. Eliminating the manual exchange of pipes has reduced beamline setup time substantially. In addition, an automatic filling system has been installed for the liquid nitrogen cooled XH detector, that has removed the need for manual intervention on a daily basis. Lastly, improvements in data quality have been made by developing a sample spinning system such that samples in a tube furnace can be spun in the beam path to present a more homogeneous sample to the beam.

Community support and development

Aside from supporting the beamlines and the operational science programme, the Spectroscopy Group has continued its efforts to support the development of the spectroscopy user community through running workshops covering best practice for the analysis of XRF and XAS data.

A two-day workshop on X-ray Fluorescence Analysis was organised by the Spectroscopy Group for the first time in November 2019. This event focused on the use of PyMca, a versatile software package for the analysis of X-ray Fluorescence (XRF) data, and was delivered by A. Sole (ESRF), the main developer of the code. In March this year the group organised the annual three-day X-ray Absorption Spectroscopy workshop, covering a brief introduction to the spectroscopy beamlines at Diamond, as well as methods to process and analyse spectroscopy data. As was the case in previous years, the workshop was in high demand, with more than 150 applications.

Diamond, through the Spectroscopy Group, together with Newcastle University, are the principal partners of the COllaborative NEtwork for X-ray Spectroscopy (CONEXS), an EPSRC funded network that aims to bring together experimentalists and theoreticians who are working in the area of X-ray spectroscopy to improve their ability to fully exploit and interpret experimental data. As part of the activities of the network, a Summer School was organised in September 2019, and an International Conference 'CONEXS 2020: Emerging Trends in X-ray Spectroscopy' was held in February 2020. Both events were very well attended.

Nanoengineering a fully reversible multielectron cathode for lithium-ion batteries

Related publication: Rana J., Shi Y., Zuba M. J., Wiaderek K. M., Feng J., Zhou H., Ding J., Wu T., Cibin G., Balasubramanian M., Omenya F., Chernova N. A., Chapman K. W., Whittingham M. S. & Piper L. F. J. Role of disorder in limiting the true multi-electron redox in ε-LiVOPO$_4$. *J. Mater. Chem. A* **6**, 20669 (2018). DOI: 10.1039/C8TA06469E

Publication keywords: Photocatalyst; Metal oxide; X-ray Photoelectron Spectroscopy; Electronic structure

Electric vehicles (EV) are expected to replace the internal combustion engine by 2050. Despite impressive progress over the last decade, several technological hurdles still need to be overcome to make EVs practical and economical. One of the major challenges to the EV industry is the driving range, which is dictated by the energy density of the battery pack. This, in turn, is governed by the number of electrons that can be exchanged per transition-metal (TM) cation in the cathode materials. Currently, the state-of-the-art cathode materials used in EV, such as the Tesla Model 3 battery pack, exchange less than one electron per TM cation.

One strategy being explored to improve energy density is to use intercalated ('doped') compounds capable of multiple electron transfer per TM cation. Vanadyl phosphates (VOPO$_4$) are an appealing class of compounds, since they offer two-electron exchange within the voltage window safe and suitable for EV applications.

Researchers used core X-ray Absorption Spectroscopy (XAS) at beamline B18 to directly monitor the vanadium oxidation state of ε-VOPO$_4$. This technique was vital for identifying side reactions promoted by high energy ball milling-induced disorder and defects and for identifying a path to realising fully reversible two lithium ion intercalation.

The results demonstrate that realising full two lithium intercalation in ε-VOPO$_4$ requires the consideration of different kinetics and reaction pathways associated with multielectron reactions. In addition, parasitic side reactions associated with electrolyte degradation can complicate the analysis of the electrochemistry.

Realising full two lithium intercalation in ε-VOPO$_4$ requires the consideration of different kinetics and reaction pathways associated with multielectron reactions[1].

The two-electron exchange in vanadyl phosphates (VOPO$_4$) involve V^{5+}/V^{4+} and V^{4+}/V^{3+} redox reactions (Fig. 1). Various polymorphs of VOPO$_4$ exist but the epsilon (ε) phase is considered to be the most promising for full reversible two lithium ion intercalation. The insertion of Li^+ into ε-LiVOPO$_4$ (V^{4+}/V^{3+} redox at ~2.5V vs. Li/Li^+) during discharge is kinetically favored over the extraction of Li^+ from ε-LiVOPO$_4$ (V^{5+}/V^{4+} redox at ~4.0V vs. Li/Li^+) during charge[2].

As a result, overcoming the kinetic limitations of the high-voltage region was critical for realising full two lithium ion intercalation in ε-VOPO$_4$. Reducing the Li-ion diffusion pathways can reduce the kinetic barriers of high-voltage region. High-energy ball milling is an essential step in the synthesis to obtain materials with finer particles. However, increased ball milling deteriorated the electrochemical performance of our cathodes[3]. Our operando XAS measurements revealed the lack of evolution of vanadium oxidation state despite significant capacity during charge, which clearly indicated that side reactions were promoted by the high-energy ball milling[4].

To investigate how the ball milling was further hindering the already sluggish kinetics and promoting side reactions, rate dependent XAS studies were performed at beamline B18 of Diamond Light Source. Tracking of vanadium oxidation state in the ε-LiVOPO$_4$ electrodes lithiated/delithiated at different rates revealed the expected reduction of V^{4+} to V^{3+} upon inserting the second lithium ion into ε-LiVOPO$_4$ and subsequent oxidation of V^{3+} back to V^{4+} upon its extraction, irrespective of rate[4]. In contrast, the extraction of Li^+ from ε-LiVOPO$_4$ was found to be sluggish as the oxidation of V^{4+} to V^{5+} increased at slower rates (Fig. 2). Yet, even at the slowest cycling rate of C/100

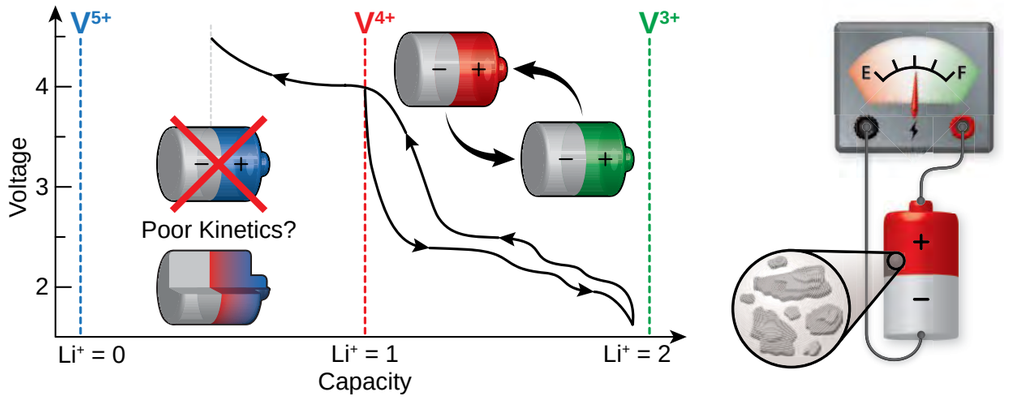

Figure 1: Schematic illustration of the voltage profiles of ε-VOPO$_4$ indicating poor kinetics of the high-voltage region caused by high energy ball milling-induced disorder/defects.

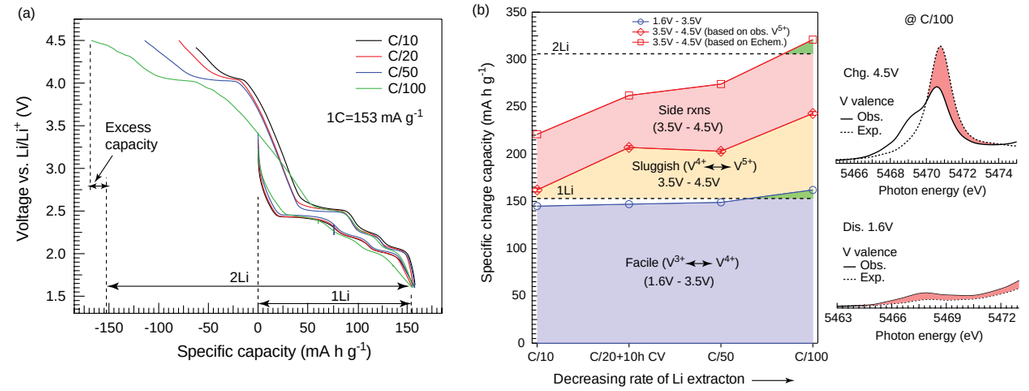

Figure 2: (a) voltage profiles of ε-LiVOPO$_4$ at different cycling rates and (b) sluggish kinetics of the high-voltage region giving rise to side reaction contributions at all rates. Reproduced from [4].

(which exceeded the theoretical capacity for two Li^+ extraction) only half of the vanadium was oxidised to the expected V^{5+}. Quantitative analysis of the XAS data further revealed a significant portion of the capacity arose from side reactions during charge in the high-voltage region at all rates. These data demonstrate the kinetic limitations imposed by ball milling-induced disorder and/or defects that ultimately trigger detrimental side reactions and hinder full $V^{4+/5+}$ redox.

Prompted by this finding our recent work employed hydrothermally synthesised (i.e. ball milling-free approach) ε-VOPO$_4$ with highly crystalline nanosized particles, which demonstrated reversible full 2Li intercalation without any indication of side reactions[5]. This research was awarded a Ten at Ten Scientific Ideas award by the U.S. Department of Energy.

Future efforts are dedicated to further improve rate-capabilities and minimise the voltage gap between the high-voltage and low-voltage plateaus through chemical substitutions of nanoengineered ε-VOPO$_4$. In summary, the present research reiterates the need for synchrotron studies in battery research to identify detrimental side reactions in multielectron cathodes, which would otherwise remain elusive based on the electrochemical characterisation alone.

References:

1. Lin Y.-C. *et al.* Thermodynamics, Kinetics and Structural Evolution of ε-LiVOPO$_4$ over Multiple Lithium Intercalation. *Chem. Mater.* **28**, 1794-1805 (2016). DOI: 10.1021/acs.chemmater.5b04880
2. Wangoh L. W. *et al*. Uniform second Li ion intercalation in solid state ε -LiVOPO$_4$. *Appl. Phys. Lett.* **109**, 053904 (2016). DOI: 10.1063/1.4960452
3. Shi Y. *et al*. Electrochemical Performance of Nanosized Disordered LiVOPO$_4$. *ACS Omega*. **3**, 7310-7323 (2018). DOI: 10.1021/acsomega.8b00763
4. Rana J. *et al*. Role of disorder in limiting the true multi-electron redox in ε-LiVOPO$_4$. *J. Mater. Chem*. A. **42**, 20669-20677 (2018). DOI: 10.1039/C8TA06469E
5. Siu C. *et al*. Enabling multi-electron reaction of ε-VOPO$_4$ to reach theoretical capacity for lithium-ion batteries. *Chem. Commun*. **54**, 7802-7805 (2018). DOI: 10.1039/C8CC02386G

Funding acknowledgement:
This work was supported as part of the NorthEast Center for Chemical Energy Storage (NECCES), an Energy Frontier Research Center funded by the U.S. Department of Energy, Office of Science, Basic Energy Sciences under Award# DE- SC0012583.

Corresponding author:
Dr Louis F. J. Piper, Binghamton University, lpiper@binghamton.edu

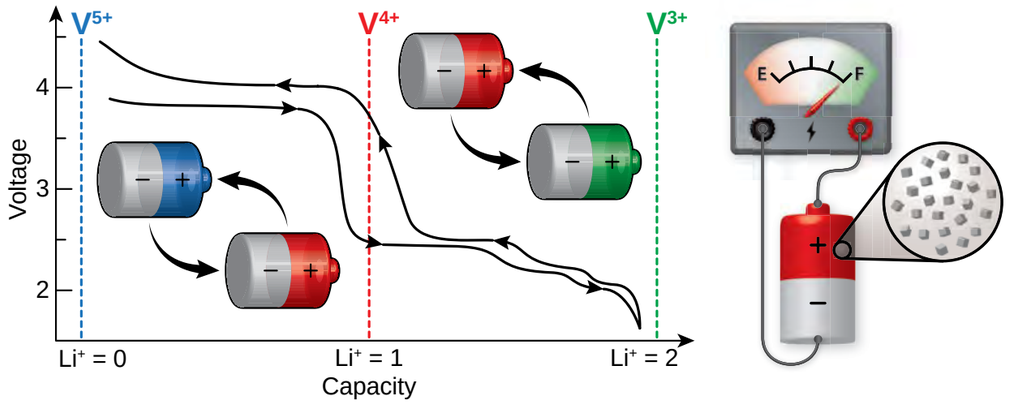

Figure 3: Schematic illustration of the voltage profiles of highly crystalline, nanoengineered (ball milling-free synthesis) ε-VOPO$_4$ showing reversible full 2Li intercalation.

Adding colour to the past: investigating the pigmentation of a three-million-year-old mouse

Related publication: Manning P. L., Edwards N. P., Bergmann U., Anné J., Sellers W. I., van Veelen A., Sokaras D., Egerton V. M., Alonso-Mori R., Ignatyev K., van Dongen B. E., Wakamatsu K., Ito S., Knoll F. & Wogelius R. A. Pheomelanin pigment remnants mapped in fossils of an extinct mammal. *Nat. Commun.* **10**, 2250 (2019). DOI: 10.1038/s41467-019-10087-2

Publication keywords: Pheomelanin; Pigment; Mouse; Synchrotron; Fossil

Colour has played a vital role in evolution for hundreds of millions of years. Until very recently, techniques used to study fossils could not explore the pigmentation of ancient animals. Researchers using the Microfocus Spectroscopy beamline (I18) have achieved a breakthrough in the ability to resolve fossilised colour pigments. They mapped key elements associated with the pigment melanin in an extinct, three million-year-old species of mouse. Different forms of melanin can give rise to a black or dark brown colour, or a reddish or yellow colour.

By bathing fossils in intense X-rays, the research team were able to discern the trace metals in the pigments and to reconstruct the reddish colour in the mouse's fur. They were able to determine that the fossilised mouse fur incorporated trace metals in the same way that trace metals bond to pigments in animals with red fur.

Their work provides a new chemical method for resolving melanin pigments in both recent and extinct tissue (e.g. hair, skin, feather) samples. Along the way, they learned much more about the chemistry of pigmentation throughout the animal kingdom. The team hopes that their results will allow us to reconstruct extinct animals with more confidence, adding another dimension to the study of the evolution of life on Earth.

Colour plays a vital role in the selective processes that have steered the evolution of life for hundreds of millions of years. The many techniques used to study fossils, until recently, were not capable of exploring the pigmentation of ancient animals, a character pivotal to reconstructing what an organism might have looked like. A breakthrough in synchrotron-based imaging techniques now gives insight into the chemistry in long-extinct species by mapping key elements associated with soft tissue structures (Fig. 1), but also with the pigment melanin, the dominant group of compounds that colour life (both in vertebrates and invertebrates). Eumelanin pigment gives a black or dark brown colour, but in the form of pheomelanin, it produces a reddish or yellow colour. Until recently, research has focused on the traces of elements known to be associated with eumelanin[1]. Previous experiments revealed dark and light pigment patterns in feathers of the Jurassic bird *Archaeopteryx*[2] and the Cretaceous *Confuciusornis sanctus* (Fig. 1). However, even though melanin pigments are a critical component of biological systems, the exact chemistry of melanin is still imprecisely known. The combination of new synchrotron-based imaging techniques with unique fossils has enabled the chemistry of this illusive molecule to be further refined.

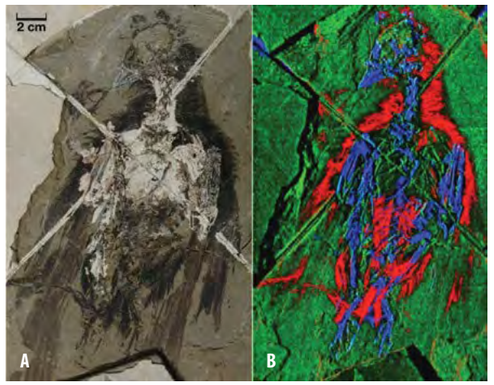

Figure 1: Optical (a) and Synchrotron Rapid Scanning X-ray Fluorescence (SRS-XRF) map (b) of Confuciusornis sanctus (MGSF315). SRS-XRF false-colour image of MGSF315 main slab (red, Cu; blue, Ca; green, Zn). Additional spectroscopy indicated that the copper was residue of eumelanin pigment preserved within the feathers of C. sanctus, (reproduced from Wogelius et al., 2011).

A suite of new imaging techniques, including elemental mapping techniques used at synchrotron light sources, provides one with the ability to peer deep into the chemical history of a fossil organism and also unpick the processes that preserved its tissues (Fig. 1)[1,2]. Where once we simply saw minerals, now we aim to resurrect 'biochemical ghosts' of long extinct species, mapping the whole organism and embedding matrix but without causing any damage to often fragile fossils.

A key goal from an earlier study undertaken by the team was to differentiate between eumelanin and pheomelanin pigment chemistry in modern bird feathers[3]. The feathers analysed in this earlier study possessed a distinct chemical signature for zinc and sulfur, with a significant portion of the zinc inventory bonded to sulfur, almost certainly through the sulfur contained within the pheomelanin molecule (not the sulfur bound within the surrounding keratinous feather matrix)[3]. This was a tipping point for the understanding of pigments and being able to identify chemical signatures that could help resolve pigmentation in ancient animals, especially those that exhibit exceptionally preserved 'soft' tissue (feathers, hair and even skin). A strong foundation had to be built using the modern animal tissue (feathers) before the technique could be applied to more ancient samples[4]. Through using synchrotron-based imaging techniques, this work provided a chemical 'fingerprint' for our most recent study of a three-million-year-old mouse, *Apodemus atuvas* (Fig. 2)[4]. Two well-preserved fossil specimens of *Apodemus atavus* from Willershausen (Germany) were selected, the holotype GZG. W.20027b (Fig. 2) and a second specimen GZG. W.17393a. This Pliocene species of field mouse is closely related to the extant (living) related species *Apodemus sylvaticus* and *Apodemus flavicollis*. Extant members of this genus are reddish coloured and thus the close relationship of these extant species would imply that the related extinct species would also have had significant amounts of pheomelanin pigment in their fur.

The spatial mapping of the mouse fossil (Fig. 2), at the Stanford Synchrotron Radiation Lightsource (USA), provided a beautiful chemical image of the fossil using Synchrotron Rapid Scanning X-ray Fluorescence (SRS-XRF). However, the chemistry of the melanin pigment required careful X-ray Absorption Spectroscopy (XAS) to be undertaken at Diamond Light Source to constrain the precise geometry and electronic structure of any compounds present. The study used a large number of chemical standards (Fig. 3) to provide comparative XAS spectra. The SRS-XRF showed that the distributions of zinc and organic sulfur correlated within the fossil *Apodemus* fur, just as in pheomelanin-rich modern integument (feathers) observed by the earlier study[3]. Furthermore, the zinc coordination chemistry within this fossil

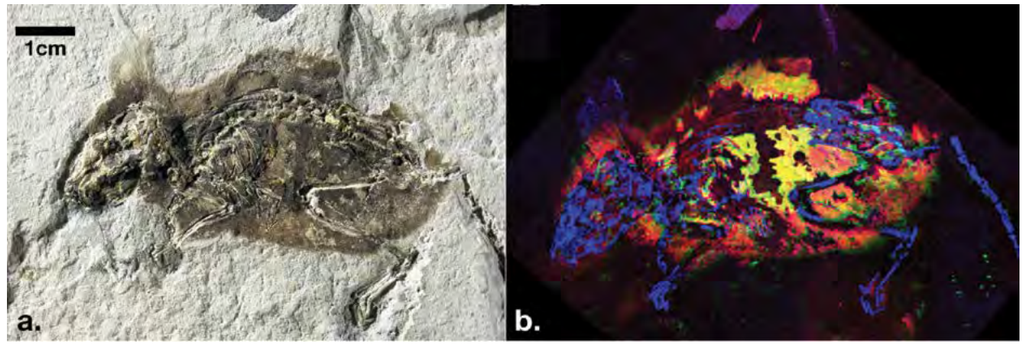

Figure 2: Optical and X-ray images of Apodemus atavus. (a) Optical image of A. atavus (GZG.W.20027b). (b) False-colour SRS-XRF image reveals exceptional preservation of integument as well as bone. This image is a combination of three maps, two standard single-element maps (blue = phosphorus, green = zinc), plus a third map that has been produced to especially emphasise the distribution of a specific oxidation state of organic sulfur (red = organic S (thiol)) in order to highlight the clear correlation between the distribution of zinc and organic sulfur which together appear as bright yellow (reproduced from Manning et al., 2019).

fur was closely comparable to that determined from pheomelanin-rich fur and hair standards that were also analysed using X-ray Absorption Near Edge Structure (XANES) spectroscopy at Diamond (Fig. 3b). The XANES showed that the zinc was directly bonded to the associated organic sulfur compounds, which is diagnostic of pheomelanin. However, given that the fossil soft tissue displayed enrichment in organic sulfur compounds, and that both the structural protein (keratin within fur) and red pigment (pheomelanin) in extant mouse fur contain sulfur species, it was critical that detailed sulfur XANES studies were undertaken in order to accurately characterise the oxidation state and origin of the sulfur inventory. Fig. 3a presents the results from fossil and extant material along with several sulfur standard compounds used to resolve each species. All spectra are quite different from each other, reflecting the strong impact that changing the oxidation state and coordination environment has on XANES spectra for sulfur[4].

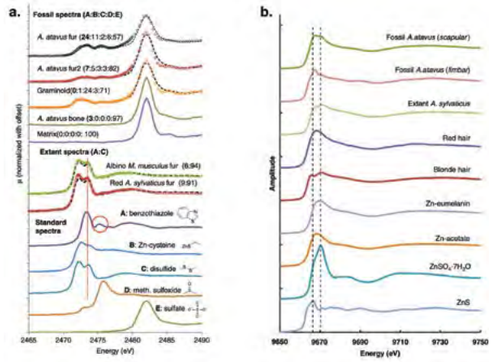

Figure 3: (a) Sulfur K-edge XANES standard, extant/fossil specimens. A benzothiazole, key component of pheomelanin, B Zn-cysteine (terminal S organic functional group), C oxidised glutathione (disulfide) comparator for sulfur in keratin, D methionine sulfoxide, E Zn sulfate. Two extant mice spectra with linear combination fits (dashed-lines) computed as a binary benzothiazole/disulfide system. Red circles highlight resonance in the benzothiazole standard resolvable in red fur. Dashed vertical line indicates benzothiazole peak discernible in red fur, not albino fur. Normalised spectra from fossils presented with Linear Combination Fitting (LCF) fits calculated using standards. Fits shown as dashed lines for soft tissues analysed. (b) Fossil/extant mouse zinc K-edge XANES, human hair, Zn-bonded eumelanin, Zn-acetate heptahydrate, and ZnS. Vertical lines indicate absorption spectrum maxima (pure first shell Zn-S and pure first shell Zn-O species).

Melanins (e.g. pheomelanin and eumelanin) are complex molecules and their chemistry is hard to resolve, even in modern samples. However, the detailed spectroscopy undertaken at synchrotron light sources has shed new light on the structure of these molecules and identified the key elements, such as zinc, copper and sulfur, that are at the very heart of the pigment[1,2,3]. Probing the preserved chemical environment with X-rays allowed the team to reconstruct a reddish colour in the 3-million-year-old pelt. The study on the three-million-year-old mouse concludes that the zinc-organosulfur compounds present within the fossil were the residue of pheomelanin and indicated that *Apodemus atavus* was pigmented in a similar way to its extant related species[4]. The results also helped explain why the detection of pheomelanin pigment residue is challenging, as the high original quantities of sulfur ubiquitous with keratinous integument (e.g. feather, hair, skin) produce degradation products rich in oxidised sulfur, which obscure the organic sulfur residue derived from pheomelanin pigment. In order to resolve the pheomelanin signal embedded within the complex mixture of organic degradation products, the bonding environment for organically complexed zinc was the most sensitive and stable chemical indicator. The study clearly shows that the resolution of pheomelanin pigment residue is possible, using a combination of chemical imaging and X-ray spectroscopy at synchrotron light sources, at least for specimens with an age equal to or less than three million years.

References:

1. Wogelius R. A. *et al.* Trace metals as biomarkers for eumelanin pigment in the fossil record. *Science* **333**, 1622 (2011). DOI: 10.1126/science.1205748
2. Manning P. L. *et al.* Synchrotron-based chemical imaging reveals plumage patterns in a 150 million year old bird. *J. Anal. At. Spectrom.* **28**, 1024 (2013). DOI: 10.1039/C3JA50077B
3. Edwards N. P. *et al.* Elemental characterisation of melanin in feathers via synchrotron X-ray imaging and absorption spectroscopy. *Sci. Rep.* **6**, 34002 (2016). DOI: 10.1038/srep34002
4. Manning P. L. *et al.* Pheomelanin pigment remnants mapped in 3 million year old mammal fossils. *Nat. Commun.* **10**, 2250 (2019). DOI: 10.1038/s41467-019-10087-2

Funding acknowledgement:
The University of Göttingen graciously loaned us the fossil A. atuvus specimens. Funding was provided by a UK Natural Environment Research Council grant NE/J023426/1. Portions of this research were also carried out at Diamond Light Source, beamline I18 (UK, allocations SP12948, SP11865, SP9488, SP8597, and SP7749). Portions of this research were carried out at the Stanford Synchrotron Radiation Lightsource (CA, USA), a national user facility operated by Stanford University on behalf of the U.S. Department of Energy, Office of Basic Energy Sciences. We thank support staff at DLS and SSRL. PLM thanks the Science and Technology Facilities Council for their support (ST/M001814/1). We are grateful for access to the DRIAM Analytical Service, Dalton Research Institute, Manchester Metropolitan University.

Corresponding author:
Prof Phillip Manning, University of Manchester, phil.manning@manchester.ac.uk

The discovery of a new type of uranium will inform radioactive waste disposal

Related publication: Townsend L. T., Shaw S., Ofili N. E. R., Kaltsoyannis N., Walton A. S., Mosselmans J. F. W., Neil T. S., Lloyd J. R., Heath S., Hibberd R. & Morris K. Formation of a U(VI)–Persulfide Complex during Environmentally Relevant Sulfidation of Iron (Oxyhydr)oxides. *Environ. Sci. Technol.* **54,** 129-136 (2020). DOI: 10.1021/acs.est.9b03180

Publication keywords: Iron; Redox reactions; Sulfides; Uranium; Extended X-ray absorption fine structure

When packaged, there will be 750,000 m³ of higher activity radioactive waste in the UK that needs to be disposed of safely - enough to fill 2/3 of Wembley Stadium. The plan is to dispose of this waste deep in the subsurface of the Earth, in an engineered facility known as a Geological Disposal Facility (GDF). To safely dispose of waste in a GDF, we need to understand the processes that could affect the mobility of uranium in the environment.

One key process that affects uranium mobility in the environment is the reaction with sulfide (sulfidation) produced by microbes naturally present in the subsurface. This means that the effects of sulfidation on uranium in a GDF scenario need to be further understood.

Researchers used X-ray Absorption Spectroscopy (XAS) on the I20-Scanning branchline to investigate what happened to the chemistry of uranium. The high sensitivity of this powerful beamline allowed them to look at the low, environmental concentrations of uranium in their samples.

In an unexpected result, the scientists saw the reaction with sulfide caused uranium release into solution for a very brief time, before moving into a highly immobile state. They attributed this unusual chemistry to the formation of a new form of uranium known as a U(VI)-persulfide, which had not been previously identified in an environmental system. The presence of this new form of uranium gives significant insight into uranium environmental chemistry and highlights the unique insight Diamond Light Source can provide in underpinning radioactive waste disposal.

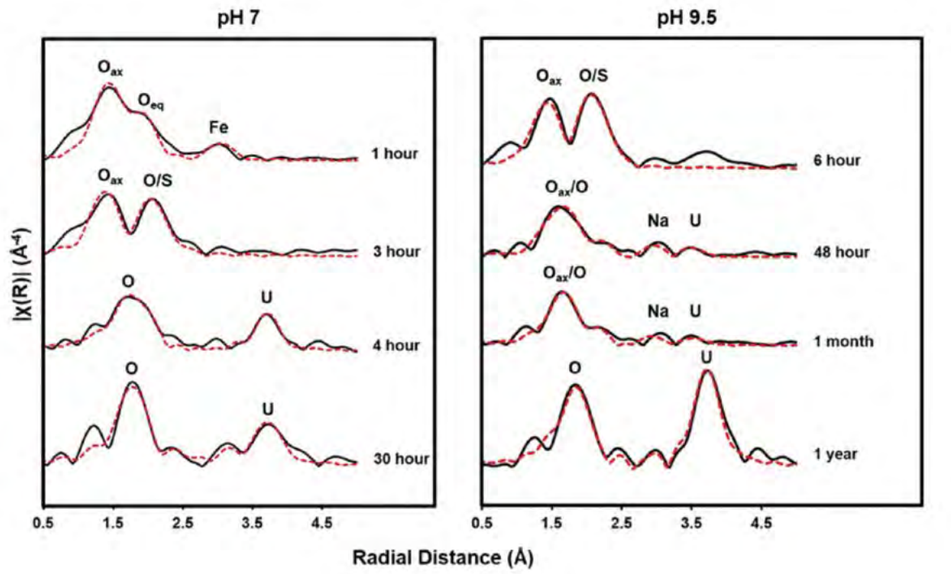

Figure 1: XAS data obtained from I20-Scanning branchline taken throughout the experiments run at pH 7 and pH 9.5.

In the UK, radioactive waste is planned to be disposed of deep in the subsurface in a Geological Disposal Facility (GDF). In order to ensure this disposal is effective, safe and implemented correctly, a safety case underpinned by fundamental and applied scientific research is needed to support the development of this nationally significant infrastructure project. This research involves understanding how the radioactive elements within the waste are affected by, and interact with, the environment once disposal has taken place. As uranium is the largest radionuclide by mass in radioactive waste, it is important to thoroughly understand how the naturally occurring processes in the deep subsurface will affect its chemistry and therefore its mobility in the environment.

One of the biogeochemical processes that takes place in subsurface environments is the production of sulfide by microbes that are naturally present. This sulfide can then react with minerals that are ubiquitously present in this GDF subsurface environment and other elements, like uranium, in a process known as sulfidation. These reactions need to be understood if a GDF is to be commissioned as previous field and laboratory studies have suggested that sulfidation may affect environmental mobility, although a molecular scale understanding was not achieved[1-3].

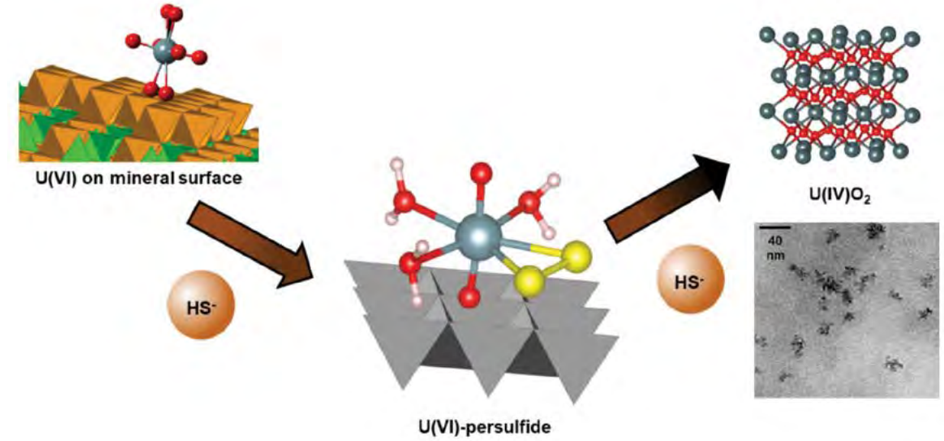

Figure 2: Overall reaction scheme for the sulfidation experiment performed in this study.

In order to fully understand the effects of sulfidation on uranium environmental behaviour, experiments were performed at the University of Manchester, using a highly controlled abiotic methodology under conditions mimicking natural subsurface conditions (i.e. pH 7 and pH 9.5), to produce samples that could be analysed at Diamond Light Source using X-ray Absorption Spectroscopy (XAS). XAS is a particularly useful method of analysis due to its ability to provide information about the local atomic environment and chemistry on the element of interest (in this case uranium) within a highly complex sample. Through the power of the I20-Scanning branchline, samples with very low concentrations of analyte could be analysed and the chemistry of uranium elucidated throughout the process of sulfidation. The results of the study have produced a molecular-scale understanding of the mechanisms that control uranium mobility under sulfidic conditions relevant to geological disposal of radioactive waste.

Upon initiation of sulfidation, uranium was observed to be liberated into solution transiently, in spite of the highly reduced conditions that would usually partition uranium to the solid phase as a reduced species known as uraninite or $U(IV)O_2$. This unusual uranium chemistry was studied further using XAS on I20-Scanning and revealed that a new environmental form of uranium was present during sulfidation. Through detailed analysis of the X-ray Absorption Near Edge Structure (XANES) and Extended X-ray Absorption Fine Structure (EXAFS) (Fig. 1), this new form of uranium, known as a U(VI)-persulfide, was shown to be key in understanding why uranium was present in solution during this reaction. This new, transient form of uranium was shown to consist of a persulfide ligand (S_2^{2-}), in addition to water molecules, coordinated to the equator of a uranyl moiety (UO_2^{2+}) (Fig. 2). To reinforce the findings from the XAS data, computational modelling of the U(VI)-persulfide and its interactions with mineral surfaces present in the system was performed. The modelled structure (Fig. 2) matched well with the values produced through analysis of the XAS data and highlighted how this form of uranium was weakly associated with the surface of minerals, providing a possible explanation for why uranium is released into solution during sulfidation.

Not only does this result provide significant insight into science underpinning a GDF, it also sheds light on uranium environmental chemistry that had not previously been identified. Whilst U-S complexes have been previously identified and synthesised in laboratories[4,5], the conditions used to produce these species were not representative of natural, environmentally relevant systems.

However, this form of uranium, and the release of uranium to solution, was transient, lasting only a matter of hours. The ultimate fate of uranium was the reduced form of uranium, U(IV), in a nanocrystalline solid mineral phase known as uraninite ($U(IV)O_2$) (Fig. 2). This means that uranium will likely be immobile over long timescales and under conditions relevant to geological disposal of radioactive waste. The results of this study have highlighted the complexity surrounding uranium chemistry in environmental systems, particularly under sulfidic conditions. The new, transient form of uranium, U(VI)-persulfide, has been shown to play a key role in uranium mobility, however, ultimately uranium is immobile as a solid U(IV) mineral phase. These findings are key to underpinning the safety case for the implementation of geological disposal of radioactive waste in the UK, in addition to broadening and deepening the knowledge of uranium chemistry in environmentally relevant systems.

References:

1. Anderson R. T. *et al.* Stimulating the In Situ Activity of Geobacter Species To Remove Uranium from the Groundwater of a Uranium-Contaminated Aquifer. *Appl. Environ. Microbiol.* **69**(10), 5884-5891 (2003). DOI: 10.1128/AEM.69.10.5884-5891.2003
2. Alexandratos V. G. *et al.* Sulfidization of lepidocrocite and its effect on uranium phase distribution and reduction. *Geochim. Cosmochim. Acta* **142**, 570-586 (2014). DOI: 10.1016/j.gca.2014.08.009
3. Alexandratos, V. G. *et al.* Fate of adsorbed U(VI) during sulfidization of lepidocrocite and hematite. *Environ. Sci. Technol.* **51**(11), 2140-2150 (2017). DOI: 10.1021/acs.est.6b05453
4. Grant, D. J. *et al.* Synthesis of a Uranyl Persulfide Complex and Quantum Chemical Studies of Formation and Topologies of Hypothetical Uranyl Persulfide Cage Clusters. *Inorg. Chem.* **51**(14), 7801-7809 (2012). DOI: 10.1021/ic3008574
5. Ward, M. D. *et al.* The $[U_2(\mu\text{-}S_2)_2Cl_8]^{4-}$ anion: synthesis and characterization of the uranium double salt $Cs_5[U_2(\mu\text{-}S_2)_2Cl_8]I$. *Inorg. Chem.* **54**(6), 3055-3060 (2015). DOI: 10.1021/acs.inorgchem.5b00234

Funding acknowledgement:
EPSRC and Radioactive Waste Management Ltd. co-funded the PhD studentship to L.T.T. via the Next Generation Nuclear CDT (EP/L015390/1). We are grateful to the Science and Technology Facilities Council for a PhD studentship to N.E.R.O. (ST/R504580/1). We would further like to acknowledge the support of Env Rad Net (ST/K001787/1 and ST/N002474/1) and the HEC Materials Chemistry Consortium, which is funded by the EPSRC (EP/L000202, EP/R029431) for access to ARCHER, the UK National Supercomputing Service (http://www.archer.ac.uk).

Corresponding author:
Dr Luke Townsend, University of Manchester,
luke.townsend@manchester.ac.uk

Looking exhaust catalysis up and down

Related publication: Dann E. K., Gibson E. K., Catlow C. R. A., Celorrio V., Collier P., Eralp T., Amboage M., Hardacre C., Stere C., Kroner A., Raj A., Rogers S., Goguet A. & Wells P. P. Combined spatially resolved operando spectroscopy: New insights into kinetic oscillations of CO oxidation on Pd/γ-Al2O3. *J. Catal.* **373**, 201 (2019). DOI: 10.1016/j.jcat.2019.03.037

Publication keywords: XAFS/DRIFTS; CO oxidation; Pd/Al_2O_3; Operando spectroscopy

The catalysts that remove harmful pollutants from vehicle exhaust are exceedingly dynamic. To truly understand how they operate and improve their efficiency, we need to know how and why their structure changes. This requires the use of combined methods to provide complementary data that can track changes in both space and time.

One of the processes that occurs in automotive exhausts is CO oxidation. This reaction has a quirky behaviour where the performance of the catalyst oscillates between high and low limits. Despite this being an extensively studied reaction, this phenomenon is not well understood. Researchers performed a combined study using X-ray Absorption Fine Structure (XAFS) to see how the catalyst structure is changing, and Diffuse Reflectance Infrared Fourier Transform Spectroscopy (DRIFTS) which gives information about molecules adsorbed on the catalyst surface.

Using the I20-EDE beamline, they were able - for the first time - to observe the structural changes that drive the oscillatory performance of palladium nanoparticles. They found that the structural changes were spatially localised to a minor component of the overall catalyst profile.

Their experiment shows that developing X-ray methods for probing catalysts in space and time is essential to the understanding of mechanisms at play in catalysis. These methods will allow us to design better catalytic processes for environmental protection, emerging energy technologies, and the production of sustainable chemical feedstocks.

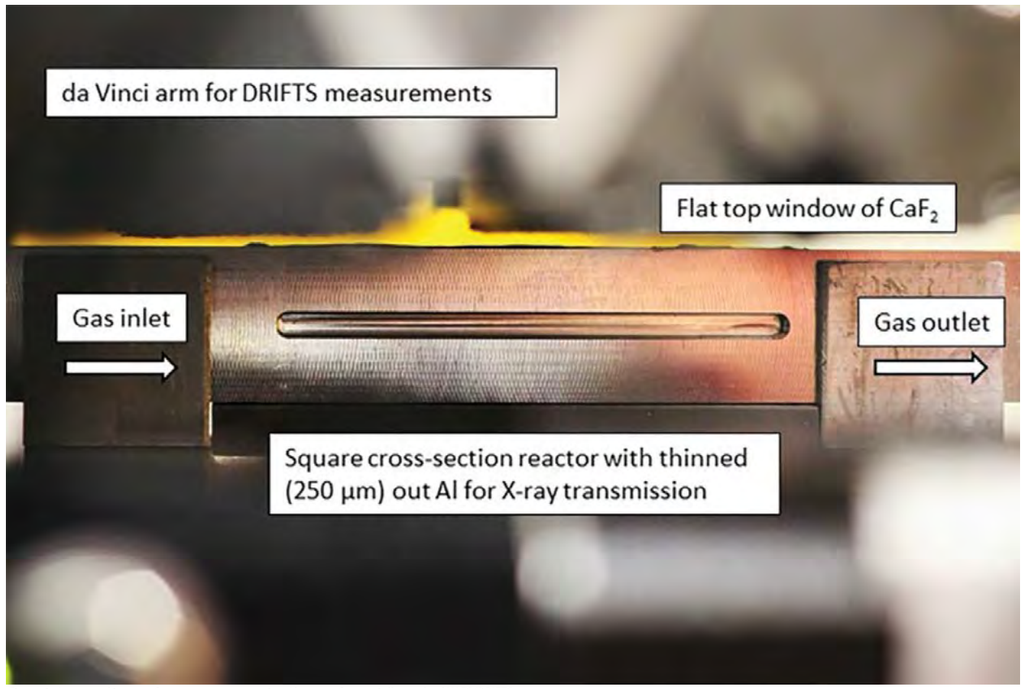

Figure 1: Annotated image of our square cross-section Al reactor for spatially resolved XAFS/DRIFTS.

One of the most widely studied catalytic reactions is the oxidation of CO to CO_2, which is an important process in cleaning the exhaust fumes from automotive vehicles. The traditional class of catalyst used for this process is supported metal nanoparticles, normally Pd, Pt, or Rh. Formulating the metal as a nanoparticle is important, both to thrift the expensive metals used and to control the catalytic properties. One of the fascinating catalytic properties of Pd nanoparticles supported on Al2O3, or for that matter Pt or Rh, is the process known as the 'CO oxidation kinetic oscillations'[1]. In this process the catalytic performance spontaneously see-saws between high and low limits, even though the temperature and gas feed applied remain constant.

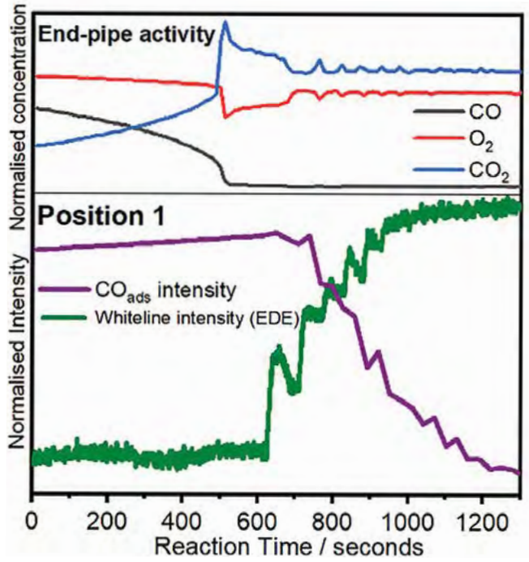

Figure 2: Bottom panel shows EDE Pd K-edge white line intensity (green) and DRIFTS CO adsorption intensity (purple) of catalyst Pd/Al_2O_3 at spatial position 1 (nearest to the reactor inlet) of the fixed catalyst bed in reactant (1% CO/3% O_2/Ar) gas feed during temperature ramp experiment (100 - 135°C). Top panel shows the simultaneous end-pipe mass spectrometry signals for O_2 (red), CO (black) and CO_2 (blue) concentrations of the reactor exhaust.

The proposed rationale for this puzzling phenomenon is that the catalyst structure oscillates between reduced, more metallic, and oxidised forms at these low and high points of conversion, respectively. At a temperature lower than the catalytic 'light off', the catalyst surface is saturated with CO in a reduced state. As the temperature is increased there is enough energy in the system to release some of the adsorbed CO from the surface, which allows the excess O_2 in the surrounding atmosphere to fill these vacant sites. For this catalytic reaction to happen it requires both CO and O_2 to be adsorbed on the surface simultaneously. Once the reaction starts, it propagates further as the exothermic reaction releases energy during the process.

This explanation is relatively straight-forward, however, these structural changes have proved elusive to conclusively track down[2]. For such an extensively studied process why is this? It is well known that the supported metal nanoparticles are dynamic and readily adapt their structural properties dependent upon the precise conditions. When catalysis is performed in a fixed bed reactor, similar to that found in automotive catalytic converters, the conditions across the length of the bed are not uniform. At the inlet of the reactor the atmosphere is made up of reactants, in this case CO and O_2, and at the outlet of the reactor the exhaust is dominated by products, for this reaction, CO_2. Moreover, we also need to consider the temperature fluctuation imparted by the exothermic reaction. If this phenomenon was to be understood, we needed a method that could probe the spatial profile of the reactor assessing both the Pd nanoparticle structure and the adsorbed gases at each point. To achieve this, we developed a reactor that can measure X-ray Absorption Fine Structure (XAFS) spectroscopy and Diffuse Reflectance Infrared Fourier Transform Spectroscopy (DRIFTS) data simultaneously across the length of the reactor, from inlet to outlet of the catalyst bed. The XAFS method provides information on the nanoparticle structures and the DRIFTS inform us about the surface adsorbates. To measure XAFS data of these systems, an intense source of photons (X-rays) provided by a synchrotron is required. Further to this, to carefully map the rise and fall of the kinetic CO oscillations we needed a form of XAFS analysis called Energy Dispersive EXAFS (EDE) that can measure data much faster (for our needs <1 second) than traditional approaches[3]. The infrared spectrometer, for the DRIFTS analysis, is an external machine which can be positioned on the beamline for the combined analysis. In this work we designed a customised square cross-section aluminium reactor (Fig. 1). The aluminium walls were thinned along the length of the catalyst bed to allow the X-rays to pass through the reactor without too many losses. A top window of CaF_2 was affixed to the reactor to allow for our DRIFTS studies; CaF_2 is an infrared transparent material within our region of interest.

During our experiments we assessed multiple points along the reactor profile during a temperature ramp from low to high temperature that induced catalysis. Although these oscillations are known to occur at set temperatures (isothermal conditions), the temperature ramp experiment allowed us to 'sweep' the range of temperature conditions that could be experienced. When the catalyst was operating, e.g. CO_2 was being produced, we observed the change from reduced to oxidised Pd nanoparticles that arises as the catalyst transitions from the CO poisoned catalyst to the highly active, oxidised Pd surface. This transition occurs initially at the end of the catalyst bed, nearest the outlet, and propagates upstream with increasing temperature of the reactor. Most importantly, we were able to observe the oscillatory behaviour of the catalyst structure and adsorbed CO that changed with the same frequency as the CO oxidation kinetic oscillations (Fig. 2). These structural oscillations can be easily visualised by looking at the intensity of specific features in the X-ray Absorption Near Edge Structure region of the XAFS spectrum during the temperature ramp. What was most interesting was that these changes only occurred at the very inlet (first 1 mm) of the catalyst bed. We proposed that these kinetic oscillations can only occur at the front of the catalyst bed where there is sufficient concentration of CO in the gas phase to compete with O_2 for adsorption sites at the catalyst surface.

In this work we further demonstrated the complex nature of the evolving catalyst structures and surface reactivity during catalytic operation. Furthermore, this is a clear indication of the need for spatially resolved methods for understanding and optimising highly active catalysts essential for future sustainable technologies.

References:

1. Ertl G. Oscillatory Kinetics and Spatio-Temporal Self-Organization in Reactions at Solid Surfaces. *Science* **254**, 1750 (1991). DOI: 10.1126/science.254.5039.1750
2. Figueroa S. J. A. *et al.* What drives spontaneous oscillations during CO oxidation using O2 over supported Rh/Al2O3 catalysts? *J. Catal.* **312**, 69 (2014). DOI: 10.1016/j.jcat.2014.01.006
3. Newton M. A. *et al.* Bringing time resolution to EXAFS: recent developments and application to chemical systems. *Chem. Soc. Rev.* **31**, 83 (2002). DOI: 10.1039/B100115A

Funding acknowledgement:

UK Catalysis Hub Consortium and EPSRC (portfolio grants EP/K014706/1, EP/K014668/1, EP/K014854/1, EP/K014714/1 and EP/I019693/1.

Corresponding authors:

Dr Peter Wells, University of Southampton, ppwells@soton.ac.uk and Prof Alexandre Goguet, Queen's University Belfast, a.goguet@qub.ac.uk

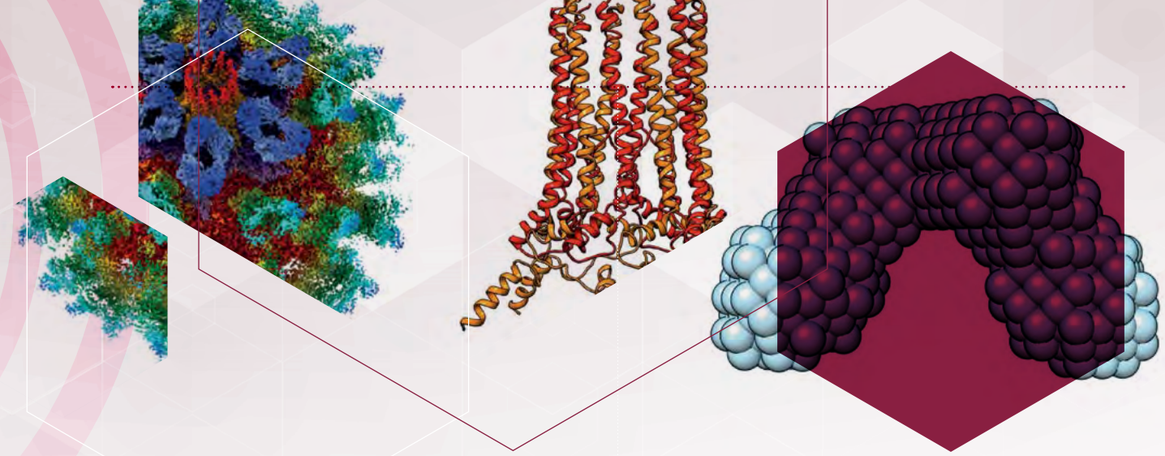

Soft Condensed Matter Group

Robert Rambo, Science Group Leader

The Soft Condensed Matter (SCM) Group provides the Infrared (IR) and Circular Dichroism (CD) microspectroscopy and both Small and Wide Angle X-ray Scattering (SAXS and WAXS) capabilities of Diamond Light Source. These capabilities are provided by the four beamlines: High Throughput SAXS (B21), the Multimode Infrared Imaging And Microspectroscopy (MIRIAM) beamline (B22), SAXS and Diffraction (I22) and the CD beamline (B23). This unique portfolio of beamlines can analyse a range of samples that include two-dimensional thin-films (photovoltaics), living mammalian cells, three-dimensional matrices (e.g. metal-organic frameworks, gels and waxes) and nano-particles in non-crystalline states. SCM now offer mail-in services for SAXS and CD measurements through UAS announcements. In addition, I22, B22 and B23 offer off-line access to IR microscopy and imaging, CD spectroscopy, and SAXS measurements.

In the last year, the SCM Group contributed to 132 scientific publications with B21 increasing their publications to a new record of 57. SCM publications include topics such as photo-chemistry examining the stacking arrangements within photosynthetic membranes, light induced chirality in thin-films, the structure of a Type III CRISPR, engineering of metal-organic frameworks for catalysis, the discovery of a new liquid crystalline hexagonal phase and food sciences that showed SAXS has the required sensitivity to follow the early stages of fat crystallization.

The SCM group joined with the newly formed UKRI-BBSRC funded FoodBioSystems doctoral training program (DTP) based at the University of Reading. The DTP involves six universities: University of Reading, Cranfield University, University of Surrey, Queen's University Belfast, Aberystwyth University, and Brunel University London. The DTP will develop the next generation of food scientists utilising techniques within the SCM group and Diamond. In addition, the SCM group was awarded three new doctoral studentships for 2020 that will be shared with the University of Cambridge, Durham University and the University of Manchester. The new cohort of students will join our existing SCM doctoral students associated with the Universities of Pisa (Italy), Surrey and Chalmers, Southampton, College London, Sheffield and Reading. The studentships will support development in infrared nanospectroscopy, SAXS of light activated soft materials and computational methods for modelling 3-dimensional structures of proteins.

2020 will be a transformative year for B22, B23 and I22. B22 will be upgrading its atomic force microscopy (AFM)-IR end station along with a new micro-sample environment for studying catalysis at high temperatures. B23 will be completing its CD-imaging upgrade integrating the new technique fully into the B23 user program. Finally, I22 will complete its BCO project providing world leading capabilities in SAXS based scanning of 2-D and 3-D samples.

B21 update

B21 studies noncrystalline, randomly oriented particles using high-throughput approaches. SAXS measurements can be made on any type of sample and in any physical state. The life sciences community comprises our largest user group since such measurements provide the opportunity to study biological machines in conditions that are comparable to their liquid, hydrated environment.

B21 has been operating with its in-vacuum Eiger 4 M detector for the past year where the entire camera is in a 10^{-4} millibar vacuum. The beamline optimised its vacuum configuration improving the instruments' signal-to-noise whilst allowing sample cell changes to happen within minutes. The new configuration expedites the analysis of non-liquid soft condensed matter samples such as gels and waxes.

B21 welcomed a new post-doctoral fellow who will be supporting structural biologists in lipidic phases while developing automation for the study of semi-solid, gel-like samples. The automation will contribute to a large goal for B21 that will integrate the HPLC and bioSAXS robot fully into the beamline control software enabling full and remote operation of the beamline

B22 update

The Multimode Infrared Imaging and Microspectroscopy (MIRIAM) beamline B22 is used to assess the molecular composition and microscopic spatial distribution of a sample at the highest, optically-achievable resolution in the infrared (IR). B22 operates two end stations for scanning IR spectro-microscopy and IR imaging, with a suite of single and 2-D detectors that seamlessly cover the whole IR range, from near-IR to mid-IR and further into THz. B22 has been used in the analysis of inorganic-organic combinations in biomineralogy or composite materials, chemical degradation in conservation and archaeology, as well as studying live mammalian cells under the IR microprobe for *in situ* drug response, an important tool in anti-cancer research. This past year, B22 provided insights on a variety of catalytic systems that included enzymes, metal-organic frameworks (MOFs) and zeolite crystals interacting with gas and liquid phase reagents.

In 2019, scientists from the University of Oxford (Dr Kylie Vincent) used synchrotron IR microspectroscopy to study catalysis of nickel-iron hydrogenases. These are bi-metal enzymes that that have specific CO (carbon-oxygen) and CN (carbon-nitrogen) bonds that can be followed by IR. Dr Vincent's group invented PFIRE, a method that allowed them to control the enzymes using electrochemistry and follow the catalytic cycle by IR microspectroscopy at B22. Their approach reconciled observations from solid-state approaches, namely X-ray Crystallography (MX), electron paramagnetic resonance and X-ray absorption spectroscopy with solution-state activity studies of enzyme catalysis.

The beamline continues to provide collaborative calls for IR nanospectroscopy in photothermal mode (AFM-IR) by synchrotron radiation (SR). This cutting edge method is suitable for molecular analysis of submicron to micron scale organic matter and biomaterials -from mammalian cells to microplastic- with exceptional sub-micron resolution (i.e. up to 100 times below the IR wavelength scale). B22 has approval for a new AFM end station allowing for tapping AFM-IR and scattering-SNOM measurements by SR. The modernisation will improve data acquisition rates and spatial resolution allowing IR nanospectroscopy to be performed at tens of nanometers resolution. This increased sensitivity and spatial resolution will expand B22's experimental capacity, e.g. surface sciences and the study of thin-films such as organic photovoltaics.

B23 update

The synchrotron radiation Circular Dichroism (CD) beamline (B23) uses circularly polarised ultraviolet (UV) light to characterise the structure of complex materials in solution and in solid-state films. Many molecular systems have a handedness (chirality) to them akin to our right and left hands and surprisingly, this molecular handedness will differentially absorb light that has been polarised. Specifically to B23, the UV light generated is modulated between right-polarised (spins to the right) and left-polarised (spins to the left). B23 measures precisely the differences in how much a material absorbs the right versus left polarised light through the technique of CD. In thin-films, quantification of CD at 50 micron resolution can inform on how materials prefer to orient themselves and for biological samples, CD spectra can be used to monitor conformational changes, drug binding or instabilities in a protein as a function of temperature, pressure, ionic strength, surfactant, pH, ligand interactions and ageing.

B23 is at the forefront of a new CD Imaging (CDi) technology. CDi exploits the highly collimated synchrotron light for scanning thin-films and surfaces of solid materials. Unlike absorption methods, CDi can inform on the chiral supramolecular structure of the material. Last year, B23 had secured funding for a dedicated Mueller-Matrix Polarimeter (MMP) instrument that was delivered and installed in November 2019. The MMP is under commissioning and will see full user schedule later in 2020.

CDi measurements require precise knowledge of the sample thickness that often varies throughout the material. To complement the MMP instrument, B23 acquired the ProFilm 3D profilometer for precise sample thickness measurements. The instrument can provide thickness measurements down to 10 nanometers (1000 times smaller than the thickness of a sheet of paper). Many thin-film materials are made from polymers and these polymers will preferentially form a chiral structure. Currently, the chiral homogeneity throughout the material cannot be interrogated efficiently using non-destructive methods. B23 is the first beamline capable of CDi, the essential tool for the screening of the chiral homogeneity of novel optoelectronic materials for photovoltaic and display systems that are also based on peptides and DNA. Combined with Diamond high-resolution microscopy, B23 is the unique worldwide facility for material science and life sciences.

I22 update

The Small Angle Scattering and Diffraction beamline (I22) offers combined Small and Wide Angle X-ray Scattering (SAXS and WAXS) studies on a range of low order biological, natural and synthetic samples. I22 excels at providing structural information on partially ordered materials ranging from colloidal nanoparticles and thin-films to large hierarchical structures such as bone.

I22 made a major change to its experimental hutch as part of a Beam Conditioning Optics (BCO) upgrade project. The BCO project will significantly improve data quality through a completely embedded microfocus mechanism, providing variable beamsizes, and energy through an evacuated flight tube. In the last phase of the project, the experimental hutch was stripped down to the floor and rebuilt which allowed a significant removal of legacy equipment and cables. A new granite base was installed to provide a solid, temperature-insensitive, anti-vibration platform to host an array of low scatter slits, a laser alignment tool, beam position monitor (QBPM), fast shutter and most importantly, an in-line microscopic viewer of the mounted sample. Samples can now be viewed in real-time with a virtual X-ray beam overlaid on the image. The new optical layout has significantly reduced divergence for microfocus experiments and has provided access to much lower q (scattering vectors) than previously available. The upgrade has been a step-change in mapping experiments particularly examining deformation in bones and eye lenses.

Last year, the I22 Principal Beamline Scientist Dr Nick Terrill, in collaboration with Professor Michael Rappolt from the School of Food Science and Nutrition at the University of Leeds, was awarded an Engineering and Physical Sciences Research Council (EPSRC) grant to support an offline SAXS facility at Diamond and managed by the SCM Group. The Multi-User Facility for SAXS/WAXS (DL-SAXS) now has an installed Xenocs Xeuss 3.0 instrument operating with an Eiger-2R 1M detector. The facility is under commissioning and will accept a limited number of users in AP28. This instrument will be critical to the SCM Sample Environment Development Laboratory for independent development/testing of sample environments prior to beamtime. Studying materials under intended use, such as lubricants under frictional strain or simply the stretching of a novel bioengineered material requires bespoke sample environments. Testing these sample environments prior to beamtime drives innovation and optimises the available beamtime.

How viruses that cause winter-vomiting disease infect host cells

Related publication: Conley M. J., McElwee M., Azmi L., Gabrielsen M., Byron O., Goodfellow I. G. & Bhella D. Calicivirus VP2 forms a portal-like assembly following receptor engagement. *Nature* **565**, 377-381 (2019). DOI: 10.1038/s41586-018-0852-1

Publication keywords: Calicivirus; Portal; VP2; Endosome escape; CryoEM; SAXS

The notorious norovirus that causes winter vomiting disease is part of the calicivirus family. Norovirus is highly contagious and can be very difficult to contain. Other caliciviruses are animal pathogens, including 'cat flu' that can cause very high mortality rates in domestic cats.

MRC researchers used a combination of cryo-electron microscopy and very high-quality small-angle X-ray scattering (SAXS) (performed on beamline B21) to analyse feline calicivirus (FCV).

When viruses infect, they bind to and then enter cells. They often use a process called 'endocytosis', which cells use to bring in nutrients from their environment. Viruses trigger endocytosis, causing the cell to enclose the virus particle in a sort of bubble called an endosome. The virus then needs to escape the endosome to infect the cell properly, but how it does this was not understood.

The results of this new research show that after they bind to the cell surface, caliciviruses rearrange their protein shell to extrude a funnel-shaped structure. They believe the virus uses this portal-like assembly to inject its RNA into the host cell and begin the infection process.

The team were also able to calculate an atomic model of the portal protein - known as VP2. Although VP2 was known to be critical for the production of infectious virus, its exact function was not known.

These insights into the early stages of calicivirus infection provide a new target for the development of antiviral drugs.

Viruses are intracellular parasites that require a host cell to replicate or multiply. Viruses enter cells by binding to specific receptors on the cell surface. Receptor binding subsequently triggers uptake of the virus into the host cell, folding the host membrane around the virus forming a membranous compartment known as an endosome. The virus must escape the endosome in order to take over the host cell for viral replication.

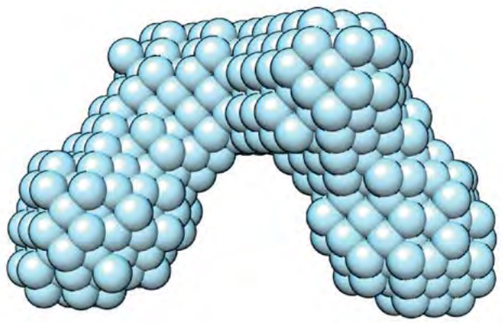

Figure 1: Dummy atom model of feline junctional adhesion molecule A (fJAM-A) computed with the program DAMMIF from size-exclusion chromatography small angle X-ray scattering (SEC-SAXS) data.

Caliciviruses are small viruses that can infect many species such as humans, cats, sealions and rabbits. The most notable of the caliciviruses is norovirus, the cause of winter vomiting disease outbreaks across the globe, particularly affecting humans in enclosed spaces e.g. cruise ships, hospital wards and classrooms. Until relatively recently, studies on norovirus have been limited by the inability to grow the virus in laboratories and so related veterinary pathogens such as feline calicivirus (FCV) are often used to study calicivirus biology.

Caliciviruses have a width of approximately 40 nm (that is 2,500 times smaller than the thickness of a sheet of paper). Viruses are containers for viral genetic information and the calicivirus container is composed of a protein shell mainly composed from 180 copies of a single viral protein (VP1). An additional viral structural protein known as VP2 is also found in the protein shell, although until this study, the function (and structure) of VP2 was unknown.

In this study, cryo-electron microscopy (cryoEM) was used to determine the high-resolution structures of FCV, both unbound and bound to its cellular receptor (feline junctional adhesion molecule A (fJAM-A)[1]). The structure of human and murine JAM-A proteins had been previously determined; however, the structure of feline JAM-A had not. CryoEM studies samples in a close-to-native state and to complement the virus cryoEM studies, small angle X-ray scattering (SAXS) was used to study the portion of fJAM-A that extends into extracellular space where the virus can interact with it. SAXS[2] is a useful technique for studying proteins in solution, as they would be found in a cell.

CryoEM and image analysis produced a three-dimensional image reconstruction of the free (Fig. 2) and fJAM-A receptor bound (Fig. 3a) FCV. The structures were of sufficient detail to allow visualisation of structural changes in the virus upon fJAM-A binding. Regions of the VP1 proteins undergo a 15° anti-clockwise rotation whilst some (at the two-fold symmetry axes) also tilt off axis (see below). Interestingly, fJAM-A bound to the virus appeared to adopt different structures than observed by SAXS (Fig. 1). Whilst in solution, fJAM-A proteins appear to couple together to form doublets/dimers consistent with the related human and murine forms. Upon binding to the virus, fJAM-A was found to be present in a head-to-tail arrangement that disrupts/alters the coupling of two fJAM-A proteins. Thus, we concluded that FCV binding appears to disrupt fJAM-A dimeric complexes despite the virus binding site occurring in a region distinct from the fJAM-A dimerisation site suggested by our SAXS data.

Due to the highly symmetric (icosahedral) nature of caliciviruses, icosahedral symmetry was imposed during the image reconstruction process,

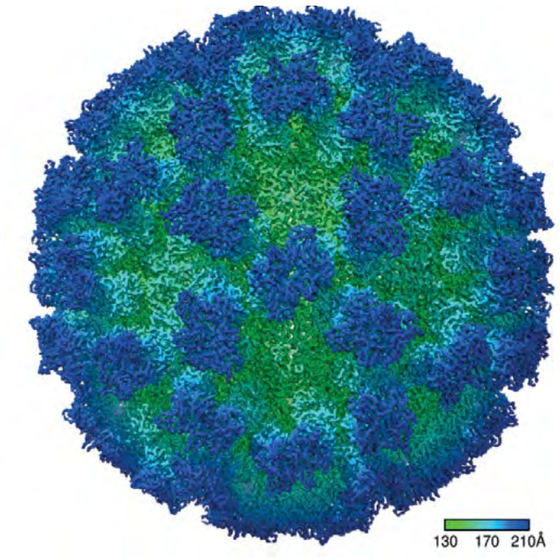

Figure 2: Structure of feline calicivirus at 3 Å resolution as determined by cryo-electron microscopy and three-dimensional image analysis.

a common practice used in virus structure determination. In some cases, this can lead to a loss of information. Due to this loss of information, a recently developed method of image analysis, known as focussed classification, was adopted. Focussed classification permits the reconstruction of small regions of density without imposing any symmetry[3,4,5]. Whilst performing focussed classification on the three-fold symmetry axes of FCV decorated with fJAM-A, a novel structure was discovered. A portal-like assembly was found at a single three-fold symmetry axis per virus particle (Fig. 3). The portal-like assembly is composed of 12 VP2 proteins in alternating conformations which form a channel-like structure projecting out from the surface of the virus. The distal tips of the VP2 proteins are highly hydrophobic (water fearing) which suggests the portal-like assembly inserts into the membranous endosome during virus entry and acts as a mechanism for delivery of the viral genetic information into the host cell for replication to proceed. This study was the first description of this kind of structure in a mammalian virus.

References:

1. Makino A. *et al.* Junctional adhesion molecule 1 is a functional receptor for feline calicivirus. *Journal of Virology*, **4482** (2006). DOI: 10.1128/JVI.80.9.4482-4490.2006
2. Franke D. *et al.* DAMMIF, a program for rapid ab initio shape determination in small-angle scattering. *J. Appl. Cryst.* **42**, 342 (2009). DOI: 10.1107/S0021889809000338
3. Scheres S. H. W., Processing of structurally heterogeneous cryo-EM data in RELION. *Methods in Enzymology* **579**, 125 (2016). DOI: 10.1016/bs.mie.2016.04.012
4. Zhou M. *et al.* Atomic structure of the apoptosome: mechanism of cytochrome c- and dATP-mediated activation of Apaf-1. *Genes & Dev.* **29**, 2349 (2015). DOI: 10.1101/gad.272278.115
5. McElwee M. *et al.* Structure of the herpes simplex virus portal-vertex. *PLoS Biol.* **20**, e2006191 (2018). DOI: 10.1371/journal.pbio.2006191

Funding acknowledgement:
We acknowledge Diamond Light Source for time on Beamline B21 under proposal MX11651-24. M. J. Conley was supported by a PhD studentship from the UK Biotechnology and Biological Sciences Research Council (BBSRC WestBIO DTP: BB/J013854/1). D. Bhella was supported by the UK Medical Research Council (MC_UU_12014/7).

Corresponding author:
Dr Michaela Jayne Conley, MRC-University of Glasgow Centre for Virus Research, Michaela.Conley@glasgow.ac.uk

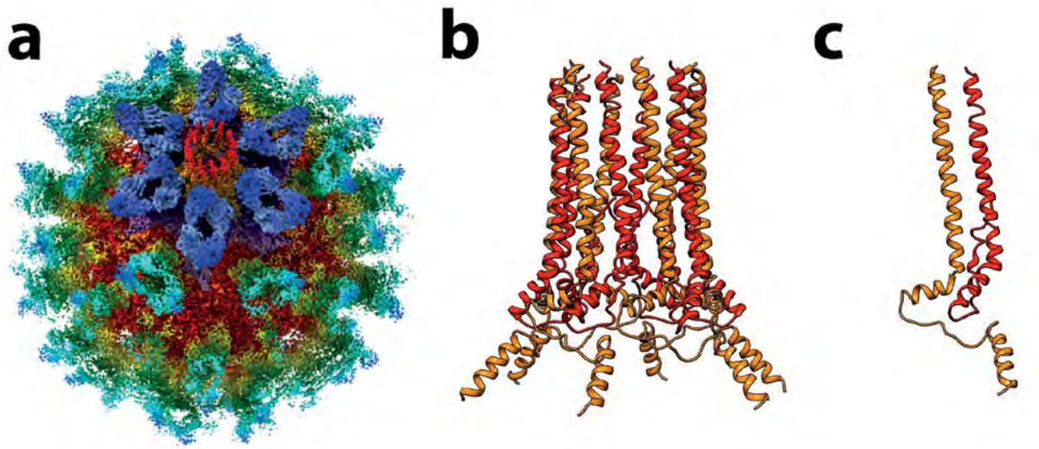

Figure 3: Interaction of feline calicivirus with fJAM-A results in the formation of a portal-like assembly. (a) Full virus structure (coloured by radius) showing the portal-like assembly (orange) and surrounding fJAM-A proteins (blue). (b) Atomic model of the portal-like assembly (coloured by VP2 conformer). (c) Atomic model of the two conformers of VP2 present in the portal-like assembly.

Development of a mesopore Metal-Organic Framework catalyst

Related publication: Kang X., Lyu K., Li L., Li J., Kimberley L., Wang B., Liu L., Cheng Y., Frogley M., Rudić S., Ramirez-Cuesta A., Dryfe R., Han B., Yang S. & Schröder M. Integration of mesopores and crystal defects in metal-organic frameworks via templated electrosynthesis. *Nat. Commun.* **10**, 4466 (2019) DOI: 10.1038/s41467-019-12268-5

Keywords: MOFs; Electrosynthesis; Defects; Mesopores; Catalysis

Metal-organic frameworks (MOFs) are compounds made by linking together organic and inorganic units with strong bonds. Since their discovery over 20 years ago, scientists have synthesised tens of thousands of unique structures. MOFs have an exceptionally porous structure, and by synthesising structures with differing pore sizes, researchers can tune MOFs to filter, trap, or transport molecules. MOFs have a wealth of potential applications, in areas such as hydrogen storage, catalysis, drug delivery and carbon capture.

Mesopores are between 2 and 50 nm in width. Incorporating mesopores and active sites into MOFs is challenging, but can lead to the discovery of efficient new catalysts. An international team of researchers has created a mesoporous MOF, within 100 seconds at room temperature, by templated electrosynthesis using an ionic liquid as both electrolyte and template. This material incorporates crystal defects with uncoupled Cu(II) centres as evidenced by confocal fluorescence microscopy and by Fourier transform infrared and electron paramagnetic resonance spectroscopy. FTIR measurements were collected on the Multimode Infrared Imaging And Microspectroscopy (MIRIAM) beamline (B22).

Prepared in this way, the MOF shows exceptional catalytic activity for the aerobic oxidation of alcohols to produce aldehydes in near quantitative yield and selectivity under mild conditions. It also displays excellent stability and reusability over repeated cycles.

Incorporation of mesopores and active sites into metal-organic framework (MOF) materials to uncover new efficient catalysts is a highly desirable but challenging task. A mesoporous MOF has been obtained within 100 seconds at room temperature by templated electrosynthesis using an ionic liquid as both electrolyte and template. This material incorporates crystal defects with uncoupled Cu(II) centers as evidenced by confocal fluorescence microscopy and by fourier transform infrared and electron paramagnetic resonance spectroscopy. MFM-100 prepared in this way shows exceptional catalytic activity for the aerobic oxidation of alcohols to produce aldehydes in near quantitative yield and selectivity under mild conditions, as well as having excellent stability and reusability over repeated cycles.

The application of metal-organic frameworks (MOFs) in catalysis is often restricted by the hindered mass transport of substrates through micropores and the lack of accessible active sites. Significant efforts have been devoted to the synthesis of mesoporous MOFs to facilitate substrate transport for catalysis and creating crystal defects to serve as active sites[1]. Many MOF systems are built from metal centres with saturated coordination environments and thus do not incorporate labile sites. Also, the removal of coordinated solvents from metal centres to generate open sites can have a detrimental effect on the overall stability of the framework in activated MOFs. Open metal sites are readily saturated by solvent molecules used in catalytic reactions, and thus remain inaccessible to target substrates. Defects can be produced intentionally during synthesis or *via* post-synthetic treatment.[2] Integration of mesopores and active sites within crystal defects in MOFs *via* readily scalable synthetic routes could in principle greatly facilitate their applications in catalysis. Additionally, electrosynthesis can be used for materials production at varying scales[3].

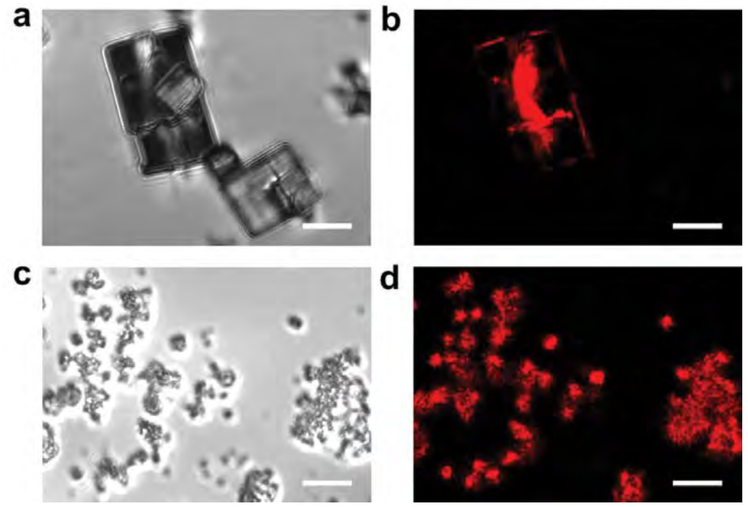

Figure 1. Comparison of the micrographs and CMF images of MFM-100a (a, b) and MFM-100d (c, d). The scale bar is 5 μm in all images. The fluorescence (red colour) indicates crystal defects determined by the oligomerization of furfuryl alcohol.

The Mesoporous MOF MFM-100 has been successfully obtained by rapid (<100 seconds) electrosynthesis at room temperature. The structure, morphology and porosity of MFM-100 can be readily controlled by choice of energy input and ionic liquid (IL) in the synthesis. These MFM-100 materials contain crystal defects [*e.g.*, uncoupled Cu(II) ions as Lewis acid sites], which have been characterised by confocal fluorescence microscopy (CFM), inelastic neutron scattering (INS), electron paramagnetic resonance (EPR) and Fourier transform infrared (FTIR) spectroscopy. Significantly, the integration of mesopores and active sites within the MFM-100 scaffold has endowed the resultant MOF with exceptional activity for the aerobic oxidation of a range of aldehydes and alcohols in high yield and selectivity. The MFM-100 catalysts also exhibit excellent stability and reusability.

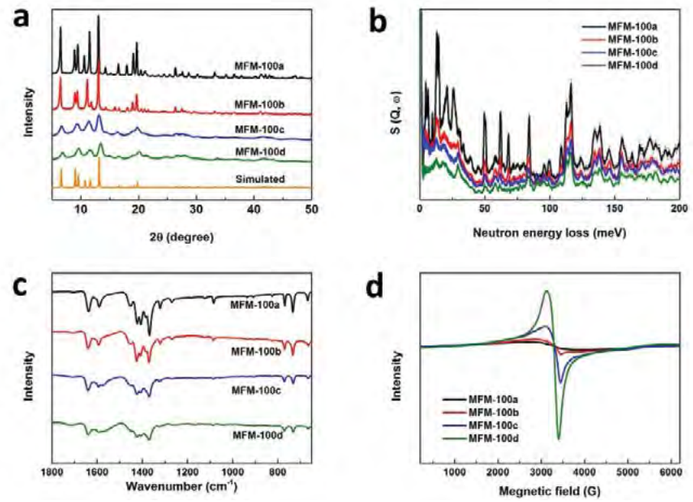

Figure 2. Characterisations of samples of MFM-100 samples obtained by solvothermal reactions and by electrosynthesis. (a) PXRD patterns; (b) INS plots; (c) FTIR spectra; (d) solid state EPR spectra at same sensitivity and concentration of material.

Four samples (denoted as a, b, c and d) of MFM-100 (also known as NOTT-100[4]) have been synthesised. MFM-100a was synthesised in a solvothermal reaction. MFM-100(b,c,d) were obtained by electrosynthesis at different temperature with different IL concentration. The microphotographs and CFM images reveal a stark comparison between MFM-100a and MFM-100d in furfuryl alcohol (Fig. 1). Large crystallites of MFM-100a only show fluorescence response at the crystal boundaries (*i.e.*, the edge and gaps), while smaller particles show no fluorescence response. In contrast, all particles of MFM-100d exhibit strong fluorescence that is distributed evenly across the entire particle, directly confirming the presence of homogenous active Cu(II) sites as Lewis acid sites at defects within MFM-100d.

MFM-100(a,b) are more crystalline than MFM-100(c,d) as measured by PXRD (Fig. 2a) and the INS features of MFM-100c and MFM-100d are heavily convoluted and broadened (Fig. 2b) suggesting that the latter have substantial crystal defects leading to reduction in long-range order of the sold-state lattice.

Powder X-ray diffraction (PXRD) and INS give the average property of samples, while FTIR from Beamline B22 offers detailed information on a single particle. FTIR spectra show notable decrease in intensity and increase of band broadening on going from MFM-100a to MFM-100d (Fig. 2c). These results are consistent with the reduced crystallinity and presence of crystal defects in MFM-100(c,d) and indicates that every particle exhibits defects. A small increase in intensity at 1574 cm^{-1} (assigned to the C=C vibration of the imidazole ring) is observed in the FTIR spectra of MFM-100c and MFM-100d, indicating the presence of trace IL cations.

The EPR spectrum confirms that the defects are uncoupled Cu(II) centres (Fig. 2d)[5], which can be considered as active centers for oxidation of alcohols. The presence of mesopores is another important factor for catalysis. The highly crystalline MFM-100a shows high surface areas (1586 $m^2 g^{-1}$) with the pore size distribution centred at 6.5 Å. There is thus an absence of mesopores in MFM-100a. In contrast, mesopores centred at 4.6 nm are observed in MFM-100d (V_{meso} = 1.17 $cm^3 g^{-1}$ and S_{meso}/S_{total} = 0.65), which shows a total BET surface area of 1353 $m^2 g^{-1}$.

The Cu(II)-based MOFs, HKUST-1 and MOF-2, have also been prepared by solvothermal synthesis and by templated electrosynthesis. Analysis of the structure and porosity of these samples confirms that the electrosynthesised MOFs show reduced crystallinity and the presence of significant amounts of mesopores compared with the samples obtained by solvothermal synthesis. This result indicates that the strategy based upon templated electrosynthesis developed here has general applicability to the synthesis of mesoporous, defective Cu(II)-MOFs.

Oxidation of alcohols over Cu(II)-based catalysts is an efficient method to synthesise aldehydes, and we therefore tested the catalytic activity of MFM-100, HKUST-1 and MOF-2 for the oxidation of a range of primary and secondary alcohols. Crystal defects consisting of uncoupled Cu(II) ions in MFM-100(c,d) play a positive role in the observed catalytic activity, leading to the quantitative conversion of benzyl alcohol with MFM-100(c,d). Similarly, electrosynthesised HKUST-1 and MOF-2 show better catalytic performance than catalyst materials synthesised by solvothermal methods.

Mesoporous MOFs are particularly beneficial for oxidation of large molecules such as 3,3′,5,5′-tetrakis(trifluoromethyl)benzhydrol. Thus, MFM-100(c,d) exhibit notably higher activity than MFM-100(a,b), and MFM-100d affords quantitative production of the corresponding aldehyde. We have found that the co-presence of crystal defects and mesopores greatly promotes catalytic oxidation, with exceptional catalytic performance being observed for MFM-100d. Stronger interaction between MFM-100d and alcohol was observed by INS spectroscopy, indicating the defective structure plays a significant role in enhancing catalytic activity. The methodology developed here paves a new and easy-scalable pathway to synthesise mesoporous and defect MOFs as efficient catalysts.

References

1. Drake T. *et al.* Site isolation in metal-organic frameworks enables novel transition metal catalysis. *Acc. Chem. Res.* **51**, 2129-2138 (2018). DOI: 10.1021/acs.accounts.8b00297
2. Shearer G. C. *et al.* Tuned to perfection: ironing out the defects in metal-organic framework Ui0-66. *Chem. Mater.* **26**, 4068-4071 (2014). DOI: 10.1021/cm501859p
3. Li M. *et al.*. Reductive electrosynthesis of crystalline metal-organic frameworks. *J. Am. Chem. Soc.* **133**, 12926-12929 (2011). DOI: 10.1021/ja2041546
4. Lin X. *et al.* High H_2 adsorption by coordination-framework materials. *Angew. Chem. Int. Ed.* **45**, 7358-7364 (2006). DOI: 10.1002/ange.200601991
5. EL Mkami, H. *et al.* EPR and magnetic studies of a novel copper metal organic framework (STAM-I). *Chem. Phys. Lett.* **544**, 17-21 (2012). DOI: 10.1016/j.cplett.2012.06.012

Funding contribution:
Diamond Light Source; ISIS Facility; University of Manchester; Institute of Chemistry, Chinese Academy of Sciences; Royal Society.

Corresponding authors:
Dr. Sihai Yang, University of Manchester, Sihai.Yang@manchester.ac.uk
Prof. Martin Schröder, University of Manchester, M.Schroder@manchester.ac.uk

A potential new method of producing high-quality supercrystals

Related publication: Lehmkühler F., Schroer M. A., Markmann V., Frenzel L., Möller J., Lange H., Grübel G. and Schulz F. Kinetics of pressure-induced nanocrystal superlattice formation. *Phys. Chem. Chem. Phys.* **21**, 21349-21354 (2019). DOI:10.1039/c9cp04658e

Publication keywords: Nanocrystal self-assembly; High pressure; Kinetics

Nanoparticle (NP) supercrystals can demonstrate tunable and collective properties that are different from that of their component parts, with potential applications in areas such as optics and electronics. Although the formation of high-quality supercrystals is usually a slow and complicated process, recent research by a team of German researchers has shown that applying pressure can induce gold nanoparticles to form supercrystals.

They investigated the self-assembly of gold nanocrystals with a special polymer surface coating, in suspension after performing a rapid pressure-jump. Using time-resolved small-angle X-ray scattering (SAXS), they were able to follow the formation of supercrystals and understand the assembly process. They performed these experiments on beamline I22, which provides an integrated high-pressure setup for SAXS experiments of soft matter and nanoscale systems, at pressures of up four kbar.

The specific solubility properties of the polymer coating mean that pressure can lead to the formation of high-quality supercrystals directly in aqueous suspension. This formation process is homogeneous, takes place within milliseconds and can be tuned by the type of pressure-jump.

By demonstrating the pressure-induced crystallisation of nanocrystals and its kinetics, this research provides a potential new method of producing high-quality supercrystals. These supercrystals have potential applications in many technical fields, including electronics and optoelectronics.

Highly ordered supercrystals built from metallic nanocrystals (NC) have potential applications in optics, electronics, and sensor platforms because they can exhibit collective properties different from their component parts. In particular, assemblies of gold nanocrystals (AuNC) show collective plasmonic properties that may be utilised for future optical metamaterials[1]. The most popular route to obtain such supercrystals is the self-organisation from nanocrystals in a liquid solvent. Here, the nanocrystals are dispersed throughout the solvent and as the solvent is loss due to evaporation, the nanocrystals will self-organise into a supercrystal[1]. However, the self-assembly of high-quality supercrystals is a very slow process and may take up to several hours or even days.

Recently, the formation of supercrystals from AuNC with a coating based on polyethylene (PEG) in salt solutions was observed at pressures up to 4 kbar. The PEG forms a shell around the AuNC keeping the AuNC happy in its water environment. While salt leads to a reduced solubility of PEG in water (so-called salting out), pressure in the kbar range was reported to compress the PEG shell and thus fosters attractive interaction between the nanocrystals[2,3]. Experiments that searched throughout different pressures and salt types and concentrations

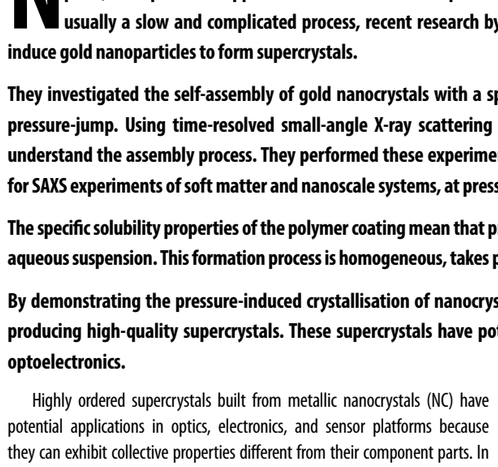

Figure 1: Schematic pressure-salt concentration phase diagram of PEGylated AuNC at the studied concentration of about 1 vol. %. The initial pressure used for the pressure jumps is marked by a blue circle at 2 mol/l RbCl, the final pressures are given by green circles.

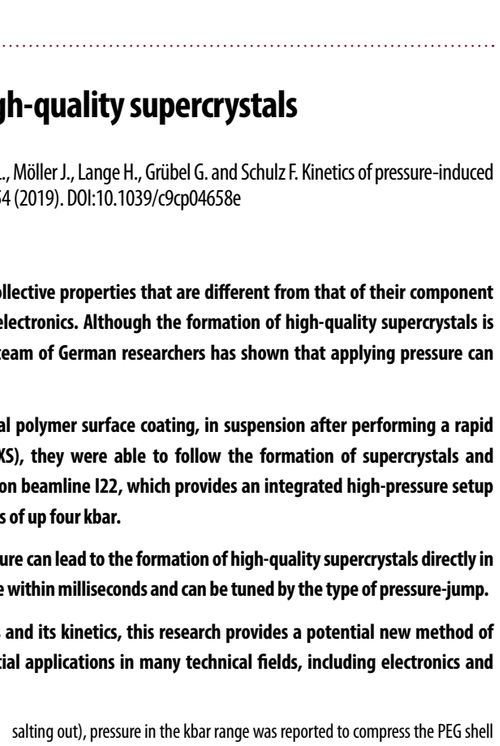

Figure 2: SAXS patterns. (a) Parts of 2D patterns of the dispersion before (initial) and after (final) the pressure jump. The initial data resembles the form factor of spherical particles while the final data shows a rich collection of Bragg reflections matching close-packed supercrystal structure. (b) SAXS curves before (initial) and at different times after the pressure jump as indicated.

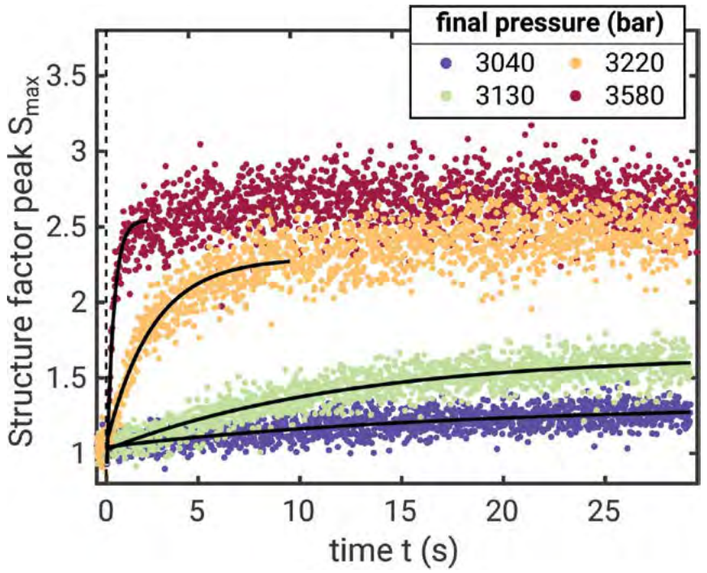

Figure 3: Structure factor peak value (i.e. brightness of the Bragg reflections) as function of time. The dashed line marks the pressure jump at 0 s. Solid lines represent an exponential growth model.

produced a map (phase diagram), Fig. 1, that showed AuNC supercrystal formation is very sensitive to the salt type and concentration [4]. Different salt types include the common sodium and potassium salts, but also rubidium salts. Most importantly, this pressure-induced crystallisation happened within a few seconds and thus promises to be a fast alternative to the standard assembly methods.

Experiments at high pressure demand a special pressure-sustainable sample environment, and beamline I22 offers a dedicated high-pressure sample environment that uses small diamond windows to resist the pressure and allow X-rays through into the sample. I22 is a small-angle X-ray scattering (SAXS) beamline that specialises in studying materials from the smallest, nano-scale, to larger micro-scale. I22 has been used in previous experiments on PEGylated AuNC[2-4] studying the structure of the dispersion up to 4 kbar. Furthermore, because the I22 sample environment was designed for performing pressure jumps within 1/1000th of a second, SAXS experiments can be performed detailing the nanoscale changes during formation of the supercrystals. Gold nanocrystals coated with a PEG called PEGMUA (α-methoxypoly(ethylene glycol)-ω-(11-mercaptoundecanoate)) and dispersed in an aqueous salt solution with rubidium chloride were used. This salt shows the lowest crystallisation pressure (Fig. 1) and thus allows a broader range of pressure to be explored during supercrystillisation. The samples were set on a pressure of 2.7 kbar, just below the crystallisation pressure. I22 is a giant X-ray camera, and by collecting a series of exposures after the pressure jump, changes at the nanoscale can be followed like a movie. More importantly, as the nanocrystals form a supercrystal, the SAXS movie frames will show a new intense spot called a Bragg reflection (Fig. 2). The data in Figure 2 shows onset and evolution of these Bragg reflections after the pressure jump, indicating a fast growth of AuNC supercrystals.

The behavior of the AuNC after the pressure jump was studied quantitatively by extracting the brightness of the supercrystal Bragg reflection from each of the SAXS movie frames (Fig. 3). For all pressure jumps studied, the supercrystal Bragg reflection forms rapidly. The time scale of this process depends on the depth of the pressure jump, i.e. the larger the jump, the faster the growth. Characteristic timescales between few 10s of milliseconds and 10 seconds have been found. In contrast to this crystallisation speed, the melting of the AuNC supercrystals studied by sudden pressure releases has approximately been one order of magnitude slower. Furthermore, the final brightness values of each supercrystal Bragg reflection as well as the position on the movie frame and width of the Bragg reflection itself shows a strong dependence on the pressure jump. In particular, brightness and position are larger and the width smaller for larger pressure jumps. This indicates first an increasing crystalline quality at larger pressure jumps. Second, fine-tuning of next-neighbour distances in the superlattice becomes possible within fractions of the nanocrystal size.

The results demonstrate that pressure variation on nanocrystal systems may help to study and understand phase transitions beyond temperature variations and allow for extremely fast formation of plasmonic supercrystals. Recently, high-pressure SAXS has been extended to supercrystal formation from non-isotropic particles[5]. Fixation of the nanocrystal assembly will enable the preparation of high-quality superstructure with desired properties from concentrated nanocrystal dispersions by 'freezing' the assembly at a certain selection of the width of pressure jump and time.

References:

1. Boles M. A. *et al.* Self-Assembly of Colloidal Nanocrystals: From Intricate Structures to Functional Materials. Chem. Rev. **116**, 11220-11289 (2016). DOI: 10.1021/acs.chemrev.6b00196
2. Schroer M. A. *et al.* Tuning the Interaction of Nanoparticles from Repulsive to Attractive by Pressure. *J. Phys. Chem. C* **120**, 19856-19861 (2016). DOI: 10.1021/acs.jpcc.6b06847
3. Schulz F. *et al.* Structure and Stability of PEG- and Mixed PEG-Layer-Coated Nanoparticles at High Particle Concentrations Studied In Situ by Small-Angle X-Ray Scattering. *Part. Part. Syst. Char.* **35**, 1700319 (2018). DOI: 10.1002/ppsc.201700319
4. Schroer M. A. *et al.* Pressure-Stimulated Supercrystals Formation in Nanoparticle Suspensions. *Phys. Chem. Lett.* **9**, 4720-4724 (2018). DOI: 10.1021/acs.jpclett.8b02145
5. Schroer M. A. *et al.* Supercrystal Formation of Gold Nanorods by High Pressure Stimulation. *J. Phys. Chem. C* **123**, 29994-30000 (2019). DOI: 10.1021/acs.jpcc.9b08173

Funding acknowledgement:
This work is supported by the Cluster of Excellence 'Advanced Imaging of Matter' of the Deutsche Forschungsgemeinschaft (DFG) – EXC 2056 – project ID 390715994. Further funding is acknowledged by the DFG (grant no. SCHU 3019/2-1) and Röntgen-Ångström cluster project TT-SAS (Bundesministerium für Bildung und Forschung project No. 05K16YEA)

Corresponding authors:
Dr Felix Lehmkühler, Deutsches Elektronen-Synchrotron DESY, felix.lehmkuehler@desy.de and Dr Martin A. Schroer, European Molecular Biology Laboratory EMBL c/o DESY, martin.schroer@embl-hamburg.de

Designing metal-organic frameworks to detect chiral molecules

Related publication: Han Z., Wang K., Guo Y., Chen W., Zhang J., Zhang X., Siligardi G., Yang S., Zhou Z., Sun P., Shi W. & Cheng P. Cation-induced chirality in a bifunctional metal-organic framework for quantitative enantioselective recognition. *Nat. Commun.* **10**, 5117 (2019). DOI: 10.1038/s41467-019-13090-9

Publication keywords: Chiral metal-organic frameworks; Ions exchange; Enantioselective recognition; Enantiomeric excess

A molecule that cannot be superimposed on its mirror image is called *chiral*. Chirality can be crucial in chemical processes, as pairs of chiral molecules (known as enantiomers) can have different properties. This is particularly important in pharmaceuticals, where one of the molecules can be a valuable drug while its mirror image is toxic. Identifying unwanted enantiomers is there for a vital task, but it is challenging. State-of-the-art methods to recognise chiral molecules (such as high-performance liquid chromatography, capillary electrophoresis and gas chromatography) can be slow and expensive.

Luminescent sensors are an attractive alternative due to their low-cost, high efficiency and ease of operation. Integrating luminescence and chirality into metal-organic frameworks (MOFs) allows the development of advanced luminescent sensors.

A team of researchers were able to introduce chirality into a zinc-based MOF via simple cation exchange. The material they created has dual luminescent centres and a chiral centre in the pores, and they were able to characterise its chiral binding properties using the Circular Dichroism beamline (B23) at Diamond Light Source.

The researchers showed that this MOF has excellent sensitivity and effectively selects enantiomers. It is notably cheaper to synthesise than current state-of-the-art systems based upon complex, chiral organic linkers. Their methods could potentially be used to detect other chiral molecules. This study paves a pathway for the design of multifunctional metal-organic framework systems as a useful method for rapid sensing of chiral molecules.

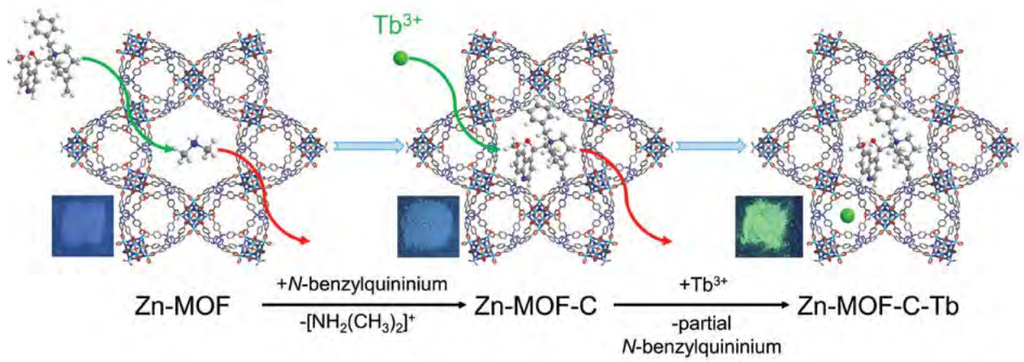

Figure 1: Ions exchange of Zn-MOF. First step: the replacement of $(CH_3)_2NH_2$+ with N-benzylquininium cations. Second step: the lead-in of minute quantities of Tb^{3+}. The inserted photos were taken under 254 nm irradiation with Xe ultraviolet lamp. Green ball stands for Tb, blue for N, gray for C, white for H and turquoise for Zn.

Chirality is crucial to many chemical processes in pharmacy, agriculture and biology. Enantiomers often display different properties in these processes and, in particular cases, certain isomers can cause fatal effect on living cells[1]. Therefore, the recognition of enantiomer is a vital but challenging task. State-of-the-art methods to recognise chiral molecules usually require capital instrument, such as high-performance liquid chromatography, capillary electrophoresis or gas chromatography with high running cost and delays in response. By contrast, luminescent sensors have attracted great attention for their easy-operation, low-cost, high efficiency and ideal portability[2]. To construct a chiral luminescent sensor, chiral materials that show selective binding to certain chiral enantiomers are required. Small organic chiral molecules, especially the binaphthyl and its derivatives, and macrocyclic rigid scaffolds have been studied attentively[3]. These materials, however, have limited recyclability and are often subject to high cost and synthetic challenges.

The theory and applications of coordination chemistry have been greatly promoted by the research on metal-organic frameworks (MOFs) over the last two decades with their tunable chemical composition and tailored-to-property crystal structures. Due to the designable functionality and porosity of MOFs, a wide range of applications, such as chemical recognition, gas storage and separation, and catalysis, have been studied[4]. Small molecules such as volatile organic compounds, persistent organic pollutants and large molecules such as biomakers and, in exceptional cases, chiral molecules can be recognised by designed MOFs via luminescence sensing which is facile for operation. Compared with other luminescence materials, porous materials have the ability of adsorbing molecules into the pores achieving local enrichment. However, the recognition of chiral molecules remains a highly challenging task due to the similar interactions of the enantiomers with the MOF host.

To exhibit the function of chiral recognition and discrimination, MOFs have to be chiralised. Currently, there are three main approaches to construct chiral MOFs: (i) direct synthesis using chiral ligands, (ii) chiral-template synthesis and (iii) post-synthetic chiralisation. All these methods introduce the chirality to the frameworks of MOFs and usually rely on the use of complex chiral ligands that require multi-step synthesis and purification. As a promising alternative, the introduction of chirality to the pores of MOFs could be easily conducted

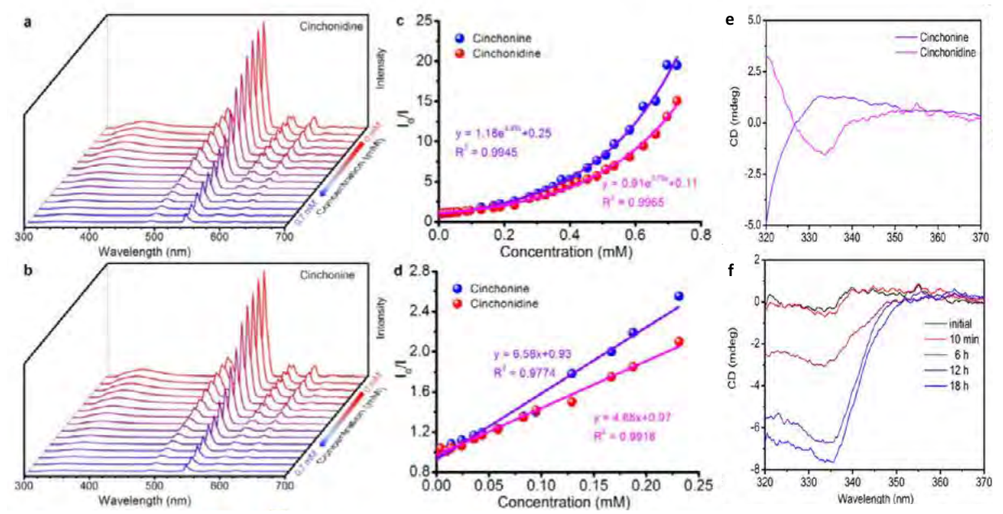

Figure 2: a, b Emission spectra of Zn-MOF-C-Tb dispersed in DMF upon incremental addition of Cinchonidine and Cinchonine. c, d Fluorescence intensity changes at 544nm and lower concentrations (the solid lines are fitting results). e, CD spectra of Cinchonidine (pink) and Cinchonine (violet) in DMF. f, CD spectra the of the equal proportion of the Cinchonidine and Cinchonine mixture with the addition of Zn-MOF-C-Tb showing in solution the increased fraction of the unbound Cinchonidine as a function of time as Cinchonine is sequestered by Zn-MOF-C-Tb.

via exchanging the guest molecules or counter ions with chiral molecules or ions, which to our knowledge has remained unexplored to date. On the other hand, although numerous chiral MOFs containing luminescent centers have been reported, very few of them can be used as sensors for enantioselective recognition because of the very small difference of host-guest interactions between the enantiomer and the MOF host. The introduction of additional chiral binding sites could effectively overcome this problem.

Here, we report the introduction of a commercial optically pure compound, N-benzylquininium chloride, with five chiral sites into a luminescent Zn-MOF ($[(CH_3)_2NH_2]_{1/2}[Zn_2(adenine)(TATAB)O_{1/4}]\cdot 6DMF\cdot 4H_2O$, H_3TATAB = 4,4′,4″-s-triazine-1,3,5-triyltri-p-aminobenzoic acid) that contains dimethylamine cations in the one-dimensional hexagonal channels[5], to generate Zn-MOF-C, which exhibits targeted chirality. We then introduced Tb^{3+} as the second luminescent center into the channels of Zn-MOF-C to produce Zn-MOF-C-Tb. Importantly, this chiral and luminescent bi-functional MOF with dual luminescent centers has enabled the quantitative enantioselective recognition of chiral molecules for the first time, demonstrated by the epimers of Cinchonine and Cinchonidine, which are potent antimalarial drugs with different half lethal dose and also used as asymmetric catalytic agents. Thanks to the dual luminescence from both the ligand and Tb^{3+}, the enantiomeric excess (ee) value of the epimers can be determined based upon the ratio of luminescence from two centers. Zn-MOF-C-Tb has shown general applicability towards a range of epimers and enantiomers with excellent stability and reusability.

Although the lead-in of the chiral cation is easy and controllable, it is a challenge to characterise the success of the introduction directly by single crystal X-ray diffraction because of the unambiguous determination of the location and orientation. In this case, we attempted to use solid-state circular dichroism, ^1H nuclear magnetic resonance, elemental analyses and thermal gravimetric analyses to confirm the existence of this cation in the pores. Unfortunately, also because of the low contents of the chiral cations compared with the framework, we could not detect the obvious Cotton effects on JASCO J-715 circular dichroism. Thanks to the forceful beamline at Diamond, we found the obvious negative Cotton effects of our cation-exchanged MOF. This further certificated the chiral cation in the pores.

In summary, we report a novel strategy to construct bifunctional (chiral and luminescent) MOFs for enantioselective fluorescence recognition and quantitative determination of ee values for enantiomers. The competition for the absorption of the enantiomers to the post-modified pore chirality is responsible for the recognition property. Based upon the methods developed here, anionic MOFs can be generally modified to be used for enantioselective fluorescence recognition, paving a new pathway for the design and development of new functional sensors of organic chiral molecules.

References:

1. Wang Y. *et al.* Emerging chirality in nanoscience. *Chem. Soc. Rev.* **42**, 2930 (2013). DOI: 10.1039/c2cs35332f
2. Jung H. S. *et al.* Recent progress in luminescent and colorimetric chemosensors for detection of thiols. *Chem. Soc. Rev.* **42**, 6019 (2013). DOI: 10.1039/c3cs60024f
3. Zhang X. *et al.* Recent advances in development of chiral fluorescent and colorimetric sensors. *Chem. Rev.* **114**, 4918 (2014). DOI: 10.1021/cr400568b
4. Zhou H. -C. *et al.* Introduction to metal-organic frameworks. *Chem. Rev.* **112**, 673 (2012). DOI: 10.1021/cr300014x
5. Du M. *et al.* Ligand symmetry modulation for designing a mesoporous metal-organic framework: dual reactivity to transition and lanthanide metals for enhanced functionalization. *Chem. Eur. J.* **21,** 9713 (2015). DOI: 10.1002/chem.201500457

Funding acknowledgement:

This work was supported by the National Natural Science Foundation of China (grant numbers 21622105, 21861130354, and 21931004), the Natural Science Foundation of Tianjin (grant number 18JCJQJC47200), and the Ministry of Education of China (grant number B12015). S.Y. and W.S. acknowledge the receipt of a Royal Society Newton Advanced Fellowship. We thank Prof. Shou-Fei Zhu from Nankai University for his helpful discussion on chiral recognition. We thank Diamond Light Source for access to Beamlines B23 and I19.

Corresponding author:

Dr Wei Shi, Key Laboratory of Advanced Energy Materials Chemistry (MOE), Nankai University, shiwei@nankai.edu.cn

Integrated Facilities and Collaborations

With a large number of scientific collaborations and integrated facilities on site, Diamond Light Source is in the unique position of being able to offer a diverse and powerful resource for the advancement of research. With a breadth of techniques available, and a dedicated team of expert scientists, these complementary assets continue to allow us to enable inter- and multi-disciplinary research.

The integrated facilities at Diamond have gone from strength to strength, allowing more in-depth and longer-term research to take place, truly taking advantage of the expertise here on campus. With exciting developments in our state-of-the-art facilities, we are able to provide new capabilities through our complementary facilities.

Our collaborations continue to expand and improve, strengthening and gaining momentum as we progressed through 2019. Through the evolution of our existing partnerships, our collaborations have achieved world-changing projects this year across many disciplines. One such collaboration was announced between Diamond and The Pirbright Institute, cementing a long and productive association that has resulted in vital research developments.

These uniquely placed and complimentary resources promise to continue to address 21st century challenges through internationally-leading cooperation.

Integrated Facilities

The electron Bio-Imaging Centre (eBIC)

eBIC is the first high-end cryo-electron microscopy (cryo-EM) facility worldwide to be embedded in a synchrotron, and its user operations mirror the well-established synchrotron beamline model. eBIC was established following the initial award of a £15.6 million grant from the Wellcome Trust, the Medical Research Council (MRC), and the Biotechnology and Biological Sciences Research Council (BBSRC). After successful review by the Scientific Advisory Committee (SAC) in 2018, eBIC is now fully integrated into Diamond's core programme as part of the Biological Cryo-Imaging science group. The partnerships, and the unique location of eBIC at Diamond, enable scientists to combine their techniques with many of the other cutting-edge approaches that the synchrotron offers.

eBIC provides scientists with state-of-the-art experimental equipment and expertise in the field of cryo-EM, for both single particle analysis and cryo-electron tomography. For the academic user programme, eBIC houses four Titan Krios microscopes, a Talos Arctica, a Scios and an Aquilos cryo-FIB/SEM. In addition, a partnership with the University of Oxford allows users to access a Krios in high containment located at Oxford, and a collaboration with Thermo Fisher Scientific provides another Titan Krios and a 200 keV microscope (Glacios) dedicated for industry users.

New cryoEM capabilities have been developed and/or incorporated in eBIC, these include:

- All 4 Krios are equipped with K3 detector
- High-throughput data collection with up to 800 movies/hour was enabled with aberration-free image shift (AFIS) and soon with fringe-free imaging (FFI)
- Development of a cryoCLEM workflow with recent acquisition of Leica cryoCLEM
- Establishment of a Relion pipeline with ISPyB for on-the-fly SPA processing, while in-house tomography pipeline showed promise

There have been several key developments and events for eBIC, including a new collaboration with The Rosalind Franklin Institute and Thermo Fisher Scientific on tomography. eBIC also held a number of successful workshops over the last year, including the 4th 'Cryo-EM Sample Preparation Workshop' in November 2019, which focused on teaching new cryo-EM users how to prepare samples for imaging in a three day, intensive hands-on course. This was supported by the electron microscopy facility at the Astbury Biostructure laboratory at the University of Leeds, the Institute of Structural and Molecular Biology at Birkbeck College, the Division of Structural Biology at the University of Oxford (STRUBI), MRC Laboratory of Molecular Biology, Thermo Fisher Scientific, Leica Biosystems, TTP Labtech, CryoSol-World and Quorum Technologies. The first hands-on practical microED workshop was held in November 2019 in collaboration with Thermo Fisher Scientific, which attracted overwhelming applications. Leading experts in microED, including Tamir Gonen, Xiaodong Zou and David Waterman, presented lectures in the three day workshop.

The Scios and Aquilos cryo-focused ion beam scanning electron microscope at eBIC started its user program in May 2019, following a commissioning period (October 2018 – March 2019). eBIC is the first and only facility to date offering a user service program on cryoFIB/SEM. During the past year, eBIC has set up a workflow for microED of nanocrystals and thin crystal lamella. We hosted a microED workshop on practical data collection and data processing using DIALS in November 2019. A commissioning call for microED proposals will be announced once we are back to normal schedule. Additionally, eBIC director Dr Peijun Zhang gave 20 invited or keynote presentations at international meetings. Several eBIC scientists also presented at national and international meetings.

To date, eBIC has produced 112 user publications, nearly doubled from the last report.

The electron Physical Science Imaging Centre (ePSIC)

ePSIC at Diamond is a national centre for aberration-corrected transmission electron microscopy. Since its opening in 2017, researchers from around the world have brought their samples to ePSIC to image their atomic structure with sub-ångström resolution.

The two transmission electron microscopes which make up the centre, a JEOL ARM 200 and a JEOL GRAND ARM 300, were brought to Diamond through collaboration with Johnson Matthey and the University of Oxford respectively.

The ARM 200 (E01) is a state-of-the-art probe-corrected analytical microscope capable of imaging, electron energy loss spectroscopy and X-ray spectroscopy at atomic resolution. It is aligned at accelerating voltages (incident electron beam energies) of 80 and 200 keV.

The ARM 300 (E02) is a dedicated imaging instrument aligned across a wide range of accelerating voltages (30 - 300 keV). This enables the experimental conditions to be carefully tailored to the specific sample being studied. The ARM300 is both probe- and imaging-corrected and has numerous detectors including a fast direct electron detector, which can operate at up to 2000 fps. This detector is used for both fast movie acquisition when operating in broad-beam Transmission Electron Microscopy (TEM) mode and for the collection of large arrays of far-field diffraction patterns (4D-STEM) when operating in focused probe STEM mode. These combined capabilities have enabled ePSIC to become an international leader in cutting-edge material science electron microscopy and is a unique resource within the UK.

ePSIC have recently added a Focused Ion Beam microscope (E03) and low energy ion slicer to its arsenal, enabling the preparation of incredibly thin samples – just a few-hundred atoms thick – for further analysis at ePSIC. This capability will enable users, who might otherwise have not been able to prepare the high quality samples required for atomic resolution imaging, to access ePSIC.

With *in situ* sample holders, users at ePSIC can perform variable temperature measurements from 100 to 1,600 K to directly image the atomic structure of materials during thermally driven transitions. Staff at ePSIC have recently commissioned two new sample holders for *in situ* experiments. These new capabilities include the ability to image samples in the microscope while passing an electric current through them and the ability to transfer samples to the microscope without exposing them to air.

The Membrane Protein Laboratory (MPL)

The Membrane Protein Laboratory (MPL) is a well-established, state-of-the-art facility that enables membrane protein research. Since its inception, the MPL has supported visiting researchers from all around the world to work towards the visualisation of their membrane protein of interest at atomic resolution. Membrane proteins are important targets for medical, agricultural and fundamental research. Approximately half of all approved medicines target membrane proteins while some plant membrane proteins can be used to improve crop yield and resistance towards plant pathogens. Understanding the structure and function of these proteins helps us to develop new medicines.

As a Diamond facility located within the Research Complex at Harwell, and as an established member of the Harwell Cell and Structural Biology Partnership, MPL staff and visiting scientists are at the centre of structural biology on the Harwell campus. Traditionally we have grown membrane protein crystals, an extremely difficult step on the way towards solving a membrane proteins structure. Having a dedicated laboratory with cutting-edge equipment, close to the experimental stations where membrane protein structures can be solved, greatly enhances scientists' ability to successfully crystallise membrane proteins and further our understanding of these important targets. Recently with the cryo-EM revolution, a new method has been opened up providing an alternative route towards solving the structure of these difficult to work with proteins. The close proximity of the MPL and eBIC is now enhancing our ability to understand the structures of membrane proteins by cryo-electron microscopy. We are currently in the process of recruiting a joint postdoctoral research associate across the MPL and eBIC to improve our capabilities further in the membrane protein and cryo-EM fields.

The MPL is open to user applications from anywhere in the world, and proteins crystallised here have been used in experiments in other facilities. Recently published work in Nature Communications[1] details research supported by MPL facilities that has led to the structure of ferric-enterobactin in complex with its transporter protein (PfeA) from *Pseudomonas aeuginosa*. Bacteria use small molecules called siderophores to scavenge and bind to iron. These complexes are imported into the periplasm through outer-membrane transporters such as PfeA. The crystal structure has been solved by the Naismith group of a mutant ferric entrerobactin receptor from *P. aeruginosa* and demonstrates that PfeA recognises enterobactin using extracellular loops distant from the pore. These results will provide starting points that could lead to the rational development of siderophore-antibiotic Trojan horse conjugates able to hijack more efficiently the enterobactin-dependent iron uptake system in *P. aeruginosa*.

In Collaboration with the National Physics Laboratory and B23 beamline at Diamond Light Source research was published in the International Journal of Molecular Sciences[2] that discusses various biophysical methods for the characterisation of membrane proteins. This included characterisation of membrane protein-detergent complexes by *in situ* dynamic light scattering, multi-angle light scattering, Circular Dichroism of Membrane Proteins and Lipidic Cubic Phase Fluorescence Recovery After Photobleaching (LCP-FRAP).

1. Moynie. *et al*., 2019. DOI:10.1038/s41467-019-11508-y
2. Kwan. *et al*., 2019. DOI:10.3390/ijms20102605

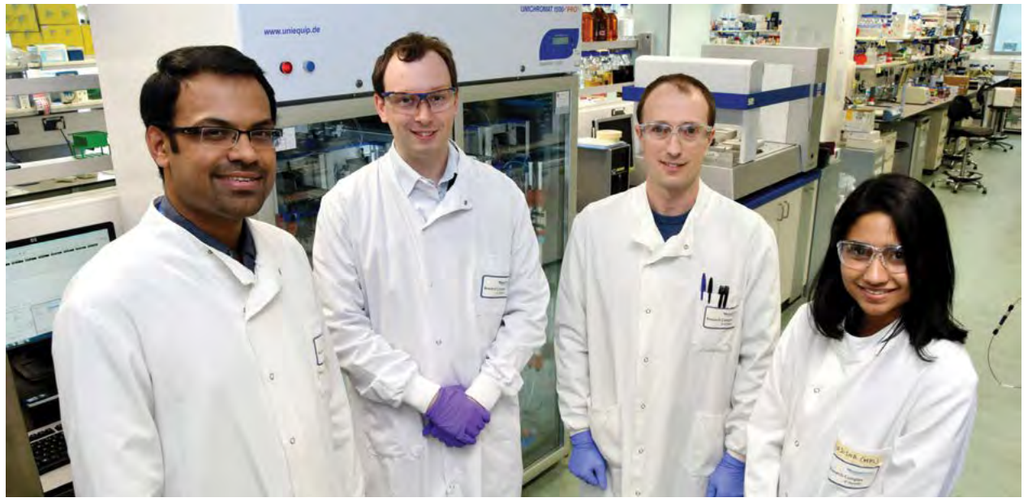

MPL Team.

XChem

Diamond's XChem facility specialises in X-ray structure-accelerated, synthesis-aligned fragment medicinal chemistry. Integrated into the I04-1 beamline and nearby Lab XChem, offering a highly streamlined process for full X-ray screening experiments. XChem allows up to 1,000 compounds to be screened individually in less than a week (including 40 hours of unattended beamtime). The process covers soaking, harvesting, automatic data collection, and data analysis.

This year has seen some exciting developments for the XChem facility. The team had already added another 50,000 samples to its experience by September 2019, half the output of the previous four years in eight months, following speedups in the beamline and the consolidation of its core team. Differently from its early operation, from 2019 XChem started offering access through two routes: exploratory projects, where only one eight hour shift is allocated and established projects, for which 32 hours of beamtime are awarded. The expectation is that projects can establish first whether they are ready for a fragment campaign and enrich the case for a full fragment campaign. The programme is now operating with a dedicated 40 hours of beamtime per week, split between commissioning projects, in-house projects and XChem projects.

The XChem computational team secured and started implementing an exciting collaboration with Janssen Pharma. This project will take the Fragalysis software, which reviews XChem hits and generates the next follow up series, to the next level with the STFC-IRIS cloud computing infrastructure and new web interfacing technology. The objective is to make the XChem datasets widely available through a much more responsive approach to data delivery.

From Spring 2019 XChem users were able to run even faster gridscans and X-ray scans using the new beamline electronic controls including the Zebra signal controls box in line with Diamond's other MX beamlines. Improvements to dataset delivery times kept building 22 datasets per hour in January 2019 to 28 per hour in December 2019 using the new, faster, fully automated X-ray centring mode.

Since February 2020, Diamond is ensuring that it is doing everything possible to support researchers in their efforts to discover more about global disease challenges - such as COVID-19 - by working on non-infectious samples.

One such research is the Covid Moonshot project where an XChem campaign on the main protease (M^{pro}) enzyme from SARS-CoV-2 from the Walsh group at RCaH was undertaken, yielding 91 M^{pro}:fragment complexes deposited on the Protein Data Bank, of which 66 fragment molecules in the M^{pro} binding site. That campaign was used to leverage a consortium effort with Oxford University scientists and the PostEra and Enamine companies to crowdsource designs for a molecule in the hope of shortcutting a process that usually takes years. The non-profit endeavour has yielded more than 3,500 designs, with one compound already being hailed as a therapeutic possibility. An effort that delivered results in weeks instead of months, subsequently released in an open science approach. A diagram of the effort undertaken is seen below (credit: David Owen/Walsh group).

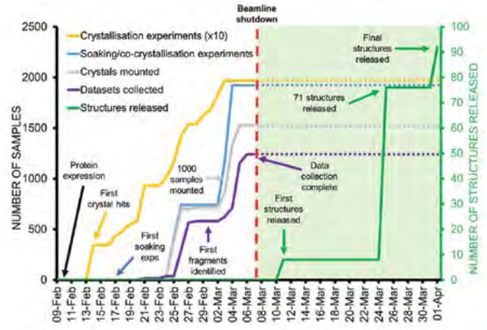

Timeline of crystallographic fragment screen. Credit David Owen/Walsh team in Crystallographic and electrophilic fragment screening of the SARS-CoV-2 main protease, Nature Comms (accepted).

XFEL Hub

Funded initially by the Wellcome Trust and the Biotechnology and Biological Research Council (BBSRC), and now within the annual Diamond operations budget, the XFEL Hub at Diamond aims to provide expertise and support to the UK community engaged in XFEL-related life science research; from experimental conception to beamtime proposals, through sample preparations and testing, to XFEL data collection, analysis and publication. The XFEL Hub is integrated within the Macromolecular Crystallography Science Group. Our Diamond based activities continue to include organising and running the block allocation group – Dynamic Structural Biology at Diamond and XFELs – for serial crystallography and time-resolved studies.

We participated in user-assisted commissioning of an on-demand picolitre sample delivery method for serial femtosecond crystallography (SFX) in the downstream interaction region at the SPB/SFX Instrument at the European XFEL in Hamburg, Germany. These preliminary results demonstrated on-demand 30 picolitre droplet delivery that was synchronised to European XFEL pulse train with an intra-train frequency of 28 kHz and without wasting sample between pulse trains. The XFEL Hub travel support program for UK scientists participating in XFEL experiments around the world remains open and active. This helped researchers conduct their experiments at the European XFEL, SACLA in Japan, SwissFEL in Switzerland and PAL-XFEL in South Korea as well as in the coming months at the LCLS in the USA. Thus, the XFEL Hub at Diamond and UK scientists are taking advantage of all five facilities.

With funding support from the Wellcome, BBSRC/UKRI, The Rosalind Franklin Institute and Diamond Light Source, Dr Orville, Jasper van Thor and Xiadong Zhang organised the 'Dynamic Structural Biology Workshop: Examining the Life Science Case for a UK XFEL' on 5th November 2019 at the Francis Crick Institute in London. It attracted nearly 200 participants and included speakers highlighting recent progress with XFELs, cryo-EM and NMR. The workshop was part of the larger effort to develop the science case for a potential UK XFEL. To that end, we are seeking input to the process from across the scientific community. More information can be found at this link: https://www.clf.stfc.ac.uk/Pages/UK-XFEL-science-case.aspx

Collaborations

The Rosalind Franklin Institute

Diamond became a founding member of the Rosalind Franklin Institute, joining ten Universities and UKRI-STFC. A number of joint staff positions already exist between our two organisations. Diamond is a partner in a major initiative of the Franklin, in collaboration with Thermo Fisher Scientific, to develop advanced cryo-electron tomography instrumentation and methods, the AMPLUS project, which is funded in large part by the Office of Life Sciences to the Franklin and Thermo Fisher Scientific. AMPLUS brings in Diamond expertise from the Macromolecular Crystallography and Biological Cryo-Imaging science groups, in particular the electron Bio-Imaging Centre (eBIC) and the Versatile MX micro (VMXm) beamline, as well as leveraging the extensive expertise and experience Diamond has in nanoscale engineering, that is being brought to bear to develop a vision for next generation electron tomography and electron diffraction instruments.

Another key contribution of Diamond to this collaboration is partnering in the development of electron imaging simulation software that not only assists in the optimisation of analysis software, but can also drive the specification and design of electron microscope instrumentation. Diamond's substantial experience in nanoscale engineering is being brought to bear in developing a vision for next generation electron tomography and electron diffraction instruments. A major Diamond undertaking in this area will be HeXI (Hybrid electron-X-ray Instrument), a dedicated electron diffraction beamline for sub-micron macromolecular and small molecule crystallography.

In future we expect that the Franklin will form a productive symbiotic relationship with Diamond, whereby the Franklin is able to address high-risk high-reward challenges in the life sciences and have Diamond partner in these novel developments turning them into user accessible facilities, while using its wealth of expertise in instrumentation, methods, software development and high performance computing to feed into Franklin developments.

Diamond looks forward to a long and productive partnership.

The University of Manchester at Harwell

The University of Manchester at Harwell (UoMaH) is hosted by Diamond as part of the partnership The University of Manchester (UoM) is setting up with facilities at Harwell. UoMaH provides the interface with the Harwell national facilities, enabling UoM researchers to access world-class research at Diamond and all the Science and Technology Facilities Council (STFC) facilities at Harwell, including the ISIS Neutron and Muon Source (ISIS), Scientific Computing Department (SCD) and the Central Laser Facility.

UoMaH is comprised of core administrative and technical teams and research fellows and their groups. The core technical team specialises in developing sample environments and equipment in support of experiments, involving high risk materials and extreme sample environments, fielded at the national facilities. UoMaH research fellows, are affiliated with different departments within the University's Faculty of Science and Engineering, and pursue research in critical themes to both the University and the facilities. Currently, UoMaH has a growing contingent of fellows based at Harwell; the two fellows working on resilience and catalysis are sponsored by Diamond and the one fellow working on fusion sponsored by ISIS. Alongside them, five further fellows and their groups are based in Manchester. The fellows strengthen the University's link with Harwell by bringing their research, networks and new users from industry and Faculty academics to Diamond.

In the past year, UoMaH has built new, and deepened existing, connections with Diamond and the other Harwell facilities by engaging in Harwell events and hosting colloquia. The last of these brought together over 50 people from across campus and was transmitted virtually back to Manchester.

In May 2019, UoMaH was joined by representatives from Diamond, ISIS and SCD at the first of their annual roadshows in Manchester. Senior staff from the University, STFC and Diamond introduced the new collaboration to an audience of university staff and key workers from Harwell. Case studies illustrated the research undertaken at ISIS, SCD and Diamond and participants contributed to sandpit sessions identifying future opportunities and areas for development for UoMaH. The event has stimulated attendees' engagement in new beamtime experiments and requests for new specialist equipment from the UoMaH core team.

We are engaging with Diamond in our teaching and learning mission; in June 2019, UoMaH welcomed 33 PhD students, to Diamond and ISIS, as part of the Materials for Demanding Environments and Advanced Metallic Systems CDTs.

Finally, in November 2019 UoMaH hosted a meeting at Diamond, linking up current capabilities at Harwell national facilities with researchers working on nuclear materials. Attendees from eight UK universities and national laboratories discussed near term activities, new sample environment requirements and the means to work together to achieve these demanding experiments. UoMaH will work with Diamond and the Dalton Nuclear Institute to organise a second event to develop some of these ideas further and to explore more ambitious projects for the future.

UK Catalysis Hub

Catalysis is a core area of contemporary science, engineering and technology that has substantial economic and societal impact, and is of significance to the UK's Industrial Strategy, making it a strong area of focus for Diamond. The physical home of the UK Catalysis Hub – a national network with over 40 collaborating universities – is located next to Diamond at the Research Complex at Harwell (RCaH). It provides a platform for researchers to work collectively, and to gain frequent access to the synchrotron, alongside other facilities at Harwell.

The UK Catalysis Hub was established in 2013 with funding from the Engineering and Physical Sciences Research Council (EPSRC). An additional £14 million in funding from the EPSRC was committed in October 2018. The Hub seeks to coordinate, promote and advance the UK catalysis research portfolio. The project has four new interrelated themes:

Core

- Optimising, Predicting and Designing New Catalysts
- Catalysis at the Water Energy Nexus
- Catalysis for the Circular Economy and Sustainable Manufacturing

The Hub promotes a whole system approach to the study of catalysis combined with high throughput, which allows optimal experiments to be carried out which shorten the path to development of commercially useful products and promote the UK catalysis effort and expertise on a global stage.

One of the main continued benefits of the Catalysis Hub is sustained access to a synchrotron radiation source. Professor Andrew Dent, Diamond's Deputy Director of Physical Sciences, explains, "The UK Catalysis Hub has a Block Allocation Group (BAG) on the X-ray Absorption Spectroscopy (XAS) beamline B18 at Diamond. The Hub coordinates the experiments they perform in that time, which allows them to more effectively carry out their research."

This access route increases the efficiency of data acquisition and allocates small amounts of time for proof of concept investigations and rapid access for *in situ* and *ex situ* applications before a full study starts. Applications are judged by a panel of expert academics and beamline scientists, who consider (i) the quality of the underpinning science, (ii) the likely success of the experiments, (iii) bringing in new users of synchrotron radiation, and (iv) coordinating time effectively to maximise efficiency. This opportunity is open to every academic working in catalysis in the UK.

Machine Operation and Development

Richard Walker, Technical Director

In 2019/20, our 13th year of operations, a total of 208 days (4,992 hours) were scheduled for beamline operations, 203 days of User Mode, and 5 beamline start-up days. The majority of the beam delivery was in standard multibunch mode (900 bunch train) or "hybrid" mode (686 bunch train + a single bunch) with total current of 300 mA. In addition, there was one day in May 2019 and two days in August 2019 of "low-alpha" mode to produce short bunches (3.5 ps rms). All beamline operations were carried out in top-up mode.

The annual operating statistics are shown in Fig.1. The Mean Time Between Failures (MTBF) for the year was 104.7 hours, an improvement over the previous year and our 5th successive year exceeding the target minimum of 72 hours. The overall uptime (beam delivered as a percentage of scheduled hours) also remained high at 98.2%.

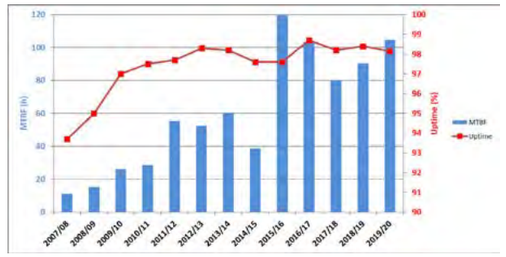

Figure 1. Mean Time Between Failures (MTBF) and Uptime by operating year.

Cryogenic Permanent Magnet Undulator

The first of a new series of cryogenic permanent magnet undulators (CPMUs) has been installed in Diamond, to provide an increase in photon flux on a number of beamlines, especially in the hard X-ray region. These devices differ from an earlier type of CPMU that was installed several years ago, in that they use more advanced permanent magnet material PrFeB, which is cooled to liquid Nitrogen temperature (77K) rather than NdFeB cooled to 150K. The new device (see Fig. 2) was designed and built in-house.

RF upgrades

Diamond's two new normal conducting radiofrequency (RF) cavities are now fully operational in the storage ring, providing a valuable back-up to the superconducting cavities. Use of these cavities in recent low-alpha special beam conditions for users, allowed the superconducting cavities to be operated at a reduced voltage, resulting in a clear increase in reliability. Diamond has recently taken delivery of a third normal-conducting cavity, that will be installed in the storage ring in 2021, to give further machine resilience.

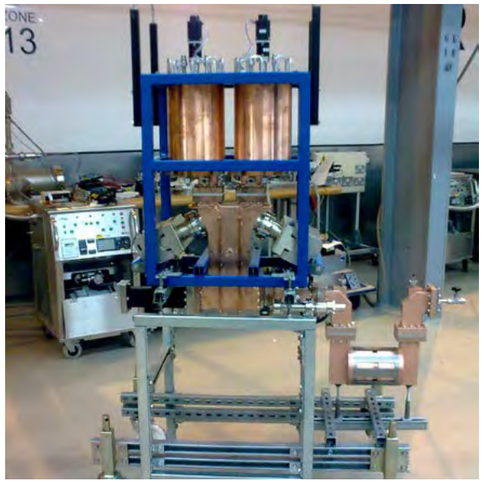

Figure 3. The SLED cavity during assembly on its support structure.

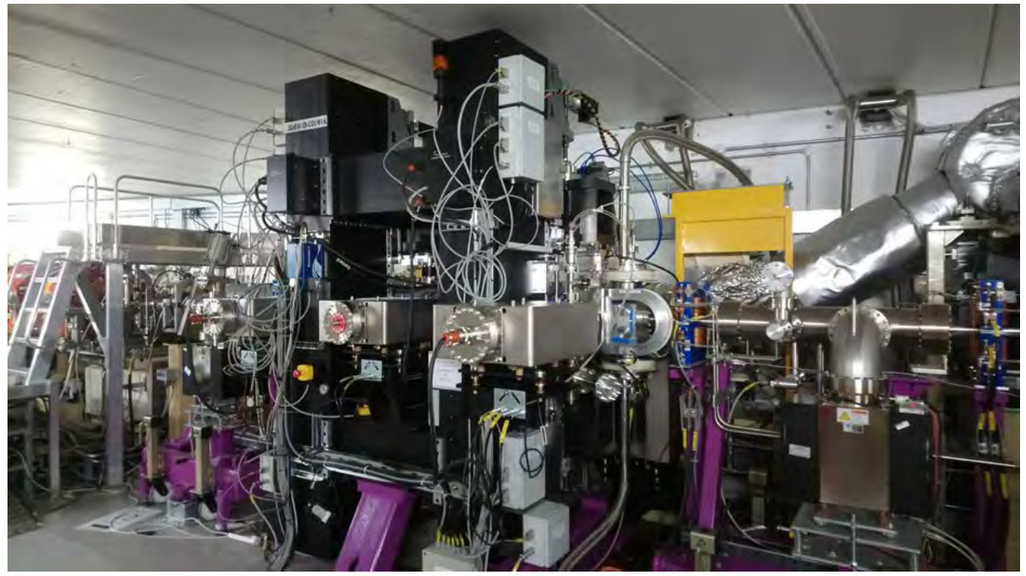

Figure 2. The recently installed Cryogenic Permanent Magnet Undulator.

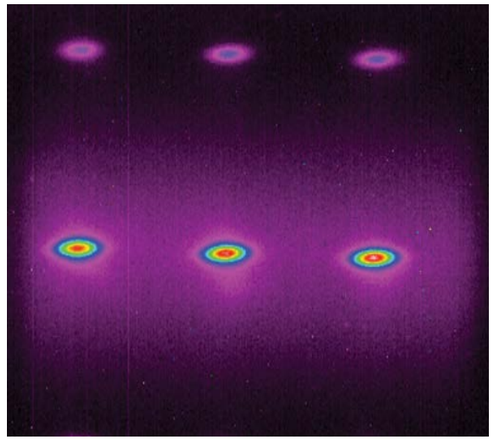

Figure 4. X-ray pinhole camera images of the electron beam in the storage ring. The images are from nine identical 12.5 micron pinhole apertures, but only the central three are illuminated fully by the X-ray beam.

Accelerating fields in the normal conducting cavities are regulated by two new digital low-level RF (DLLRF) units, which offer an adaptability and flexibility that the previous analogue control loops did not have. Further DLLRF units are in development to give a common platform for all RF cavities.

An RF pulse-compression, so-called SLED (SLAC Energy Doubler) cavity, is being tested in the linear accelerator (linac). The SLED cavity (see Fig. 3) will double the instantaneous power delivered by either one of the two high-power klystron amplifiers, ensuring continuity of linac operation even in the event of failure of one of the two klystrons.

Diagnostics developments

Emittance is a key performance parameter for all modern synchrotron light sources, since it determines the brightness of the radiation served to user beamlines. Diagnostics with high spatial resolution are needed both to measure the emittance accurately, particularly in the vertical plane, but also provide a suitable signal for a feedback system. Diamond uses X-ray pinhole cameras to image the electron beam via its emitted X-rays. To improve the spatial resolution of the cameras, we are investigating the use of LIGA (X-ray lithography) technology. LIGA enables the fabrication of high-aspect ratio structures using highZ materials, such that the pinhole aperture size can be precisely controlled at the micron level, much more precise and reproducible than our standard pinholes built using tungsten blades and shims. Furthermore, each 10mm x 10mm LIGA screen can have 15 different pinhole sizes (in order to optimise the resolution) with nine apertures each, providing redundancy in case of any deterioration (see Fig. 4).

The Diamond Multi-Bunch Feedback (MBF) system requires a critical timing reference derived from the machine master oscillator, that locks data converter sampling to the bunch arrival time at a Beam Position Monitor (BPM) output. Any operational adjustment to the Radio Frequency (RF) and injection systems can change this timing relationship and require manual adjustment, typically every 20 days. Recently, a Delayed Orbit Reference Improvement Scheme (Doris) has been developed, that directly phase locks the MBF timing to the BPM outputs, automatically compensating for any operational changes to the beam timing. Doris has been in operation in the storage ring now for three months, and no operator manual adjustments have been needed during that time. Fig. 5 shows the significant improvement in phase stability of the MBF since Doris was installed.

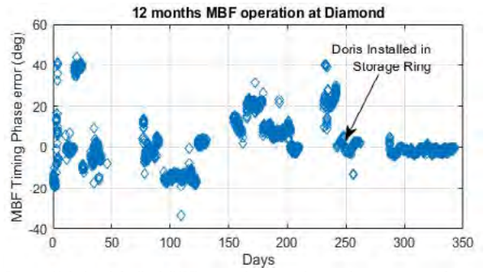

Figure 5. Multi-bunch feedback (MBF) timing phase error showing the improvement after "Doris" was installed.

Diamond-II

Work on Diamond-II, the planned upgrade of Diamond, has also progressed significantly during the year. A draft Conceptual Design Report (CDR) was reviewed and endorsed by an international committee of experts in April 2019, and the final version of the CDR subsequently published in May 2019. We then entered the Technical Design Report phase of the project which should complete at the end of 2021. An international Machine Advisory Committee has been established to provide advice to the project, which met for the first time in February 2020. Accelerator physics, engineering and vacuum studies are continuing. Fig. 6 shows an example of a full CAD model for one of the four girder types, which makes up one half of a cell of the storage ring.

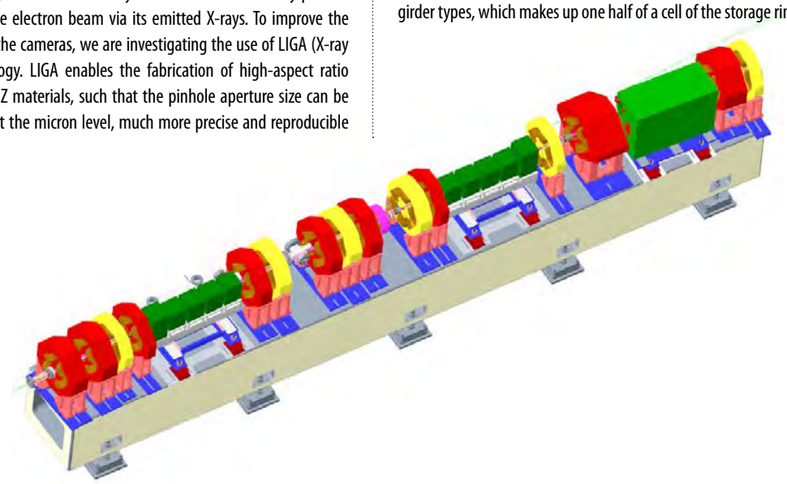

Figure 6. 3D CAD model of one of the Diamond-II girders: green – dipole (bending) magnets, red – quadrupole (focusing) magnets, yellow – sextupole (1st order non-linear correction) magnets, pink – octupole (2nd order non-linear correction) magnets.

Optics and Metrology Group

Kawal Sawhney, Optics and Metrology Group Leader

The Optics and Metrology Group is guiding Diamond Light Source and other facilities with state-of-the-art capabilities[1-6], which it continues to expand. For current upgrades and Diamond-II, we are enhancing our techniques for simulation, manufacturing and measurement. Our new ion beam figuring system will allow rapid manufacture of complex, precise mirrors. Novel adaptable refractive correctors are boosting the effectiveness of nano-focusing optics. *Ex situ* measurements of vibration and positional accuracy are being brought to 50 nrad and nm precision. X-ray topography is now a standard tool for detecting micron-sized surface defects on crystals. The versatile optics Test Beamline (B16) continues to support all these efforts while running a well-subscribed program of external user experiments. These advances continue to keep Diamond competitive worldwide.

The Optics Metrology Lab (OML) and the Precision Metrology Lab (PML) continue to provide high quality testing of beamline X-ray optics and motion systems. Both labs provide a valued service to help assemble, install, and pre-commission major beamline components, thereby improving the scientific output of all beamlines.

To remain competitive with other facilities around the world, many beamlines are now actively upgrading their optics and motion stages, including: crystal monochromators with angular vibrations less than 50 nrad rms; X-ray mirrors with slope errors better than 100 nrad rms; and micro- and nano-positioning stages with nm level parasitic errors. To keep one step ahead of such developments, the OML and PML are both embarking on a series of innovative research and development projects. The aim is to improve the accuracy of Diamond's metrology instruments and analysis algorithms for measuring distances, angles, and vibrations. To enhance these activities, collaborations have been developed with national metrology institutes such as the UK's National Physical Lab and the Physikalisch-Technische Bundesanstalt (PTB), the National Metrology Institute in Germany.

Monochromatic X-ray topography is now a standard technique available on B16 for inspecting crystal surfaces for micron-size defects. Surface quality can be measured over large areas on test crystals facing up, down or sideways depending on the required mount. White-beam topography is also possible. Topography helped us lead the development of monochromator crystals for the Dual Imaging And Diffraction (DIAD) imaging branch through several trials to success. We are now providing X-ray topography not only to Diamond, but also to commercial users. Our in-house capability ensures that new crystals are fit for purpose at installation.

The planned Diamond-II upgrade brings opportunities and challenges for beamline optics, requiring upgrades to match evolving needs and emerging opportunities in several scientific and technical areas. The Optics & Metrology group is performing extensive optics simulations and optimisation of sources for all beamlines given the new machine characteristics, the analysis and mitigation of thermal load effects on optics, and developing additional metrology capabilities to test high-quality optics. Specifically, this includes a further enhancement of our world-class in-house metrology facility to enable X-ray optics of ~50 nrad rms slope error to be reliably measured and characterised as well as at-wavelength metrology (i.e. using X-rays) complemented with simulations, to allow the development of procedures for fast, automatic optics alignment and for compensation of drift and beam vibrations. The work started a few years ago and will continue throughout the Diamond-II project.

Ion beam figuring (IBF) system

Meeting the X-ray beam performance demands of Diamond's beamlines (in terms of micro/nano-focusing, extreme energy resolution, high coherence, etc.) necessitates the use of mirrors with an ultra-high-quality surface finish, with the most demanding applications requiring deviations from the ideal surface profile of less than 1 nm rms. In the final stages of manufacturing such mirrors, deterministic polishing methods such as ion beam figuring (IBF) are often used. These techniques employ precise measurements of the optical surface and carefully controlled removal of material to produce the desired mirror shape.

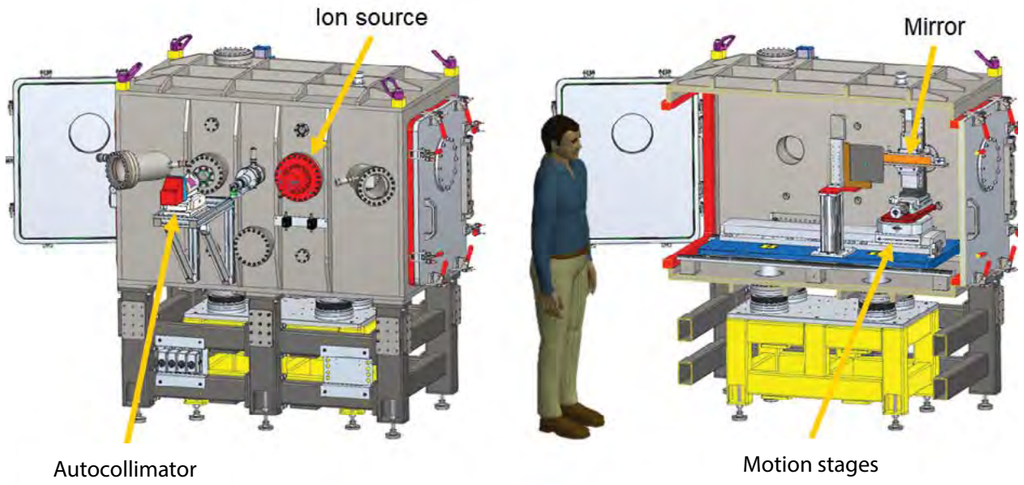

Figure 1: IBF system designed and developed in-house: external (left) and internal (right) views.

A new in-house designed IBF system has recently been developed by the Optics Group to bring high-precision optics finishing capability to Diamond (Fig.1). A DC gridded ion source is paired with a set of apertures to produce a shaped ion beam which erodes the mirror surface as it is moved past by a 4-axis motion system. 'Malcolm' continuous scanning software, previously developed at Diamond, provides precise control of the dwell time at each location on the optical surface to ensure the correct material removal profile is achieved. Onboard optical metrology will allow for rapid surface measurement feedback and is complemented by a wide range of optical and X-ray metrology tools provided by OML and B16.

The IBF system is currently in the early stages of commissioning and calibration, but it is ultimately expected to provide extremely high-quality finishing of mirrors within a much shorter timeframe than can currently be achieved. This capacity for rapid development and testing of mirrors greatly increases the feasibility of novel designs such as multi-lane mirrors and other complex mirror shapes like aspheres.

Adaptable refractive correctors: a new optical device for extreme focusing of X-rays

High-quality mirrors and lenses are commonly used at X-ray beamlines to focus the X-ray beam into small (sub-1 micrometre) focal spots allowing materials to be studied with high spatial resolution. The design and manufacture of X-ray optical elements is highly specialised and at this level, any small imperfections cause the intensity distribution of the focal spot to be spoiled.

The Optics Group have devised a new type of optical element that is able to dynamically correct for the effect of the imperfections by applying a spatially dependent phase shift to the wavefront of the focused X-rays[1]. The new element is known as an "adaptable refractive corrector". The device consists of two phase plates fabricated with a special thickness profile that apply a phase correction to the X-rays as shown in Fig. 2. The phase correction can be varied in form and size by independent adjustment of the positions of the two phase plates, allowing the correction to be adapted to compensate for the unique effect of imperfections in optical elements.

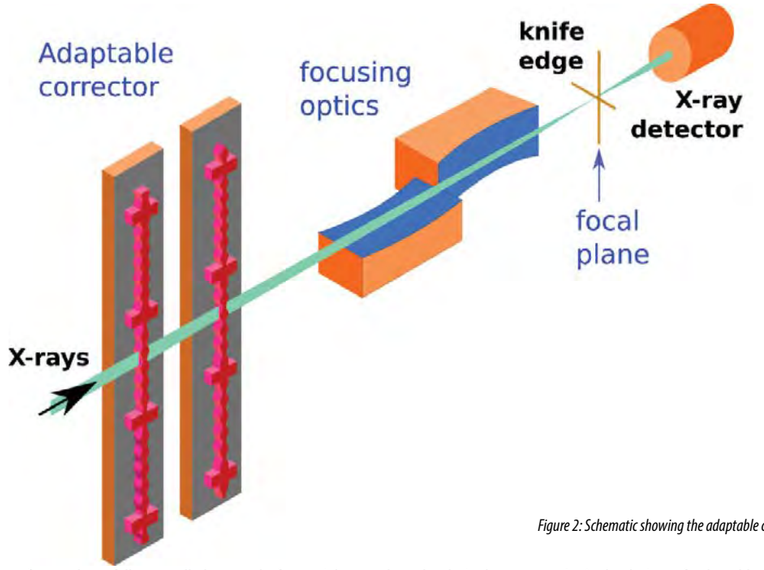

Figure 2: Schematic showing the adaptable corrector with a double mirror system.

A single design of adaptable refractive corrector could be used on different beamlines and with different optical elements to compensate for X-ray wavefront errors. A device was manufactured using microfabrication techniques and was then used on B16 to test a variety of mirror and lenses. A sensitive technique was used to measure the X-ray wavefront, to determine the X-ray phase error at the optical element and to allow the adaptable corrector to be optimised. The measurements showed that after optimisation of the corrector, the effect of the imperfections in the optical elements was reduced by a factor of up to 7.

A further experiment was carried out on the X-ray Imaging and Coherence beamline (I13) in which the adaptable corrector was used to overcome the imperfections of an elliptical focusing mirror. The highly coherent X-ray beam allowed us to achieve a focused beam size after correction of 70 nm, which is close to the theoretical diffraction limit. This demonstrates that such optics will be essential to exploit the planned low-emittance Diamond-II upgrade and future low-emittance X-ray sources elsewhere worldwide.

References

1. Laundy, D. et al. Adaptable refractive correctors for x-ray optics. *Optica* **6**, 1484-1490, (2019). DOI:10.1364/OPTICA.6.001484
2. Wang, H. et al. High-energy, high-resolution, fly-scan X-ray phase tomography. *Scientific Reports* **9**, 8913, (2019). DOI:10.1038/s41598-019-45561-w
3. Hand, M. et al. Ion beam figuring and optical metrology system for synchrotron x-ray mirrors. *Proc. SPIE 11109, Advances in Metrology for X-ray and EUV Optics VIII* **111090A** (2019). DOI: 10.1117/12.2528463
4. Sutter, J. P. et al. 1 m long multilayer-coated deformable piezoelectric bimorph mirror for adjustable focusing of high-energy X-rays. *Opt. Express* **27**, 16121-16142, (2019). DOI:10.1364/OE.27.016121
5. Nistea, I.-T., et al. Controlling an active bimorph deformable mirror with sub-nanometre resolution. *Proc. SPIE SPIE 11109, Advances in Metrology for X-ray and EUV Optics VIII* **111090E** (2019). DOI: 10.1117/12.2529322
6. Nistea, I.-T., et al. The Optical Metrology Laboratory at Diamond: pushing the limits of nano-metrology. *Proc. SPIE SPIE 11109, Advances in Metrology for X-ray and EUV Optics VIII* **1110906** (2019). DOI: 10.1117/12.2529401

A new generation of fast, high-sensitivity X-ray detectors

Related publication: Mykhaylyk V. B., Kraus H. & Saliba M. Bright and fast scintillation of organolead perovskite $MAPbBr_3$ at low temperatures. *Mater. Horiz.* **6**, 1740-1747(2019). DOI: 10.1039/C9MH00281B

Publication keywords: Organoled perovskite; Cryogenic scintillator; Decay time; Light yield

Scintillators are materials that turn ionising radiation into visible light. They're used to detect radiation and have applications in, for example, cancer diagnosis; scintillators can identify the precise location of a tumour. Fast and efficient materials are highly sought-after for such applications, but little progress has been made in identifying new systems in recent decades.

Hybrid metal-organic halide perovskites are attracting considerable attention for photovoltaic applications, and for their extraordinary performance in light-emitting and light-detecting devises. They are also very promising materials for radiation detection and, in particular, for scintillation detectors.

Researchers wanted to investigate the temperature dependence of decay time and scintillation light output of methylammonium lead bromide ($MAPbBr_3$) after excitation with ionising radiation, as these crystals exhibit very bright emission during cooling.

They carried out measurements of scintillation decay curves on the Test beamline (B16), using monochromatic X-ray radiation for excitation. Their results demonstrate that the performance of this new material exceeds that of the best modern commercial scintillators used for X-ray detection. Its properties are indispensable for ultrafast X-ray imaging where sweeping improvement of image quality can be achieved by introducing time-of-flight methods of X-ray detection.

The potential benefits from introducing such technique - reduced exposure to ionised radiation and enhanced signal-to-noise ratio - easily outweigh the need to develop a low-temperature scintillation detector. The moderate cooling requirement and the flexibility of the production technology of the metal-halide perovskites make this a very attractive approach.

Scintillators detect ionising radiation by converting energy deposited in them to a proportional number of photons. They are omnipresent in many areas of physics, security scanners, or medical applications such as nuclear imaging for cancer diagnostics. The ideal scintillator emits a maximum number of scintillation photons per energy deposited, has a high absorption coefficient for gamma quanta, and exhibits a narrow timing profile for its scintillation photons. Brighter and faster scintillator facilitate better timing resolution which is crucial for measuring the time of the radiation interaction with high precision. At present, the dominant limitation of modern scintillators is their timing resolution. The state-of-the-art in the coincidence timing resolution is just breaking the 100 ps barrier with the lowest value of 73±2 ps reported for LSO-Ce scintillators[1].

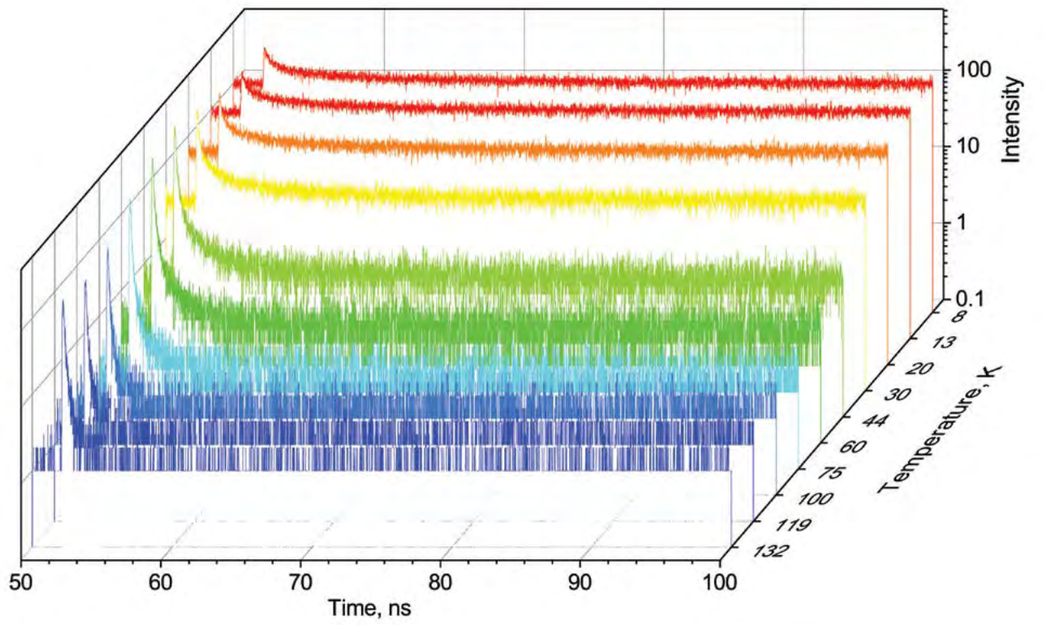

Figure 1: Decay curves of X-ray luminescence measured in the $MAPbBr_3$ crystal at different temperatures in the range 8-132 K (where the emission is most pronounced). The luminescence is excited by 50 ps pulses of monochromatic synchrotron radiation (E=14 keV).

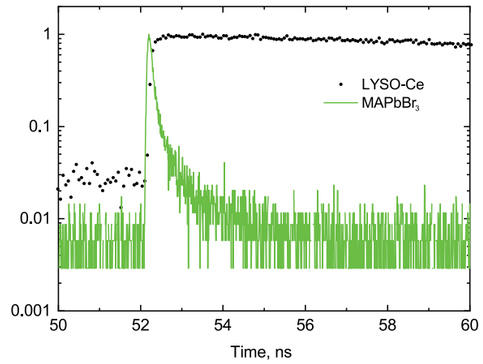

Figure 2: Normalised scintillation decay curves observed at excitation by 14 keV X-ray pulses in LYSO-Ce and $MAPbBr_3$.

Recent advances in development of hybrid metal-organic halide perovskites - materials with the general formula $MAPbX_3$ where MA= methylammonium, and X=Cl, Br, I and remarkable physical characteristics - triggered sharp upsurge of interest to their application for the detection of ionising radiation. The possibility of X-rays detection using intrinsic photoelectric effect has already been demonstrated in $MAPbX_3$ crystals[2]. It has been swiftly realised that the materials have great promise for the application as scintillation detectors with the key advantage of exhibiting a very fast response time, governed by the probability of radiative decay of excitons, while retaining high conversion efficiency.

This notion motivated present study of temperature dependences of the scintillation light yield and scintillation kinetics of relatively easy to synthesise $MAPbBr_3$ crystals over the 8-295 K temperature range. When excited with X-rays, $MAPbBr_3$ exhibits narrow, near-edge emission bands peaking at 560 nm with a very pronounced temperature dependence[3]. Fig. 1 shows the scintillation decay curves of $MAPbBr_3$ crystals measured at pulsed X-ray excitation over 8-132 K temperature range. The decay curves exhibit very fast, non-exponential kinetics that is characteristic of bimolecular recombination of the charge carriers. Quantitative analysis of decay curves revealed that the fast and slow decay time constants in the crystal are about 0.1 and 1 ns at T>50 K. With cooling to lower temperatures, the decay rate of the luminescence kinetics in $MAPbBr_3$ exhibits steep changes, resulting in a significant increase of the decay time constants. At the same time, the amplitude of the background exhibits a steady rise with cooling indicating that at this temperature the radiative dynamics is dominated by the slow recombination processes due to trapping and release of charge carriers.

One of the most important features of scintillation in $MAPbBr_3$ is that the major fraction of scintillation response from the crystal is released over a nanosecond time interval following an excitation pulse. This is of primary importance for the applications that rely on a fast timing resolution of the scintillator. Evidence of the extraordinary speed of the scintillation response in the crystals under study can be seen in the Fig. 2 where the luminescence decay curves of $MAPbBr_3$, and LYSO-Ce scintillator are juxtaposed. It is very clear from these figures that the timing performance of $MAPbBr_3$ is by far better in comparison with the modern commercial inorganic scintillator LYSO-Ce which exhibits the decay time of 33 ns and exemplifies the one of the best results in the coincidence timing resolution that relies on fast timing.

To assess the scintillation performance of the $MAPbBr_3$ the energy spectra induced by α-particles from ^{241}Am as a function of temperature were measured. Fig. 3 shows the variation of the scintillation light output of the $MAPbBr_3$ crystal with temperature together with LYSO-Ce. A clearly measurable scintillation response can be detected when the crystal is cooled to below 180 K. The scintillation efficiency of $MAPbBr_3$ increases gradually as the temperature is decreased until a plateau is reached at around 60 K. Further increase of the light output by about 20% is observed as the temperature decreases to below 30 K. This rise correlates with the rapid increase of the fractional contribution of the afterglow observed at very low temperatures. Taking the light yield of LYSO-Ce equal to 34,000 ph/MeV at room temperature, the light yield of $MAPbBr_3$ is determined to be 90,000 ph/MeV at 77 K and 116,000 ph/MeV at T = 8 K.

A comparison of the $MAPbBr_3$ parameters with modern commercial scintillators shown reveals that organolead perovskites are very promising scintillation materials. Of particular interest is the excellent initial photon density calculated as the ratio of light yield to decay time. This is an important parameter that determines the timing precision of the scintillator detector. The higher density of photons in the initial part of the scintillation peak facilitates higher precision in determining the time of interaction. A conservative evaluation shows that this parameter is higher by a factor 20 in $MAPbBr_3$ compared to the best modern scintillator $LaBr_3$-Ce. The stopping power of $MAPbBr_3$ that is defined by the photoelectric fraction of the absorption coefficient is also very competitive in comparison with other scintillators; only two other materials exhibit higher value. The results of this study place $MAPbBr_3$ in an excellent position for the development of a new generation of cryogenic, efficient scintillation detectors with nanosecond response time, marking a step-change in opportunities for scintillator-based applications.

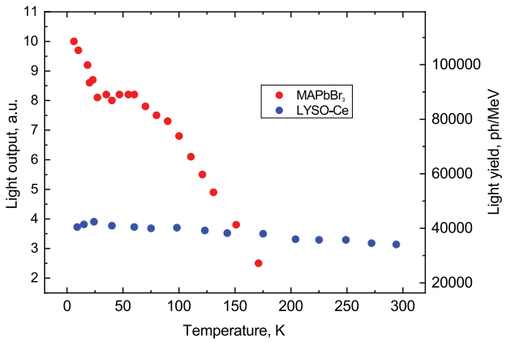

Figure 3: Scintillation light yield as function of temperature for the $MAPbBr_3$ crystal (red) measured at excitation with 5.5 MeV alpha particles from 241Am. The plot also displays the comparison with measurements of the commercial scintillator LYSO-Ce (blue).

References:

1. Gundacker S. *et al.* State of the art timing in TOF-PET detectors with LuAG, GAGG and L(Y)SO scintillators of various sizes coupled to FBK-SiPMs. *JINST* **11**, P08008 (2016). DOI: 10.1088/1748-0221/11/08/P08008

2. Yakunin S. *et al.* Detection of gamma photons using solution-grown single crystals of hybrid lead halide perovskites. *Nat. Photonics* **10**, 585-589 (2016). DOI: 10.1038/nphoton.2016.139

3. Birowosuto M. D. *et al.* X-ray scintillation in lead halide perovskite crystals. *Sci. Rep.* **6**, 37254 (2016). DOI: 10.1038/srep37254

Corresponding author:
Dr Vitaliy Mykhaylyk , Diamond Light Source, vitaliy.mykhaylyk@diamond.ac.uk

Detector Group

Nicola Tartoni, Detector Group Leader

The most important achievement of the Detector Group within the past year was to start the scientific exploitation of the time-resolved Tristan detector, developed entirely by the group, by carrying out multiple user experiments from August to December 2019.

The goal of the Tristan project is to deliver an area detector for time resolved crystallography experiments. Tristan is based on the Timepix3 read-out ASIC, which works in event driven mode (time stamp and location of an event sent out for any occurrence), rather than in frame based mode. Although initially designed for experiments on the Small-Molecule Single-Crystal Diffraction beamline (I19), this detector technology provides new capabilities for a variety of scattering techniques such as Small-Angle X-ray Scattering (SAXS).

The area detector to be delivered for I19, known as Tristan10M, will tile ten detector modules. Each module uses a monolithic silicon sensor with 16 Timepix3 ASICs[1] bump-bonded for a total of more than one million pixels per module. All the hardware parts required to assemble a Tristan10M have been developed and procured, and are now ready to be assembled. The firmware and software for Tristan10M is ongoing.

Whilst the delivery of Tristan10M is in the final stages, the Tristan project achieved full functionality for a single detector module system. The Tristan1M[2] has been used at Diamond in different user experiments on the Test beamline (B16) and I19.

The most significant results with Tristan1M have been obtained at B16 where a set-up to carry out an experiment of Diffracted X-ray Tracking (DXT) was designed. Two experiments were performed by members of the Soft Condensed Matter Science Group, who specialise in bio-SAXS, in collaboration with Prof Yuji Sasaki (University of Tokyo) and Dr Hiroshi Sekiguchi (SPring-8). In these experiments a coiled coil protein, a protein-protein complex, and an RNA binding protein were investigated. A DXT experiment uses the white beam and measures the movement of Laue diffraction spots given by Au nanoparticles attached to the studied molecule under study. By tracking the movement of the diffraction spots the scientists were able to reconstruct the slow dynamic motion of the molecule. A fast detector is necessary to be able to track the fast movement of the spots and Tristan1M was ideal for this because it can time-stamp events with a time resolution of the order of a few nanoseconds. The data produced by Tristan1M were a stream of events with time and position stamps. These data were analysed after the experiment to reconstruct image sequences with the desired time resolution. Despite the high scattering background intrinsic to the white beam set-up, a pilot experiment in August 2019, and subsequent beam time in December 2019 have led to already impressive results. As shown in Fig. 1, the team could track the paths of the Laue diffraction spots within a 20 ms window, with a time resolution of 1 ms. The scattering signal was too weak in this experiment to allow for a finer time-binning of the data, which would have allowed for tracking with a better time resolution. However, Tristan will be able to bring the time resolution of DXT experiments comfortably into the microsecond regime due to its improved experimental conditions enabling higher signal to background ration.

Tristan1M was employed during pump-probe experiments at I19 in September 2019. An Ag-Cu compound crystal was photo-excited with a 390 nm laser with a repetition rate of 10 kHz, and as the system relaxed into the ground state, the X-ray scattering determined the crystal structure. The experiments were carried out in stroboscopic mode to achieve sufficient statistics and were performed by both following a single reflection and obtaining full datasets. The trigger from the laser was fed into the Tristan continuous readout data stream. Tristan1M can acquire up to two external trigger signals and includes their time stamps in the data stream. By using

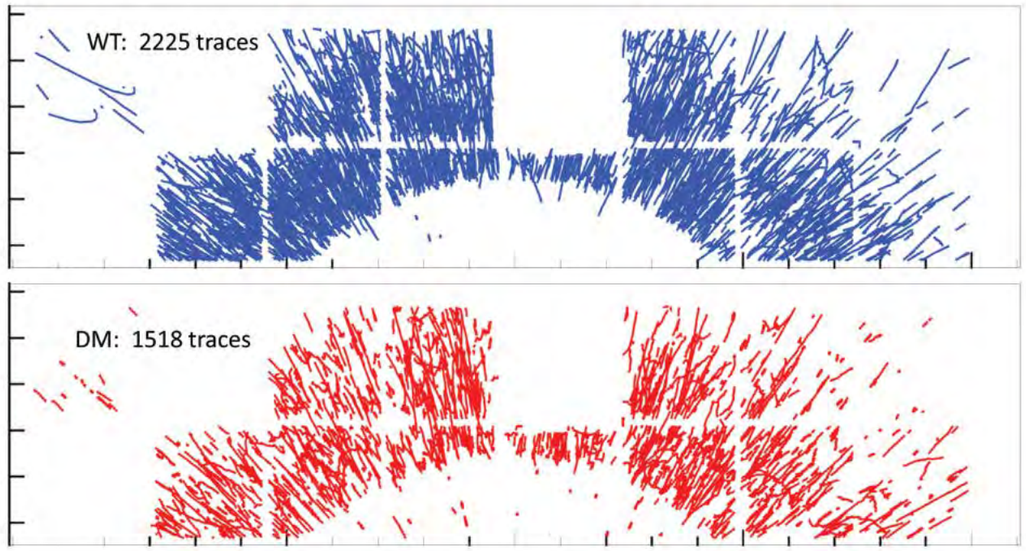

Figure 2: Reconstructed images (20 ms duration) of the path of the diffraction spots on the Tristan sensor.

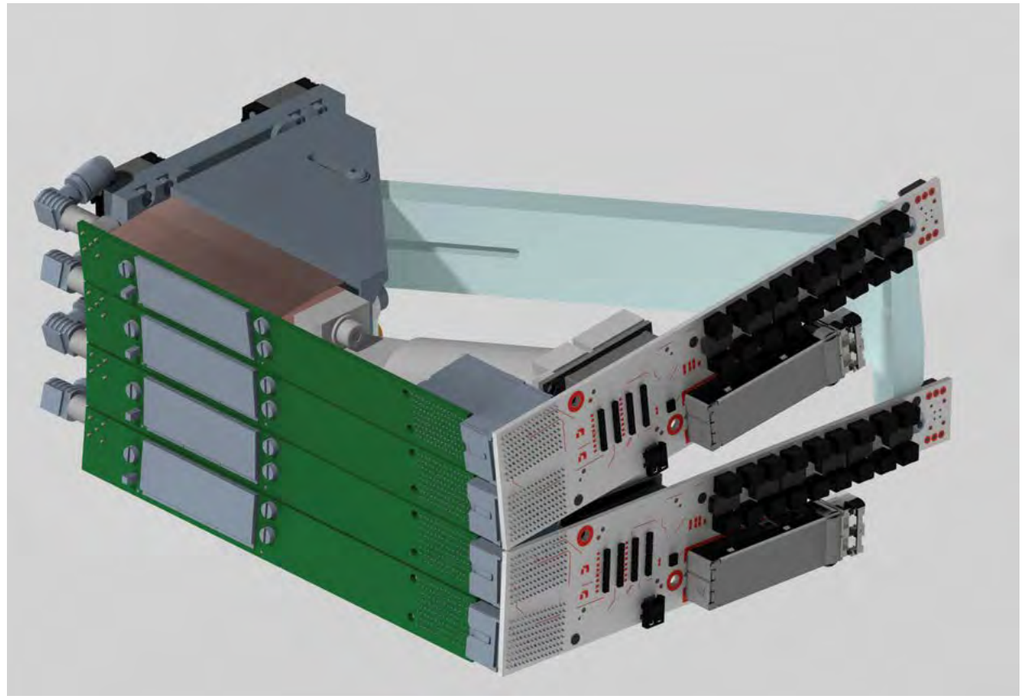

Figure 2: Arc-detector super-module drawing. The four grey rectangles represent the four sensors mounted on a printed circuit board in green. On the side, orthogonal to the sensor boards, the two cards which serialize the data by an Artix-7 FPGA are shown.

the laser synchronism signal as the external trigger point, the delay for each event is determined with respect to the preceding trigger pulse. Histograms of the data for the 100 ms corresponding to the laser repetition period were produced with 2 ms bins. Tristan1M enabled data to be acquired 50 times faster than with the conventional technique of gating the detector and moving the delay of the gate with respect to the laser pulse. Data with healthy statistics have been achieved, thus opening the door for experiments covering a larger volume of reciprocal space for quantitative analysis. Moreover, the processing pipeline has been further optimised for quick feedback for future experiments.

The group is also pleased to report significant progress with the development of the arc-detector for Pair Distribution Function (PDF) experiments at the X-ray PDF beamline (I15-1)[3]. The detector is an essential component of the beamline project that aims to radically improve the throughput of PDF experiments at Diamond and allow for a higher level of automation. The detector is a custom-made photon-counting detector based on a high Z sensor to benefit from negligible noise, large dynamic range and good efficiency at high photon energy. The conceptual architecture of the detector has been defined; the development of the parts is ongoing; and some parts including the sensor modules have already been delivered.

Electron collection CdTe 1 mm thick sensors with Schottky contacts were selected due to their capability of quickly refreshing the polarisation effect by turning off and on the bias voltage[4,5]. The area of the CdTe sensor (14.2 mm × 42.6 mm) was chosen to match the area of three Medipix3RXv2 with readout ASICs of 55 µm × 55 µm pixel size[1,6]. The 48 low-voltage differential signalling (LVDS) data lines coming from two sensors (six ASICs) are sent to an Artix-7 FPGA which converts the data into a serial data stream. The data are then transmitted by a fibre optic to two data acquisition cards based on the Virtex7 FPGA located a few metres apart on a 19″ rack. The fibre optic link between the detector head and the data acquisition cards enables the weight and size of the detector head to be substantially reduced. The data are then streamed at 25 fps (meeting I15-1 requirements) to a Linux server, via two QSFP+ transceivers on each FEM-II card, which runs the Odin DAQ framework[7]. The complete detector head consists of 24 modules, four modules are assembled in a single mechanical unit called super-module as shown in Fig. 2. Every module is arranged in an arc shape, covering a scattering angle of 100° for a total of 4.7 million pixels. The detector will be mounted on a goniometer in order to rotate and collect data from both above and below the beam, covering an even larger region of interest. The installation of the detector at I15-1 is currently planned for July 2021.

References:

1. MEDIPIX Collaboration, CERN: https://medipix.web.cern.ch/home
2. Crevatin G. Oral communication at IEEE NSS-MIC 2019
3. Gimenez E.N. *et al*. NSS-MIC Conf. Record 2019
4. Gimenez E. N. *et al*. Development of a Schottky CdTe Medipix3RX hybrid photon counting detector with spatial and energy resolving capabilities. *NIM A*. **824**, 101-103 (2016) DOI: https://doi.org/10.1016/j.nima.2015.10.092
5. Astromskas V. *et al*. Evaluation of Polarization Effects of e^- Collection Schottky CdTe Medipix3RX Hybrid Pixel Detector. *IEEE TNS* **63(1)**, 252 – 258 (2016). DOI: 10.1109/ TNS.2016.2516827
6. Gimenez E. N. *et al*. Medipix3RX: Characterizing the Medipix3 Redesign With Synchrotron Radiation. *IEEE TNS* **62 (3)**, 1413 – 1421 (2015). DOI: 10.1109/ TNS.2015.2425227
7. Yandell G. *et al*. Odin - a Control and Data Acquisition framework for Excalibur 1M and 3M Detectors. *ICALEPS2017 Proceedings* (2018). DOI: 10.18429/JACoW-ICALEPCS2017- TUPHA212

Scientific Software, Controls and Computation

Mark Heron, Head of Scientific Software Controls and Computation

Having been created in 2018, the Scientific Software, Controls and Computation (SSCC) department is now established as part of the management structure of Diamond Light Source. The overall function of the department is tuned to provide the best possible support to deliver Diamond's scientific output, through outstanding and evolving software, computing and control systems. It functions as eight groups: Scientific Computing, Data Analysis, Data Acquisition, Beamline Controls, Accelerator Controls, Electronic Systems, Business Applications, and Cyber Security.

Business Applications and Cyber Security groups have both been introduced over the course of the past year. The introduction of the Business Applications group was in recognition of the increased importance of both information management and business software to support both the scientific and corporate functions of Diamond. The creation of a Cyber Security group recognises that Diamond must deliver a level of cyber security maturity, across a large and complex IT infrastructure, consistent with best practice to address continually developing and changing cyber security threats.

As many beamlines introduce new detectors to enhance their data collection capabilities, the department is responding to the up-and-coming Big Data challenges. As part of the planning for the proposed Diamond-II upgrade, SSCC are developing exciting new capabilities in these areas.

To ensure that forthcoming challenges are met, a medium term strategy for SSCC was developed during the year. This involved extensive consultation within Diamond to explore and understand future science needs and drivers. This then informed a set of critical objectives to define future direction and to give consideration to their realisation through a series of roadmaps. Following an internal review at the end of 2019, the strategy will be reviewed externally during 2020, before being presented to the Science Advisory Committee.

The following are examples of some of the interesting developments across the broad range of activities that have taken place within the SSCC department during the past year.

Automatic Reconstruction of Diffraction Tomography Data

The Microfocus Spectroscopy beamline (I18) was the first spectroscopy beamline built at Diamond and has the ability to explore the elemental makeup up of a sample under investigation with very high resolution; around two microns (about 50 times smaller than the width of a human hair). Over the past three years there have been major improvements to the hardware and software on I18 to enable significantly faster continuous scanning measurements, facilitating live data processing and visualisation. These improvements were made as part of the Mapping project and it resulted in a step change in data collection performance of the beamline.

During the past year a new detector, called an Excalibur 3M, was installed on I18 running with new Odin data acquisition software for fast readout and support of the Mapping project capabilities. This allowed data from diffraction experiments to be collected at similar exposure times to the traditionally faster fluorescence measurement, enabling more efficient multi-modal measurements to be made. As well as being able to run faster with more informative scans the development made it easier to connect the scan information to external systems, e.g. information management and automatic processing applications.

At the beginning of December 2019, all the software pieces were in place to enable live data processing of the new Excalibur detector and automatic tomographic reconstruction of fluorescence and diffraction data, using Diamond's data processing framework, SAVU. All the processing applications were managed by a new micro-services framework, for triggering the automatic processing, and recording its status. The resulting processed data files produced were registered back with the original data collected in the experiment information management database, ISPyB, and so were viewable in the ISPyB webpage by the users.

The first user group to use this new system were very happy with its performance stating, "As an experienced Diamond user, I have to say this is one of the most enjoyable beamtimes I've had so far. I am very impressed by the upgrade of the experimental set-up (detector), data acquisition and almost real time data analysis."

Fastest Detectors in Diamond

Over the past year Diamond has installed several best-in-class X-ray detector systems, ensuring provision of world leading beamlines. For example, two of the Macromolecular Crystallography (MX) beamlines I03 and I04 had a new detector called an Eiger 2 XE detector, with 16 million pixels running at up to 560 frames per second. These modern detectors present extensive challenges to the software and IT support groups due to the high rates with which data can be acquired, leading to challenges in transporting the data, and subsequent processing and storage.

Odin data acquisition software, a collaborative development between Diamond and STFC, was specifically developed to control and collect data from high data-rate detectors by being highly scalable and configurable to cater for specific detectors and applications. The Eiger 2 XE, and several other types of detectors around Diamond, successfully use the Odin software to acquire data at data-rates of multi-gigabytes per second. For the Eiger 2 XE models on the MX beamlines, Odin enables data acquisition speeds of up to 28,800 frames in 58 seconds routinely.

In MX beamlines radiation damage is the single biggest limiting factor to data quality and must be balanced against the signal to noise of the data, in order to obtain collection of an optimal data set. One option is to perform stepped transmission measurements where the same scan is repeated a number of times with increasing photon flux: at lowest flux the data collected are too weak, at highest flux the sample is damaged, the optimum is in between. While this is a reliable and conservative approach to data collection, with the previous generation of detectors this was expensive in terms of time taken, as each scan would take two minutes or more, making for a time greater than 10 minutes for the complete run of four acquisitions. With the Eiger 2 XE detectors being able to run at 500 Hz, the full four scan acquisition can be performed in less than a minute - half the time of a single run with the old detector. With the automated analysis in place, a user is easily able to identify the best available data sets from the selection.

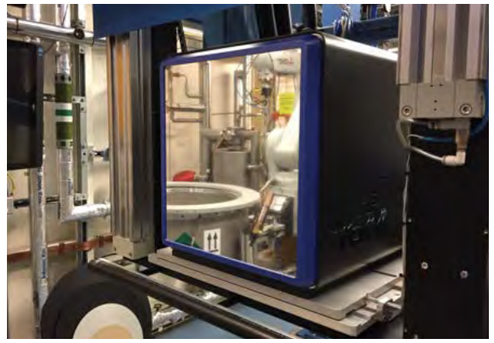

Eiger 2 XE Detector on beamline I03.

Scientific Computing in the Cloud

Collecting, processing and analysing large volumes of experimental data requires an ever-increasing suite of computer resources in order for users of Diamond to achieve this as effectively and efficiently as possible. Cloud computing offers a flexible way to realise this.

For Diamond, the big data challenge is the need to transfer many 10's of Terabytes's (TB) of data around the network daily (1 TB is roughly equivalent to 250,000 photos on a phone with a 12MP camera). The consequence is that it is not feasible for all parts of the data acquisition and analysis pipeline to be moved off-site to the public cloud, because of the amounts of data that would need to be exchanged. To address this, Diamond is developing a hybrid cloud model; this requires determining which computational problems can be moved to the off-site cloud providers, and which computing challenges need to be kept on-premise.

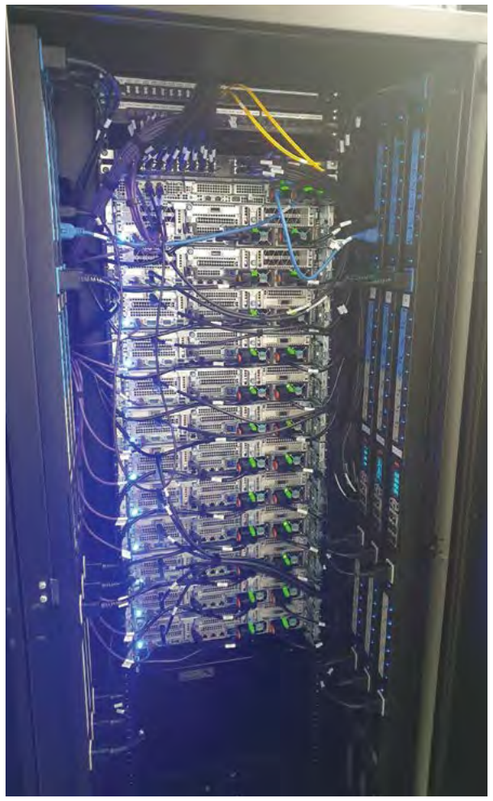

On-premise Cloud Computing Infrastructure.

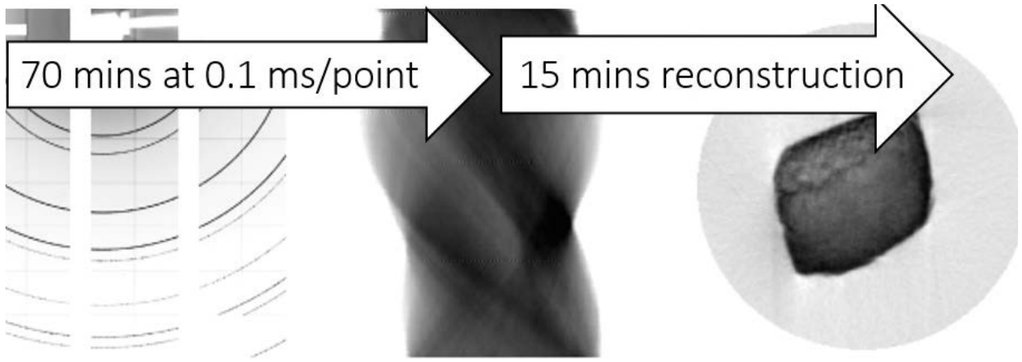

Example of I18 auto processing. One of forty thousand diffraction images collected during the tomography scan (left) used to generate a sinogram of the scan (each pixel corresponds to a single diffraction image) (centre) and a sample cross-section of the reconstructed volume from the sinogram (right). Data for images courtesy of Dr Tan Sui's research group at the University of Surrey.

Although public cloud providers offer low level resources, such as Virtual Machines as a service, there has been a strong trend towards containerisation as a method to provide a consistent software environment on which workloads run. This minimises changes users will need to make when using cloud and on-premise services. The dominant technology for running containers is Kubernetes, a project developed originally by Google. To extend this common layer to Diamond's on-premise infrastructure, a recent deployment of a Kubernetes cluster has been undertaken. This enables software developers to experiment and adapt existing workflows to run in any cloud environment that offers Kubernetes as a service.

Adopting cloud techniques and containerising applications enables workflows and applications to become decoupled from the underlying infrastructure. Whilst building or adapting workflows to be containerised requires a significant investment of time, it has the potential to allow future users to take both data and analysis software away from Diamond easily. In this way, users can leverage large scale cloud platforms for data analysis that are either provided by commercial cloud companies, or the increasing number of clouds within academia that are developing, without significant overhead.

Controlling Helium Recovery

Helium, although abundant in the universe, is a very rare and finite resource on earth. When helium gas is vented into the atmosphere it is lost as it eventually escapes earth's gravity because it is such a light element. To help preserve this important resource, an extensive Helium Recovery System has been installed at selected beamlines and other areas that have a high usage of helium. The control system for this has been designed and supplied by the Electronic Systems Group to manage the whole process from collection, low pressure storage, purity selection, high pressure storage and ultimately transfer to the liquefaction plant.

The system is more sophisticated than commonly installed as it checks the purity of collected gas to ensure suitability for liquefaction. It monitors purity at each collection point and only gathers gas of suitable quality, rejecting low grade gas automatically. The gas that passes this first check is then stored in a gas bag before being compressed and stored in local storage banks after a second purity assessment. This ensures that all gas collected is suitable for liquefaction, saving unnecessary energy costs associated with compression and storage of unsuitable gas. Control of collection and storage is all automatic, managed by a distributed system of Programmable Logic Controllers, and a local Human Machine Interface, all communicating over Ethernet.

Software and computing graduate programme

The SSCC graduate training programme provides a route to recruit recent university graduates and offer training in one of the highly specialized software engineering and computing roles at Diamond. Established in 2015, the programme has expanded to encompass all the software and computing groups. It is now well recognised, with an intake of five graduate engineers per year, from a variety of backgrounds in science, engineering, mathematics and computing.

The programme consists of two years of training. In the first year, participants undertake four projects in different groups within SSCC, and occasionally elsewhere in Diamond. The second year is spent as a member of one team, in mentored, "on-the-job" training, building responsibility within that team. At the end of the two years, participants are equipped to operate independently at the level of experienced engineers.

Participants build a broad base of knowledge and experience, and a network of contacts throughout the organisation, in turn bringing different perspectives and new ideas to the host groups. The first year projects consist of a meaningful piece of work which is owned by the host group, and many involve working across group boundaries, which promotes collaboration and breaks down organisational barriers. In total, 50 projects have been completed to date. To complement the practical experience, training is provided on a range of technical topics, through organised training courses and online learning. There is also a programme of informal talks on projects and topics of interest. In 2019,

Recovered Helium quality checking instrumentation to select gas suitable for storage.

Graduate Trainee Away Day: Year two cohort help induct the new starters.

the first SSCC Graduate Away Day was held to promote the inclusion of the new starters and build strong links within the internal graduate community.

Cyber Security and Information Management

Diamond is on a journey to increase Cyber Security and Information Management maturity in order to protect and enhance the science programme delivery. During the past year Cyber Essentials certification was achieved. This focussed on demonstrating good practice in five technical controls: securing the internet connection, securing devices and software, controlling access to data and services, protecting from viruses and other malware and keeping devices and software up to date. Information Governance (IG) is another crucially important part of the journey; during the year an IG Committee was formed, an IG Corporate Statement agreed and an IG Framework endorsed.

Information Management requires Diamond's data, information, and knowledge (collectively 'information') to be kept confidential when necessary, to have its integrity maintained and to be guaranteed to be available when needed. A further aspect of Diamond's security journey is to improve access to information by providing relevant, performant and managed services. A project is underway to deliver a managed SharePoint Online service which will ensure Diamond's information is held securely, in one place, and is findable- as some would describe it, 'a single point of truth'.

The process to increase Diamond's cyber security and information management maturity is well underway, and is expected to continue through 2020 and into 2021.

The Role of the Business Applications Group

The Business Applications group is a new grouping of components from a number of teams from across SSCC that deliver systems and services supporting Diamond in delivering science benefits. There are currently three main areas that the group supports which map across an external user's journey while at Diamond.

When a user first applies for access to Diamond's facilities, they will do this using the User Administration System (UAS) which manages application, review and visit or session management. These systems ensure that time at Diamond is managed efficiently and effectively to deliver a good experience for users, reviewers and Diamond staff. Experiment management systems, such as, ISPyB, handle the users' experience during the course of the experiment – it enables them to manage their experiments when on site or off site, and also ensure that experiment samples for external users are delivered to site speedily. Other systems are used to help manage assets and logging information. Finally, at the end of the data journey, data management systems ensure that the data created during the experiment is curated and archived in the data catalogue and repository called ICAT. At this point the data needs to be findable and retrievable by users, and, in due course, be made openly accessible.

A key objective of the Business Applications group is to align the software systems and services a user utilises to provide a more coherent experience. It will look to embed good practice in terms of quality assurance and design throughout the systems.

In addition to the systems described, the Business Applications group is also involved in a broad range of business IT Services, looking to provide new capabilities that will deliver greater efficiencies across Diamond, new systems to help reduce administrative burden, and to deliver services that can be accessed more widely. The overall aim is to improve services and help Diamond to continue to grow and thrive.


nccgroup

This is to certify that

Diamond Light Source Limited

Diamond House, Harwell Science and Innovation Campus, Fermi Ave, Didcot OX11 0DE

Has been assessed
by Yousef Abdulrahman for NCC Group PLC
against the Cyber Essentials Scheme Test Specification

Level of certification: Cyber Essentials

Scope: Diamond Light Source Limited External Infrastructure

Certification date: November 21st, 2019
Recommended re-assessment date: November 20th, 2020
Certificate no.: 3724983103737082

CREST

Cyber Essentials Certificate.

Key Facts and Figures

Facility usage

In our thirteenth year of operations (1st April 2019 to 31st March 2020), we received 2,138 proposals for experiments on our instruments via peer reviewed access routes, requesting a total of 26,543 shifts. After peer review, 1,232 proposals were awarded beamtime. This resulted in 13,462 experimental shifts being awarded across 30 beamlines and 11 electron microscopes. We welcomed 6,454 onsite user visits from academia across all instruments, with an additional 5,851 remote user visits. The machine continues to perform to the highest standard with 98.1% uptime and 104.7 hours mean time between failures (MTBF).

User shifts requested, awarded and delivered by group, beamline and electron microscope 2019/20

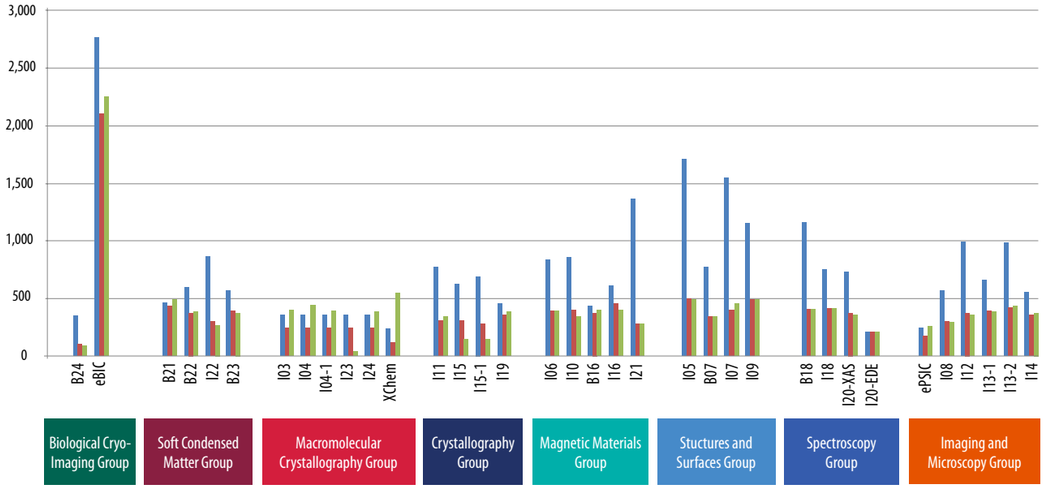

Total user shifts requested, awarded and delivered

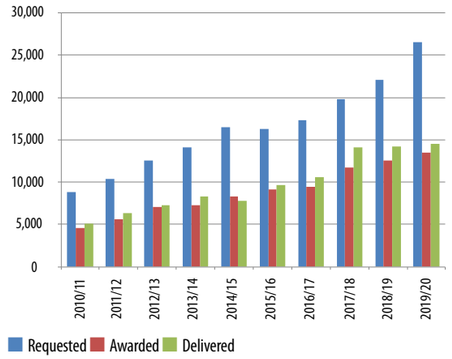

Various improvements have been made regarding the count of requested shifts for rapid access as well as regarding the count of requested shifts for proposals requesting more than one instruments.

Total numbers of proposals and users per year

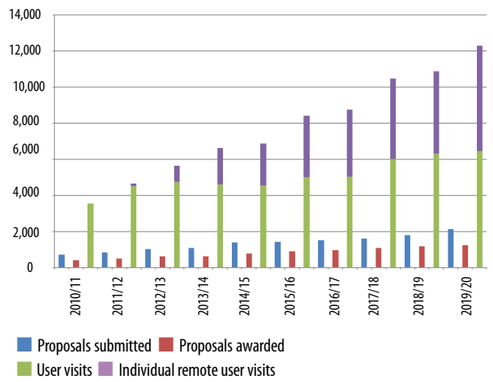

Members of staff visiting as part of peer reviewed access routes are now included in the count for user visits. In-house research is still excluded from this report.

Proposals by discipline and research theme

Experimental shifts scheduled by Diamond by main subject area for 2019/20

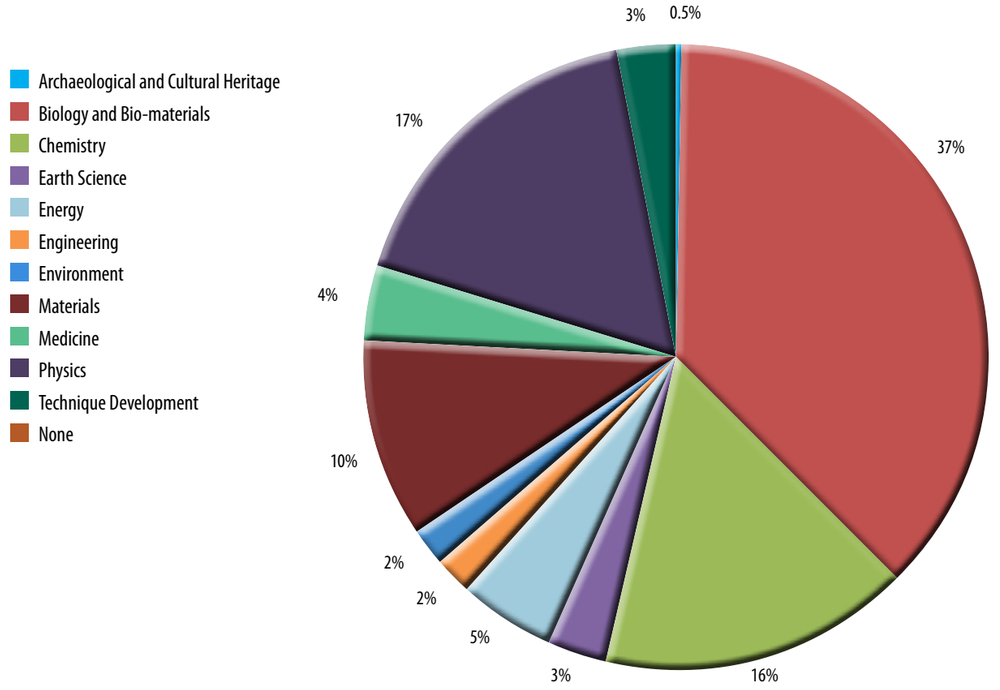

Cumulative number of items in Diamond Publications Database by our scientists and users and cumulative number of protein structures solved

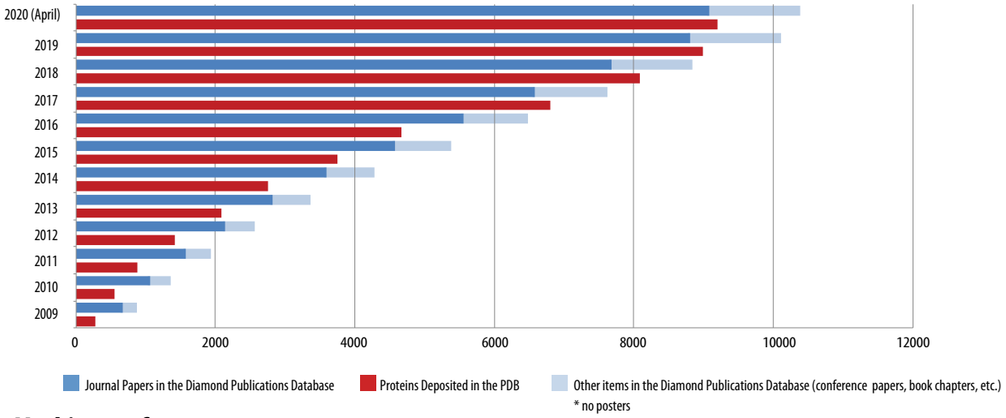

Machine performance

	2009/10	2010/11	2011/12	2012/13	2013/14	2014/15	2015/16	2016/17	2017/18	2018/19	2019/20
Total no. operational beamlines by end FY	17	19	20	22	24	25	26	28	31	32*	32*
Scheduled hours of machine operation	5712	5808	6000	5832	5976	5808	5928	5688	6072	5904	5913
Scheduled hours of user operation	4728	4728	5064	4872	5088	4944	5040	4584	5160	4992	4992
Machine uptime %	97.0	97.5	97.7	98.3	98.2	97.6	97.6	98.7	98.2	98.4	98.1
Mean time between failures (hours)	26.2	28.5	55.4	52.4	60.3	38.6	119.4	103.1	79.9	90.3	104.7

** Across all access routes.*

Industrial Liaison

Elizabeth Shotton, Head of Industrial Liaison

We are pleased to report that the industrial programme at Diamond Light Source continues to build on the successes of previous years, and we have experienced another year of substantial growth. Clients range from the large multinational household names, through to SMEs and start-ups, with over 170 companies worldwide making use of Diamond's facilities in their R&D programmes by 2020. We would like to take this opportunity to thank our clients for their support and their valuable feedback that helps us to continually improve our facilities and services. While clients represent a wide range of sectors, from aerospace engineering through to battery research, and with samples as diverse as aerospace alloys, antibodies and chocolate, proprietary use of Diamond continues to be heavily dominated (~75%) by the pharma and biotech industries.

In order to meet the demand for our structural biology services, we have recruited additional team members to support our clients. This year we welcomed Adriana Klyszejko and Christofer Björkelid to the team. Adriana has transferred to the team from an existing role at Diamond's electron Bio-Imaging Centre (eBIC), and now focuses on providing professional scientific services to Diamond's industrial clients in the field of cryo-electron microscopy (cryo-EM). Christofer comes to us from Sweden and has joined our life science team as an Industrial Liaison Scientist for MX, supporting industrial structural biology experiments at Diamond.

We also welcomed a new PhD student in September. Paul Edwards is jointly supervised by the Head of Industrial Liaison, Elizabeth Shotton, and by Sven Schroeder at the University of Leeds, and is based at Diamond in the Industrial Liaison team. Paul's research will focus on the modelling of soft X-ray XPS investigations of materials, and he will be conducting experiments on the Versatile Soft X-ray (VERSOX) beamline (B07) during his graduate studies.

Our global industrial engagement can take many forms, but the commercially sensitive nature of the projects that are delivered by the Industrial Liaison team mean that the majority cannot be shared. However, due to the support of various funding schemes, we are able to showcase exemplars of industrial research by partnering with other organisations using grant funding.

In the last three years we have been undertaking a number of projects through the Newton Fund, in addition to our core business. The Newton Fund builds research and innovation partnerships with participating countries to support their economic development and social welfare, and to develop their research and innovation capacity for long-term sustainable growth. The fund is managed by the UK's Department of Business, Energy and Industrial Strategy, and delivered through a number of partners including UKRI's Science and Technology Facilities Council (STFC). The programme run by STFC provides access to large-scale research facilities across the UK to promote the economic development and welfare of collaborating countries.

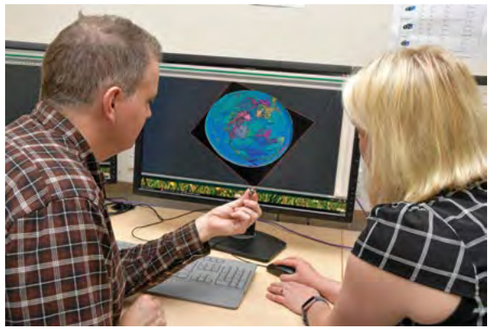

Data analysis from imaging experiments.

Dr Ferensa Oemry is one of a number of scientists from OECD DAD countries who have participated in the Newton Fund programme. An accomplished scientist from Indonesia, Ferensa spent the year with the Industrial Liaison Team at Diamond, working with Anna Kroner, developing the design of a new catalyst to produce sustainable biofuels using palm oil waste as the main feedstock. Ferensa's project, part of a year-long collaboration between the Indonesian Institute of Sciences (LIPI), Diamond and the ISIS Neutron and Muon Source, has enabled scientists from Indonesia to conduct ground-breaking work on sustainable biofuels. This research has the potential to have an immense impact on the Indonesian economy. Along with Malaysia it supplies 85% of the world's palm oil, but also faces a growing need for fuel, most of which is currently imported. By developing a catalyst that uses the waste produce of palm oil, Ferensa and his team aim not only to support the country's fuel supply, but also make the production of biofuels much more sustainable.

The eBIC4i team conducting industrial cryo-electron microscopy experiments.

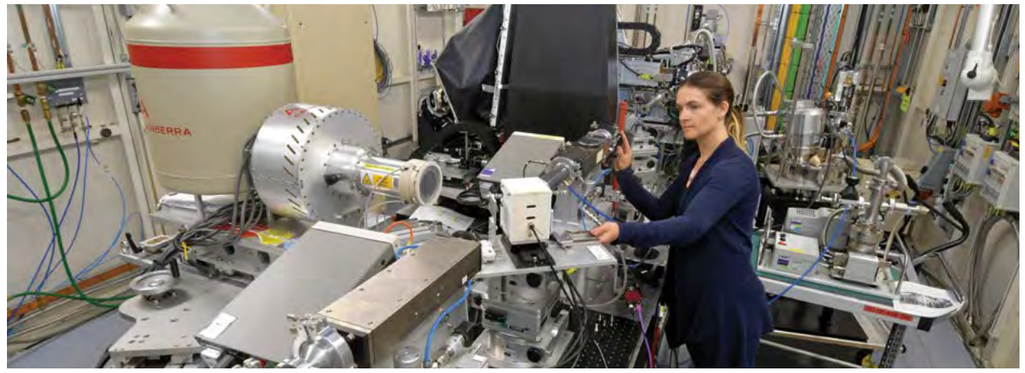

Industrial spectroscopy experiments in action.

As part of our Newton Fund activities, we have also established strong links with scientists at the SLRI synchrotron based in Nakhonratchasima, Thailand. Over the last year, supported by the Newton Fund programme, we have collaborated with Thai synchrotron scientists and their commercial partners to perform three different experiments at Diamond. These experiments had a dual purpose; to make use of the advanced instrumentation and expertise at Diamond to aid in further understanding a commercial product or process, and also to provide an opportunity for upskilling our Thai synchrotron partners.

One of the experiments that took place as part of this programme was focused in the area of food and nutrition, in particular in the field of meat substitutes. The ability to provide a credible meat substitute, in terms of taste and blood-red appearance, is very challenging for the food industry. However, haem, taken from haemoglobin, has been proven to mimic the key qualities of meat when cooked, so can be used as a supplement in plant-based meat alternatives. The Thai team are working to develop a plant-based precursor to replicate the taste and appearance of meat, using chlorophyll, which has a similar structure to haem, an existing supplement in the meat analogue market.

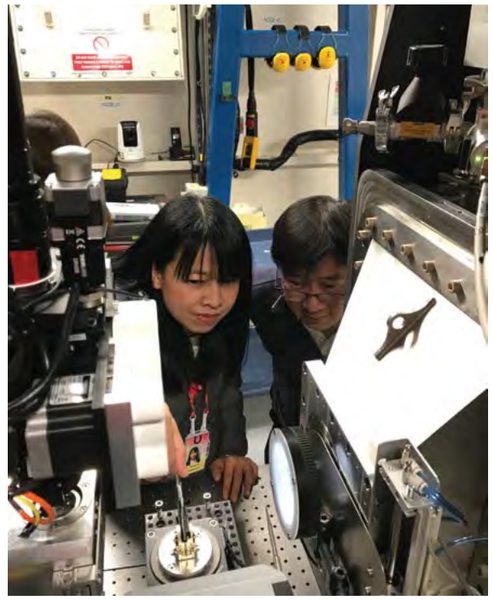

Thai researchers performing an experiment on I22 under the Newton Fund scheme.

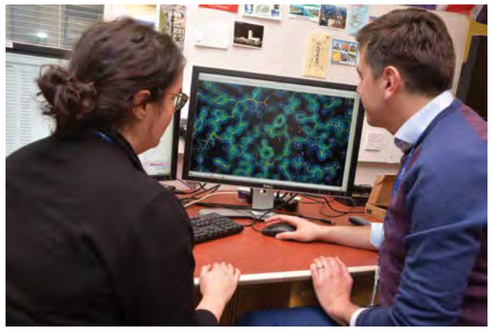

Industrial liaison scientists can support all stages of the experiment from experiment design to data analysis.

The research focused on the substitution of magnesium in chlorophyll with iron. Once formed, the Fe-chlorophyll complex was characterised using UV-Vis Spectrometry, FITR and X-ray Absorption Spectroscopy (XAS). Sukanya Chaipayang, Worawikunya Kiatponglarp and Somchai Tancharakorn collaborated with Anna Kroner from the Industrial Liaison team to design and perform experiments. The research instruments at Diamond have greater flux than at the synchrotron in Thailand, enabling the team to quickly and effectively study the structure and bonding between atoms of the haem substitute, using Extended X-ray Absorption Fine Structure (EXAFS). XAS provided valuable information on the internal structure of the Fe-chlorophyll compound, and detailed data analysis, performed in collaboration with Anna, revealed different bonding behaviours than those expected from the existing predictive models of the system. A key benefit of the process was the opportunity for the Thai scientists to gain hands-on experience of performing EXAFS experiments and develop their data analysis skills.

Participation in funding schemes such as the Newton Fund allows us to support regional development activities with our collaborators overseas, and provides an excellent opportunity to showcase non-confidential examples of commercially relevant work taking place at Diamond. This can, in turn, help to raise awareness of the benefits of synchrotron techniques across a range of industrial sectors. If you'd like to know more about the projects outlined here, or for further information about any of the work of the Industrial Liaison Office, please do contact us on industry@diamond.ac.uk.

Engaging with Diamond Light Source

Communications and Engagement Team

Diamond continues to commit to engage with a diverse range of audiences, connecting people with the wide range of science and engineering that we undertake. Over the past year, we have developed new audience bases while maintaining our commitment to work with, train, and learn from members of our user community and the wider public.

In total over the past year, Diamond has welcomed **5,038** visitors to the facility, including: **1,284** for scientific and technical events, **947** undergraduate and postgraduate visitors, **2,242** school students and members of the public, and **565** VIPs and Stakeholders.

This year, Diamond has increased its support for encouraging younger schools' audiences and has partnered with Science Oxford to support the delivery of their Big Science event, which works with over 80 primary schools. We have also worked on new ways to promote careers in STEM; two of our scientists have been awarded a grant to produce a Diamond boardgame to help in schools, and at a university level we have worked with the Open University careers department to develop an interactive Diamond visit event.

> "My highlight of the finals day itself was when one of my children came outside for lunch and said: I want to be a scientist now!"
>
> *- Chesterton CE Primary School Staff Member, 2019*

Students from Whitchurch Combined School, Buckinghamshire winners of the Big Science Event final.

Towards the end of the year the outbreak of the global Coronavirus pandemic affected onsite activities, but we reacted swiftly by producing more remote resources for schools, users and the general public.

Diamond continues to run a core program of public engagement activities, which prove increasingly popular. The majority of our interactions are onsite, at one of our regular Inside Diamond public open days or community group visits. But we also attend many external events to reach a wider range of audiences. This year we attended, for example, the IF Oxford Science and Ideas Festival, Big Bang South East, Wantage Museum and we partnered with our student engagement team and The Rosalind Franklin Institute to engage with participants of the Bluedot festival.

> *"The day exceeded what we were expecting. The level of interaction was fantastic and was great for my children and the facility itself really took my children's breath away and they haven't stopped talking about it."*
>
> *- visitor to Inside Diamond open day, November 2019*

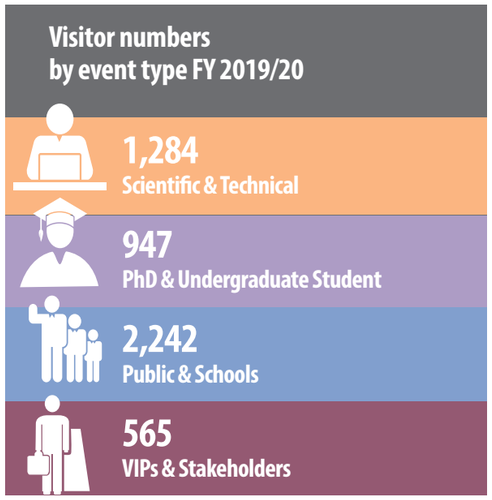

Our school/college level core events continue to offer students the chance to partake in specific tailored event days, such as particle physics, engineering, and a girls-only science day, as well as more general open day events. Many of these are partnered with our engagement colleagues at STFC and across site, which helps offer students a broader experience. Our school level work experience program ran again and took the largest cohort so far, offering 28 students the chance to come to Diamond for a week and partake in a range of talks, activities and a central project. All our activities are supported by staff across the organisation.

> "my project was really well run and the staff were friendly and supportive throughout, it was an amazing experience and I am very grateful to have been given the opportunity to be involved."
>
> *- School work experience student*

Higher Education engagement

As part of the organisation's vision, to continuously plan for Diamond's technical and scientific future, the training of students through our Undergraduate placements and PhD programme continues to be one of the core engagement activities. Diamond offers students a range of opportunities to engage with and learn from world leading staff and resources, developing and inspiring the next generation of scientists and engineers.

In autumn 2019 we welcomed 14 new PhD students, co-funded with 10 different universities and world leading research facilities. This brings the total number of ongoing Diamond PhD studentships to 73. There were 66 submissions to the 2020 Diamond Doctoral Studentship call for proposals and proposals were received from 26 different institutions. Following the internal review process, we will be welcoming 32 students in October 2020. All PhD students linked with Diamond have an annual review with the student

Several of the 2019 undergraduate placement 12-month Year in Industry cohort.

engagement team, these have proved to be valuable interaction points and the benefits of being linked with Diamond was mentioned by many students.

The Diamond undergraduate placement scheme welcomed 30 new students in June 2019. The projects ranged from scientific software and computing projects, life and physical science projects to a scientific communications project. There were 15 12-week summer placements who finished their placements in September 2019 and 10 12-month year in industry projects which are still ongoing. As well as the main student projects, Diamond also provides undergraduate students with training on presentation skills, media and public engagement.

The demand for student visits remains high and Diamond supported 35 visits from undergraduate and postgraduate groups, offering a range of access, talks and training.

> *"The tour was a great and a rare opportunity to see some science done and explained in a great way – and for the academics on the trip, was an excellent opportunity to think about research ideas."*
>
> *- Research Fellow visiting with Master's students group from the University of Southampton, February 2020*

Scientific workshops and conferences

Diamond organises a broad portfolio of scientific and technical workshops, training courses and conferences tailored towards the needs of our staff and user community, with whom we continue to train, inform and learn from.

In July 2019, Diamond became the first UK hosts of the biennial 8th International Workshop on Strong Correlations and Angle-Resolved Photoemission Spectroscopy (CORPES), held at Worcester College in the city of Oxford. Taking place over five days, we welcomed international experimentalists and theorists working in the broad areas of many-body electronic structure theory and angle-resolved photoemission Spectroscopy (ARPES) to meet and collaborate.

This year also saw an increase in requests for running new computer-based workshops. These popular practical workshops covered a wide range of synchrotron science and delivered training to the user community on Diamond's latest tools and capabilities, such as X-ray PDF data collection and PyMca software data analysis techniques.

Date	Event	Participants
15 - 18 April 2019	CCP-EM Icknield Workshop	35
2 - 3 May 2019	BPM Button Design and Manufacturing Workshop	40
8 May 2019	Collaborative Network for X-ray Spectroscopy (CONEXS) Kick-off Meeting	50
13 - 14 May 2019	Wellcome Trust SuRVoS/Zooniverse Workshop and Board Meeting	27
16 May 2019	Diamond Scientific Software, Controls and Computation (SSCC) Away Day	150
21 May 2019	Nexus Implementation Workshop	25
4 - 7 June 2019	Small Angle Scattering (SAS) Training School and S4SAS Conference	100
10 - 19 June 2019	EMBO Practical Course - High Throughput Protein Production & Crystallization	60
27 - 28 June 2019	Super Resolution Imaging Development Symposium	90
12 July 2019	Operando and In Situ Methods for Energy Materials Workshop	80
15 - 19 July 2019	International Workshop on Strong Correlations and Angle-Resolved Photoemission Spectroscopy (CORPES19)	130
24 - 26 July 2019	XPDF Workshop	30
10 September 2019	ImagingBioPro Workshop	50
26 September 2019	Quantitative Imaging of Electrochemical Interfaces Workshop	50
26 September 2019	SSCC Graduate Training Programme Away Day	15
14 October 2019	Early Career Scientist Symposium	100
15 - 16 October 2019	I19 Remote Access Training Course	18
24 - 25 October 2019	European Synchrotron Light Sources RF (ESLS-RF) Meeting	30
28 - 29 October 2019	MooNpics 3rd Workshop	30
4 - 5 November 2019	Photons and Neutrons for Research in Electrochemistry Workshop	60
5 November 2019	Dynamic Structural Biology Workshop: Examining the life sciences case for a UK XFEL	155
6 - 7 November 2019	HDMRX Workshop	27
6 - 7 November 2019	MX Workshop	30
6 - 7 November 2019	PYMCA Training Course	31
6 - 8 November 2019	MicroED Workshop	12
13 - 15 November 2019	eBIC CryoEM Sample Preparation Course	40
1 - 9 December 2019	Diamond Light Source-CCP4 Data Collection and Structure Solution Workshop	40
9 January 2020	Extreme Conditions Research Day	23
4 February 2020	Crystallography Student Meeting	45
10 - 14 February 2020	EPICS Collaboration Code-a-thon	35
20 - 21 February 2020	Beamline Jockey Workshop	35
25 - 26 February 2020	I19 EH2 Workshop	25
2 - 3 March 2020	HyperSpy Workshop	40
10 - 12 March 2020	X-ray Absorption Spectroscopy (XAS) Workshop	33
10 - 12 March 2020	PULPOKS Workshop	33

Governance and Management

Diamond Light Source Ltd was established in 2002 as a joint venture limited company funded by the UK Government via the Science and Technology Facilities Council (STFC), now under UK Research & Innovation (UKRI), and by the Wellcome Trust, owning 86% and 14% of the shares respectively. Diamond now employs almost 742 scientists, engineers, technicians and support staff from 43 countries worldwide. The Chief Executive and Directors are advised by committees representing key stakeholder groups, including the Science Advisory Committee (SAC), Diamond Industrial Science Committe (DISCo) and Diamond User Committee (DUC).

Diamond is free at the point of access for researchers accessing Diamond via peer review, and provided the results are published in the public domain for everyone's benefit. Allocation of beamtime is via a peer review process to select proposals on the basis of scientific merit and technical feasibility. Eight peer review panels meet twice a year to assess the proposals submitted for each six-month allocation period. Diamond also welcomes industrial researchers through a range of access modes including proprietary research.

Board of Directors

Prof Sir Adrian Smith (Chairman)
Director, Alan Turing Institute

Prof Andrew Harrison
Chief Executive Officer, Diamond Light Source

Marshall Davies
Business Advisor, Science and Technology Facilities Council

Prof Michael Fitzpatrick
Pro-Vice-Chancellor, Coventry University

Prof Mark Thomson
Executive Chair, Science and Technology Facilities Council

Prof Mike Turner
Acting Director, Wellcome Trust Science Division

Andrea Ward
Director of Finance & Corporate Services, Diamond Light Source

Prof Keith Wilson
Professor of Chemistry, University of York

Company Secretary
Andrew Richards, Diamond Light Source

As at April 2020

Executive

Prof Andrew Harrison took the helm as CEO of Diamond Light Source in January 2014. He was previously Director General of the Institut Laue-Langevin neutron source in Grenoble, France, where he had worked since 2006. With a background as an inorganic chemist and Professor of Solid State Chemistry at the University of Edinburgh, Prof Harrison brings a wealth of experience of scientific leadership to the organisation.

Prof Laurent Chapon joined Diamond as Director of Physical Sciences in 2016 from the Institut Laue-Langevin in Grenoble, France. Whilst there, Prof Chapon was Senior Fellow and Leader of the Diffraction Group for over five years. He is an expert in materials science as well as X-ray and neutron diffraction techniques. His principal interests include transmission metal oxides, frustrated oxides, and multiferroics.

Prof David Stuart is MRC Professor of Structural Biology at the University of Oxford, and Joint Head of the Division of Structural Biology at the Department of Clinical Medicine. He was appointed Director of Life Sciences at Diamond in 2008. His principal research interests include the structure of viruses and viral proteins as well as cellular proteins, especially those that interact with viruses.

Prof Richard Walker joined Diamond Light Source as Technical Director in January 2002. He was previously Director of the Light Sources Division at Sincrotrone Trieste in Italy, and prior to that he was a key member of the Daresbury Laboratory SRS team. He is a visiting Professor of Physics at the University of Oxford.

Andrea Ward joined Diamond as Director of Finance and Corporate Services in 2019, with 15 years' experience as a Senior Finance professional. During a 12-year tenure at Vertex Pharmaceuticals, she worked with the Board to lead finance and procurement functions in Europe, later moving to Canada with the business to assist with acquisition and commercialisation opportunities. Andrea has also worked at ResMed and the Ontario Lottery and Gaming Corporation.

Staffing and Financial Information

Outline Organisational Chart

Chief Executive's Office
Communications
Industrial Liaison
Safety, Health & Environment

Science Division

Science Groups:
Biological Cryo-Imaging
Crystallography
Imaging and Microscopy
Macromolecular Crystallography
Magnetic Materials
Soft Condensed Matter
Spectroscopy
Structures and Surfaces

Scientific Software, Controls & Computation Groups:
Accelerator Control Systems
Beamline Control Systems
Data Acquisition
Scientific Computing
Scientific Software

Detector Group
Experimental Hall Labs Services
Optics & Metrology
Planning & Projects Office
User Office

Technical Division
Accelerator Physics
Diagnostics
Engineering
Insertion Devices
Installation & Facility Management
Operations
Power Supplies
Radiofrequency Systems
Vacuum

Finance and Corporate Services
Business IT
Commercial Management, Governance & Legal
Finance
Human Resources
Procurement
Soft Facilities

Summary of Financial Data

	2009/10	2010/11	2011/12	2012/13	2013/14	2014/15	2015/16	2016/17	2017/18	2018/19	2019/20
Operating Costs £m	30.5	33.5	36.5	39.9	42.5	44.5	54.6	56.9	62.8	64.5	65.7
Total Staff (Year End)	401	419	438	481	507	534	582	609	639	680	742
Capital Expenditure – Operations £m	5.7	8.6	5.1	8.0	7.5	6.2	8.0	10.5	12.8	17.4	17.8
Phase II £m	22.0	16.2	9.9	2.8	0.8	0.2	0.0	0.0	0.0	0.0	0.0
Phase III £m	0.3	3.0	10.3	14.2	17.2	23.7	20.6	11.5	3.7	1.0	0.0
Other capital projects £m						4.8	5.6	7.3	4.3	5.3	1

Figures up to and including 2014/15 exclude VAT, thereafter figures include VAT.

Committee Membership

The Scientific Advisory Committee (SAC) advises the CEO and the Science Directors on the scientific and technical questions impacting the specification, design, commissioning and operation of the facility; experimental and user support facilities, and opportunities for scientific exploitation.

Dr Tom Hase (Chair)
University of Warwick (UK)

Dr Lisa Miller, (Vice-Chair)
Brookhaven National Lab/NSLS-II (USA)

Dr John Barker, Evotec
(DISCo Representative)

Dr Bridget Carragher
New York Center for Structural Biology (USA)

Prof John SO Evans
University of Durham (UK)

Prof Philip Hofmann
Aarhus University (Denmark)

Prof Peter Hatton
University of Durham (UK)

Prof Ken Lewtas
Lewtas, Lewtas Scientific (DISCo Representative)

Dr Adrian Mancuso
European XFEL

Prof Arwen Pearson
The Hamburg Centre of Ultrafast Imaging (Germany)

Dr Jörg Raabe
PSI (Switzerland)

Prof Andrea Russell
University of Southampton (UK) - (Chair of the DUC)

Prof Mary Ryan
Imperial College (UK)

Prof Christian Schroer
DESY (Germany)

Prof Sam Shaw
University of Manchester (UK)

Prof Titia Sixma
Netherlands Cancer Institute (Netherlands)

Prof Moniek Tromp
University of Groningen (Netherlands)

The Diamond Industrial Science Committee (DISCo) advises the CEO and Directors on opportunities for industry to be engaged in research at Diamond, industrial research priorities that will help shape operational strategy, including the best way to exploit the current suite of beamlines and to develop the case for investment in future beamlines, and to develop best practice for industrial engagement.

Dr Malcolm Skingle
GlaxoSmithKline (Chair)

Dr John Barker
Evotec

Dr Andrew Barrow
Rolls-Royce

Prof. Dave Brown
Institut de Recherches Servier

Dr Paul Collier
Johnson Matthey

Dr Rob Cooke
Sosei Heptares

Dr Cheryl Doherty
GlaxoSmithKline

Prof. Peter Dowding
Infineum

Prof. Jonathan Hyde
NNL

Dr Andrew Johnson
IQE

Dr Olga Kazakova
NPL

Prof. Ken Lewtas
Lewtas Science & Technologies

Dr Ellen Norman
RSSL

Dr John Pollard
Vertex Pharmaceuticals (Europe) Ltd

Dr Richard Storey
AstraZeneca

Dr Pamela Williams
Astex Pharmaceuticals

The Diamond User Committee (DUC) has been set as a platform for discussion between Diamond and the user community of matters relating to the operation and strategy of Diamond.

Dr Imad Ahmed
University of Oxford

Dr Arnaud Basle
University of Newcastle

Dr Gavin Bell
University of Warwick

Dr Jamie Blaza
The University of York

Dr David Briggs
The Francis Crick Institute

Dr Ann Chippindale
University of Reading

Dr Sean Connell
CIC bioGUNE

Dr Kevin Edmonds
The University of Nottingham

Dr Enrique Jimenez-Melero
The University of Manchester

Dr Tim Knowles
University of Birmingham

Dr Marcus Newton
University of Southampton

Dr Robin Perry
University College London

Prof Andrea Russell
University of Southampton (Chair)

Dr Neil Telling
Keele University

Dr Andrew Thomas
The University of Manchester

Dr Arwen Tyler
University of Leeds

Membership as at April 2020

Diamond Light Source Ltd
Harwell Science & Innovation Campus
Didcot, Oxfordshire OX11 0DE
Tel: +44 (0)1235 778 639
Fax: +44 (0)1235 778 499
www.diamond.ac.uk

Acknowledgement:
We would like to thank the authors and all
colleagues who contributed to this publication.

Printed on Forest Stewardship
Council (FSC) accredited paper stock.

Published Aug 2020